Dynamics of Sessile Droplet Evaporation in Laminar Convective Environments

Omar Jameel Abdulrazzaq Al-Rawi

Submitted in accordance with the requirements for the degree of
Doctor of Philosophy

The University of Leeds
Institute of Thermo-Fluids (iTF)
School of Mechanical Engineering

December, 2020

The candidate confirms that the work submitted is his own and that appropriate credit has been given where reference has been made to the work of others.

In the papers contributing to this thesis, the candidate (first author) carried out all the experiments involved simulations, analysis and preparation of the manuscripts. All other authors contributed by proof reading and providing insight on the discussions.

Papers contributing to this thesis

- Al-Rawi, Omar, and Wilson, Mark, *Influence of forced convection on the evaporation and internal dynamics inside of an array of salt solution droplets*, MATEC Web of Conferences, Vol. 240. EDP Sciences, 2018.

Acknowledgements

Firstly, I would like to express my deepest gratitude to my supervisor Dr Mark Wilson for the continuous support of my PhD study, for being such a supportive and encouraging supervisor, and for his immense knowledge. His guidance is invaluable and helped me on both an academic and personal level. I could not have imagined having a better advisor for my PhD study. I would also like to thank my co-supervisor Professor Nik Kapur for his valuable efforts for suggesting the current crucial work.

I am very grateful to the Higher Committee for Education Development in Iraq (HCED) for the fully funded scholarship granted to embark on this research. I would also like to thank Mr. Martin Callaghan for his great efforts in supporting me in using the High-Performance Computing machines to present this crucial work.

My deep thanks to the staff of University of Leeds – School of Mechanical Engineering for the great help and support they offered to complete my PhD. I would not forget any effort and advice that my colleagues provided during my PhD study.

Last but not the least, I would like to dedicate this work to my father and mother who have supported me throughout my life, and I could not achieve my dreams and to be in this position without their sacrifice, patience, and prayers. A very deep thanks to my wife, daughter, and son for being with me and supporting me in my life in general. A very big thanks to my brothers who are always pushing me towards achieving my dreams under all circumstances.

Abstract

Evaporation of multiple sessile droplets is a fundamental physical phenomenon encountered in many industrial and scientific applications, and attention is still directed towards understanding the complex physics controlling this process. This thesis presents a detailed numerical analysis of sessile droplet evaporation, focusing on the effects of a forced airflow over the droplets, and the effect of droplet arrangement with respect to the airflow on the interactions between droplets. A 3D transient diffusion-convection model fully coupled with the Arbitrary Lagrangian-Eulerian finite element method is used to allow the droplet shapes to evolve in response to local evaporation rates. An “infinite element domain” is used – seemingly for the first time in this context - to allow boundary conditions at infinity to be imposed appropriately using a much smaller computation domain for the natural convection condition than typically used previously. The thesis encompasses four study cases in order to determine the best droplet configuration in which droplets can evaporate independently from each other.

Firstly, the evaporation of an isolated single sessile droplet exposed to the forced airflow is investigated comprehensively, and a new mass transfer correlation for the Sherwood number in terms of Reynolds and Schmidt numbers is identified. The evaporation of a pair of sessile droplets arranged along a line either perpendicular or parallel to the airflow is then considered, focusing on the effects of droplet separation and air speed on the interaction of the droplets. Results reveal that increasing the forced convection or droplet separation accelerates the evaporation, and at sufficiently high air speed, the perpendicular droplets become effectively decoupled as the flow sweeps vapour out of the interaction region between the droplets. In contrast, the airflow produces a substantial difference in the evaporation rates of the parallel droplets, with the upstream droplet evaporating more rapidly than the perpendicularly aligned droplets, but the downstream droplet evaporation being slowed by the downstream vapour transport from the leading droplet.

The third part discussed in the thesis focuses on the internal dynamics and concentration distribution inside salt solution droplets under a forced convective environment. Findings emphasise that the air passing over the droplets causes a shear-induced circulation inside the droplets in addition to the buoyancy-driven flow by the density increase with increasing salinity. At sufficient air speed, much more uniform concentration fields are observable inside the droplets due to the dominance of the shear-induced flow over the gravity-driven flow. Findings also show that solute concentration levels in the downstream droplet are less than in the upstream droplet due to the effect of the downstream advection from the leading droplet. Further, the maximum speed of the circulation flow pattern inside the droplets caused by the forced airflow passing the droplets is approximately 1% of the forced air speed.

Finally, staggered droplet arrangements in which the second droplet is shifted laterally and downstream from the first droplet is considered in the fourth part of the thesis for achieving uniformity of evaporation behaviour across an array of multiple droplets. Predictions indicate that the lateral and downstream distances contribute together with the velocity of airflow in reducing the interaction in the gap between the droplets, and hence isolating the droplets from each other across the array.

Table of Contents

List of Figures

List of Tables

Nomenclature

Terms	Units	Description
a	m	Capillary length
A	m^2	Area
b	kg/(m^3 K)	Thermal gradient of saturated vapour concentration
Bo	-	Bond number
c	kg/m^3	Concentration
D	m/s^2	Fluid diffusivity
E	-	Evaporative cooling number
g	m/s^2	Gravitational acceleration
h	m/s	Mass transfer coefficient
H	-	Relative humidity of air
j	kg/(m^2 s)	Local total evaporative flux
J	Kg/s	Total evaporation rate of the droplet
k	N/(s K)	Thermal conductivity
$\mathbf{K}$	-	Unit vector in the z-direction
L	m	Length
L_{fg}	kJ/kg	Latent heat of vaporisation
m	kg	Mass of fluid
M	kg/mol	Molar mass of fluid
$\mathbf{n}$	-	Unit vector in the normal direction
P	Pa	Pressure
Pe	-	Peclet number
r	m	Droplet radius
R	J/(mol. K)	Universal gas constant
Re	-	Reynolds number
S	m	Droplet separation distance
Sc	-	Schmidt number
Sh	-	Sherwood number
t	s	Time
T	°C	Temperature
$\mathbf{u}$	m/s	Velocity vector

U	m/s	Fluid velocity
V	m^3	Droplet volume
We	-	Weber number
X	-	Mole fraction of solvent

Greek symbols

Terms	Units	Description
β	m^3/mol	Solution expansion coefficient
γ	N/m	Surface tension
θ	degree	Contact angle of a droplet
μ	Pa.s	Fluid dynamic viscosity
ρ	kg/m^3	Fluid density
σ	kg/m^3	Stress tensor
η	-	Shape factor
Γ	-	Droplet free surface
∞	-	Environmental conditions

Subscripts

a	Air
amb	Ambient
avg	Average
d	Droplet
$diff$	Diffusion
$entr$	Entrance
$evap$	Evaporation
g	Gas phase
l	Liquid phase
s	Surface or solid phase
sat	Saturated
sol	Solution
$sph.$	Sphere
v	Vapour

Chapter 1 Introduction

1.1 Droplets and their importance

A droplet as a scientific term is a small drop of liquid, and it is formed by the accumulation of liquid due to the intermolecular attraction between liquid molecules. This intermolecular attraction induces what is known as the surface tension phenomenon that makes the droplet take up a spherical shape to minimize the surface area of liquid as a results of the unbalanced attraction forces at the droplet surface [1]. Since the first interest in this topic by Thomas Young in the early 1800s, statistics show that the topic of “droplets” has been mentioned in more than 10000 articles in the last 100 years in different areas of research such as engineering, material science, chemistry, health and physical sciences fields, and so on, as shown in Figure 1-1 and Figure 1-2. This statistic was generated by searching Scopus for articles with “droplets” featured in the title, abstract or keywords. Therefore, due to its technological importance in this range of application, it is worth studying this fundamental topic in detail to open the gate for further future investigations.

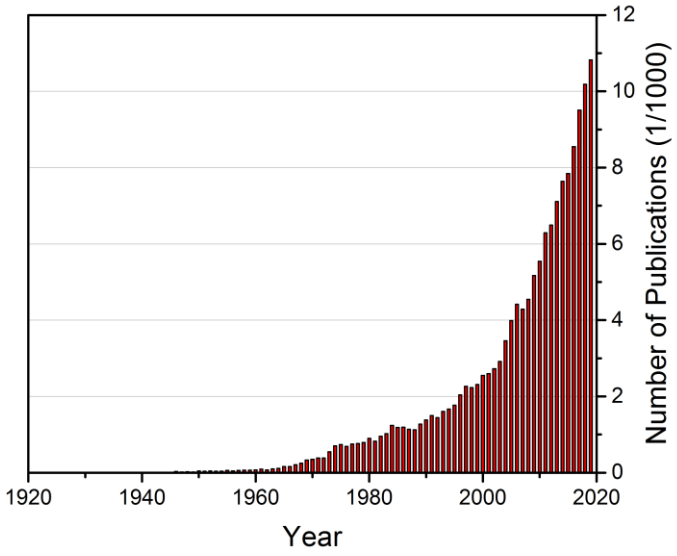

Figure 1-1: Number of papers referenced in the Scopus® database between 1919 and 2019 that feature “droplets” and their applications.

In general, there are three types of droplets in term of their positions which are [2]:

- A “pendant droplet” is suspended by a solid boundary. If such a droplet is able to grow (e.g. by condensation), eventually the increase of the droplet weight (gravity force) will overcome the forces of the surface tension, and the droplet will fall down into the surroundings inducing the second type of droplets.
- A “free droplet” moves freely through its surrounding fluid medium (usually air) without contacting any solid surface.

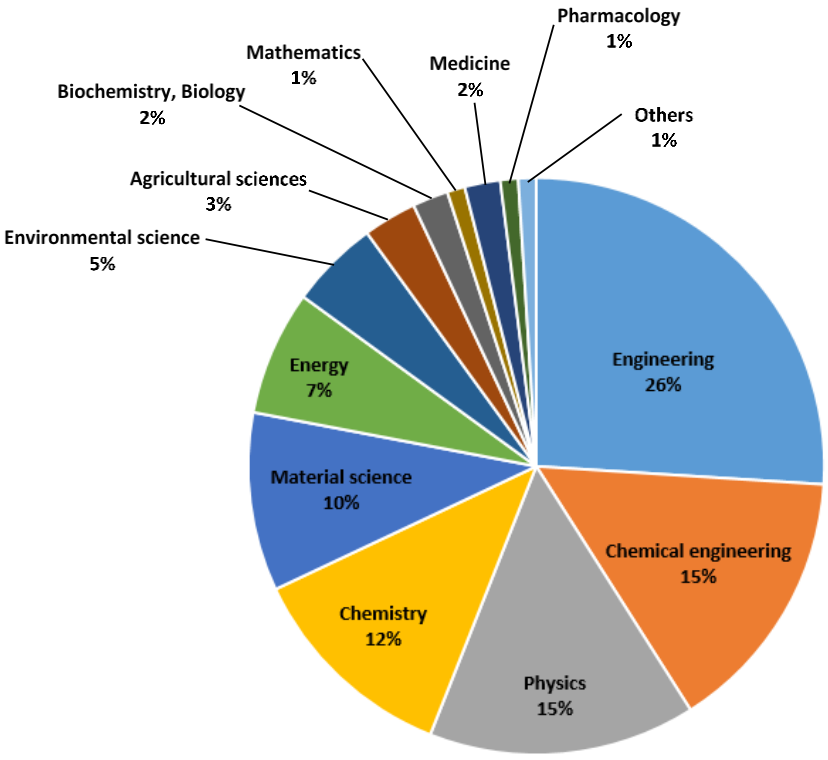

Figure 1-2: Subject areas regarding the topic of “droplets” Scopus® in 2019.

- A “sessile droplet” is one that is supported from below by a solid substrate in still ambient air/fluid.

The evaporative behaviour and internal dynamins inside each one of these three types of droplets might be different depending on mechanisms controlling its shape and evaporation, and interaction/movement with/within the surrounding. Here, attention will be focused towards the sessile droplet and the physics appearing during its evaporation; the fundamental mechanisms governing the

deposition pattern of colloidal suspended particles that are dispersed into the sessile droplet; and the ability to investigate this process in one of many practical applications.

Droplets generally are encountered in a wide variety of scientific and engineering applications, and even in nature such as rain, fog and dew. Their evaporation and drying are also involved in a variety of important industrial areas such as metallurgy, food processing, automotive, aerospace, chemicals, paper, power generation, medicine and pharmaceuticals. Good examples of these areas are: spray combustion (e.g., diesel engines, spark ignition engines, gas turbines, domestic heating boiler), spray drying (e.g., milk powder processing, food processing and chemical processing), spray cooling (e.g., cooling of nuclear cores, cooling of turbine blades), aerosol spray (e.g., firefighting, humidification/air conditioning and pollution/dust control), spray cleaning (e.g., gravel washing, vegetable cleaning and surface treatment), paint spray (e.g., substrate finishing and substrate coating), metal welding/soldering, lubrication, and ink-jet printing applications [3-6], see Figure 1-3 as an example of some these applications of the droplet evaporation. Furthermore, the phenomena of droplet resting, spreading, evaporating and drying on a solid substrate, which are often accompanied by simultaneous heat and mass transfer, also attract a significant interest in a wide range of applications. All these physics in association with the phenomenon of particles deposition on the substrates after droplet drying have been widely investigated in order to utilise them in appropriate applications [7].

On the medical side, large numbers of scientific studies have been published in recent years to exploit the advantages of this process in this type of applications. For example, there is a wide usage of the droplet evaporation process in medical diagnostics fields such as drug targeting and bioseparation and magnetic particles applications [8]. Magnetic particles recently have attracted the attention of many scientists and engineers because of their essential usages in cancer diagnosis (MRI), hyperthermia, tissue engineering, and magnetic separation [9-12]. Christopher et al. [13] exploited the occurrence of the deposition of particles phenomenon for diagnosing Malaria as a novel investigation. Moreover, recently, a multiscale investigation of blood droplet drying has been conducted to visualise

the red blood cell deposition during the desiccation [14]. An interesting investigation is carried out on the patterns in dried of whole human blood droplets that can be changed due to presence of some diseases [15]. In line with this area, pharmaceutical particle engineering also involves the micronisation process to form a suitable size of particle during the drying of solvent [16].

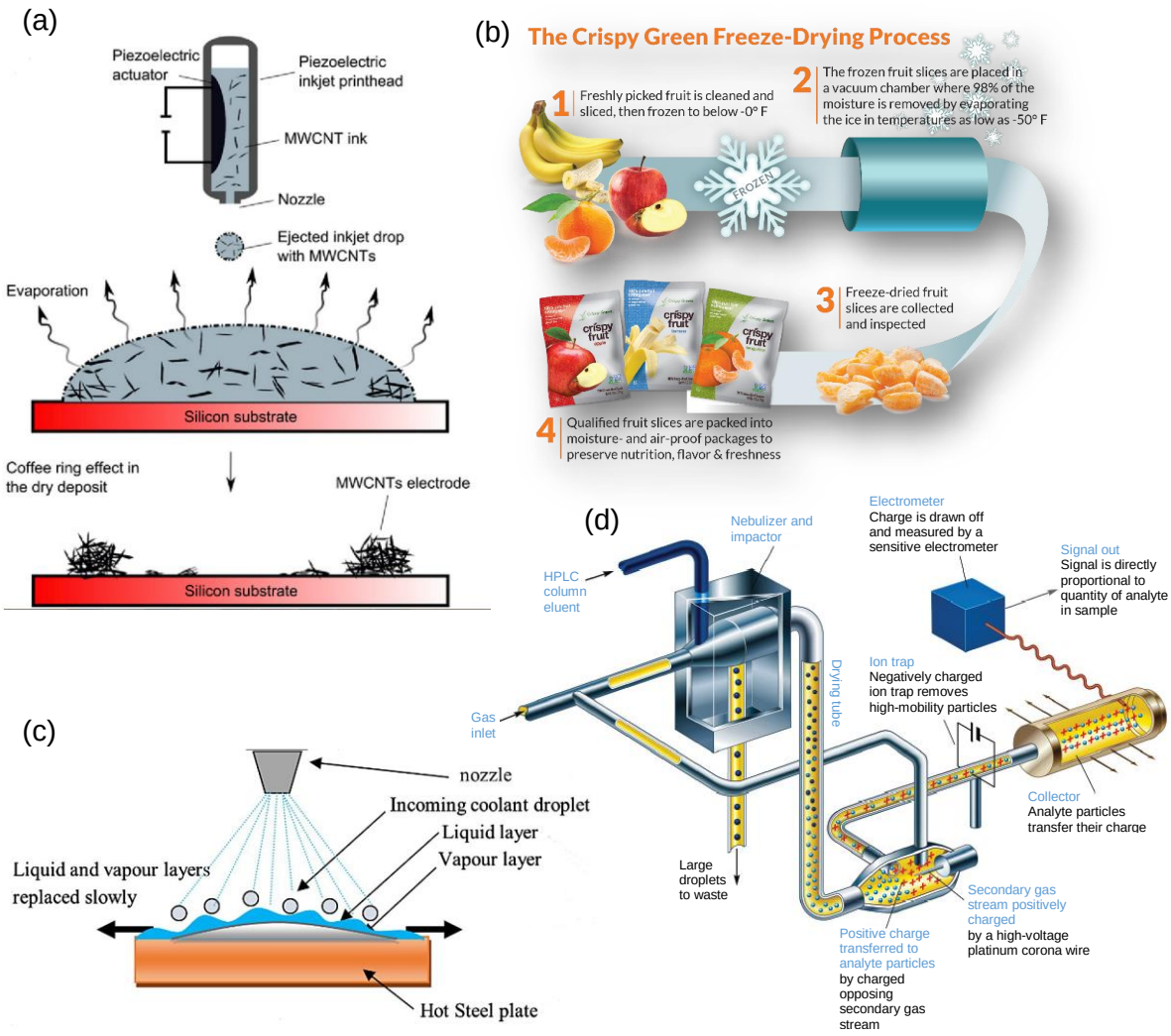

Figure 1-3: illustration of some examples of the droplet evaporation applications; (a) inkjet printing [17], (b) food processing “available from: http://fiberisthefuture.com/category/fruit/, (c) spray cooling process [18], and (d) pharmaceuticals manufacturing process [19]. Reprinted from above references, Copyright (2020), with permission from publishers.

On another side, the phenomenon of the deposition of micro and nano particles on the substrates has been employed in inkjet printing and 3D printing applications that have been improved in order to incorporate these materials into practical manufacturing processes such as fabricating organic transistors, full-colour emissive polymer displays, and functional ceramics [20]. The type and shape of dispersed suspended particles in the inkjet droplet and the composition of ink solution also have a significant role in the production of accurate quantities of material where it was noticed that the dispersion of silica micro-particles in different ink compositions gave a homogenous pattern of the particles deposition as shown in Figure 1-4 [21].

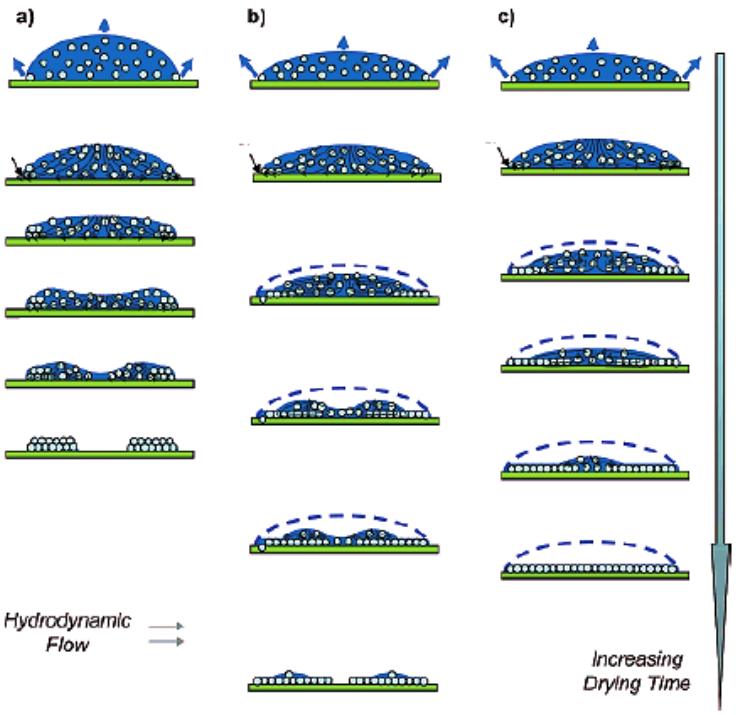

Figure 1-4: Schematic cross-section view of the morphologies of SiO_2 particle deposits produced from three different ink compositions; (a) water-based ink; (b) water/diethylene glycol (DEG)-based ink; and (c) water/ formamide (FA)-based ink. Reprinted with permission from ref. 22. Copyright (2020) by the American Physical Society.

Moreover, the phenomenon of particles deposition on the substrates has been recently used in the so-called drop coating deposition Raman (DCDR) technique to enhance the sensitivity of Raman spectroscopy that is used to observe vibrational, rotational, and other low-frequency modes in a system [22]. Droplets are also used in fabrication fields where the deposition of suspension particles during droplet drying is exploited to fabricate transparent flexible conductors which are commonly used in many modern electronic devices such as touch screens for smart phones [23, 24]. In addition, droplet formation may be considered a key step for synthesising some semiconductor thin films and composite materials [25].

In some other processes, breakup of a liquid is essential in droplet generation where there are several techniques to achieve this goal. Atomisation is one of the important techniques that are used to generate droplets by a variety of mechanisms; mechanically, electrostatically, aerodynamically, or ultrasonically [26]. These techniques have been used in a wide range of applications such as spray combustion, spray drying, spray cooling, aerosol spray, spray cleaning, and paint spray as are mentioned earlier. Spray combustion is a commonly important process in the operation of diesel engines where it involves the atomisation and burning of liquid fuels. Meanwhile, spray drying also aims to atomise a solution or suspension in a hot gaseous surrounding in order to dry the solution and produce solid powder. In both processes, selecting the appropriate atomisers and atomisation media are necessary parameters to achieve the optimum performance, and to avoid any undesirable amount of solute remaining [3].

In conjunction with the spray technique, the strong need for effective thermal management solutions, which provide higher heat flux cooling for future microelectronic systems, has recently attracted the attention from many of industrial companies due to the inefficient conventional techniques such as air cooling and water cooling systems [27, 28]. Spray cooling with phase change appears to be the feasible method to dissipate high heat from surfaces in comparison with other effective cooling techniques, and has been utilised in remove space such as fire protection, cooling of hot gases and substrates, high performance electronic devices, metal production, and biomedical industry [29, 30].

Table 1-1 shows a comparison of the respective heat flux of comparative cooling techniques [30]. It can be seen clearly that although micro-channel (790 W/cm^2), sub-cooled flow boiling (129 W/cm^2) and jet impingement (1820 W/cm^2) cooling methods have very high heat fluxes, spray cooling has been preferred over the other techniques due to its characteristics which are: high heat transfer due to exploiting the phase-change process, uniformity of heat removal, small fluid inventory, low droplet impact velocity, and no temperature overshoot.

Table 1-1: Cooling Techniques and Respective Heat Fluxes [30].

Mechanism	**Cooling Method**	**Highest Heat Flux (W/cm^2)**
Single Phase	Free Air Convection	15
Single Phase	Forced Air Convection (Heat Sink with a fan)	35
Single Phase	Natural Convection with FC	0.1-3
Single Phase	Natural Convection with water	5-90
Two Phase	Heat Pipes (water)	250
Single Phase	Micro-channel	790
Electrical	Peltier Cooler	125
Two phase	Pool boiling with porous media	140
Two Phase	Sub-cooled Flow Boiling	129
Two Phase	Micro-channel Boiling	275
Two Phase	Spray Cooling	1200
Two Phase	Jet Impingement	1820

1.2 Evaporation of interacting droplets

Most of the practical applications for example; spray coating, inkjet printing and food processing involve multiple droplets spontaneously evaporating in proximity to each other. An interaction in the region between droplets will be generated as a result of the influence of each droplet on others via the liquid vapour space

around each droplet. This subject has recently attracted the attention of researchers due to its importance, and this interaction might lead to essential physical changes inside those droplets and in the surrounding space. For example, many researchers [31] mentioned in their studies that the liquid vapour accumulated in the nearest point between droplets forms a weak area of evaporation, and hence less movement of particles towards this area compared to the rest regions of the droplet. In addition, Pradhan and Panigrahi [32] observed experimentally and numerically the influence between the interacting droplets on the hydrodynamics inside those droplet in comparison with the evaporation of an isolated droplet. As a result of this interaction, the evaporation rate of the interacting droplets is less than for the isolated droplet, and hence longer lifetime of these droplets.

However, reducing the interaction effects between droplets is crucial to increase the rates of evaporation and decrease the lifetime of these droplets as it is important for some applications such as cooling of hot surfaces. Therefore, increasing the gap between droplets [33] might help in reducing the liquid vapour concentration levels in the gap between droplets, and consequently increasing the evaporation rates of those droplets. Providing a gentle forced air convection is also essentially for sweeping the liquid vapour away from the droplets to reduce the concentration levels of the liquid vapour around the droplets, and hence increase the rate of evaporation [34]. The subject of the evaporation of multiple droplets, as one of the objectives of the present work, will be discussed further in the next chapters.

1.3 Aim of the research

The aim of this research is to understand the effect of a forced convection on the evaporative behaviour of multiple sessile droplets arranged in various configurations with respect to the overlying airflow. This includes the internal dynamics and concentration distributions of salt solutions, with the purpose of

achieving uniformity in the behaviours within the droplet array. To achieve this aim, the research has following objectives:

1. Develop a transient 3D numerical model of sessile droplet evaporation under forced laminar airflow.
2. Validate the simulation approach using previous pioneering experimental and numerical works on the evaporation of a single sessile droplet under a natural convection.
3. Quantify the effect of a forced airflow on the evaporation of a single sessile droplet.
4. Explore how an airflow affects the evaporation of a pair of sessile droplets arranged either parallel or perpendicular to the airflow.
5. Extend the model to include the evaporation of a salt solution droplet and analyse the effects of a forced airflow and droplet placement on the internal dynamics of salt solution droplets.

1.4 Organisation of research

This thesis contains nine chapters which cover the aim of the present numerical work. After presenting the importance of droplets in the academic and industrial applications in Chapter 1, literature review on the fundamental concepts of droplet evaporation under different situations, and hence internal dynamics and patterns of the deposited colloidal particles inside these droplets are demonstrated in Chapter 2. In addition, a review of the most previous numerical studies conducted in such problem of research is summarised in this chapter. The primary focus of Chapter 3 is to describe the problem statement of the evaporation of a single droplet under natural and forced convective environments with the governing equations after discussing the fundamental considerations of the modelling process involved: numerical methods, the computer platforms, and the suitable tool for solving the current problem of interest. Chapter 4 illustrates the evaluating of the numerical models described in Chapter 3 to check whether the models are well-built, and after that validating these models against experimental and numerical work available in the literature.

Chapter 5 addresses the influence of a gentle forced air convection on the evaporative behaviour of a single sessile droplet as a basis step for more complicated problems while, the evaporation of a pair of neighbouring sessile droplets in different alignments and at different droplet separations under forced convective environment is discussed in Chapter 6. Internal dynamics within sessile droplet evaporation affected by a source of a forced air convection is illustrated in Chapter 7. In Chapter 8, the capability of achieving uniformity in the evaporation rates within a regular array of multiple droplets exposed to a forced airflow is addressed via modelling the evaporation of these droplets in different alignments and separation distances. Finally, the most important results, conclusions, significance and limitation of the numerical model, and the recommended future work are summarised in Chapter 9.

Chapter 2 Literature review

2.1 Evaporation of droplets

Evaporation is the process by which a fluid changes from its liquid state to its gaseous state. During this intrinsic phenomenon, liquid molecules obtain a certain level of kinetic energy, which is represented by the latent heat of vaporisation, in order to transfer from the liquid phase such as water to the gas phase such as air environment through the liquid/gas interface, as shown in Figure 2-1 [35]. The latent heat of vaporisation is drawn out from the liquid/gas interface where the available amount of this kinetic energy at the interface influences the rate of evaporation [36, 37]. Several situations and factors control the evaporation process; however, the basis reason for the occurrence of evaporation (i.e., transmission of molecules), as a natural state, is that the atmosphere in the adjacent area of the liquid/gas interface is not saturated with the vapour of the liquid [38].

Nature provides many applications that are characterised by the evaporation phenomenon, starting from a droplet that moves freely in atmosphere to a droplet that rests on a solid substrate. This phenomenon has taken the attention of many engineers and researchers in order to implement it in many industrial and research applications. Several comprehensive review articles have been published in order to give a thorough history of mathematical and experimental work made in the evaporation of droplets such as Mugele and Baret [39], Sazhin [40], Erbil [2, 41], Eral et al. [42], Sefiane [43], Larson [44], Thiele [7], Kovalchuk et al. [45], Askounis et al. [46], Zhong et al. [47], and very recently Cordero et al. [48], Brutin and Starov [49], Mampallil et al. [50], Breitenbach et al. [51], Dhar [52], and so on.

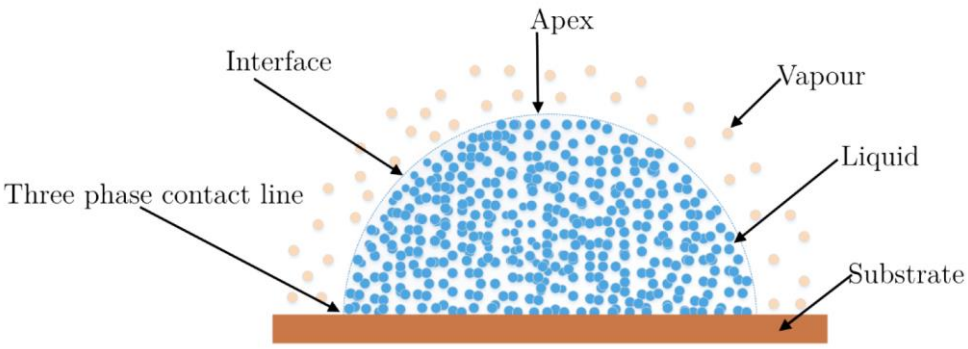

Figure 2-1: Features of a sessile droplet resting on a solid substrate [53].

2.1.1 Free droplets

Droplets can have different shapes depending on the situation and application, such as a sphere, when it is sprayed in a space, and this droplet is commonly called ‘’a free droplet’’. The evaporation of free droplets is considered an important topic of interest due to its crucial role in many of applications starting from natural processes such as fog, rain and snow, and not ending in engineering applications including spray drying and production of fine powder, spray cooling, medical care and fuel injection into combustion engines [54-59]. Under natural conditions, the evaporation process of the droplet that moves irregularly relative to a medium (i.e. freely falling) with varying temperature and vapour concentration is extremely complex, where a large portion of its mass is lost under a non-stationary process. In addition, this phenomenon occurs under three different mechanisms of heat transfer which are conduction, convection and radiation [60], and the mechanism of the liquid vapour mass transfer from the droplet surface becomes convective instead of diffusive [61]. Maxwell was the first to obtain the basic equations of droplet evaporation depending on a number of simplifying assumptions. As a result, “quasi-stationary” evaporation of the droplet is the basis of a lot of studies; this is appropriate when the diffusion process dominates the evaporation of the droplet during its movement into the medium [62].

Due to the importance of such common phenomenon, with wide industrial applications, great efforts have been made on evaporating of pure, bi-component and multicomponent liquid droplets at different droplet sizes and different conditions of temperature and pressure, in order to clarify the physics behind this fundamental phenomenon through a simple evaporation model [63-65]. The first

attempt to measure the rate of evaporation for free droplets with micrometre sized was done by Gudris and Kulikova in 1924 [66]. Following them Nestle in 1932 [67] who showed that at a saturated atmosphere with the liquid vapour, the evaporation process of the micro-sized droplets differs due to the higher pressure vapour of droplets. Woodland and Mack [68], and Shereshefsky and Steckler [69] used different liquids (phthalate and n-dibutyl phthalate respectively) with different radii (0.7-2.0 μm and 0.5-3.0 μm respectively) to examine the evaporation rate at the surface of the freely falling and stationary droplets. Their results showed that the stationary droplets evaporate slightly slower than other ones.

Since the steady-state evaporation model of a droplet in a stationary environment introduced by Spalding [70], progress has been continuously reviewed through years to accurately predict the effect of convection heat and mass transfer between the surface of the evaporating droplet and the surrounding environment when a relative velocity exists between them such as, Willians [71], Law [72], Sazhin [40], and recently Zhifu et al. [73] and Agrawal et al. [74]. The classical relations produced by Ranz and Marshall [75, 76] are widely employed for estimating the evaporation rate for a single spherical droplet subjected to a moving gas.

Meanwhile, the evaporation of the droplets with a large size has also attracted the attention of many researchers. An experimental study on water and other volatile organic liquid droplets with size 1-2 mm was done by Langstroth et al. [77] in order to determine the rate of evaporation at the surface of the droplets. The findings revealed that volatile droplets have surface temperature lower than their bulk temperature. In addition, an essential monograph on the evaporation of both millimetre and micrometre droplets was produced by Fuchs in 1959 [60] where depending on the basic equations of Maxwell and Stefan, new equations of the quasi-stationary droplet evaporation were derived. Since that time and until now, this issue is still under consideration, and numerous investigations have been conducted on this area. Imaoka et al. [64] through their numerical study on the effect of droplet interactions in symmetric, multiple-droplet arrays found there is a significant reduction in the rate of evaporation of the droplets due to the small spacing between the droplets within the arrays. Brenn et al. [63] and Sazhin et

al. [65] also based on the modelling concept to determine the evaporation rate for several bi-component and multicomponent liquid droplets.

2.1.2 Pendant droplets

When a droplet suspending from a solid surface, it takes the shape of the pendant as mentioned previously. In recent times, this type of droplets pushes the attention of researchers towards the dynamics inside these droplets during their evaporation due to the independence on the interfacial phenomena since the surface tension interaction will be less compared to the gravity forces. The concept of pendant droplet evaporation does not differ totally from the free droplet evaporation except part of the droplet surface will be in contact with a solid surface. Consequently, it will be dealt as a sessile droplet at that part of surface except the gravity force opposes the surface tension force in the pendant droplet trying to pull the droplet away from the supporting surface, whereas the gravity and surface tension forces act in same direction trying to press the droplet against the solid surface. Since the first work done by Godsave [78], numerous of studies have been conducted to analyse the characteristics changes in flow behaviour and transfer mechanism as well during the evaporation of this type of droplets such as Rossow [79], Pradhan and Panigrahi [80], and very recently Jaiswal et al. [81], Daniel et al. [82], Praveen et al. [83], Sterlyagov et al. [84] and Li et al. [85].

2.1.3 Pure liquid sessile droplets

The evaporation process of sessile droplets is important for numerous applications such as inkjet printing, the production of thin film coating, biochemical assays, deposition of DNA/RNA micro-arrays and micro/nano fabrication [2]. Thus, the understanding the fundamental physics of the sessile droplets evaporation are essential to understand the factors influencing the rate of evaporation of these kind of droplets and dynamics inside droplets.

Fundamental concepts

The phrase ‘’sessile droplet’’ describes a liquid droplet setting on a solid substrate in still air where its spreading on the substrate is limited by a three phase contact

line (i.e., the edge of the droplet) and properties of the substrate. Depending upon its nature, the droplet can either fully spread on the substrate making a thin liquid layer or partially spread on the substrate making a spherical-cap shape. Based on the principles introduced by Thomas Young in 1805 [86], the shape of the droplet is controlled by the surface tension that is caused by the inter-molecular attraction between molecules. The contact angle of the sessile droplet, which depends on the interfacial forces between the liquid-gas (γ), substrate-liquid (γ_{sl}) and substrate-gas (γ_{sg}), and the physical characteristic of both liquid and substrate, also influences the shape of the droplet, $\gamma \cos\theta_Y = \gamma_{sg} - \gamma_{sl}$, as shown in Figure 2-2. Spreading and wetting phenomena are also important interesting areas that are common occurrence in nature and everyday life, and they are required in many practical processes (for instance, metallic inks for inkjet printing and drying for medical applications). The wettability of a liquid on a substrate is governed by the contact angle of the droplet depositing on this substrate. When the contact angle is small ($\theta < 90^{\circ}$), the wettability of this liquid is large, and as a result the substrate is considered hydrophilic. Otherwise, if the contact angle is large ($\theta > 90^{\circ}$), the wettability of this liquid is small, and the substrate is considered hydrophobic. In special cases, when the substrate is rough, the contact angle might exceed 150°, and such substrate is called super-hydrophobic [87]. From above, it is noticeable that there is a complexity of this subject although the geometry of the sessile droplet is very simple. This is due to the interplay between the evaporation process and physics occurring inside and outside the droplet. Moreover, the nature of the fluid, the atmosphere surrounding the droplet, and the full coupling with substrate increase the complexity of the process. Therefore, it is important to define a simple situation to well understand the fundamental mechanism of this process.

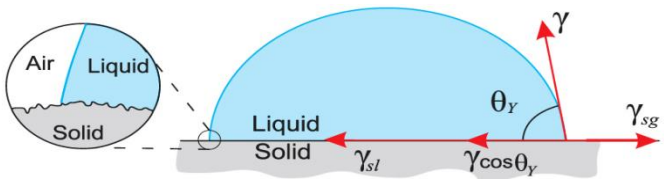

Figure 2-2: Schematic illustration of a sessile droplet setting on a substrate showing the three interfacial forces, contact angle and contact line [87].

The first opinion of the evaporation process of the droplets, as mentioned previously, was introduced by Maxwell in 1877 [57] where he think that the evaporation occurs as a pure diffusion-controlled depending on the difference in vapour concentration between the droplet surface and the surrounding air. The mathematical model derived by Maxwell assumes a spherical shape for the droplet floating in still air where the rate of mass loss by evaporation can be expressed as;

$$-\frac{dm}{dt} = -4\pi \mathrm{R}_s{}^2 D_v \frac{dC}{dR} \tag{2.1}$$

where, *m,* is the mass, *t,* is the time, *R* is the radial distance from the droplet centre, D_v, is the diffusion coefficient of the vapour, and *C,* is the vapour concentration. Based on the boundary conditions that surround the droplet during its travelling into air, after the integration the evaporation rate equation will be as shown;

$$\left.\begin{array}{ll} C = C_\infty ; & R = R_\infty \\ C = C_s ; & R = R_s \end{array}\right\} \tag{2.2}$$

$$-\frac{dm}{dt} = 4\pi D_v R_s (C_s - C_\infty) \tag{2.3}$$

where, R_s, is the radius of the spherical droplet, C_s, is the vapour concentration at the surface of spherical droplet, and C_∞ is the vapour concentration far away from the droplet surface, R_∞ . The above equation can be written in terms of the rate of volume loss by evaporation;

$$-\rho_L \frac{dV}{dt} = 4\pi D_v R_s (C_s - C_\infty) \tag{2.4}$$

where, *V*, is the volume of the spherical droplet, and ρ_L, is the density of the droplet liquid. The main limitation of Maxwell's equation is the absence of the effect of a substrate below the droplet where the vapour is prevented from diffusing at the substrate region. Therefore, Picknett and Bexon in 1977 [57] took this effect into account and developed Maxwell's equation by added factor $f(\theta)$, which is a function of the contact angle, to reduce the rate of evaporation of the sessile droplet. Thus, the rate of evaporation of the sessile droplet is given as;

$$-\frac{dV}{dt} = \frac{4\pi D_v R_s}{\rho_L}(C_s - C_\infty) f(\theta) \quad (2.5)$$

Further studies in this area have proved that Maxwell's hypothesis is incomplete, since the evaporation basically consists of two simultaneous processes which are heat and mass transfer. The heat required to evaporate the droplet is transferred from the warm surroundings to the surface of the droplet by conduction, convection and radiation, while the vapour induced by the evaporation is transferred back into the surrounding by diffusion and convection [2].

Based on the study of Picknett and Bexon [57], it is noticed that the profile evolution of the droplet volume decreases almost linearly with time, and contact line and contact angle of the droplet pass through three distinctive regimes during the real evaporation process which are illustrated in Figure 2-3. These three regimes are [43]:

- Constant contact area regime (CCR) which starts at the time that the droplet has spread on the substrate. In this regime, the droplet evaporates with constant contact line (pinned to the substrate) while the contact angle and the height of the droplet falls.
- Constant contact angle regime (CCA). Once the contact angle attains a critical value, the second regime starts with a constant contact angle and decreases contact line (de-pinned to the substrate).
- Mixed regime which the droplet evaporates with a combination of both regimes. In this regime, both the contact line and the contact angle decrease sharply until the droplet completely evaporates.

Birdi et al [88] also confirmed the observations of Picknett and Bexon studies during their experimental study on a sessile water droplet setting on a glass solid substrate. Findings revealed that the rate of evaporation is linearly proportional to the contact radius where it remains constant unlike the contact angle that reduces during evaporation process. Furthermore, Hu and Larson [89], through their experimental and numerical work on a water sessile droplet with pinned contact line, confirmed the findings of Picknett and Bexon in terms the volume temporal evolution, and observed that the critical contact angle at which the

contact line starts receding is about 2-4º. In contrast, Sefiane and Tadrist [90] studied the evaporating of de-pinning contact line droplet under three conditions, which are; reduced pressure environment, controlled substrate temperature and addition of surfactant solution. They found that unbalanced Young forces at the droplet edge seemed the responsible mechanism behind the de-pinning phenomenon. In some practical conditions, a droplet evaporates under different regime, which is termed by Stauber et al. [91] as a 'stick-slide' mode. This mode of droplet evaporation involves a combination of the two extreme regimes, i.e. constant contact area and constant contact angle Moreover, physical properties of the droplet liquid itself, such as density, molecular weight, latent heat of vaporisation and diffusion coefficient of water vapour in the air, also have a significant influence on the evaporation behaviour of the sessile droplet as was investigated by Fang et at, [92].

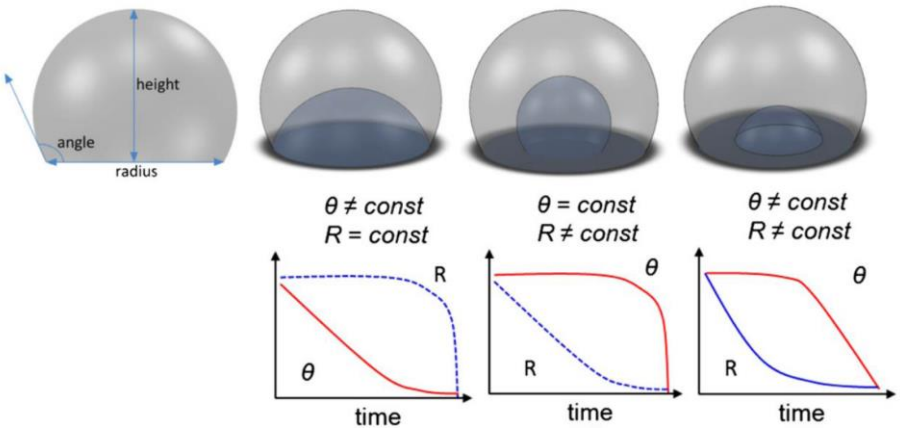

Figure 2-3: Schematic illustration of the evaporation regimes of the sessile droplet [93].

Influencing factors

Since Maxwell's time, much research has followed his hypothesis and has shown other factors affect the evaporation rate of the droplets and the particles deposition patterns inside those droplets such as profile of the droplet (i.e., contact line and contact angle), properties of the liquid and substrate upon which the droplet is deposited, and vapour pressure [45]. Cachile et al. [94, 95] and Poulard et al. [96] found through their experimental and theoretical study on a

droplet evaporation of pure, completely wetting liquid in the situation of no pinning contact line that the volatility of liquid and the properties of wetting film, which left on a substrate, controlled the mechanism of the evaporation. Moreover, the evaporation rate before the droplet disappearance becomes approximately constant due to the strong decrease of contact angle at this period. Further study was conducted by Guena et al. on different types of droplet liquids (water, alkanes and polydimethylsiloxane oligomers) resting on fully wetted silicon wafers surfaces under normal conditions [97]. Thermal gradients, gravity and the convection in the gas-phase were eliminated in this experimental study to prove the validity of the stationary diffusion theory driven the evaporation process. The validation results shown a good agreement for the droplet radius profile and contact angle profile in the case of water and alkanes unlikely with the polydimethylsiloxane oligomers droplets. In another direction, the contact line of the sessile droplet has a significant effect on the spreading and evaporation of droplets on substrates, where Haley and Miksis [98] investigated this effect numerically through a viscous droplet spreading by the use of lubrication theory. Lee et al. [99] also monitored the pattern of the droplet base radius, the contact angle and the height of alkane sessile droplet during spreading/evaporation processes in the case of complete wetting glass substrate. Experimental results confirmed that the change of volume of droplet is linearly proportional with the radius of droplet base as well as, theoretical curves for radius, contact angle, volume, and spreading/evaporation velocities with time were produced. In addition, Shahidzadeh-Bonn et al. [100] studied in the same field and at the same conditions, and concluded that the rate of evaporation, as a function of the droplet radius, follows this correlation $R \propto (t_o - t)^{1/2}$ in the case of organic liquids. Very recently, Maatar et al. [101] and Schweigler et al. [102] numerically investigate how does the contact line affect essentially the evaporative behaviour of the droplet.

In addition, the mathematical model, which was presented by Dunn et al. [103] for a thin axisymmetric sessile droplet with a pinned contact line, showed a significant dependence of the coefficient of the vapour diffusion in the atmosphere on the atmospheric pressure. Same results were obtained by Sefiane et al. [104] where they used three different ambient gases, which are: helium, nitrogen and

carbon dioxide, at different reduced pressure (40 – 1000 mbar) in order to investigate the influence of these gases on the evaporation of sessile water droplets. Different substrates which are: aluminium, titanium, Macor and polytetrafluoroethylene, were used to achieve this investigation. Observations revealed that for all ambient gases, reducing the atmosphere pressure increases the evaporation rate of sessile water droplets due to the increase of the diffusion coefficient of water vapour in the atmosphere. Surrounding humidity also has a significant role in the increase the speed of the spreading rate, where in the case of 100% humidity, super-spreading occurs. Boulogne et al. recently examined how the liquid vapour surrounding a droplet affects the evaporation mode, and hence the particles deposition inside the droplet [105].

A number of investigations has revolved around the essential influence of substrate properties on the rate of the sessile droplet evaporation, and the patterns of particles deposition on the substrate. Sefiane [106] conducted an experimental study to demonstrate the evaporation rate of sessile water droplets on two types of substrates. Aluminium and PTFE under reduced pressure were used during the experimental study. Results showed that the evaporation process on aluminium is faster than on PTFE due to the higher thermal conductivity of aluminium and the higher contact angle on PTFE which lead to lower evaporation rate. Also, David et al. [107] examined the influence of thermal properties of substrates on the evaporation rate of sessile water droplets with different values of thermal conductivity. The experimental findings revealed that the evaporation rate is much influenced by thermal properties of the substrate especially for high evaporation rate. In addition, in the case of thermal insulating of the substrate, an important cooling effect is provided to the droplet. Moreover, Dunn et al. [103, 108] demonstrated both experimentally and numerically the strong dependency of the evaporation rate on the thermal conductivity of the substrate, where a significant increase in the evaporation rate occurs with the increase of heat conductivity of the substrate. Interested results were obtained from the mathematical model that was carried out by Nagornov and Starostin [109] by the use of FEM with COMSOL software®. The numerical results showed that in the case of the substrate size is larger than the droplet radius, further heat flux releases at the edge of the droplet due to the additional horizontal heat flux at the

extra area. Researchers still continuous investigating experimentally and numerically the effect of thermal properties of substrates on the evaporative behaviour of droplets such as Bazargan and Stoeber [110], Li et al. [111] and Barash [112] where both showed that the shorter evaporation time is at the higher thermal conductivity of substrates, whereas other parameters such contact angle and volume are on the contrary. Further, the flow field patterns inside droplets can be controlled by selecting substrates with appropriate properties.

Meanwhile, other studies have been focused on the influence of the texture of the substrate on the dynamics of evaporation. Zhu et al. [113] conducted an experimental investigation to explain the spreading process of liquids containing different types of silicone surfactants on hydrophobic surfaces. The experimental data indicated that a substrate roughness has a dramatic effect on the spreading rate where will be faster than that on other substrates. Misyura [114, 115] noticed experimentally that the evaporation time of a water droplet on structured surface is less than on smooth surface while the heat transfer coefficient is on the contrary. In addition, Stauber et al. found that when a droplet evaporates on strongly hydrophobic substrate, the two extremes regimes of the droplet evaporation become indistinguishable [116]. Further, it was found that the chemical patterned surface is able not only in enhancing the evaporation process but also changing the evaporation regimes [117]. Coating of substrates also has a significant effect on the evaporation rate of droplets since an increasing of up to 20% in the evaporation rate is observed on the substrate with nanotube coating compared to the substrate without coating [118]. Very recently, Dhar et al. [119] found that the curvature of the substrate surface (i.e. increasing the convexity or concavity of the surface) strongly governs the flow field inside sessile droplets resting on a super-hydrophobic surfaces [119].

Moreover, heating of substrates also has been investigated in a wide range where Dash and Garimella [120] experimentally examined the evaporation of sessile droplets resting on hydrophobic and super-hydrophobic heated substrates. Different results were observed; the constant contact angle regime was the primary mode of the evaporating droplet under these conditions. Gao et al. recently observed that when droplets evaporate under constant heat flux in the range from 1153 W/m^2 to 6919 W/m^2, the constant contact radius regime is

dominant during the most droplet evaporation time on both hydrophilic and hydrophobic surface [121]. McHale et al. [122] also used super-hydrophobic substrates which composed of tall circular pillars with (5-15µm) of polymer photoresist to show the behaviour of small sessile droplets on these types of substrates. The results were mixed; the evaporation of some droplets followed the Cassie-Baxter mode where droplets sit partially in the air, while the others followed the Wenzel-mode (i.e. the droplets fill in between the pillars), as shown in Figure 2-4. Another study on the effect of the roughness on the wettability of the substrates was done by Duursma et al. [123] where they found that there is a significant pinning of the contact line on the substrates with a large size of roughness. Recently, Zhang et al. [124] studied the effect of surface roughness on enhancing the coffee-ring effect. They found that increasing roughness of the surface changes the patterns of particles deposition, and increases the evaporation rate as well. However, although a wide range of investigations have been published on the evaporation of the sessile droplets and the factors and mechanisms controlling it, there is still a need for many accurate theoretical and experimental studies to well understand the fundamental basis of this important phenomenon.

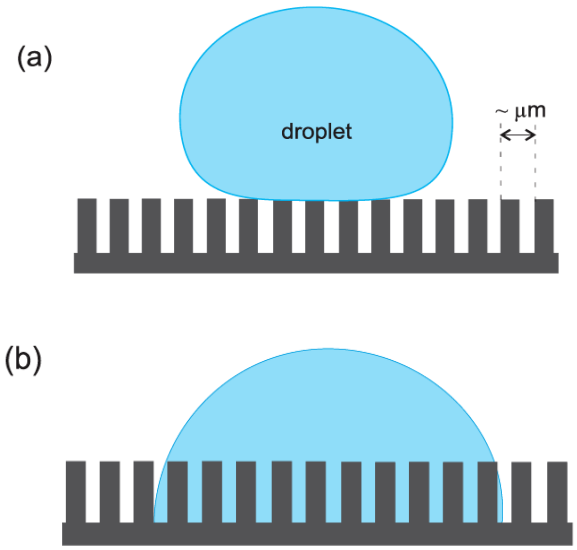

Figure 2-4: Structure of (a) Cassie-Baxter mode and (b) Wenzel-mode. Reprinted with permission from ref. 85. Copyright (2020) by the Springer Nature, Licence no. 4753560563495.

2.2 Drying of colloidal sessile droplets

Drying is one of mass transfer processes that involve the separation of liquids from solids by a heat source to remove the amount of the remaining liquid left behind the evaporation process. The essential difference between the drying and evaporation is that the residue in the later is always a liquid. However, a large number of scientists considers the drying as the last stage of the evaporation process where the continuation of the presence of the temperature difference between such as a sessile droplet and the surrounding around it, leads to dry the remaining amount of the thin liquid layer that is induced by the droplet evaporation [125].

Colloidal particles, which are micro/nanoscopic, insoluble substances, are considered an interesting field in many applications such as production of nanowire, patterning of a substrate, and particularly applications that deal with increasing surface area to enhance heat transfer. This is because of the small size of these particles that produces a large surface area-to-volume ratio for a given volume fraction of particles. With this large ratio of the surface area-to-volume, forces that scale with surface area, such as diffusion, dominate over forces scaling with volume such as gravity. However, due to the colloidal particle tendency to aggregate and cluster in some regions arising from the effect of attractive Van der Waals forces [126], it is considered a big issue for some applications. Therefore, the controlling the effect of these particles in terms of the patterns of aggregation and deposition on surfaces is also considered an interesting important area for researchers and scientists. Understanding dynamics inside droplets allows to better analysing the patterns of the strains of particle deposits on surfaces after drying process.

2.2.1 Evaporation induced flow

In fact, dynamics of the evaporation and drying of sessile droplets on heated or non-heated substrates, and the role controlled the contact line pinning in pure or colloidal liquids still motivate the attention of many investigators for both scientific and industrial applications. This is clearly due to the large number of phenomena that occurs simultaneously inside the sessile droplet which are actually not straightforward. The evaporation of the sessile droplet actually includes two parts:

diffusion part which the vapour molecules diffuse into the air through the liquid-vapour interface. The another one is evaporation part which the liquid molecules flow from inside the droplet to this interface [92]. During the evaporation part, as the droplet is deposited on a hydrophilic surface, the rate of evaporation near the contact line is more as compared to the apex of the sessile droplet because of the fact that vapour molecules near the edge of the droplet have more space to escape from the droplet surface [89]. Due to the non-uniformity of the evaporative flux along the droplet interface, an internal viscous flow generates within the sessile droplet inducing a capillary flow. On the other side, when there is a temperature or concentration gradient along the liquid/gas interface of the sessile droplet due to the droplet evaporation, especially in case a droplet is placed on a hot substrate, Marangoni effect and buoyancy force are produced inside the sessile droplet. Both phenomena occurring inside the droplet, which are considered as an internal convective flow, have taken the interest of many engineers and researchers in various applications, particularly surface patterning applications. In conclusion, the presence of colloidal suspension particles within the droplet liquid affects not only the evaporation and hydrodynamics in the edge of the droplet but increases the complexity of the physics controlling the evaporation process and the pattern of the colloidal particle depositions on surfaces after the drying process [126].

Capillary flow

The main reason for capillary flow occurrence into a droplet, as was predicted firstly by Deegan et al. in 1997 [127, 128], is the pinning of the contact line inducing a non-uniform flux diffusing to the ambient atmosphere along the liquid/gas interface during the evaporation of the sessile droplet on a structured substrate. Thereby, a large amount of liquid losses at the contact line by evaporation, and this amount of liquid lost must be replenished in order to prevent the shrinkage of the contact line and to keep the substrate wet, as demonstrated in Figure 2-5. As a result, internal radial flow of liquid movies from the centre towards the edge of the droplet. This flow usually is capable of transferring 100% of species which is left on the substrate to accumulate at the perimeter in a ring-like deposit as the droplet dries there. A common manifestation of the capillary

flow is a brown ring left of drying of coffee droplet, which usually contains a number of tiny solid species, on a counter top that leads to what it is well-known “coffee-ring” or “ring-stain” effect. This phenomenon is very important in numerous applications such as DNA/RNA microarrays, drug discovery, spotting methods for gene mapping, paint manufacturers, and the manufacture of novel electronic and optical materials [129].

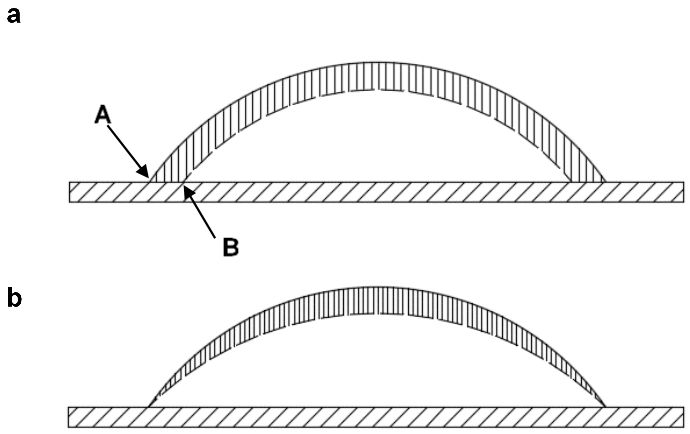

Figure 2-5: Schematic illustration of the origin of the induced internal flow. (a) representing of the unpinned contact line where uniform amount of liquid removes, the hashed layer, and the contact line will move from A to B. (b) representing of the pinned contact line where the replenishment of the liquid, which is removed from the edge, prevents the motion of the contact line.

Extensive experimental and theoretical studies of the capillary flow inducing the coffee-ring effects during the evaporation of sessile droplets have been undertaken to elucidate the underlying mechanisms behind it, and the ways of controlling this phenomenon depending on the type of applications. Deegan et al. [127] ascribed the coffee-ring phenomenon resulting from drying droplets to the effect of capillary flow. The results that were obtained by the use of microscopic technique showed that capillary flow provides the mechanism of deposition ring growth regardless of the characteristics of the substrates. Then, Deegan et al. [31] produced a comprehensive description of their predictions about the flow velocity, the rate of growth of the deposition, and the distribution of particles inside the droplet. During their experimental work, it is found that the presence of roughness of the substrate or chemical heterogeneities also help to produce

contact line pinning. An extension to the Deegan et al. work was conducted by Fischer [130] where it was concluded that the flow profile induced inside the evaporating droplet is the essential key to understand the macroscopic flow, which it also depends on the mode of droplet evaporation. Further study was carried out by Popov in 2005 [131] to calculate the width of the deposition formation ring by the use of the basic model of evaporation (i.e. diffusion-driven evaporation). Hu and Larson in 2006 [129] also indicated to the factors that increase the occurrence of the coffee-ring effect which are: pinned contact line, adhesive particles to the substrate, and high evaporation rate near the edge of droplet. In addition to previous factors, recently, it is found that the dense liquid also affects the evaporation dynamics, which deviate greatly from the dilute liquids as a result of concentration-dependent liquid property [132]. These predictions can be useful to understand modern printing technology requires dense-ink printing, and the drying-mediated printing.

Marangoni effect

Besides the previously mentioned, the evaporation process mostly creates either variation in solute and surfactant concentration or temperature gradient along the droplet interface, which result in a gradient in the surface tension and hence Marangoni flow inside the droplet. These gradients are because of the non-uniform evaporation rate along the droplet free surface. In addition, through the literature, there are two different opinions concerning the temperature gradient along the free surface of evaporating droplets. The first opinion guesses that the apex of the droplet must be the coldest region, despite being the region of smallest evaporative loss. This is because it is the furthest region from the substrate which represents the main heat source [45, 133]. The other opinion assumes that the temperature at the edge of the droplet is colder than at the apex of the droplet as a result of the high evaporation rate at the edge of the droplet [134]. Further, Hu and Larson indicates that the distribution of the droplet free surface temperature depends on the contact angle of the droplet [135]. Unlike the capillary flow, Marangoni flow carries particles that are near the droplet surface towards the centre of the droplet forming a uniform deposition. This phenomenon is widely observed in the nature and many applications. A good example on its

occurrence is that when a droplet of alcohol is allowed to fall on the centre of water film spreading on a smooth substrate, the water will immediately rush out the region where the alcohol droplet fell.

In addition to the investigations have been conducted on the capillary flow, Marangoni effects also have a great part of these investigations where numerous studies have been produced to understand the advantages of this phenomenon to exploit it in suitable applications. Hu and Larson [136] built a theoretical model to predict the flow pattern inside a pinned sessile droplet with and without the Marangoni effect during slow evaporation, where it was found that the flow reversed direction due to the Marangoni flow. Experimental investigation of the Marangoni effect in an evaporating water droplet at the normal conditions was done by Xu and Luo in 2007 [137]. Observations revealed that a stagnation point is created near the contact line due to the changing of the direction of the surface tension force along the droplet interface. Christy et al. [138] found that the maximum liquid phase velocity was observed near but not at the contact line during the evaporation of a pinned sessile droplet resting on a non-heated substrate under normal conditions.

Recent works on Marangoni and capillary flow

Evaporation induced Marangoni effect or capillary flow has received a great deal of attention due to the richness of fundamental phenomena involved, and to its importance in a wide range of manufacturing processes, fabrication of ordered structures, colloidal crystals, and pharmaceutical manufacturing. Both phenomena are complicated and need intensive studies because of being that the form of the droplet during the evaporation is a priori unknown, and because the pattern of particle deposition depends on many factors. Such factors are nature of the substrate, droplet size, particle size, the shape of particle, droplet composition, and flow patterns inside the droplet. As a comparison among them, Fischer [130] observed from his investigation on the deposition patterns of colloidal droplets during their evaporation on substrates that the distribution of particles depends on the manner of the droplet evaporation and the driving forces, and as a result on the flow profile inside the droplets. A temperature gradient, dynamic of the contact angle, and flow profile inside the droplet were

noticed by Tseng et al. [139] through their experimental and numerical studies, which form the key parameters for predicting the moving behaviour of micro-litter droplets under the Marangoni and capillary effects. In 2008, Widjaja and Harris [140] also focused on the deposition patterns of the suspended particles through the evaporation of colloidal droplets on substrates in order to figure out the evaporative flux along droplet surfaces and hydrodynamics inside the droplets. Numerical results showed different patterns of the particle deposition such as ring-like deposit and uniform particle distribution which they depend on the mass transfer of the suspended particles in the bulk liquid. Xu et al. [141] also experimentally observed the occurrence both the convection Marangoni flow and the capillary flow inside the drying droplet. In such case, only the particles in the outward flow region can be brought at the edge of the droplet. As a result, linear growth in colloidal ring deposited with time at the edge of the drying droplet will occur, as shown in Figure 2-6.

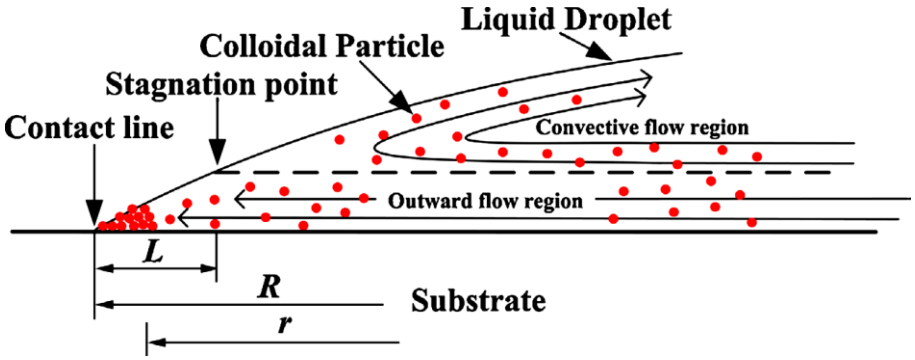

Figure 2-6: Sketch of the flow pattern inside a pinned evaporating droplet.
Reprinted from ref. 137, Copyright (2020), with permission from Elsevier.
License no. 4753550915742.

Regarding to the effect of the nature of the substrates on the deposition patterns of the suspended particles, Uno et al. [142] made an experimental comparison for the deposition patterns of polymer latex on both hydrophilic and hydrophobic substrates. They noticed that during droplets evaporation on the hydrophilic substrates, particles adsorb towards the contact line inducing ring stain. On the other hand, no particles adsorb towards the contact line through the early stages of the evaporation in the case of the hydrophobic substrates. Once the particle concentration reaches the critical value, aggregation of particles starts to adsorb

on the substrate forming tiny spots. The effect of heated substrates on the evaporation of sessile colloidal droplets was investigated by Girard and Antoni [143] and Patil et al. [144]. The findings revealed three types of deposits-namely, ring, thin-ring with inner deposit, and inner deposit, depending on the substrate wettability and whether heated or non-heated substrate. In same direction, an experimental study was conducted by Chen and Evans [145] to demonstrate the deposition patterns of particles arising from drying colloidal droplet on a super-hydrophobic substrate. Results showed different patterns of the deposition related to the normal pattern of the deposition on a hydrophobic substrate, where the evaporation rate at the contact line is restricted causing different pattern of depositions and particle shapes. Another study focused on the internal fluidity of a sessile droplet in the case of hydrophilic and hydrophobic surfaces. Authors noticed two counter circulation cells formed inside the droplet deposited on the hydrophilic surface while, the number increases to four circulation cells in the case of hydrophobic surfaces, which is attributed to the combine effect of Marangoni and buoyancy on the flow field [146]. In another direction, Shmuylovich et al. [147] provided detailed measurement of the deposition patterns as a function to the droplet radius and the size of suspended particles as well, while Bardakov et al. [148] focused on the effect of the multi-composition of the drying droplet on the pattern deposition of the suspended particles.

Other effects of both phenomena on the behaviour of droplets during their resting on substrates investigated by Nikolov et al. [149, 150] during their studies on the spreading of aqueous trisiloxane ethoxylate surfactant solutions on hydrophobic solid substrate. They found a spontaneous spreading (i.e., superspreading) of this surfactant on the substrate due to Marangoni effect arise from the high surface tension gradient induced by the resting of this surfactant on the substrate. Recently, Parsa et al. presented a detailed review of the most observed deposition patterns and mechanisms behind them [151].

2.2.2 Drying of sessile nanofluid droplets

As mentioned earlier, fluids that inherently contain insoluble substances, have different behaviours in comparison with the pure fluids, where the presence of these substances seems to increase the capability of the fluids to transfer thermal

energy to other mediums. From this fact, the idea of dispersing very tiny particles (i.e., nano-sized particles) into the base fluids has been explored further recently because predictions indicate that the presence of these nanoparticles in base fluids in different sizes and shapes might increase the performance of such fluids much beyond that of the base fluids. This increase underlies the modifications of fluid properties such as enhancing thermal conductivity, increasing viscosity and altering the evaporative behaviour of fluids as well [47]. In addition, it is clear from the large amount of research that has been published on the thermal conductivity of nanofluids, the increase of the nanoparticles concentration into base fluids leads to an increase in the thermal conductivity of these nanofluids. Therefore, special interest has been paid to understand the mechanism of the evaporation of sessile nanofluid droplets and the deposition formation of the suspended nanoparticles after droplets drying on the substrates. A great variation in evaporation rate was experimentally observed in case of the presence of nanoparticles inside a sessile droplet. This variation depends on superficial characteristics of the nanoparticle surfaces (i.e. hydrophilic or hydrophobic), nanoparticles concentration, patterns of the nanoparticle deposition, and dynamics of the contact angle, in addition to interactions between particle-substrate, particle-liquid and particle-particle as well. Trokhymchuk et al. [152] and Wasan [153] observed same results from their investigation. They found that the presence of suspended nanoparticles inside sessile droplets increases pressure inside the droplet due to the attractive interaction between particles, and hence enhances the spreading capability of sessile nanofluid droplets. Meanwhile, Vafaei et al. [154] investigated the effect of the presence of nanoparticles within the droplet liquid on the contact angle and thereby on the evaporation rate. Results revealed that the increase of the nanoparticles concentration increases the value of the contact angle and enhances the rate of the evaporation. Contrary results to what was expected, were observed by Sefiane and Bennacer where they found that the presence of aluminium nanoparticles into sessile ethanol droplets leads to a reduction of the evaporation rate compared to the case of pure fluid droplets [155]. This behaviour seemed due to the longer pinning time of the contact line resulting from the deposition of nanoparticles at the perimeter of the droplet.

From another viewing, Shmuylovich et al. [147] investigated experimentally the effect of the droplet radius and the size of suspended particles on the essentially stochastic behaviour of the contact line (i.e. pinning/de-pinning) during the evaporation of aqueous solution droplet. Meanwhile, the studies were conducted by Budhadipta et al. [156] and Darwich et al. [157], who used gold nanoparticles in their experiments, gave a clear explanation about the deposition formation of the nanoparticles during the evaporation of nanofluid droplets. They found that the capillary force is responsible on the horizontal movement of nanoparticles, and Van der Waals forces are responsible on the attachment of nanoparticles to the substrates. In addition, the ring arising from the deposition of suspended nanoparticles is the same as the coffee-ring effect that is seen in colloidal liquids. The main difference between them is in that the nanofluid droplets form more quickly and reliably on the substrates than colloidal droplets. In addition, Chon et al. [158] and Zhong et al. [159] studied the effect of nanoparticles size on the deposition patterns. It seems from experiment observations that nanoparticles size has a strong effect on the dryout stain pattern as shown in Figure 2-7, and the presence of nanoparticles with multi-sized changes the evaporative behaviour and hence the deposition patterns due to the interaction between small and large particles. The interaction strength between liquid-substrate was addressed in order to study its effect on the evaporation of a nano-droplet scale on heated hydrophilic and hydrophobic substrates [160]. No pinning was observed under these conditions in both substrates, and the increase of hydrophilicity of the substrate promotes the evaporation process because of the stronger attraction between the substrate and liquid arising from the heat transfer from the substrate to the liquid. In the same area of interest, an interesting study was carried out to investigate the evaporation-induced deposition pattern depending on the interaction between nanoparticles and droplet liquid molecules [161]. Results showed that the deposition patterns of nanoparticles on surfaces strongly depend on whether the nanoparticles-liquid interaction is weaker, comparable or stronger than liquid-liquid interaction.

Furthermore, a comprehensive model was produced by Wray et al. [162, 163] to investigate the mechanism of the evaporation of a nanoparticle laden droplet deposited on a heated substrate under the electric field effect. The results

revealed the ability of the electric field to control the coffee-ring configurations. Sefiane [164] also conducted an experimental analysis comparison on the evaporative behaviour of the sessile droplet with and without nanoparticles existing. Different types of nanofluids with different concentrations under different substrate temperatures (20 to 80 °C) were used during his analysis. Comparison results illustrated a strong dependent of the evaporative behaviour of nanofluid droplets on the nanoparticle concentration, nanoparticle material, and substrate hydrophobicity.

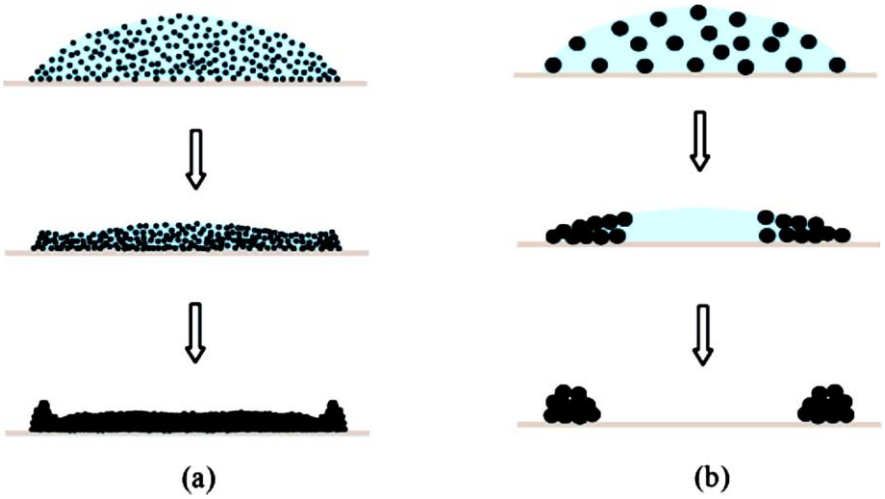

Figure 2-7: Schematic illustration of the effect of particle sizes on the nanofluid droplet‘s evaporation and dryout: (a) smaller nanoparticles (such as 2-nm); and (b) larger nanoparticles (such as 47-nm). Reprinted with permission from ref. 154. Copyright (2020) American Chemical Society.

2.3 Controlling methods of deposition patterns of particles

It was noticed in the earlier sections that the evaporation of sessile droplets containing colloidal or suspended particles under pinned contact line condition induces what is known as the coffee-stain or coffee-ring at the edge of the droplets. The presence of this phenomenon is undesirable in the majority of industrial and scientific processes and therefore, controlling the distribution of the particles deposition during drying process is crucial and complex at the same time. Thus, understanding the coffee-ring formation and the influencing

parameters should be essential to those attempting to suppress or harness this phenomenon [31]. Suppression of the coffee-ring effect has been accomplished by the use of several methods, such as enhancement of surface tension effects, addition of surfactants, surface modification, alteration of particle shape, and application of an electric field. However, several approaches have been done to utilise this phenomenon for arriving at novel processes and preparing new materials [50].

The common reason of the coffee-stain suppression is the presence of Marangoni effect inside the drying of sessile droplets that produces a countering flow to the outward flow of the deposited particles. Therefore, the enhancement of the surface tension gradient induced Marangoni flow is the best method to reduce or eliminate the effect of coffee-ring phenomenon [133, 136, 137]. Hu and Larson [129] also examined through their experimental and theoretical studies that the formation of coffee ring deposits occurs at the edge of drying water droplets. The observations showed that there is a possibility to manipulate both Marangoni flow and the deposition pattern by controlling the temperature profile through heating substrate process by the use of resistive micro-heater or radiative heat transfer to the droplet surface. Recently, an experimental and theoretical analysis on the outward flow inside drying pinned droplets in the case of the Marangoni flow presence was done by Huang et al. in 2015 [165]. The analytical data showed that deposited distribution very influenced by the pinned contact line and the Marangoni effect.

Different attempt to suppress the coffee-ring effect during droplet evaporation was carried out experimentally by Sefiane [106] where the influence of a non-ionic surfactant addition on the wetting pattern of the evaporation of sessile water droplets was examined. Results demonstrated that the addition of this surfactant with low concentration leads to increase the evaporation rate at the three-phase line, and generates a surface tension gradient along the droplet interface inducing the Marangoni effect. Contradicting results were obtained by the theoretical and experimental work of Crivoi and Duan [166] where the addition of a surfactant in a droplet containing graphite nanoparticles promotes the aggregation of nanoparticles at the edge of the droplet instead of the uniform deposition. But it was found that the simultaneous presence of the particle adsorption, long-range

attraction, and circulatory motion processes is essentially for suppressing the coffee-stain effect and obtaining an uniform deposition [167]. Cui et al. [168] also studied effects of the addition of hydrosoluble polymer additives. The use of this type of surfactants provides a motion of the contact line, and consequently, a prevention of the suspended particles flow towards the contact line is induced due to the role of viscosity and Marangoni effects. As a result, an uniform and ordered structure of the suspended particle deposition appears during the droplet evaporation. An experimental demonstration of the effect of a non-ionic surfactant addition on deposition patterns and attachment strength of colloids during the evaporation of a sessile droplet was done by Morales et al. [169]. Through the experimental work, it was noticed a great effect of the surfactant on the surface tension of the droplet during evaporation, patterns of the contact line, colloid−surface friction, depositions and attachment strength of colloids. Results revealed that the increase of the concentration of surfactant decreases the attachment strength of colloids resulting in a uniform deposition of colloids.

Modification of the substrate that a sessile droplet deposits on, has also an effect on the behaviour of fluid flow inside the droplet and thereby on the pattern formation of particle deposition due to the interactions between particles, liquid and substrate. Cui et al. in 2012 [170] used a hydrophobic silicon pillar array as a substrate to investigate the behaviour of evaporation and deposition pattern of sessile colloidal latex droplets, see Figure 2-8. Due to the structure of the silicon pillar array, a porous gel foot at the three phase contact line was formed inducing inward flow of the colloidal particles towards the droplet centre and hence reducing the coffee-ring effect. Further numerical study was conducted in 2015 by Barash [112] to demonstrate the temperature distribution and fluid flow behaviour during the evaporation of a sessile droplet under a slowly droplet evaporation condition. The results pointed out that the selection of appropriate properties of the substrates can control the fluid flow structure in the droplet evaporation.

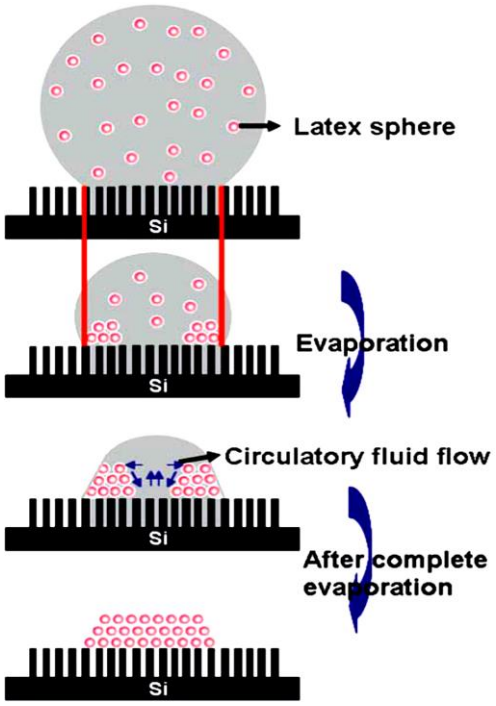

Figure 2-8: Schematic ‘‘Wenzel state’’ droplet evaporation on a hydrophobic silicon pillar array. Republished with permission from ref. 166, Copyright (2020); permission conveyed through Copyright Clearance Centre, Inc.

The effects of other factors such as droplet size, the use of nanofluids, particle shapes, and liquid-gas interface have also been extensively published by many authors. However, several experimental studies revealed that increasing the particle diameter is enough to suppress the coffee-ring effect [171, 172]. Increasing the particle size may play an important role in many applications of drying colloidal fluids. Pradhan and Panigrahi [173] illustrated experimentally the fluid flow inside a sessile water droplet resting on a hydrophobic substrate and imposed to a temperature gradient. The great role of the increasing the droplet size on the change of the flow patterns inside the droplet and reducing the dominance of the surface tension near the contact line has been addressed during the experimental results. Deposition patterns of the drying a sessile droplet consisting laponite nanoparticles were investigated experimentally and numerically by Lebovka et al. [174]. It was noticed that coffee-ring deposit was very influenced with the concentration of laponite nanoparticles, where this deposition disappears when the laponite concentration exceeded 5%. Experimentally, Yunker et al. [175] showed that one of the key parameters, which

can be used to eliminate the coffee-ring effect, is the shape of the particles that deposit on a substrate during the drying of droplets. The observed results indicated that ellipsoidal particles provide a convenient environment to create a uniform configuration of particle deposition without any modification of particles or solvent chemistry. The reason behind this behaviour is that structures formed on the droplet interface due to strong interparticles attraction between these shapes of particles. These structures would not allow particles to reach the edge of the droplet and ensure to form uniform depositions. This behaviour was supported recently by using a mixture of spherical and non-spherical particles with enhanced particle-particle interaction at the droplet interface to suppress the coffee-ring effect [176]. A unique study on hydrodynamic and particle transport inside evaporating droplets by the use of Infrared (IR) light, as an external heat source, to heat the droplet interface was conducted by Thokchom et al. [177]. As a conclusion of their investigation, hydrodynamic profiles inside the droplet and thereby deposition patterns of particles can be modified by altering the temperature of the droplet interface.

The applications of the electrowetting and electric fields have also paid the attention of many researchers and engineers due to their significant role in characterizing the deposition profile of colloidal particles. Eral et al. [178] tried from their experimental study to know the effect of the electrowetting on the reduction of the coffee-ring phenomenon arising from the evaporation of complex droplets through changing AC frequencies up to a few ten of KHz, see Figure 2-9. Two distinct results were observed from experiments which were: the time-dependent electrostatic force hindered pinning of the droplet contact line, and the electrowetting promoted internal flow field inside the droplet in which prevented the accumulation of colloidal particles at the contact line. Moreover, Wray et al. [162, 163] noticed from their investigation that the coffee-stain phenomenon could be supressed dramatically by the appropriate selection of the electric field values. Other recent important attempts were carried out to deposit colloids on surfaces in a controllable manner via using either an external point source of vapour or laser-induced differential evaporation, as shown in Figure 2-10[179, 180].

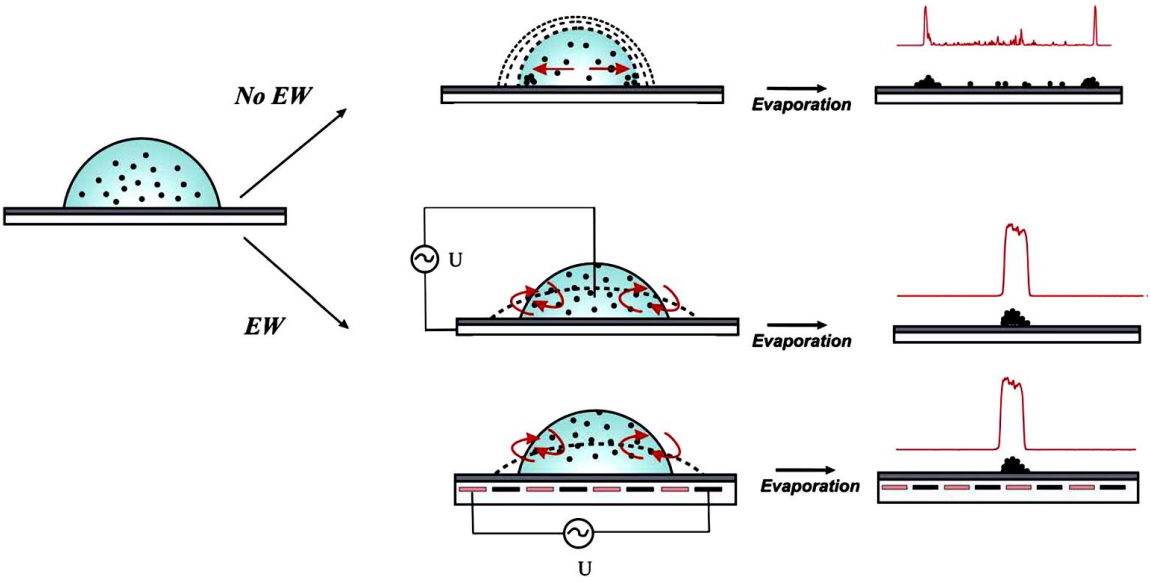

Figure 2-9: Schematic of the droplet evaporation process with and without electrowetting. Republished with permission from ref. 174, Copyright (2020); permission conveyed through Copyright Clearance Centre, Inc.

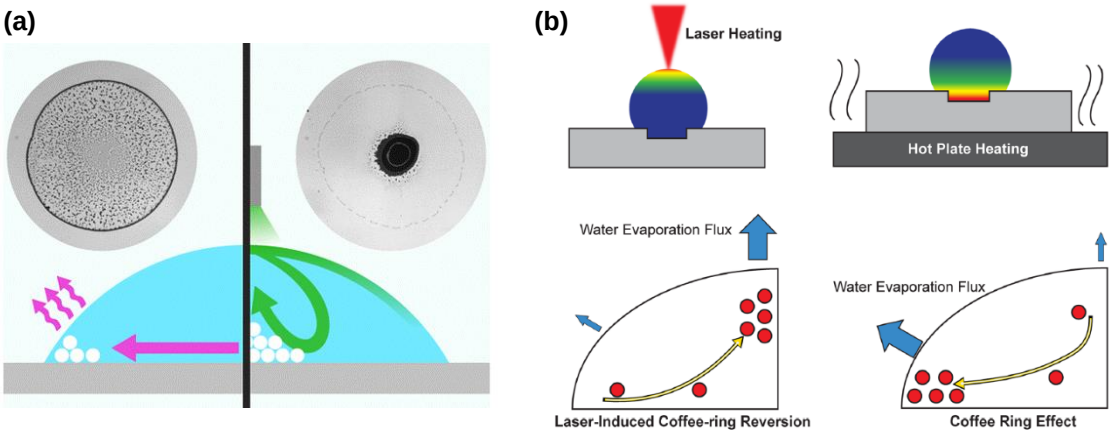

Figure 2-10: Attempts to control the particles deposit on surfaces by using (a) a vapour point source [179], and (b) laser-induced differential evaporation [180].

2.4 Convection effects on the evaporation of a droplet

As other key factors, mentioned previously in the literature, influencing the evaporation of a droplet, external flow surrounding the droplet (i.e., free or forced convection), in its turn, also plays an essential role in changing the evaporative

behaviour of the droplet, and hence hydrodynamics inside this droplet. Usually, most of theoretical studies on droplet evaporation neglects the effect of the convection in the gas domain to simplify the complexity of the problem [89, 181, 182]. Predictions revealed that diffusion-limited evaporation of droplets gives under-estimation of the evaporation rate in comparison with the experimental data, particularly for larger droplets [183] or for highly volatile liquid droplets [184, 185]. Thus, further theoretical studies are necessary to establish the importance of the convection in the gas domain on the evaporative behaviour of the droplet.

It was predicted numerically by Gogos et al. [186] that natural convection, which is induced by buoyancy effects due to density variation in the surrounding atmosphere, enhances the evaporation rate of a suspended droplet. After that, vapour clouds flowing over evaporating pinned hydrocarbon droplets were observed, which indicate the presence of the natural convection [187]. Further, an increase in the evaporation rate was noticed compared to the diffusion-driven evaporation. Additional experiments were conducted to examine the pronounced role of the natural convection in increasing the evaporation rates of different liquid droplets [184]. In a follow-up study, Saada et al. [188] observed numerically the importance of the buoyant convection in the surrounding air on evaporation rates for different droplet radii, where 20-30% increasing in the evaporation rates were observed. It can be concluded that the differences between studies, in terms of whether or not convection flow is considered, may be due to the density differences that are either very small or very big depending on a vapour liquid density in comparison to the ambient gas density.

Although much attention has been recently paid towards studying the importance role of the free convection in the surrounding space, other works have been conducted to study the evaporation of liquid droplets under a forced convective environment. Ben et al. [189] compared the evaporation rates from open water bodies under free and forced convection mechanisms. Their results showed the strong evaporative efficiency under the forced convective environment in comparison to the free convection. Numerical results of Zhang [190] indicated that the droplet lifetime is affected by increasing ambient pressure or changing the environment conditions. Experimentally, Gan and Qiao [191] observed the rapid evaporation of various fuels with addition of nanoparticles under a forced

convective hot environment which represents the realistic conditions in practical combustion systems such as gas turbines and diesel engines. Further analysis, a common method has been used to present the mass transfer from a droplet exposed to a gentle airflow in the surrounding space through a correlation as a function of dimensionless groups i.e., Sherwood number (Sh), Reynolds number (Re) and Schmidt number (Sc). This correlation can be expressed in the form;

$$Sh = CRe^{n}Sc^{m} \tag{2.6}$$

where C, n and m are the correlation factors. Sherwood number, $Sh = hL/D_v$, is the ratio of the convective mass transfer rate to the rate of diffusive mass transport, and Reynolds number, $Re = \rho UL/\mu$, is the ratio of inertial forces to viscous forces while, Schmidt number, $Sc = \mu/\rho D_v$, represents the ratio of the viscous diffusion rate to the rate of mass diffusion.

For instance, Fröessling [54] produced a correlation for the mass transfer from liquid and solid spheres under airflow for diameters of 0.02 to 0.18 cm. Then, Ranz and Marshall [56] developed this theory by including the heat and mass transfer of droplets containing dissolved and suspended solid particles for a range of Reynolds number from 0 to 200 and water droplet size of 0.06 to 0.11 cm, and at air temperature up to 220^{o} C. Their results are based on the boundary layer theory for a spherical droplet, which states that the maximum rate of transfer is on the front-side of the droplet where it faces the oncoming air stream while, the minimum rate is near the separation point. This rate of transfer increases again to a maximum rate, but lower than in the front-side, on the rear face of the droplet where it experiences velocities in the reverse direction. Garner and Grafton [192] later derived a relationship for the dissolution of 0.5 in benzoic acid sphere in a stream of water at room temperature. After that, another correlation for the dissolution of pelleted organic acid spheres at low speed of water stream (i.e, Reynolds number of 2.3 – 900) was derived [193].

Of recent years, attention has been still directed towards establishing relations for the mass transfer from sessile droplets at different conditions. Baines and James [194] presented a numerical model to develop an equation for the evaporation rate of a flat sessile droplet under convection flow as a function of Peclet number, and based on that the evaporation rate is same for all shapes of

droplets. They also considered the droplet as a spherical segment, and a uniform linear shear flow everywhere in the air. Steady-state evaporation was assumed, though mass loss with time was calculated by appropriate integration of the resulting mass transfer rate equation. Although their equation over-predicts results by 90% in some cases, it is useful in predicting the evaporation rate for other cases. Later, Danberg [195, 196] made similar assumptions to develop an equivalent model for evaporation of a sessile droplet into a Couette flow. An empirical equation of the evaporation rate is presented in terms of Sherwood, Reynolds and Schmidt numbers based on a dimensional analysis. In this analysis, the shape of the sessile droplet is assumed to be constant during the evaporation process, and the droplet profile can be described based on the droplet base diameter, d, and the shape factor $\eta = h/d$, where h is the initial droplet height. Then, other characteristics parameters such as the droplet volume and the droplet surface area can be expressed as a function of the shape factor;

$$V_d = \frac{\pi d^3}{6}\left[\frac{3}{4}\eta + \eta^3\right] \tag{2.7}$$

$$A_s = \frac{\pi d^2}{4}[4\eta^2 + 1] = f(\eta).{V_d}^{2/3} \tag{2.8}$$

Their model is identical to the Baines and James model except that later model adopted the similarity solution method to match the evaporation rate from a circular disk to that from a square. Very recently, Buffone presented a simplified analysis to account the contribution of the turbulence level of the airflow in increasing the evaporation rate of 3µl water and ethanol droplets [197]. Table 2-1 presents a summary of the theoretical equations derived previously to estimate the evaporation rate of a liquid droplet exposed to a forced airflow.

In-line with that, the later sections will present previous numerical works have been conducted to predict the evaporation rate of droplets under the effect of forced convective environment, and the assumptions have been adopted to simplify the complexity of the problem, which is still not fully resolved.

Table 2-1: Summary of theoretical equations for the evaporation rate of a droplet under the forced convective environment.

Reference	Droplet	Theoretical equation	Limitations
Fröessling [54]	Free droplet	$Sh = 2 + 0.55Re^{1/2}Sc^{1/3}$	D = 0.02 - 0.18 cm
			Re = 2 - 1000
Ranz and Marshall [56]	Free droplet	$Sh = 2 + 0.6Re^{1/2}Sc^{1/3}$	D = 0.06 - 0.11 cm
			Re = 0 - 200
Garner and Grafton [192]	Free droplet	$Sh = 44 + 0.48Re^{1/2}Sc^{1/3}$	D = 0.5 in
			Re = 2.3 - 900
Garner and Keey [193]	Free droplet	$Sh = 0.94Re^{1/2}Sc^{1/3}$	D = 0.5 in
			Re = 2.3 - 900
Baines and James [194]	Sessile droplet	$Sh = 0.84Re^{2/3}Sc^{1/3}$	Based on the shear rate
Danberg [195, 196]	Sessile droplet	$Sh = 0.852Re^{2/3}Sc^{1/3}$	Based on the shear rate
Buffone [197]	Sessile droplet	$Sh = 0.664Re^{1/2}(ReI_{\infty})^{0.066}Sc^{1/3}$	Turbulent U = up to 2m/s

2.5 Evaporation of interacting sessile droplets

To this point, we have restricted an attention to intensive discussions about the fundamental of the evaporation of a single sessile droplet, mechanisms controlling this process, the trajectory of colloidal suspended particles inside the drying droplet, and methods that have been used to control the behaviour of particles movement, and deposition on surfaces upon which the droplet is rested.

This area of interest has been the main subject of numerous of engineers and scientific researchers. In real industrial applications, however, an evaporating droplet is significantly affected by presence of neighbouring evaporating droplets placed in a close proximity to each other. This proximity can lead to change hydrodynamics inside evaporating droplets, and hence the evaporation mode resulting undesirable and uncontrolled outcomes. Therefore, understanding the physical mechanisms of such problems is of great importance.

Labowsky [198-200] studied these interactions during droplet vaporisation and combustion by using image methods. Twardus and Brzustowski [201] also investigated these interactions analytically, and then Umemura et al. [202] included the Stefan convection effect. The interaction between droplets resting on a solid substrate is considerably more complicated because in this case the heat transfer among the three phase involved will be coupled with the mass transfer between liquid and vapour. Carles and Cazabat [203] experimentally observed the propelling a PDMS droplet under the effect of the presence of a volatile trans-decalin droplet due to the difference in the surface tension for both droplets. Deegan et al. [31] also mentioned in their work the drying of two droplets rested near to each other on a substrate. Weaker deposition occurs at the nearest point of the two droplets due to the lower evaporation at this region that causes particles convection to the most rapid evaporating region. In addition, arched structures were noticed by Chen and Evan [204] during their investigation on the drying of two sessile colloidal droplets closed to each other, as shown in Figure 2-11. Cira et al. [205] also investigated the mobility of the neighbouring droplets under the effect of the vapour emitted by adjacent droplets. Another experimental and numerical work was done by Pradhan and Panigrahi [32] to demonstrate the effect of neighbouring droplet on the hydrodynamics and deposition patterns inside the evaporating droplet. Observations from this study revealed that the evaporative flux from the single droplet surface is symmetric, and consequently almost uniform deposition pattern occurred along the contact line. In contrast, the evaporative flux from the droplet surface is asymmetric around the vertical axis to the substrate in the case of the presence of neighbouring droplets. Therefore, there is less movement of particles towards the

contact line region between the neighbouring droplets forming a weak deposit at this region, see Figure 2-12.

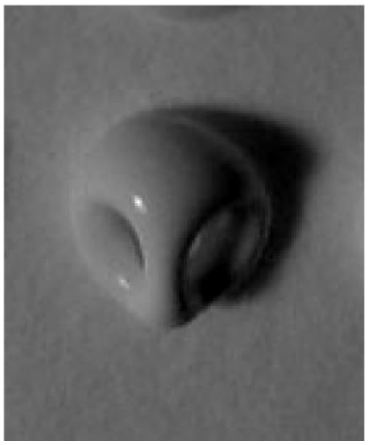

Figure 2-11: Plan view of arched residue of a 3.2 µL droplet positioned between two similar droplets after drying. Reprinted with permission from ref. 200. Copyright (2020) American Chemical Society.

In addition, a motion of the contact line and a change in the evaporation mode are noticed through the evaporation of a pair of droplets on a hydrophobic substrate [206]. Carrier et al. [183] investigated experimentally and theoretically the evaporation rates in collections of sessile water droplets, testing scaling law limitations for groups of small droplets and for very large droplets, and exploring the onset of the natural convection. Other experimental and numerical observations showed that the dissolution time of a droplet placed in between two droplets is longer than that in a single droplet as a result of the shielding effect of the two neighbouring droplets [207]. Further, observations also showed an enhancing in the buoyancy driven convective flow of the bulk compared to the single droplet evaporation. Shaikeea and Basu [208] examined three distinctive regimes in the lifecycle of a pair of sessile droplets evaporation. Their observations are illustrated in Figure 2-13. Both Pradhan and Panigrahi [33], and recently Dorra et al. [209] found that increasing the distance between evaporating droplets decreases the interaction phenomenon, which is usefull for optimising many applications. Very recently, Hegde et al. [210] studied how the morphology of a nanofluid droplet is affected by vapour-mediated interaction of an adjacent ethanol droplet. The evaporation dynamics of three droplets placed linearly in

close vicinity to each other on a hydrophobic substrate was investigated theoretically and experimentally for a range of droplet separation distances [211]. Findings revealed an increment in the lifetime of the centre droplet compared to an isolated single droplet.

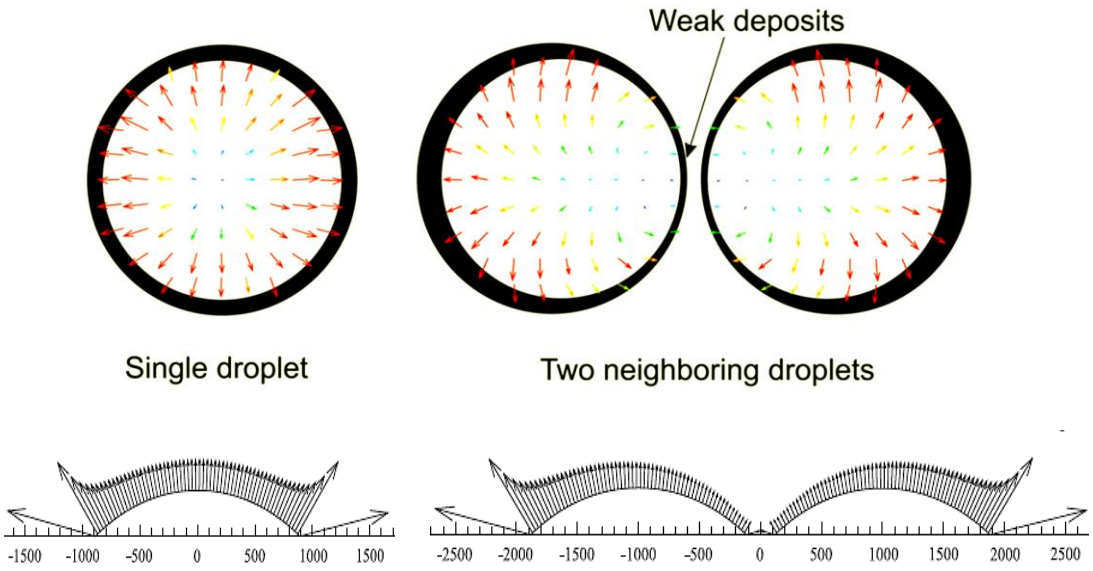

Figure 2-12: Deposition patterns and distribution of evaporative flux of the evaporation of both single droplet and two neighbouring droplets. Reprinted from ref. 30, Copyright (2020), with permission from Elsevier. License no. 4753641030634.

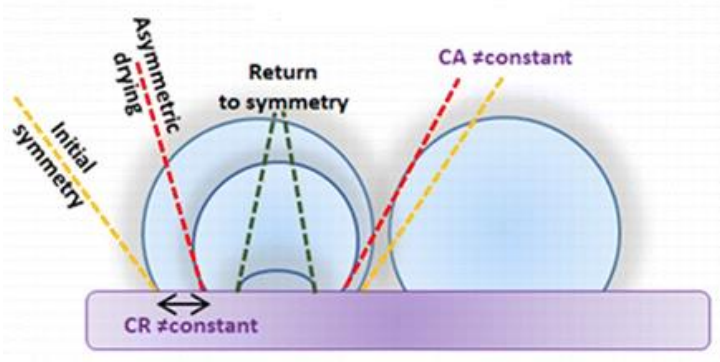

Figure 2-13: Illustration of three unique regimes in the lifecycle of a pair of sessile droplet evaporation. Reprinted with permission from ref. 204. Copyright (2020) American Chemical Society.

2.6 Modelling the evaporation of sessile droplets

In the last decade, modelling of a single sessile droplet evaporation by using appropriate mathematical models is a much adopted method because it is less time-and-cost consuming than doing experiments, gives complete information of all relevant variables, its ability to simulate realistic and ideal conditions, and can be used to guide experimental developments. Almost, all of previous numerical work have attempted to simplify the sessile droplet evaporation which involves three phase problems coupled with the moving of the droplet interface, and dynamics inside and outside the droplet, which would be extremely complex. Starting with the pioneering studies of Picknett and Bexon [57], Popov [131] and particularly Hu and Larson [89], as it is the most study considered in the present numerical work, four approximations were adopted in their numerical models; the droplet shape is regarded as spherical-cap during the evaporation process; the droplet evaporation is considered as a quasi-steady state since the vapour concentration adjusts rapidly compared to the time required for droplet evaporation; the convection role in the gas domain is neglected; and there is no big change in the droplet temperature (only 0.02 ˚C) to change the physical properties of the droplet as the evaporation of water droplet is very slow. As a result of these assumptions, the difference in the concentration of water vapour between the droplet surface and far above the droplet drives the evaporation process as represented by Laplace equation,

$$\Delta c = 0 \tag{2.9}$$

Then, to capture moving of the droplet free surface during the evaporation process, finite element method, for example, is used to solve equation (2.10), and calculate the local evaporative flux by the below expression,

$$\vec{J}(r,t) = D_v \overrightarrow{\nabla c} \tag{2.10}$$

Following researchers such, Semenov et al. [181, 182], Girard et al. [212], Dunn et al. [103, 108], Sobac and Brutin [213], Xu et al. [214], Wang et al. [215], and so on [80, 103, 108, 135, 136, 216, 217] have also adopted these simplified assumptions, particularly the spherical-cap shape assumption, in simulating the evaporation of a single sessile droplet to avoid tracing the droplet interface during the evaporation process, which is the most challenging part of the simulation of

such complex problem. Even recently, these assumptions are still considered to simulate such complex problem of interest for example; Kumar and Bhardwaj [218], Nguyen et al. [219, 220] and Schofield et al. [221]. Although, some numerical studies [101, 135, 222-228] considered the transient-term in their solution, in fact a “decoupling model” was adopted, in which the moving droplet interface problem is converted to a time series of fixed interface problem.

However, the quasi-steady state assumption is not valid in some situations for example, Maatar et al. [101] and Liu et al. [229] found that the transient effects are important to consider in modelling the sessile droplet evaporation for thicker substrates with lower thermal conductivities and for volatile droplets evaporation. In addition, Larson [44] confirmed in his recent review article the invalidity of quasi-steady state assumption in such cases, and the transient effects are necessary to get accurate results. Therefore, Yang et al. [230] developed a fully transient model for a single sessile droplet evaporation using Arbitrary Lagrangian-Eulerian method to trace the evolution of the droplet free surface during the evaporation process. In a follow-up numerical study [231], they extended the previous model to include the natural convection for both heat and mass transfer.

In the context of modelling multiple droplets evaporation, Aversana et al. [232] numerically showed that the Marangoni convection flow driven by the temperature gradient inside sessile droplets is able to prevent the droplets coalescence. Borcia and Bestehorn [233] used a phase field model to study the coalescence regimes of sessile droplets with different miscible liquids. They noticed a delay in the coalescence between droplets due to the Marangoni convection. Further, the lubrication approximation was used to investigate the possibility of propelling droplets with different fluids on surfaces due to the surface tension gradient arising from the coalescence between droplets [234, 235]. Pradhan and Panigrahi [33] investigated the influence of an adjacent droplet on hydrodynamics inside an evaporating droplet using the Finite Element Method. They adopted the quasi-steady state and spherical-cap assumptions, and neglecting the role of convection in the gas domain as well in their numerical study. Carrier et al. [183] also investigated theoretically the evaporation of collections of sessile water droplets. Another numerical study by Chakraborty et

al. [236] was conducted to analyse the feasibility of using arrays of evaporating sessile droplets as a cooling system for microprocessors. Their study was limited on analysing the evaporative cooling system of these arrays of sessile droplets without taking the interaction between droplets in the consideration. Very recently, Wray et el. [237] derived an asymptotic model for the competitive diffusion-driven evaporation of multiple thin sessile droplets. They assumed that the droplets are well separated to study the shielding effect of on evolutions and lifetimes of droplets. Through the above numerical work of multiple sessile droplets evaporation, one can see that some of the previous studies are limited to the fluid convection without considering the evaporation process, while other are adopted limited models, i.e., no convection in the gas domain, and they are still based on the quasi-steady diffusion-driven evaporation process although most of recent researches have still confirmed the importance of the role of the convection in the gas domain in getting accurate results [238-240]. Therefore, more accurate models, taking into account the convection vapour transport effect, particularly for multiple sessile droplets evaporation, are required to discover the effects of the diffusive vapour transport on the evaporation of adjacent droplets.

In the context of modelling droplets evaporation exposed to a forced convection, a few numerical studies have been carried out in which the effects of transported diffusive vapour from an evaporating droplet on the evaporative behaviour of neighbouring droplets are considered. In terms of a single sessile droplet evaporation under a forced convective environment, Baines and James [194] developed a simple single droplet evaporation model in the presence of convection, but their model was doubtful since in some cases over-prediction results were observed. A comprehensive model of the evaporation of moving and suspended spherical droplet in a forced convective high-pressure and temperature environment is presented by Zhang [190, 241]. Similar studies are performed by Navaz et al. [242], and Vik and Reif [243] to study the effect of turbulence on the evaporation process of a sessile droplet. Raimundo et al. simulated the evaporation of water droplet in a forced convection airflow at different relative humidity and water-air temperature [244]. Deformation and motion of a compound droplet exposed to a shear flow is performed numerically very recently by Shang et al. [245], and their observations showed the great

dependence on the capillary numbers of the inner and outer interfaces. The influence of Marangoni convection inside a droplet exposed to a forced convective environment was investigated by Raghuram et al. [246] using a transient diffusion-convection-driven evaporation process. In addition, Ljung and Lundström recently modelled the evaporation of a single sessile water droplet in a humid forced convection environment relevant to dishwashers [247].

In terms of multiple sessile droplet evaporation under a forced convective environment, a search of literature shows that most of studies focusing on the interaction between multiple droplets exposed to airflow are experimental, and few studies are performed numerically. Even that, there is a lack of numerical work in the literature conducted to investigate this interaction between evaporating droplets. For instance, several numerical work [248-252] were carried out for studying the interaction between neighbouring suspended bodies in an airflow. Hooshanginejed and Lee [253] also numerically investigated the behaviour of a sessile droplet in the wake of an upstream solid spherical surface as a first step to understand the behaviour of multiple droplets in wind. Recently, Razzaghi et al. [254] studied the shedding of multiple sessile droplets by a forced airflow at different patterns of arrangements. Considering the above studies, one can notice that the evaporation process has not been considered in these numerical work, and hence the effects of diffusive vapour transported from droplet to another one have not been taken in account. However, Doursat et al. [34] attempted to simulate multiple droplets evaporation exposed to a forced airflow but their model was very limited. They assumed that all droplets evaporate under approximately the same conditions therefore, only one droplet was considered in their model. Hence it did not capture any interactions between neighbouring droplets.

2.7 Motivation of the present work

Based on the above intensive overview, it appears that the evaporation of sessile droplets is an indispensable phenomenon in most of scientific and industrial applications, and it still motivates important activities. Technologies of the deposition of micro and nano-colloidal suspended particles arising from drying of

sessile droplets are also crucial processes that can be exploited in variety of applications. Therefore, large numbers of research efforts have been conducted in both experimental and theoretical fields to clarify the mysteries behind this fundamental phenomenon in order to incorporate it into practical manufacturing processes. However, although interaction between neighbouring droplets also has a substantial interest from scientific point of view, it has been found that rare investigations have explored the evaporation process of these droplets and the effect of mechanisms controlled this process under different conditions.

Through the above literature in section 2.6, one can see that references [230, 231] are the only numerical works have been studied the evolution of the droplet free surface during the evaporation process but for a single sessile droplet under natural convective environment. In addition, there are few researchers studied the interaction between a pair of adjacent evaporating droplets but under the spherical-cap shape and quasi-steady diffusion-driven evaporation process assumptions. Unfortunately, it seems that there are no prior numerical studies performed to investigate the effects of forced airflow on the evaporative behaviour of multiple sessile droplets evaporating in proximity to each other, and the evolution profile of sessile droplets under such conditions.

Therefore, the motivation of the present numerical work is to study firstly the effects of the forced convective environment on the evaporative behaviour of a single sessile droplet via a 3D transient Arbitrary Lagrangian-Eulerian finite element model, which is the first time that it is being used in this field of research, as a step towards understanding the evaporative behaviour of a pair of sessile droplets under same conditions with different patterns of droplet arrangements. Then, the dynamics, concentration distributions inside those droplets, and how an array of multiple evaporating sessile droplet behaves under such conditions will be the next step of the present work. Achieving the aim of this numerical work will open new research fields in order to improve our understanding of this fundamental phenomenon.

Chapter 3 Computational methodology

3.1 Introduction

With the rise of using computers, investigation of different engineering and scientific problems numerically via some commercial software or open source computational fluid dynamics programs, e.g. COMSOL Multiphysics®, FLOW 3D, ANSYS Fluent or OpenFOAM, becomes desirable and essential before doing experiments or fabricating device components, as mentioned previously in section 2.6 - Chapter 2. Simulations allow modellers to do as many design iterations as needed to get the right solution of a given problem. Additional insight into what can be observed experimentally can be obtained via these numerical simulations in which one can explore new ideas or identify the optimal operating parameters for certain systems.

Firstly, after addressing the equations governing the problem of interest, selecting the appropriate numerical method for approximating the solution of equations e.g., Finite Volume Method (FVM) or Finite Element Method (FEM), is crucial. In addition, providing the suitable tool including higher processor speeds and more memory obtainable to execute these mathematical models is the second essential part to achieve a successful and accurate model. Achieving that will allow to model more complicated geometries, combine more physics, and solve non-linear equations in a short running time [255].

COMSOL Multiphysics® is a powerful software built upon the FEM technique, which is a commonly applied tool for discretising and solving complex partial differential equations, e.g. Navier-Stokes equations, to either linear or non-linear simultaneous algebraic equations which they also cannot be solved analytically. In this approach, the liquid and air domains adjacent to the liquid-air interface are divided into non-overlapping elements, i.e. smaller domains, having linear or curved edges (in 2D, as shown in Figure 3-1) and surfaces (in 3D). Over each element, the field variables, i.e. concentration, temperature, velocity and pressure, are approximated by a suitable interpolating function (shape function). Polynomial functions are mostly used to determine the variables within each element. This type of interpolating functions is desirable since the order of these

functions can be increased, i.e. increasing the number of nodes forming an element, to improve the accuracy of the results, as shown in Figure 3-2. Note that for the current proposed problem, in which two-phase flow and transport of species are solved, the so-called “P2 + P1” element is used where the fluid velocity is solved via the second-order discretisation and the pressure is solved via the first-order discretisation.

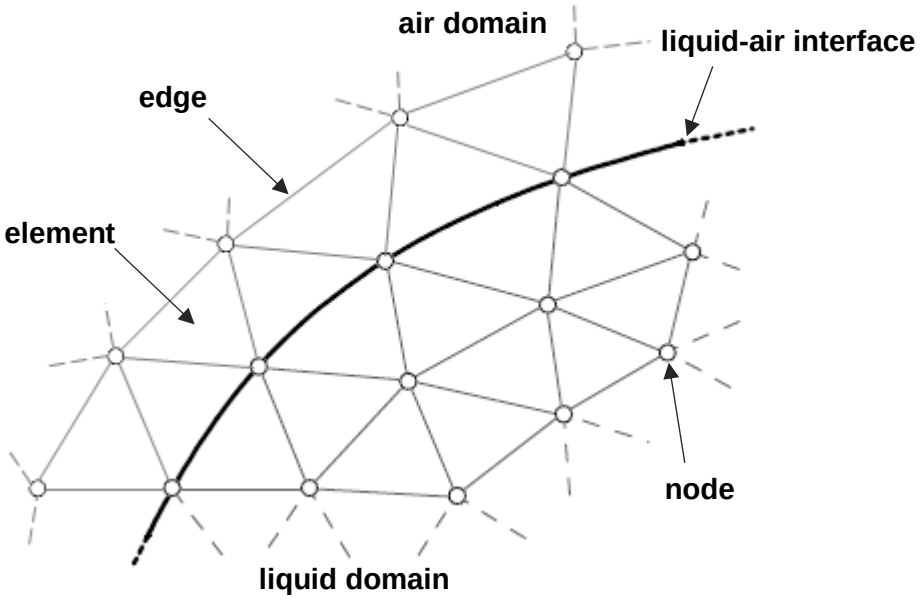

Figure 3-1: Representation of the finite element mesh fitted to the shape of the liquid-air interface.

Due to the limitation of desktop computers in executing of such models creating high computational resources which need faster processors and larger memory, models are run on High Performance Computing machines (HPC) which are more powerful and more cost-effective than standard computers. Three types of HPC machines available were used to execute the simulations presented in this thesis. These are:

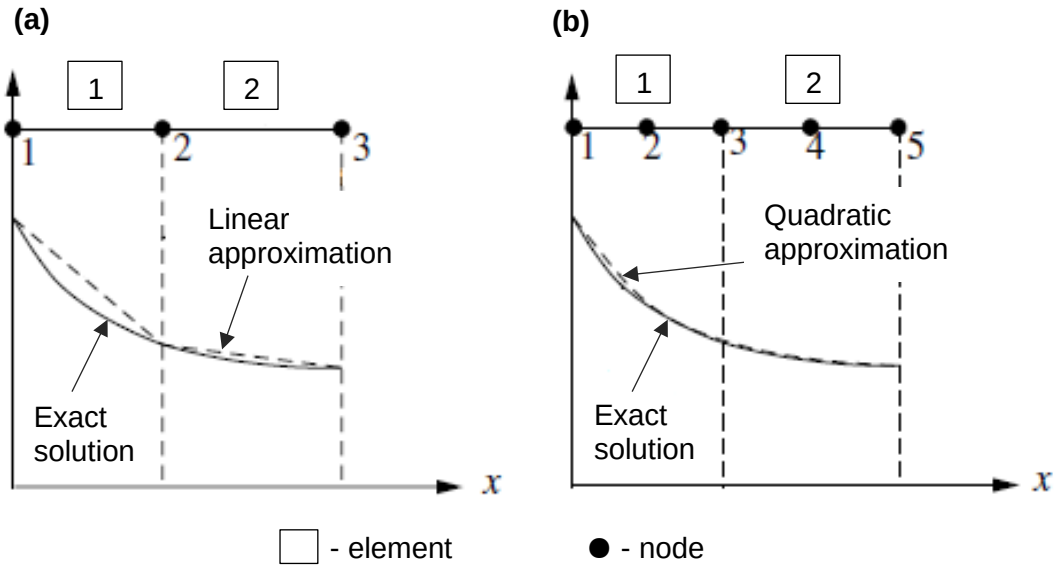

Figure 3-2: (a) linear approximation and (b) quadratic approximation of a variable over an element.

1. **N8 HPC**, **Polaris:** (now decommissioned) which was running on Intel® Xeon® E5-2670 CPU at 2.60 GHz. It had 316 nodes (16 cores per node) each with 64 GB of a total memory, and there are an additional 16 nodes each with a total of 256 GB of memory.
2. **Advance Research Computing (ARC3):** which is running on Intel® Xeon® E5-2650 CPU v.4 at 2.20 GHz. It has three types of nodes but the most widely used are: Standard nodes, 252 nodes with 24 cores and 128 GB of memory each; and High memory nodes, 4 nodes with 24 cores and 768 GB of memory each.
3. **Medical Advanced Research Computer 1 (MARC1):** (now also decommissioned) which was running on Intel® Xeon® E7-4860 CPU v.2 at 2.60 GHz. Mostly jobs were executed on the large memory (48 core / 3TB) nodes which had a maximum 96-hour job run-time.

Beside the importance of using the FEM in modelling the proposed problem in the current work, through the literature, COMSOL Multiphysics® is one of the most used and useful commercial software package available since it has been employed in a wide range of academic, scientific and industrial applications, particularly in the droplet evaporation area [33, 80, 89, 181, 182, 256-258] and others due to its capability for capturing and predicting the behaviour of very complex real-world physical phenomena as shown in Figure 3-3. Modelling by the use of this commercial software consists of three main stages which are: pre-processing unit, processing unit, and post-processing and visualisation unit. In each stage, there are several sub-processing units which are responsible on a specific part of the numerical model as indicated below:

1. Pre-processing unit.
    - Modelling geometry.
    - Modelling physical system.
    - Selecting initial and boundary conditions.
    - Generating computational mesh.
2. Processing unit, which is done on the HPC machine to execute models for the next stage.
    - Choosing solver.
    - Monitoring convergence.
    - Grid independence test.
3. Post-processing and visualisation unit.
    - Presentation and analysis of solutions.
    - Calculation of derived quantities.

Note that, from Figure 3-3, two packages are used to simulate the present problem which are: Laminar Two-Phase Flow, Moving Mesh and Transport of Diluted Species within fluid mechanics and chemical engineering packages, respectively.

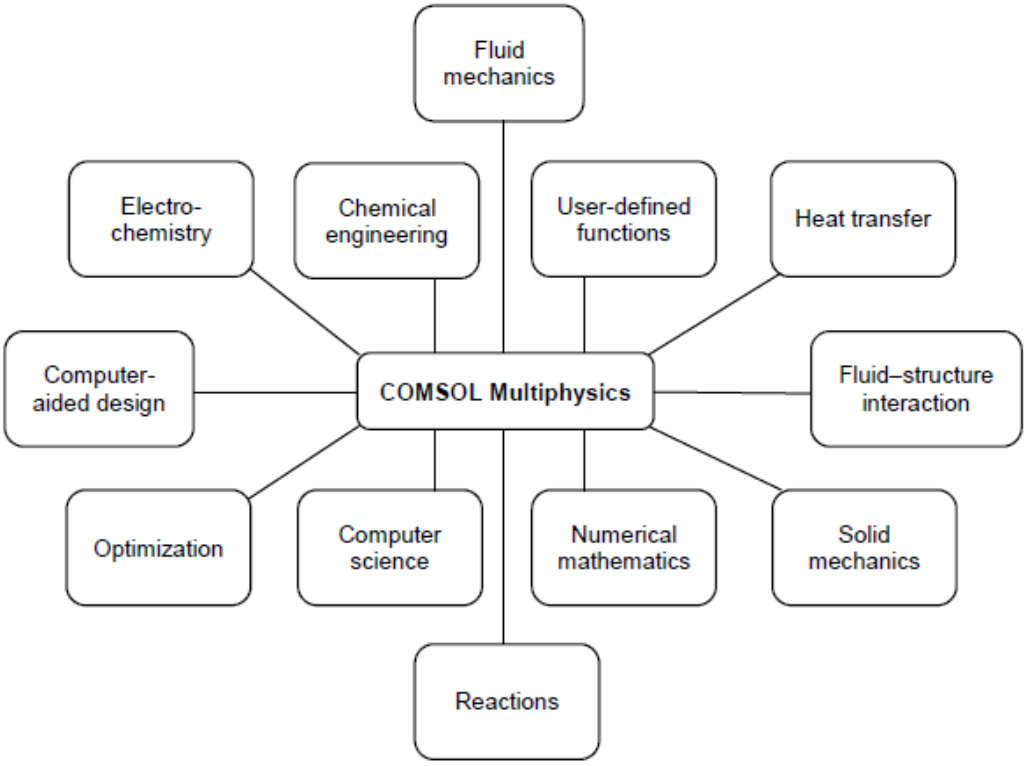

Figure 3-3: Illustration of the employment of COMSOL Multiphysics® in a wide range of applications [255].

3.2 Problem statement of a single sessile droplet

Although one might think that simulation of a droplet with this seemingly simple shape sitting on a solid substrate is a straightforward undertaking, modelling of such system, in fact, is considered a great challenge due to the dealing with the moving droplet free surface and/or the contact line during the evaporation course, which is still not well simulated, and coupling of heat and mass transfer process with the evolution of these parameters. Therefore, the problem should be simulated carefully in order to capture most physics and mechanisms involved in this fundamental process.

This chapter focuses on building the mathematical model of the evaporation of a single sessile pinned water droplet resting onto a flat solid substrate with initial height, contact angle and volume in a specific non-saturated ambient air domain at atmospheric pressure. The droplet evaporation is investigated under two

different surrounding environments, which are either natural convection or forced convection environment, in order to examine how the evaporative behaviour and internal dynamics inside the droplet are affected under such environments.

The pinned droplet contact line is adopted in current simulations based on the observations of Hu and Larson [89] as the constant contact line phase occupies the 90-95% of the total droplet evaporation time. Moreover, for solid substrates having high thermal conductivity, for instance silver (430 W/m K), copper (398 W/m K), aluminium (247 W/m K), an isothermal surface assumption and ignoring the variation of the substrate temperature, which are common assumptions that have been used in prior numerical studies [219, 220], are applicable for this kind of materials. Therefore, for simplicity, the solid substrate will not be involved in simulating the current problem since its effects on the droplet evaporation are negligible, and a solid surface at constant temperature assumption is considered here.

The surrounding ambient air is taken to be at the same temperature as the droplet and solid surfaces. A simplification of the problem is made by assuming, as in [89], that the evaporation of such fluid is sufficiently slow that changes in droplet temperature are small enough for the saturated vapour concentration along the droplet free surface (used as a boundary condition), and fluid properties to be considered constant. Very recently, Nguyen et al. [219] have produced a closed form analytical solution for droplet evaporation (under quasi-static conditions with no convection) coupled with the interfacial cooling effect. They used a dimensionless evaporative cooling number, $E_0 = bLD_v/k$, to characterise the influence of evaporative cooling on the droplet evaporation. Here b is the thermal gradient of saturated vapour concentration, and L and k are respectively the latent heat of vaporisation and the liquid thermal conductivity. As $E_0 \to 0$, the evaporative cooling effect becomes negligible and the isothermal assumption is appropriate. Nguyen et al. also provide values for E_0 for a few liquids at temperature and pressure very close to those considered here. For water, they give $E_0 \sim 0.11$ (for comparison acetone has $E_0 \sim 1.03$) so the evaporative cooling will have only a small influence on the predicted evaporative fluxes. Neglecting the interfacial cooling will result in a slight over-prediction of the flux, but this will be much smaller than the changes in flux arising as result of considering the

forced convection. An isothermal model of the evaporation process is therefore deemed suitable. Hence the key driving mechanism for evaporation is diffusion driven by vapour concentration gradients, and the effects of convection (either natural or forced) on these gradients will be explored.

Numerical studies of the evaporation process, as mentioned in the literature, are mostly carried out in still environments, neglecting the effects of convective flow over the evaporating droplet, and hence diffusion is the only mechanism controlling the evaporation process [99, 218, 219, 259]. This assumption is justified for low Péclet number ($Pe = R_d u_{a,n}/D_v$). Considering the droplet size $R_d = 10^{-3}$ m as a characteristic length and the normal air velocity, i.e. due to droplet evaporation which is of order $u_{a,n}{\sim}10^{-4}$ m/s according to computer simulations based on the local mass flux of vapour, as a characteristic convection air velocity, the estimated Péclet number is around 0.004. Here, D_v is the diffusivity of vapour in the surrounding air, taken to be 2.52×10^{-5} m^2/s according to an empirical equation [260]:

$$D_v(T) = 2.5 \times 10^{-4}\exp(-684.15/T + 273.15) \tag{3.1}$$

Thus, as suggested by Larson [44] the convection flow is influential if Pe exceeds around 10. Note that in the present work, Péclet number is changing from 0.004 to 80 corresponding to the air speeds considered for the single droplet evaporation. However, consideration of convection within the evaporation process is necessary to give more realistic conditions surrounding the evaporating droplet, and to assess the potential of convective flow for increasing the evaporation rate and changing dynamics inside the evaporating droplet in comparison to diffusion-controlled evaporation [104, 184, 186-188]. Therefore, the effects of the convection flow (natural and forced convection) will be considered in this study since the effects of forced air convection will be the main attention of this numerical study.

The numerical model simulates the evaporation of a single pinned sessile water droplet with relatively small radius, $R_d \leq 10^{-3}$m, i.e. less than the capillary length $a = \sqrt{\gamma/\rho_l g}$, and initial contact angle, $\theta_o \leq 90°$. The Bond number, $Bo = \rho_l g {R_d}^2/\gamma$, which represents the ratio of gravitational force to surface tension, and

Weber number, $We = \rho_l V^2 R_d/\gamma$, which measures the relative importance of inertial force and the surface tension, are both small (Bo and $We \ll 1$). Here, $\gamma = 0.073$ N/m is the surface tension at the water/air interface, $\rho_l = 10^3$ kg/m^3 the liquid water density, V the characteristic fluid velocity, and $g = 9.81$ m/s^2 the gravitational acceleration. Under such conditions, as the capillary forces dominate the gravity force, the droplet can be expected to be spherical, which is a simplification commonly exploited in previous work [33, 89, 182, 218] together with the assumption that the evaporation is under a quasi-steady diffusion state [89]. The latter is usually well justified since the time scale required to diffuse liquid vapour in the surrounding air, $t_{diff} = {R_d}^2/D_v \sim 10^{-2}$ s, is much faster than the evaporation time scale, t_{evap} which is of the order of $10^2 \sim 10^3$ s, as observed in several previous experimental and numerical studies [108, 213, 261, 262]. This means that liquid vapour concentration adjusts rapidly compared to the time required for evaporation.

However, since sessile droplet shape can potentially be deformed by an active system, i.e. a shearing airflow present [263], here the transient terms in the governing equations for flow and mass transport are retained in all simulations, and the free-surface shapes are determined dynamically as part of a coupled solution (discussed later in section 3.4). Hence, the droplet is only assumed to be spherical as an initial condition, and the free surface deforms locally according to local mass loss via evaporation and stresses from the passing airflow, i.e. in case of providing an active source of airflow. The schematic of the system configuration for an isolated single sessile droplet inside a hemispherical surrounding domain, i.e. to represent the natural convection environment, is shown in Figure 3-4.

3.3 Governing equations and boundary conditions

Based on the above main assumptions, together with the Boussinesq approximation for buoyancy effects (discussed later) and assuming there are no

reactions between the fluids, the governing equations for the vapour transport, continuity and momentum can be expressed as:

$$\frac{\partial c}{\partial t} + \mathbf{u}.\nabla c = \nabla.(D_v \nabla c) \tag{3.2}$$

$$\nabla.\mathbf{u} = 0 \tag{3.3}$$

$$\rho\left(\frac{\partial \mathbf{u}}{\partial t} + (\mathbf{u}\cdot\nabla)\mathbf{u}\right) = \nabla\cdot[-p\mathbf{I} + \mu(\nabla\mathbf{u} + (\nabla\mathbf{u})^{\mathrm{T}})] - \Delta\rho g\mathbf{k} \tag{3.4}$$

where c is the vapour concentration, $\mathbf{u}$ is the fluid velocity field, t is the time, p is the pressure, μ is the fluid dynamic viscosity, $\mathbf{k}$ is the unit vector in the z-direction, and $\Delta\rho g$, is the body force in the z-direction due to the concentration-dependent variation in density of the surrounding vapour-air mixture (see section 3.3.1). Equations (3.3) and (3.4) apply in all parts of the computational domain, while equation (3.2) is only solved in the vapour-air region surrounding the droplet since the dynamics inside the droplet are neglected in the present simulations, and it will be considered later in different chapters.

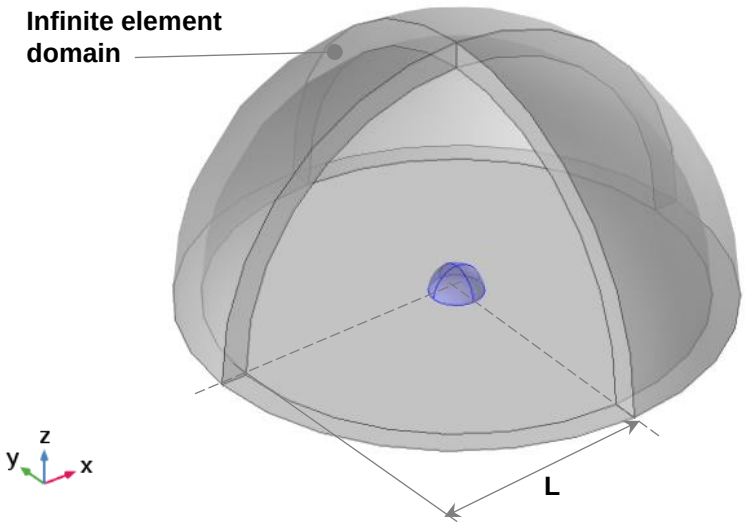

Figure 3-4: Schematic of a single sessile droplet inside an isothermal specific physical domain.

As a result of the fluid motion in the surrounding air, convection mass transfer effects will be added to the water vapour transport by diffusion. Thus, the local total molar flux, **j**, of water vapour at any point combines both mechanisms:

$$\mathbf{j} = -D_v \nabla c + \mathbf{u}c \tag{3.5}$$

As shown in Figure 3-5, at the vapour-solid boundary, the no-flux and no-slip conditions are applied:

$$\mathbf{n} \cdot \mathbf{j} = 0 \tag{3.6}$$

$$\mathbf{u} = \mathbf{0} \tag{3.7}$$

where $\mathbf{n}$ is the unit vector normal to the boundary. At the droplet free surface (indicated by the subscript Γ), the water vapour concentration is assumed to be constant and equal to the saturated value at the ambient temperature, and according to the ideal gas law, it will be:

$$c_\Gamma = c_{sat}(T_a) = P_{v,sat}/R\,T_a \tag{3.8}$$

while the concentration far away from the droplets, i.e. the outer boundary of the computational domain, is determined as:

$$c_{amb} = H c_{sat}(T_a) \tag{3.9}$$

where H is the relative humidity of the ambient air, T_a is the temperature of the surrounding air, and R is the universal gas constant. Assuming the saturation concentration at the droplet free surface to be constant is the most widely used assumption in the previous numerical work under conditions considered here. Otherwise, the temperature dependence of the saturation concentration at the droplet free surface would be taken in account, especially at lower thermal conductivity of substrates and hence significant effect of the evaporative cooling [108], reduced atmospheric pressure [104], and droplets with larger contact angle [264]. Here, as the water vapour is assumed to be saturated, the saturated vapour

pressure can be calculated according to Tetens empirical equation [265], which is more accurate over a wide range of temperatures:

$$P_{v,sat} = 0.611\exp\left(\frac{T_{sat}-273.15}{T_{sat}-36}\right) \times 17.27 \tag{3.10}$$

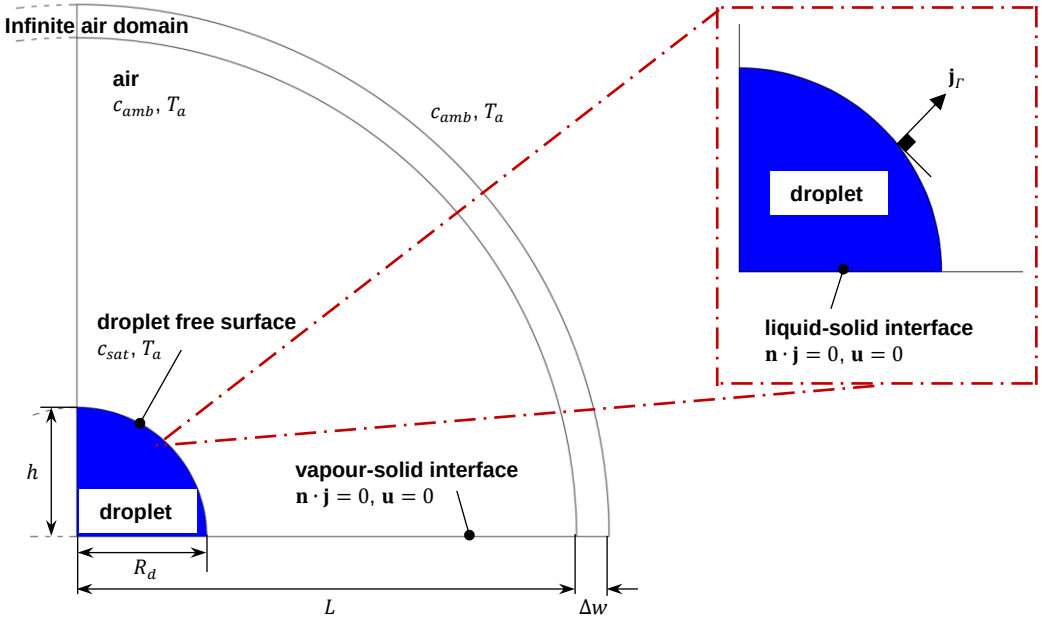

Figure 3-5: 2D sketch of half of the computational domain surrounding a single sessile droplet.

The evaporative mass transport through the droplet free surface produces a discontinuity in the normal component of velocity at this surface as a result of the difference in specific volume between water vapour and liquid water, which is so-called “Stefan flow”. Hence, at the droplet free surface, the velocity fields $\mathbf{u}_a$ and $\mathbf{u}_l$ in the air and liquid respectively must satisfy:

$$\mathbf{u}_a - \mathbf{u}_l = M_{H_2O}\left({}^{1}/_{\rho_v} - {}^{1}/_{\rho_l}\right)(\mathbf{j}_\Gamma \cdot \mathbf{n})\mathbf{n} \tag{3.11}$$

where $\mathbf{j}_\Gamma$ is the molar flux through the interface, $\mathbf{n}$ is the unit vector normal to the interface (pointing from the liquid to the air), ρ_v and ρ_l are respectively the densities of water vapour and liquid water, and $M_{H_2O} = 0.018$ kg/mol is the molar

mass of water. Since thermo-capillary effects are neglected, the balance of stresses in the liquid and air leads to the further condition

$$\mathbf{n} \cdot \boldsymbol{\sigma}_a - \mathbf{n} \cdot \boldsymbol{\sigma}_l = \gamma(\nabla \cdot \mathbf{n})\mathbf{n} \tag{3.12}$$

on the droplet free surface, where $\boldsymbol{\sigma}_a$ and $\boldsymbol{\sigma}_l$ are the stress tensors in the air and liquid respectively. At the liquid-solid boundary within the droplet, as the fluid is in contact with the solid surface, i.e. the fluid velocity is equal to the solid surface velocity, the no-slip condition, $\mathbf{u} = \mathbf{0}$, is applied at this interface, and the contact line is pinned. Other boundary conditions for the air domain change depending on the type of the flow-field in the surrounding air – i.e. either natural or forced convection.

3.3.1 Natural convective environment

For this isothermal flow problem, the main cause of natural convection over the evaporating droplet is the density difference between the vapour-gas mixture at the free surface of the droplet and the surrounding atmosphere. The Boussinesq approximation, which is the popular method for reducing the nonlinearity of small density variation problems, is employed to represent the buoyant convection in the body force term in the z-momentum equation. Neglecting thermal effects, and following the ideal gas law, the density of the air mixture varies with the water vapour concentration in the surrounding air as follows:

$$\rho_m = \frac{P_a M_a}{R T_a} + \left(\frac{M_{H_2O} - M_a}{M_{H_2O}}\right) c \tag{3.13}$$

where P_a is the air pressure and M_a is the molar mass of air. At the outer boundary of the air domain, an atmospheric pressure condition is applied.

3.3.2 Forced convective environment

When the droplet evaporates in a forced convective environment, the air stream transports water vapour diffused in the surrounding air which causes the droplet to evaporate rapidly as a result of increasing the driving-force of evaporation. In this case the Boussinesq term is neglected from equation (3.4). The air-flow is modelled as a laminar and incompressible flow, i.e. assuming that density

changes slightly where the assumption of incompressible flow is still valid, and the velocity and pressure field are independent of the air temperature due to the neglect of thermal effects in the surrounding air. For the forced convection case, a rectangular physical domain with a specific size is used as a computational domain surrounding the droplet instead of using the hemispherical physical domain shown in Figure 3-4 and Figure 3-5, which will be illustrated and discussed in the next chapters. Therefore, in addition to impose $c = c_{amb}$ at the inlet boundary of the computational domain, the inlet velocity profile is defined as a fully developed laminar flow corresponding to a specified average velocity $U_{a,avg}$ and with the entrance length, $L_{entr} = 0.06ReD_H$, where Re is the Reynolds number and D_H is the hydraulic diameter of the physical domain. At the outlet, $-\mathbf{n}.D_v\nabla c = 0$ boundary condition is applied, and the pressure is specified as atmospheric pressure.

3.4 Droplet surface evolution and domain deformation

Clearly, as the droplet evaporates under any environmental conditions (natural or forced convection) it will shrink, and hence the computational domain must adjust to allow for this shrinkage in order to preserve mass conservation law. In most previous numerical studies [33, 89, 182, 218], instead of tracing the droplet free surface automatically during the evaporation process, a series of evaporation calculations at every time-step assuming a fixed droplet profile, i.e. the spherical-cap shape will be the droplet profile during the evaporation course, is conducted and converted to describe the moving of the droplet free surface. Given the success and accuracy in adopting this technique, it is considered a very time consuming way because of the necessary re-meshing and re-arranging of the data at every single time-step. Further, it can only be adopted for simulating the spherical droplet profile case with fixed contact line or fixed contact angle regime. Therefore, this way is not able to simulate other situations of the evaporation of a sessile droplet, as mentioned previously in section 3.2, such as droplets impacting on surfaces, the motion and deformation of droplets due to a forced convection source or droplet evaporation under non-spherical droplet profile.

Here the governing equations, therefore, are solved numerically using an Arbitrary Lagrangian-Eulerian (ALE) finite element method (FEM) via the software COMSOL Multiphysics® v. 5.3, with Lagrange quadratic shape functions (as mentioned in the introduction of this chapter) and an unstructured quadratic tetrahedral mesh (the computational mesh section will be discussed in detail in Chapter 4). In COMSOL Multiphysics®, there are two approaches which work with the ALE method to control the deformation of the computational mesh, which are known as: Deformed Geometry and Moving Mesh, which will be discussed later in Chapter 4.

The ALE method is a technique combining the best features of both Lagrangian and Eulerian methods, and overcomes the shortcomings that each pure method has. Thus, these methods must be rewritten in a way to allow the mesh to follow the moving surface of the droplet. ALE technique, therefore, gives more freedom to each node of the computational mesh to move either as the Lagrangian method allows, i.e. following the associated material during motion, or fixed as the Eulerian method behaves, via the mesh coordinate system as shown in Figure 3-6.

As revealed experimentally in several previous studies, the deformation and initiation of a droplet motion on a solid substrate, especially for droplet exposed to a gentle forced air convection, depend strongly on the critical air stream velocity, the droplet size and the contact angle [263, 266-270]. Based on these observations, the air speeds, droplet size and contact angle are chosen to be sufficiently small that no displacement and deformation of the droplet is expected, and the droplet is assumed to evaporate under the ‘constant contact line’ regime, i.e. where the droplet contact line is pinned. Each mesh node lying on a droplet surface is displaced along the local normal to the surface $\mathbf{n}$ at a rate $\dot{\mathbf{x}}_\Gamma$ given by

$$\dot{\mathbf{x}}_\Gamma = (\mathbf{u}_l \cdot \mathbf{n})\mathbf{n} - \frac{(\mathbf{j}_\Gamma \cdot \mathbf{n}) M_{H_2O}}{\rho_l}\,\mathbf{n} \tag{3.14}$$

where $\mathbf{j}_\Gamma$ is obtained from equation (3.5) evaluated at the free-surface node. The first term on the right-hand side of equation (3.14) accounts for general deformations in the droplet shape, e.g. from the shearing effect of the air-flow, while the second term allows for the local mass loss through evaporation.

Away from the droplet free surface, the computational mesh representing the bulk liquid and air domains deforms via the Winslow smoothing model [271], in response to the changes in the droplet surface, subject to the constraint that nodes on the outer boundaries do not move.

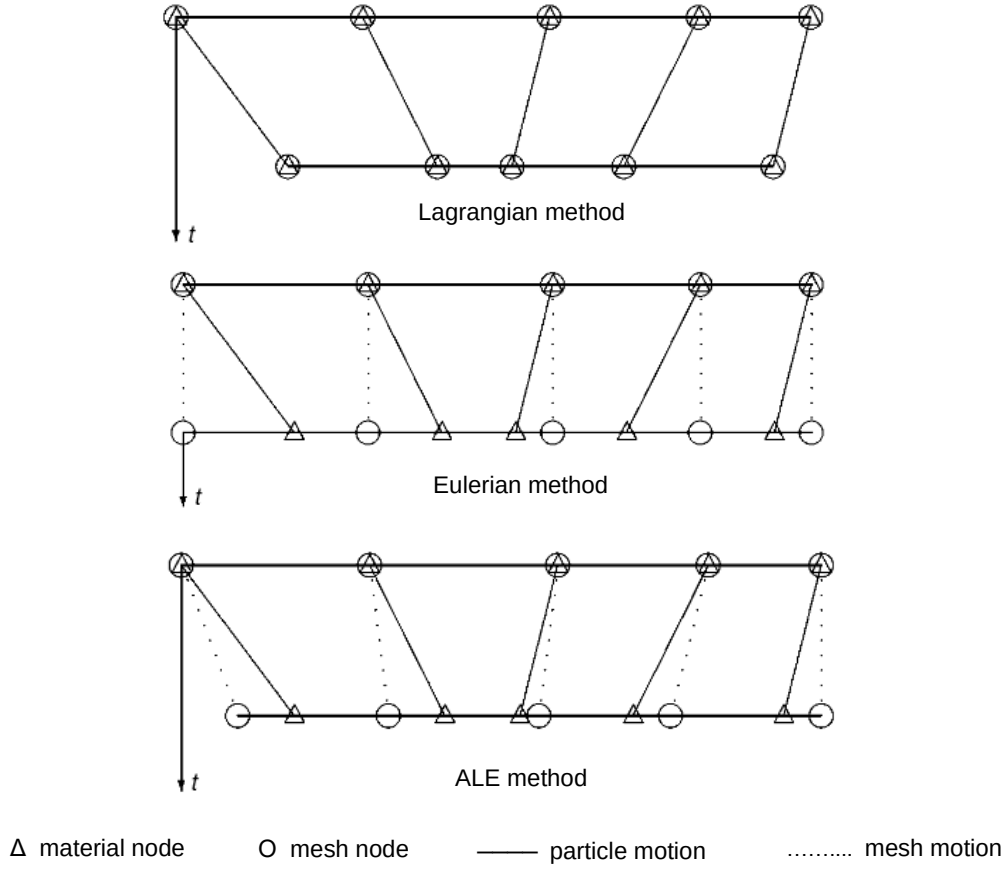

Figure 3-6: Demonstration of the mesh movement manner of Lagrangian, Eulerian and ALE methods.

3.5 Efficient representation of a large ambient domain

A key challenge in simulating open domains, as in the evaporation of droplets in a large space, is where and how to truncate the inevitably finite computational domain. The outer boundary positions and associated boundary conditions must be chosen to avoid artificial influences on the solution close to the region of interest, in this case the droplet. In previous numerical work, the outer boundary of the computational domain surrounding a single droplet was chosen to be either a hemisphere of radius $L = 20R_d$, $L = 100R_d$ or $L = 320R_d$ by Hu and Larson

[89], Chen at el. and Hu and Wu [231, 258], and Dunn at al. [103], respectively or a rectangular domain with a specified size [218, 272]. Although such large distances are effective in obtaining accurate results in axisymmetric simulations, they obviously incur a significant computational cost, which becomes particularly problematic for the three-dimensional transient studies considered here. Moreover, such distances might not be able to keep the droplet domain clearly visible in the graphical display of the model, as shown in Figure 3-7.

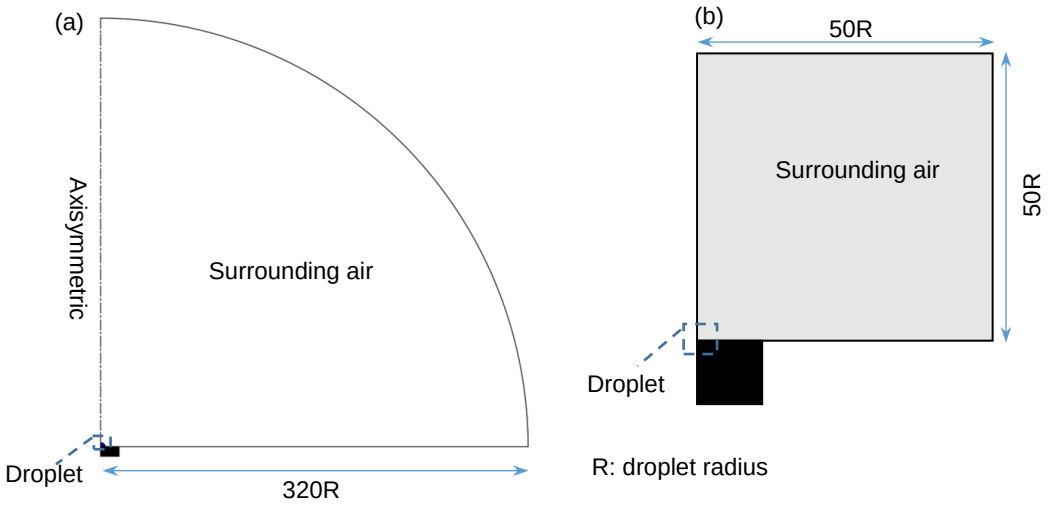

Figure 3-7: Computational domain (not to scale) used by (a) Dunn at al. [103] and (b) Manish Kumar and Rajneesh Bhardwaj [218].

The “Infinite Element Domain” feature available in COMSOL Multiphysics®, therefore, is adopted in the current work to represent the outer boundary of the computational domain for the natural convection cases. This consists of an outer shell, of thickness $\Delta w = R_d$ surrounding the hemispherical domain – see Figure 3-4 and Figure 3-5. Over this layer, a coordinate stretching is applied in the radial direction so that the outer boundary conditions are effectively imposed at a much larger distance from the droplet than the physical domain size. Within the layer, the dimensionless coordinate $\xi = (|\boldsymbol{r}| - L)/\Delta w$ is defined, where $\boldsymbol{r}$ is the unstretched position vector of a point in the domain and L is the radius of the physical domain, i.e. the innermost radius of the shell layer. Hence ξ varies from 0 to 1 across the layer. Inside the layer, the governing equations are reformulated in terms of a scaled coordinate $\boldsymbol{r}' = \boldsymbol{r}_0 + \boldsymbol{n} f(\xi)$, where $\boldsymbol{r}_0$ is the projection of $\boldsymbol{r}$

onto $\xi = 0$, $\boldsymbol{n}$ is the normal to surface $\xi = 0$. The stretching function has the form $f(\xi) = \Delta_p \xi/(\delta - \xi)$ where $\delta = (\Delta_s + \Delta_p)/\Delta_s$, with Δ_s being the scaled width of the stretching layer and Δ_p the pole distance. Here, default values of these parameters are used, specifically $\Delta_p = 3L$ and $\Delta_s = 1000\Delta_p$. This feature provides artificial boundaries limiting the computational domain via the stretching while representing an almost infinite space [271]. It is worth mentioning that this appears to be the first time that this feature has been exploited in the particular context of the problems studied here. The performance of this infinite element approach will be discussed further in the next chapter.

3.6 Physical parameters selection

Specifying a temperature of a system, in which a physical problem will be conducted, is necessary to determine physical parameters controlling this problem. Since there is no thermal effects on the behaviour of the droplet evaporation, the physical parameters variation, e.g. relative humidity, fluids density, dynamic viscosity, and so on, will be neglected unless specified otherwise, and they will be constant at the surrounding environment T_a, i.e. as a reference temperature. The physical parameters for the fluids used in all computer simulations here are summarised in Table 3-1 [273]. Any further parameters used in this numerical work will be mentioned as needed for each situation.

Table 3-1: Main fluids' physical parameters used in all computer simulations.

Physical parameters	Air	Water
Environmental temperature, T_a, [°C]	25.0	25.0
Environmental pressure, P_a, [Pa]	101325	
Saturation pressure, P_v at 25°C, [Pa]		3169
Relative humidity, H, [%]	50	
Contact angle, θ, [deg.]		90
Droplet radius, R_d, [mm]		1.0
Droplet volume, $V_{sph.}$, [µl]		2.094
Vapour diffusion coefficient, D_v, [m^2/s]		2.52×10^{-5}
Molecular weight, M, [g/mol]	29	18

Chapter 4 Model validation and verification

4.1 Introduction

For a simulation to be useful and adopted to evaluate different applicable systems, validation of its predictions against experimental observations is crucial. If a system can be simulated in a reliable way, this supports the conclusion that the physical mechanisms and models in the underlying theory are correct, and indicates that the system is well understood. The simulation can then be used as a tool for exploration, design and optimization. This chapter illustrates the main adopted approaches and processes have been done to verify the present model, and validate it against experimental works available in the literature.

4.2 Geometric model of a single sessile droplet

When the surface tension dominates over the gravity for relatively small droplets resting on a solid surface, a spherical cap shape will be the form of the droplet on that solid surface. As illustrated in Figure 4-1, the spherical cap of a sessile droplet can be characterised by four main key parameters which are; the contact radius, R_d, the contact angle, θ, the droplet height, h, and the radius of the sphere forming the spherical cap, R_s. However, the droplet can be uniquely defined using for example just R_d and θ. The geometrical functions of those characteristic parameters are as below [2, 89]:

$$R_s = R_d/\sin\theta \quad \text{or} \quad R_s = \left(\frac{3V_{sph.}}{\pi\beta}\right)^{1/3} \tag{4.1}$$

where;

$$\beta = (1-\cos\theta)^2(2+\cos\theta) = 2 - 3\cos\theta + \cos^3\theta \tag{4.2}$$

The volume of the spherical cap at any instant in time is related to the droplet radius and the height of the droplet as below:

$$V_{sph.} = \frac{\pi h\left[3{R_d}^2 + h^2\right]}{6} \tag{4.3}$$

while, the droplet height is a function to the two radii and the contact angle:

$$h = R_s(1 - \cos\theta) \quad \text{or} \quad h = R_d \tan\left(\frac{\theta}{2}\right) \tag{4.4}$$

Note that the only characteristic parameter that will be constant through the simulation time is the droplet radius, i.e. droplet contact line, as the droplet is pinned during the evaporation course whereas other parameters will change with time. Furthermore, in the current problem, where R_d =1 mm and $\theta = 90°$, a hemisphere will be the initial shape of the droplet.

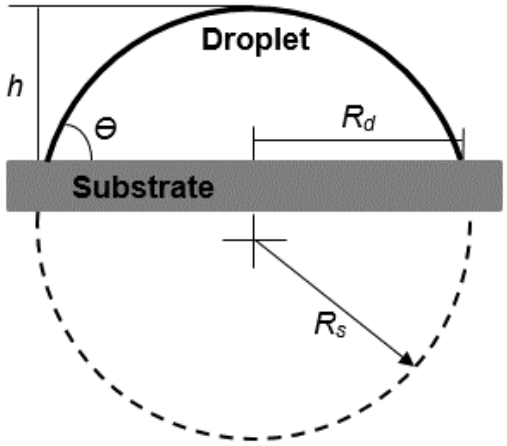

Figure 4-1: Characteristics of the spherical cap shape of a sessile droplet on a solid substrate.

4.3 Verification of the present numerical model

4.3.1 Domain size and mesh independence

Inaccuracies in the numerical solution can arise both from using a mesh that is insufficiently refined to capture gradients in the primitive variables, and from influences of outer boundaries that are too close to the droplets. This is especially so in the natural convection case. Unlike the axisymmetric simulation which is the adopted method in most numerical studies of the evaporation of a sessile droplet,

here for 3D simulation, there is a limit on how the resolution of the computational mesh can refine, due to the limitation of the available memory in the HPC machines and the run-time needed for executing a model, i.e. maximum run-time available is 48 hours. This helps ensure that the model does not fail and runs within the available run-time.

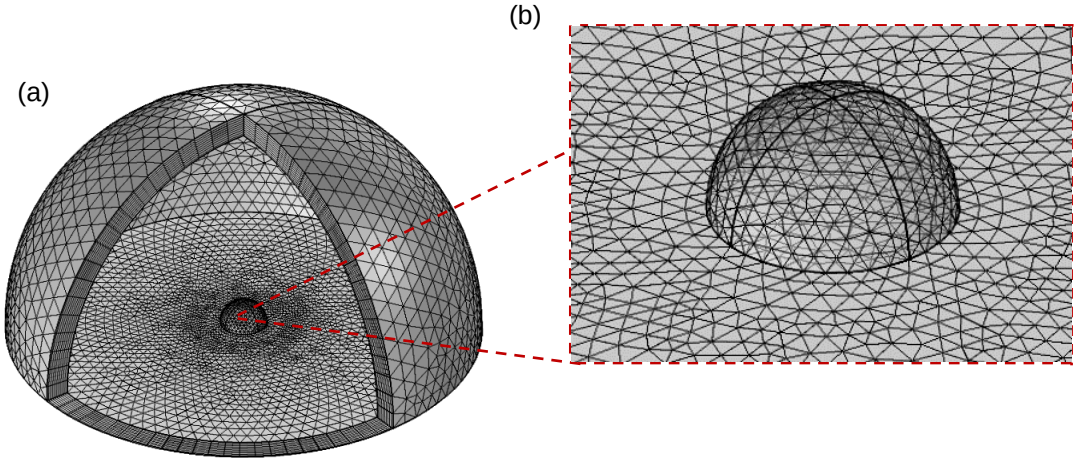

Figure 4-2: (a) A typical finite element mesh of the computational domains used in the simulation of the natural convection case, (b) Zoomed-in view of the mesh along the droplet free surface and near to the droplet edge. Note, a side of the air domain is hidden for a clear viewing of the droplet.

First a suitable mesh, therefore, was established through a systematic refinement of the mesh, with the total evaporation rate after 300s compared for each mesh considered. To achieve that, the computational domain is discretised and refined several times to satisfy the mesh independent results, and to alleviate the distortion of element mesh during the simulations. Adjacent to the droplet free surface, the mesh is refined well to obtain accurate results for the droplet evaporation rates. Further, the mesh near the droplet edge is also refined well to reduce the singularity of the pinned contact line on the numerical solutions since two boundary conditions meet at that contact line of the droplet. Figure 4-2 shows the computational mesh on the droplet and the surrounding domains. For the mesh independence test, the evaporation rate on a mesh refinement, $\mathbf{j}_{\Gamma_{m,i}}$, and that for the less refined mesh, $\mathbf{j}_{\Gamma_{m,i-1}}$, are used to calculate the convergence criterion until it satisfies the recommended value [89], $\epsilon = \frac{\left|\mathbf{j}_{\Gamma_{m,i}} - \mathbf{j}_{\Gamma_{m,i-1}}\right|}{\mathbf{j}_{\Gamma_{m,i}}} < 0.005$,

as shown in Figure 4-3. From Figure 4-3, R6 represents the refined mesh (approximately 76000 elements) used to simulate the droplet evaporation under natural convective environment. Additionally, in order to ensure an acceptable mesh quality throughout the simulation, an automatic remeshing operation is invoked to generate a new mesh whenever the distortion of an element exceeds a maximum threshold.

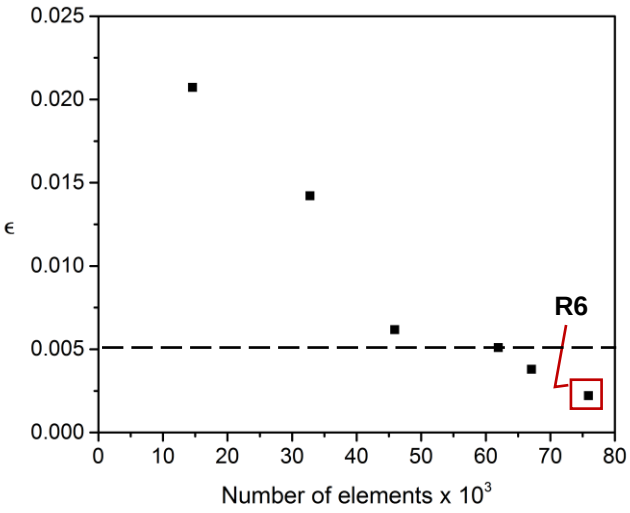

Figure 4-3: The mesh independence test for the natural convection models.

For the droplet evaporation under the forced convective environment, the problem is more complicated since there is large gradient in the velocity. Therefore, more refinement is needed around the droplet and in the surrounding domains, as shown in Figure 4-4. Furthermore, Figure 4-5 shows the satisfying of the recommended convergence criterion at approximately 117000 elements as marked in R6. It is worth to mention that any increasing in the number of mesh elements above the maximum number for both cases, models cannot be executed under the available run-time (i.e., 48 hours).

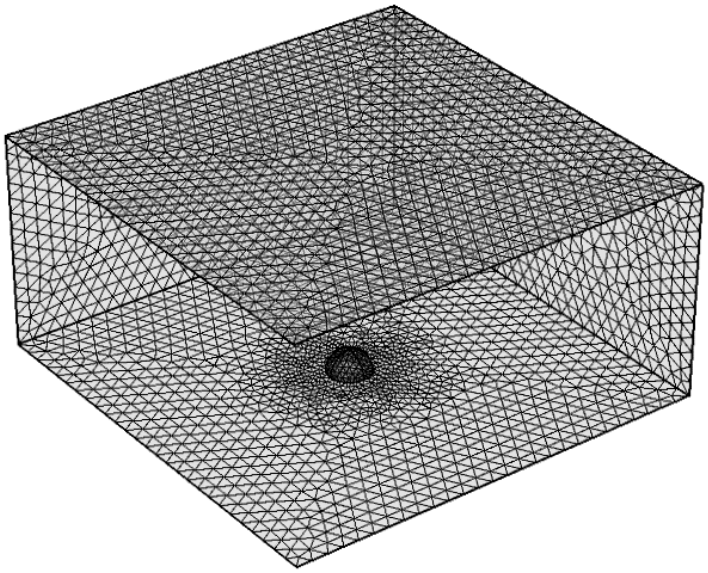

Figure 4-4: A typical finite element mesh of the computational domains used in the simulation of the forced convection case. Note, two sides of the air domain are hidden for a clear viewing of the droplet.

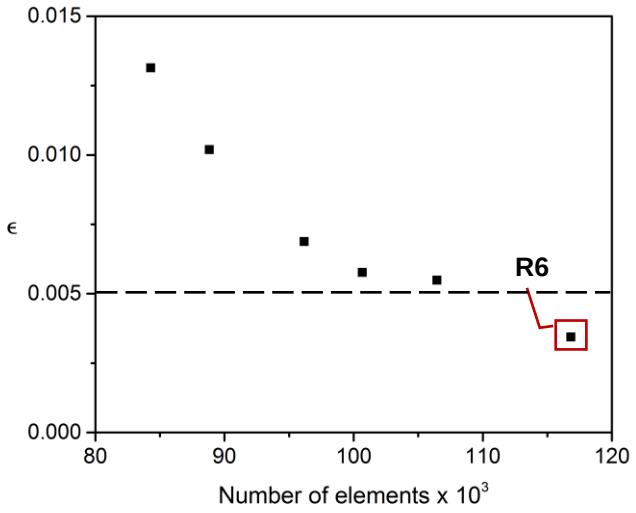

Figure 4-5: The mesh independence test for the forced convection models.

Although the above meshing approach is quite robust, there is a limit on how small the droplet can become, because the FEM does not support the complete removal of this domain during a time-dependent study. To address this issue, there are two ways in which one can execute a model without encountering convergence problems arising from the larger mesh deformation. The first way is

to add a condition which stops the solver if either the mesh quality becomes deteriorated or a defined function, e.g. the ratio of the instantaneous volume to the initial volume of the droplet $V(t)/V_o$, reaches a lower specified value. Although these techniques are valuable in investigating cases under a specific condition, it does not help in doing a systematic comparison for various cases under different conditions since each case has different behaviour under a specific condition so that the solver might stop at different conditions. The second way is to select an appropriate run-time of the problem simulations at which the solver will stop. This technique helps ensure results without convergence issues, and allows to make comparisons to different situations of problems as well. Therefore, an appropriate run-time of the problem simulations should be established under the available resources, which is chosen to be 300s. This is sufficient to observe the effects of the model parameters on the droplet evaporation, and to execute a model within the limited time available in a HPC machine.

Note that in some cases, longer times were considered by using the results of the first 300s simulation as initial conditions for a continued simulation. Although this technique is useful, it is much more time-and-cost consuming method since it creates a huge output file which needs a greater machine storage memory.

Having established the appropriate meshing parameters, a computational domain size analysis was performed to ensure that influences from the outer boundary positions were reduced to negligible levels. For the natural convection case (see Figure 3-4), using the 'infinite element domain' approach described in Chapter 3, the (hemispherical) physical domain size, L, was increased systematically from $L = 10R_d$, and in each case the total evaporation rate at $t = 300$s was calculated. Figure 4-6 presents the resulting values (as open circles), and clearly shows that they are essentially independent of L. For comparison, the domain size study was repeated using only a 'standard', i.e. unstretched, domain as used in previous numerical works. As can be seen from the filled circles in Figure 4-6, the evaporation rate calculated via the standard approach exhibits a significant variation with domain size until $L \geq 50R_d$, but the asymptotic value of the evaporation rates from the standard and stretched domains are in good agreement. In fact a least-squares fit of the three-parameter function $A_0 + A_1/(L - A_2)$ to the standard domain data produces the asymptotic value $A_0 =$

1.738×10^{-9} kg/s with a correlation coefficient of 0.998, which closely matches the evaporation rate 1.742×10^{-9} kg/s obtained from the infinite element domain approach. In addition, the deviation from the ambient concentration level near the outer boundaries satisfies $(c - c_{amb})/(c_{sat} - c_{amb}) \lesssim 0.003$, consistent with previous work [89]. Therefore, the infinite element domain approach is found to be very effective in reducing the computational resources required for accurate simulations.

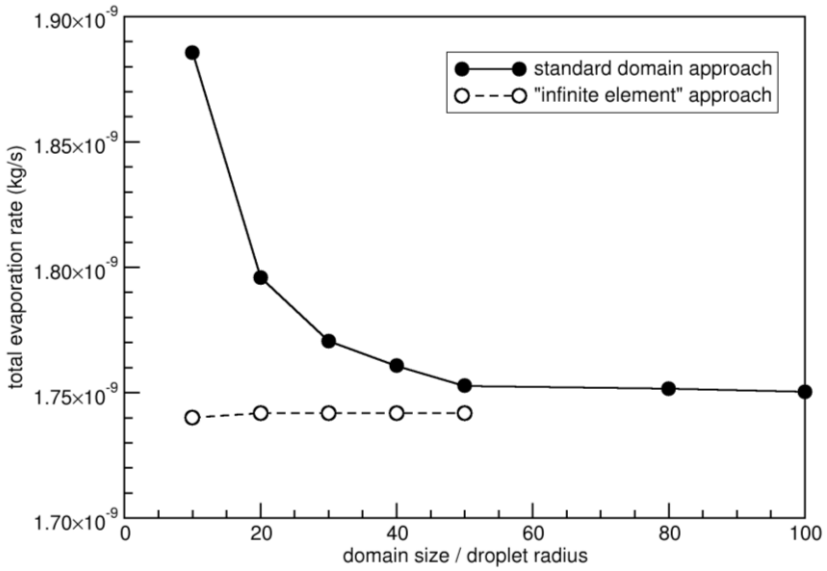

Figure 4-6: Effect of domain size and type on the calculated total evaporation rate for a single droplet evaporating under natural convection.

For the forced convection case, the primary concern for the domain size selection was in avoiding boundary-induced disturbances of the velocity field in the vicinity of the droplets, because of the key role of the air stream in transporting water vapour away from the droplets. As the cross-section area of the rectangular physical domain (width x height) is the most important parameter for selecting the appropriate size of this domain (see section 3.3.2), the cross-section area was increased systematically, and in each case the total evaporation rate of the droplet was calculated at 300s of the evaporation course. Based on the numerical predictions, a rectangular physical domain with dimensions Length (20mm), Width (20mm), and Height (10mm) was found to produce reliable results corresponding with this range of droplet size and air stream velocity, as shown in

Figure 4-7. Numerical results also show, as mentioned in the next chapter, that the length of the computational domain is sufficient to produce accurate results.

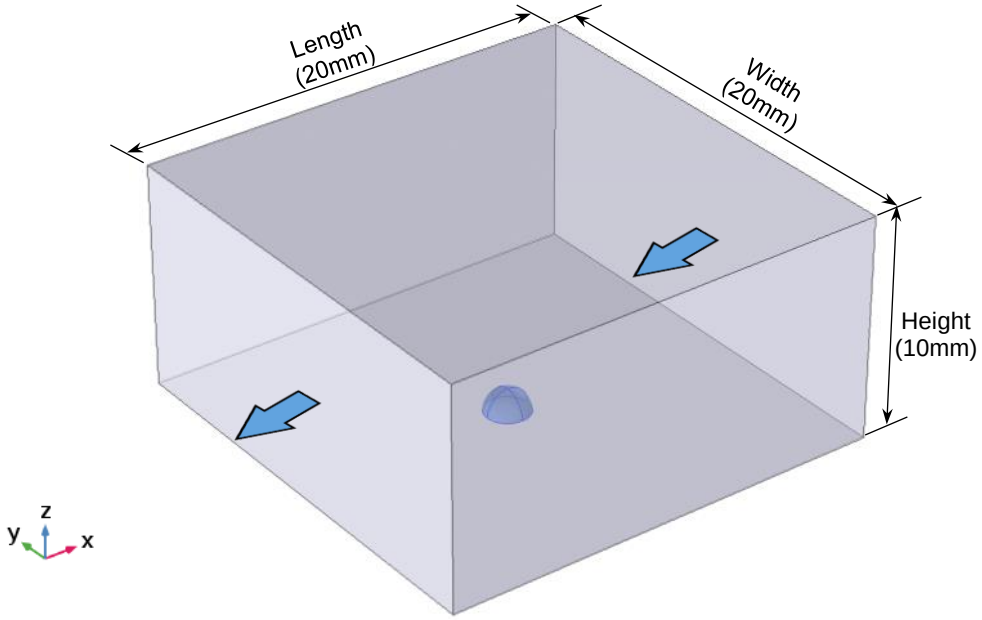

Figure 4-7: Schematic diagram of the physical domain used for the forced convection simulations. The arrow represents the direction of the forced air convection.

4.3.2 Droplet surface motion with the deformed mesh approaches

As mentioned previously in Chapter 3, to preserve mass conservation during the shrinkage of the droplet free surface via evaporation, here the ALE finite element method is used to solve the governing equations of the current problem. To achieve that, two approaches are available in COMSOL Multiphysics® employed for defining the deformation of finite element mesh in such case of problems, the deformed geometry and the moving mesh. Both approaches deal with the ALE and work identically but choosing between them depends on which physics of interest will be solved. Although there are fundamental differences in using these approaches with respect to the coordinate system, i.e. spatial frame, material frame, geometry frame and mesh frame, selected to define the deformation of the computation domain, other important differences were founded during experiencing these approaches for simulating the current problem of interest. Using the deformed geometry approach, the droplet free surface retains a spherical-cap shape while continuously shrinking during the evaporation course

even there is a significant source of distortion e.g., very high air stream. This can be attributed to that each node lying on the droplet free surface is displaced along the local normal to the surface at same rate of displacement given by:

$$u_\Gamma = \frac{-J_\Gamma}{\rho_l A_\Gamma} \tag{4.5}$$

where $A_\Gamma = \frac{2\pi {R_d}^2 (1-\cos\theta)}{\sin^2\theta}$ is the surface area of the droplet and J_Γ is the total evaporation rate of the droplet obtained by integrating the local evaporation flux, Equation (3.5), over the droplet free surface, as expressed below:

$$J_\Gamma = \int \mathbf{j}_\Gamma . \mathbf{n}\, dA \tag{4.6}$$

Moreover, this approach does not determine automatically the effect of Stefan flow, and it might need further work to connect this physical mechanism with other physics controlling the evaporation process. In addition to that, observed results indicate that the pressure seems to be not connected perfectly with the local evaporative flux, particularly in the region of a high velocity gradient.

Therefore, based on these observations, the moving mesh approach is adopted to simulate the current problem, as it is more realistic method, since the droplet profile is assumed a spherical-cap shape as an initial condition, and then the droplet free surface deforms according to the local evaporation rate, see Equations (3.5) and (3.14). In addition, Stefan flow is employed automatically through Equation (3.11).

4.4 Validation against experimental observations

In order to validate the numerical predictions by the current adopted method, the experimental results of Hu and Larson [89] for the measured droplet profile at different times are chosen for this purpose. The experiment of Hu and Larson was conducted on a water droplet with initial radius of $R_d = 0.85$ mm and height $h_o = 0.329$ mm deposited on a clean glass coverslip, and covered with a cylinder open to the air for evaporation. In addition, their experiment was done at environmental conditions of temperature 25℃ and relative humidity 40%. They measured the evaporation rate of the droplet via measuring the droplet surface profile and volume by using the microscopic particle tracer method. The findings

revealed that the droplet remains as a spherical cap shape and pinned at all time of the evaporation course.

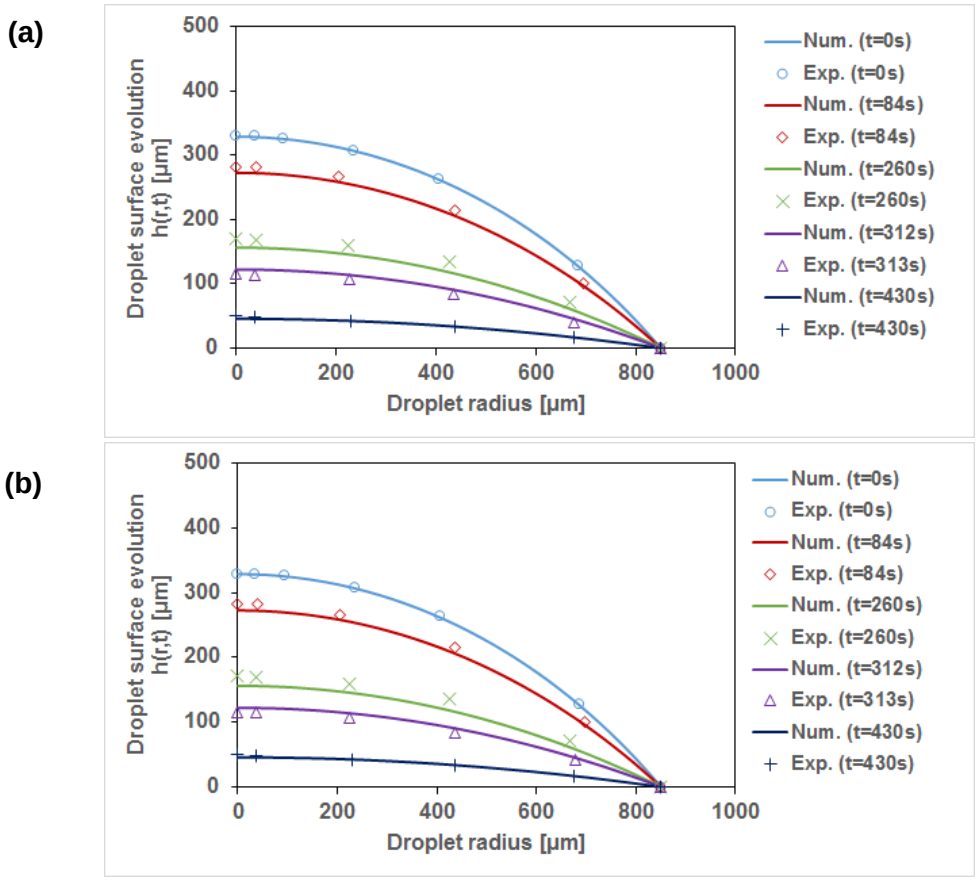

Figure 4-8. Comparison of the current numerical results with the experimental results [89] for the measured droplet profile at different times and at different computational domain size (a) L=10 mm, (b) L=20 mm.

Therefore, their experimental conditions are adopted to simulate the evaporation of a single pinned water droplet via the current numerical model. The comparison results are shown in Figure 4-8(a), in which it can be seen that the predicted droplet profile and its evolution agree well with the experimental results of Hu and Larson. Quantitative errors in the droplet height do not exceed 8.2%. As a conclusion, the current model and numerical method can be considered a convenient and effective approach. In addition, Figure 4-8(b) shows the comparison results in the case of using larger size of the hemispherical computational domain (L=20 mm). As one can see that there is no discernible

difference compared to the case of L=10 mm of the computational domain which further demonstrates the effectiveness of the infinite element domain approach adopted in the current numerical model in allowing boundary conditions at infinity to be imposed appropriately using a much smaller computational domain than typically used previously.

Further comparison with Hu and Larson findings, and numerical results of Picknett and Bexon [57] are shown in Figure 4-9. Here, a water droplet with initial radius of $R_d = 0.95$ mm and height $h_o = 0.364$ mm at 25℃ and 38% relative humidity are used as experimental conditions. It can be seen that numerical results from the present model are very consistent with those from Hu and Larson's model and experiments, and from Picknett and Bexon's model with relative errors 1.9%, 2.8% and 3.8%, respectively in the lifetimes of the droplet, where the droplet evaporates completely.

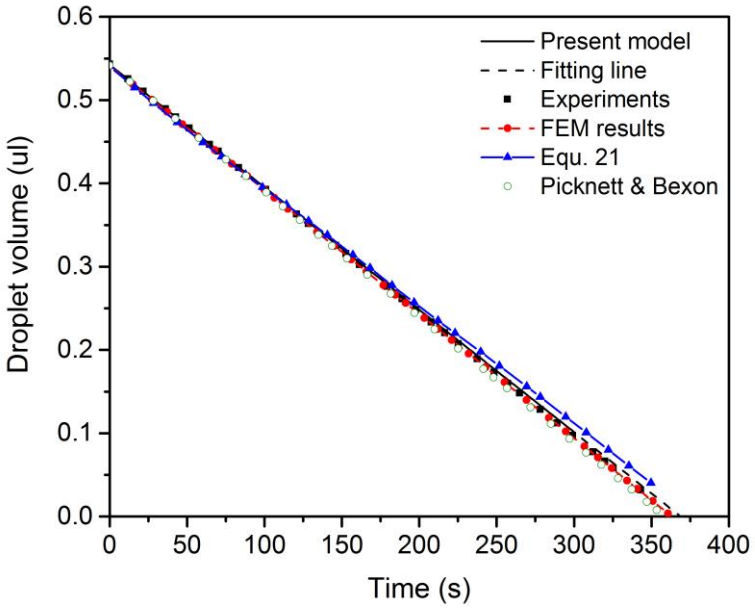

Figure 4-9: Comparison of the current numerical results with the experiments and model results of Hu and Larson [89], and results of Picknett and Bexon's model [57].

Chapter 5 Evaporative behaviour of a single sessile droplet under a forced airflow

As mentioned in the literature review of Chapter 2, simulating a single sessile droplet evaporating into the atmosphere (i.e. under natural convective environment) has been conducted intensively even in recent times [239, 274, 275]. Different droplet sizes, liquids, surrounding gases, and thermal conductivity and structure of solid substrates have been used to investigate the effect of all these parameters on the evaporation rate of the droplet [80, 218, 227, 231, 276], and so on. Further, different mechanisms affecting droplet evaporation (e.g. diffusion, buoyancy flow in both liquid and gas sides, Stefan flow, and Marangoni flow in both liquid and gas sides) have been considered to examine their influences on the evaporative behaviour of the droplet [219, 220, 277-281], and so on.

However, the evaporation of a single sessile droplet exposed to a gentle forced air convection is much more complicated than that under natural convective environment, and has not been well investigated numerically. The interaction between the convective air and the diffusive flux dispersed from the droplet surface via evaporation is also complicated, and is a challenging topic for coupling the mass transfer of two phase flow and the forced air convection. In addition, both the effect of the surrounding gas on the droplet and the effect of the droplet on the surrounding gas, in their turn, should be also considered to understand the interaction between them. Thus, usually, many researchers attempted to simplify the problem by some assumptions for instance, Hongtao Zhang [190], Raghuram et al. [246] and Ljung and Lundström [247] assumed that the droplet shape always remains spherical during the evaporation, and Stefan flow was not considered in their numerical models. Moreover, recent experimental and numerical studies in the literature [254, 282] show clearly the strong influence of an evaporating droplet by an upstream spherical solid body in changing the airflow path passing the evaporating droplet, which confirms the importance of the above interactions.

Therefore, the work presented in this chapter will not just discuss the concept of the evaporation of a single sessile droplet in a convective environment, but rather

focus on the action of both the droplet on the surrounding and the forced air on the concentration field surrounding the droplet, and hence the evaporative behaviour of the droplet. This will provide more insight on the most effective mechanism influences the droplet evaporation, disclose how this mechanism influence the evaporation of an array of multiple droplets.

5.1 Evaporation rate of a single sessile droplet

Simulations of the evaporation of a single pinned sessile water droplet under a wide range of forced airflow velocities (from 0.02 m/s up to 2.0 m/s) are performed in this chapter to capture the influence of the forced airflow on the temporal evolution of the droplet volume, and hence the evaporation rate of this droplet. This range of the air stream velocities is chosen in order to achieve a laminar flow regime; to prevent the motion and deformation of droplets on solid surfaces; and to maintain pinning of the droplet on those surfaces at this range of droplets size and contact angle [263, 268]. The evaporation of same droplet under natural convective environment is also performed as a reference case for comparison. All physical properties mentioned in Chapter 3 in Table 3-1 are used to simulate these numerical models.

Referring to the semi-static condition, where the flow in the air domain is driven by the difference in density of the vapour-gas mixture at the droplet free surface and surrounding atmosphere, as discussed in Chapter 3, results of Figure 4-9 and the dashed blue line in Figure 5-1 show clearly that the droplet volume decreases almost linearly with time during the evaporation course. Hence, the droplet volume evolution can be well-fitted by a linear expression. In parallel, at the forced convection case as shown in Figure 5-1, although the droplet is exposed to different air speeds, the evolution of the droplet volume with time for all cases has mostly a similar trend. In addition, at lower air speeds the decreasing of the droplet volume with time is slow, while it decreases quickly as the air speed is increased. Further analysis of Figure 5-1 shows that the droplet volume decreases almost linearly at the lower air speeds as a result of the insufficient effect of the airflow convection, which is very consistent with the evolution profile of the droplet in the natural convection case shown in Figure 4-9.

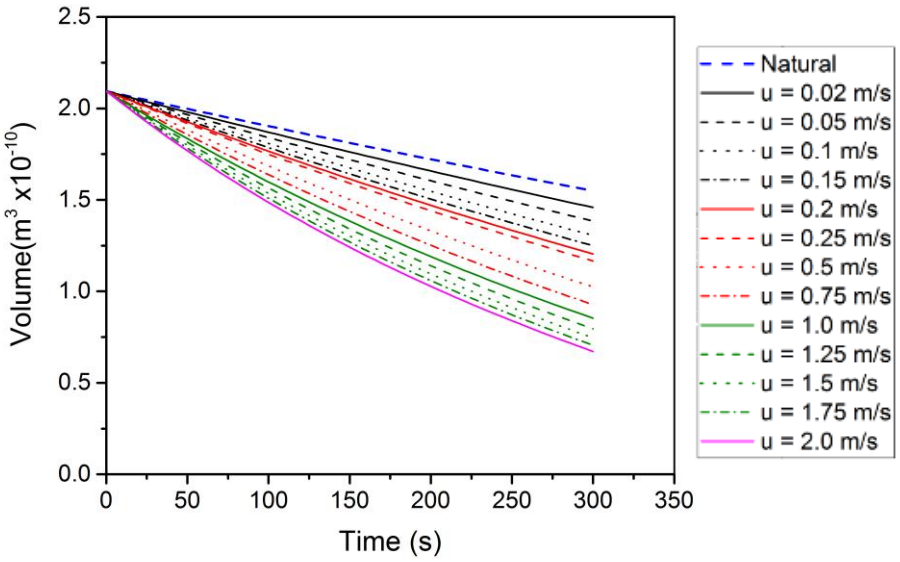

Figure 5-1: Evolutions of the volume of a single droplet under natural convective environment and various forced airflow velocities, and at 300s from the whole period of the evaporation process.

As the air speed is increased, the linear fitting does not agree well with the temporal evolution of the droplet volume and therefore, the exponential fitting is more match with the evolution of the droplet volume at the higher air speeds. Thus, for consistency, the exponential fitting will be considered for the droplet volume evolution at all air speeds, as expressed below and shown in Figure 5-2;

$$V(u,t) = V_o - \mathrm{A}(1 - e^{Bt}) \tag{5.1}$$

where $V(u,t)$ is the droplet volume at any time and velocity of the airflow, V_o is the initial volume of the droplet at t = 0 s, and A, B are the fitting coefficients which are dependent on the airflow velocity. The coefficients A, B are themselves well represented by the following functions:

$$A = \alpha_A - \beta_A \ln(u + C_A) \tag{5.2a}$$

$$B = \alpha_B + \beta_B u^{C_B} \tag{5.2b}$$

where α_A, β_A , C_A, α_B, β_B and C_B are the fitting coefficients which are listed in Table 5-1. From Equation (5.1), the lifetime of the droplet, t_f, where the droplet evaporates completely, can be obtained as:

$$t_f = \frac{\ln\left(1-{}^{V_o}/_{A}\right)}{B} \tag{5.3}$$

Using the fitting coefficients in Table 5-1 together with Equation (5.1), the influence of the air speed on the droplet lifetime can be constructed, and this is shown in Figure 5-3 in which it is very clear to see how the droplet lifetime decreases rapidly with increasing air speed as a result of accelerating the evaporation rate. Note that, Appendix A provides further details of the fitting coefficients of Equations (5.2a) and (5.2b).

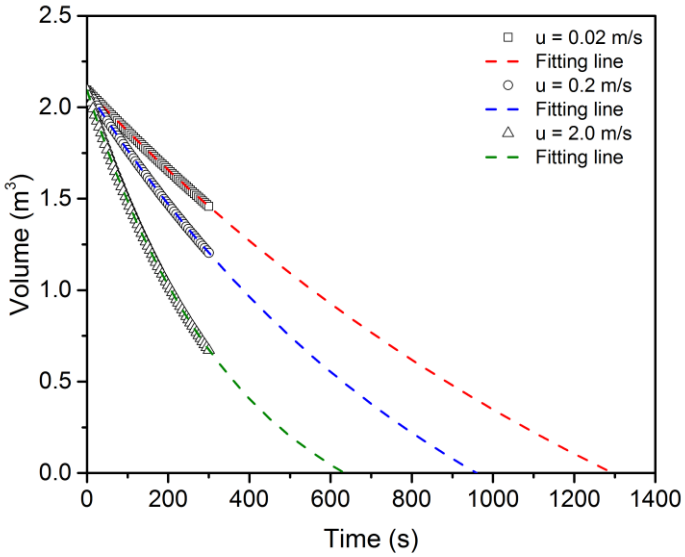

Figure 5-2: Evolutions of the volume of a single droplet and the fitting lines for forced airflow velocities.

Table 5-1: Fitting coefficients in Equations (5.2a) and (5.2b) at a range of validity (U = 0.02 – 2.0 m/s).

α_A	β_A	C_A	α_B	β_B	C_B
2.79427×10^{-9}	3.25023×10^{-10}	0.01291	-4.5341×10^{-4}	-0.0015	0.58414

For further analysis on the relationship between the droplet evaporation rate and the forced convective environment, the evaporation rate can be expressed in terms of the Sherwood (Sh), Reynolds (Re) and Schmidt (Sc) numbers as discussed previously in the literature review of Chapter 2 - see Table 2-1. Having the evaporation rate equal to the change of the droplet mass with time and from Equation (5.1), it can be expressed as;

$$E(u,t) = \rho \frac{dV(u,t)}{dt} = \rho \mathrm{AB} e^{Bt} \tag{5.4}$$

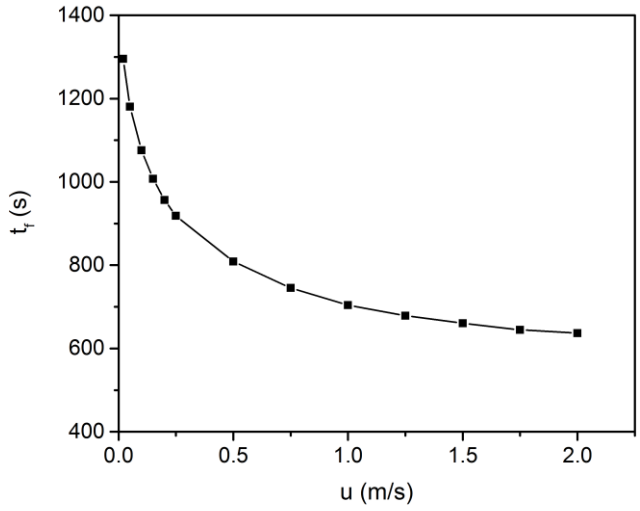

Figure 5-3: Variation of the droplet lifetime with the airflow velocity.

where E is the droplet evaporation rate at any time and airflow velocity. According to the initial evaporation rate at $\mathrm{t} = 0$ and the set of dimensionless numbers, where Sherwood number can be also expressed as $Sh = E.L/A_s D_v(C_s - C_\infty)$, the result of plotting Sherwood number against Reynolds number, as shown in Figure 5-4 (a), can be well-fitted by this correlation with maximum deviation 0.5%, which represents the evaporation rate of a single sessile droplet under forced convective environment:

$$Sh_i = 1.91 + 0.473 Re^{0.478} Sc^{1/3} \tag{5.5}$$

An estimate of the final value of Sh can be obtained from Equation (5.1) together with the extrapolated droplet lifetime from equation (5.3), which is also shown in Figure 5-4 (a), and well described by the correlation

$$Sh_f = 0.67 + 0.035 Re^{0.665} Sc^{1/3}. \tag{5.6}$$

It is very clear to conclude from Figure 5-4 (a) that as the velocity of the airflow is increased the droplet evaporation rate increases as a result of accelerating the evaporation process through removing the diffusive water vapour away from the droplet surface. Hence, the driving force of the evaporation process (i.e., concentration gradient of water vapour) is increased. In addition, for each air speed, the Sherwood number decreases with time.

Note that in the present work, and in expressions (5.5) and (5.6), the Reynolds number is defined differently from that in Baines and James [194] and Danberg [195, 196] as mentioned previously in the literature. Here it is based on the average speed of the airflow, U, i.e. $Re = \rho U L_d/\mu$, while they defined Reynolds number in terms of the shear velocity, i.e. $Re_\tau = \rho u_\tau L_d/\mu$, where $u_\tau = \sqrt{\mu\dot{\gamma}/\rho}$ and $\dot{\gamma}$ is the shear rate. The length scale $L_d = 2R$, i.e. the diameter of the droplet base. In the vertical centre plane of the forced convection duct (see Figure 4-7), the velocity profile well upstream of the droplet has the parabolic form

$$u(z) = \frac{4U_{max}}{H^2} z(H - z) = \frac{8U}{H^2} z(H - z), \tag{5.7}$$

which has a corresponding shear rate of

$$\dot{\gamma} = \frac{\partial u}{\partial z} = \frac{8U}{H^2}(H - 2z). \tag{5.8}$$

On the solid surface, $z = 0$, equation (5.8) gives a shear velocity of $u_\tau = \sqrt{8\mu U/\rho H}$, which leads to the following relationship between the Reynolds numbers:

$$Re = \left(\frac{H}{16R}\right) Re_\tau^2. \tag{5.9}$$

In the simulations presented here, $H = 10R$, and hence $Re = \frac{5}{8} Re_\tau^2$.

Moreover, the models of Baines and James and Danberg were based on the assumption of steady-state evaporation from a flat droplet, and hence their expressions (see Table 2-1) do not account for the changes in evaporation rate over time (other than via a change in available droplet surface area). The evaporation rate predicted by the present full 3D transient simulations is not constant, even when accounting for the changing surface area, so a specific time needs to be chosen.

Figure 5-4 (b) shows the initial and final Sherwood numbers given by Equations (5.5) and (5.6) compared with the Baines and James [194] and Danberg [195, 196], with the Reynolds number adjusted using (5.9). The Ranz-Marshall correlation [56] is also included for comparison. The Sherwood numbers from the Baines and James and Danberg equations lie between the initial and final values of Sh obtained from the finite element analysis. Interestingly, their predictions are closer to the initial values of Sh, when the droplet protrudes further into the airflow, and produces a greater disturbance to the shear flow. At later times, the droplet becomes flatter, and hence closer to the completely flat form assumed by Baines and James. Their result should therefore perform better under these conditions, but it over-predicts the evaporation rate significantly, which is expected as they were well aware of the limitations of their model, and acknowledged that it can over-predict by as much as 90%.

Besides the steady-state and flat droplet assumption, another key assumption in their model was that a uniform shear flow exists everywhere in the air. However, numerical results show that the droplet produces a significant disturbance to the airflow, with a slowing of the flow immediately upstream of the droplet, and an acceleration over the top of the droplet, resulting in a non-uniform shear around the droplet surface. Further, the Baines and James and Danberg models also do not properly account for the limit of vanishing air speed – there is no constant term in their expression, and hence these expressions predict that no evaporation takes place in still air. This is of course not the case, unless the ambient air is fully saturated.

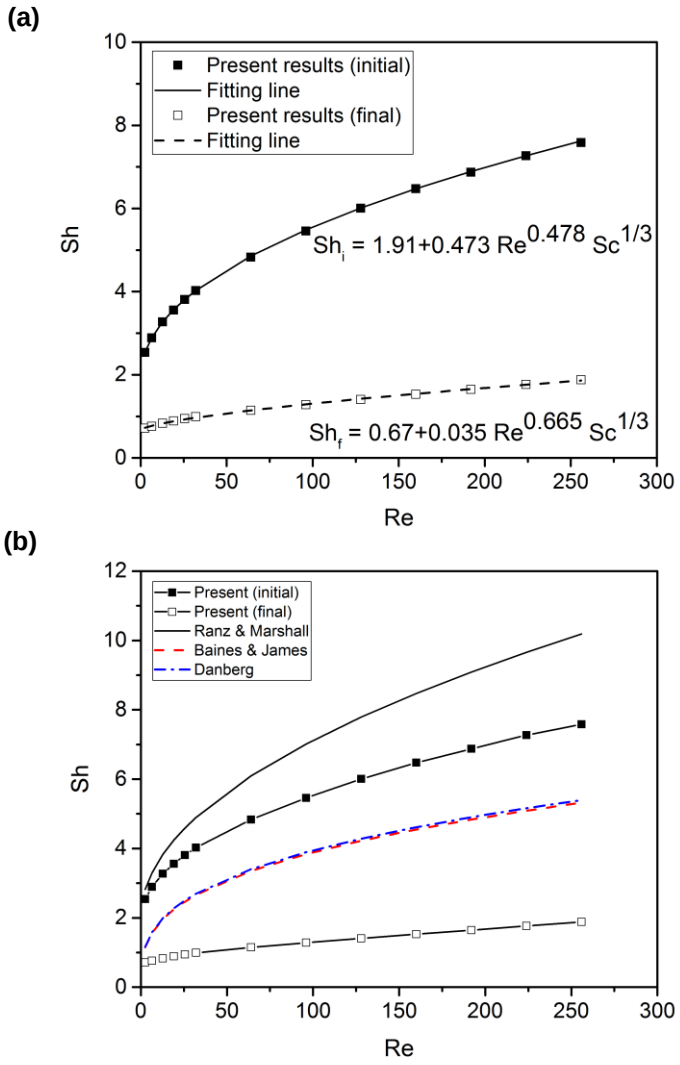

Figure 5-4: (a) Initial and final Sherwood number from 3D finite element simulations as a function of Reynolds and Schmidt numbers and (b) a comparison of the new correlations with available correlations in the literature.

5.2 Anticipated 'zone of influence' around a single droplet

As mentioned previously, providing a gentle forced airflow over a single droplet will sweep downstream any vapour evaporated from this droplet. Hence, there will be an area or zone of competition between the downstream convective flux and the diffusive flux from the droplet free surface acting along concentration

gradients in all directions. The influence of this zone of competition is great, and it is decreasing with increasing distance from the droplet or reducing the speed of the airflow therefore, a boundary of this zone should be specified. A “zone of influence” – representing the area over which raised vapour concentration levels occur as a result of evaporation from the droplet – is anticipated, and can be defined by plotting contours along which the vapour concentration is (say) 1% higher than the ambient vapour concentration, i.e. which is the concentration in the air entering at the inlet of the domain. Figure 5-5 shows these contours for different air speeds and for two times: 5s and 300s after the initial state of evaporation, where the concentration everywhere in the air is at the ambient level.

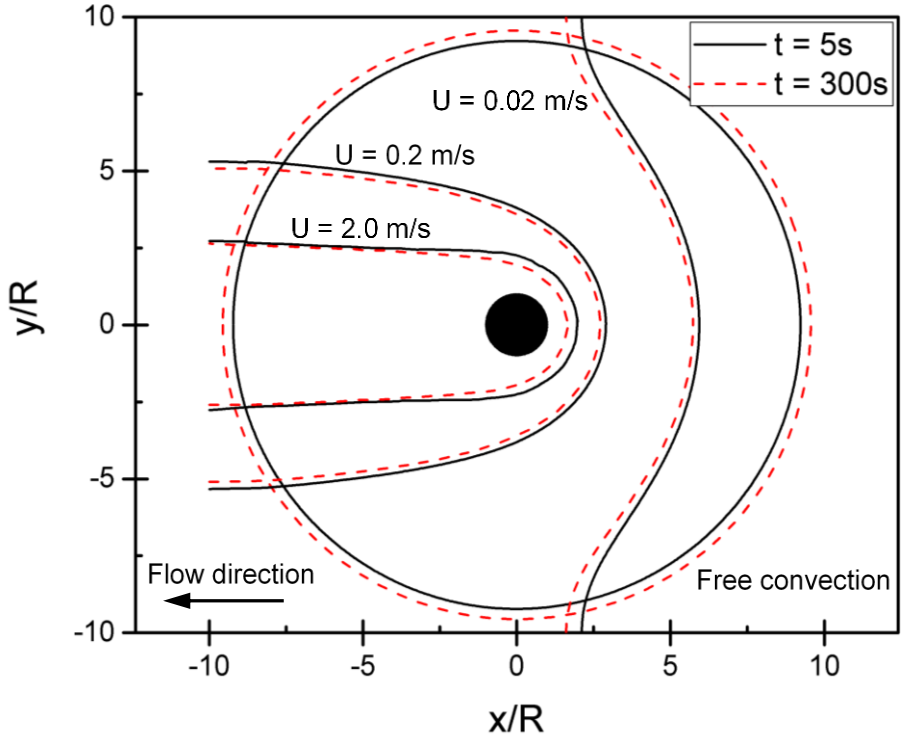

Figure 5-5: ‘Zone of influence’ around a single droplet in an airflow, defined by contours along which the vapour concentration is 1% higher than the ambient (inlet) concentration. The black circle is the droplet. Contours are plotted on the plane of the solid surface. The zone of influence around a single droplet in a natural convective environment is also considered represented by the black solid line circle and the red dashed line circle.

The contours show the expected structure, with higher air speeds producing stronger concentration gradients upstream of the droplet (resulting in enhanced evaporation rates there), and a greater restriction in the transverse spread of the contours. The structure is quickly established and is almost unchanged throughout the time period considered here. However, the contours do shift slightly downstream as the droplet evaporates, and its evaporation rate decreases, as there is insufficient diffusive flux to maintain the concentration level at the t = 5 s location. Note that the U = 0.02 m/s contours bend to meet the y = ±10 extremes of the domain as a result of the zero flux condition applied there. In contrast to the forced convection case, as the droplet evaporates in a natural convective environment, water vapour concentration increases with time and spreads outward to the whole air field as a result of absence of the forced airflow, and it is very clearly shown in Figure 5-5 where the contours do shift slightly outward as the droplet evaporates unlike to what observed in the forced convection case.

For the natural convection, the evaporative flux, as predicted previously, is symmetric along the droplet surface, i.e. higher at the contact line compared to the apex of the droplet, see curve (a) and vector plot (a) in Figure 5-6. Note that, the vector plots in Figure 5-6 show the scaled evaporative flux along the droplet free surface. The presence of a gentle forced airflow over a droplet leads to a decrease in the density of water vapour in the upstream part of the droplet compared to the rest of droplet as a result of the sweeping downstream water vapour diffused from this part of the droplet. Hence, an asymmetric distribution of the evaporative flux along the surface of the droplet is observed where higher evaporative flux at the upstream part, lower at the rest of the droplet, and ends up with a bit higher evaporative flux at the downstream contact line as a result of the singularity of the contact line, as shown in curves (b-d) and vector plots (b-d) in Figure 5-6. Further enhancement in the evaporative flux on the upstream part of the droplet is observed as the speed of the airflow is increased compared to the rest of the droplet.

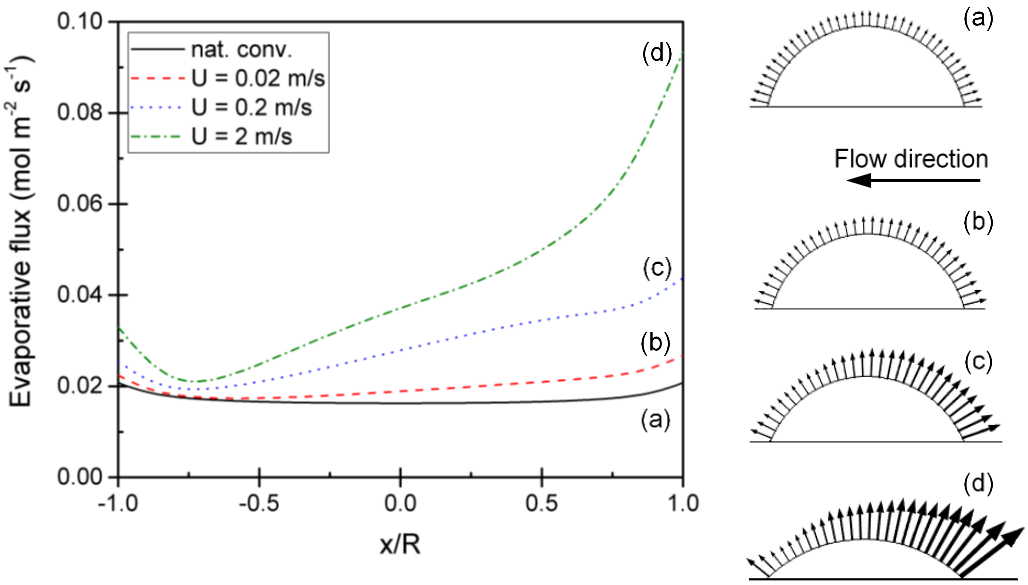

Figure 5-6: Evaporative flux along the droplet free surface at t = 300s under (a) natural convection, and forced convection of air speeds (b) 0.02 m/s, (c) 0.2 m/s and (d) 2.0 m/s. The velocity arrows are normalised to the same scale in all plots.

Observations show a remarkable enhancement in the evaporation rate of the droplet in case of a gentle forced airflow passing over the droplet in comparison to the natural convection case. The evaporation rate at 300 s is increased by 12% by switching from natural convection to a 0.02 m/s forced airflow over the droplet. By increasing the air speed to 0.2 m/s and 2.0 m/s, further enhancement in the evaporation rate is observed, i.e. 46% and 91%, respectively. This enhancement in the droplet evaporation rate is clearly seen in Figure 5-6 (a-d) where a significant difference in the droplet height is noticed with increasing the airflow speed compared to the natural convection.

Further analysis of the influence of the evaporating droplet on the surrounding environment is illustrated in Figure 5-7, which shows clearly how the transported water vapour from the upstream part of the droplet raises the concentration level of water vapour downstream the droplet. In addition, it is very important to notice that as the air speed is increased, the evaporation rate of the droplet is not fast enough to “keep up with” the flow compared with the lower air speed. Figure 5-7 also shows the sufficient length of the computational domain where the

concentration of water vapour for all airflow velocities ends up approximately at same level. Appendix A also shows developing of the concentration levels of water vapour at different heights from the solid surface and at various airflow velocities. These figures clearly illustrate how increasing the air speed reduces the influence of the transported water vapour from the evaporating droplet on the surrounding space above the droplet even at higher levels from the solid surface. Note that, as mentioned in the previous section, the range of air speeds quoted correspond to the average speed of the flow; the speed varies from zero at the solid surface to a maximum of 2U at the vertical centre of the domain. At the level z = 1 mm, corresponding to the initial height of the droplets considered in all numerical models, the air speed is 0.75U.

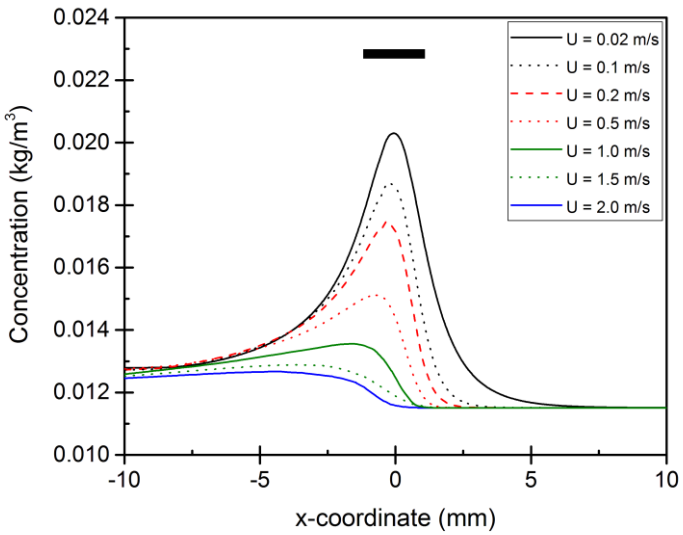

Figure 5-7: Concentration levels along horizontal line (i.e. duct's length) located in the y = 0 centre plane and at 1mm above the solid surface, at t = 300s, and at various air speeds. The flow is from right to left. The position of the droplet is indicated by the thick horizontal black bar.

In parallel to the above results, it is worth to see how the forced airflow affects the flux field in the space surrounding the droplet to introduce a clear understanding to the overall behaviour of both diffusive and convective mass transfer under the effect of the forced air convection. Figure 5-8 shows the diffusive flux and total flux (i.e. combines both convection and diffusion mass

transfer – see Equation (3.5)) around the droplet on a horizontal plane raised by 50 μm from the solid surface, and at various air speeds. Note that the arrow scales are normalised to the same scale in the three figures, but the maximum corresponding fluxes are as mentioned in each figure.

As can be seen from Figure 5-8 (a), the diffusive flux (overlaid red arrows) and the total flux (overlaid black arrows) are almost identical and in the same direction, which indicates the lower convective flux compared to the diffusive flux as a result of the lower air speed. As observed earlier, the flux in the downstream part is less than in the upstream part of the droplet due to the influence of vapour transported from the upstream half of the same droplet. Further, away from the droplet, the total flux is less than near the droplet, which is an indication to the lower both diffusive and convective fluxes there. As the air speed increased to 0.2 m/s, see Figure 5-8 (b), the total flux is shifted slightly from the diffusive flux as a result of increasing the strength of the convective flux caused by increasing the air speed. Further increase in the flux at the upstream half of the droplet is observed as the air speed is increased compared to the rest of the droplet due to increase the sweeping downstream water vapour diffused from the upstream part of the same droplet. In addition, the total flux in the space away from the droplet is more remarkable compared to the lower air speed as a result of increasing of the convective flux.

From Figure 5-8 (c), it is very clear to see how the highest air speed is able to increase the deviation of the total flux from the diffusive flux in the direction as an indication to increase the effect of the convective flux. Again, a remarkable increase in the magnitude of the total flux away from the droplet is noticed as a result of the dominant of the convective flux compared to the diffusive flux, which is mostly uninfluential. Note that, from the three figures, the maximum total flux is increased significantly with increasing the velocity of the airflow.

Again, Figure 5-7 shows clearly how the water vapour transported from the upstream part of the droplet by the airflow rises the concentration levels at the downstream part of the droplet, and hence reduces the evaporative flux at this part as observed previously in Figure 5-6. To understand comprehensively whether the sweeping downstream water vapour diffused from the upstream part of the droplet is more influential than the geometrical shape of the droplet in

reducing the evaporation rate at the downstream part of the droplet, further investigation is needed.

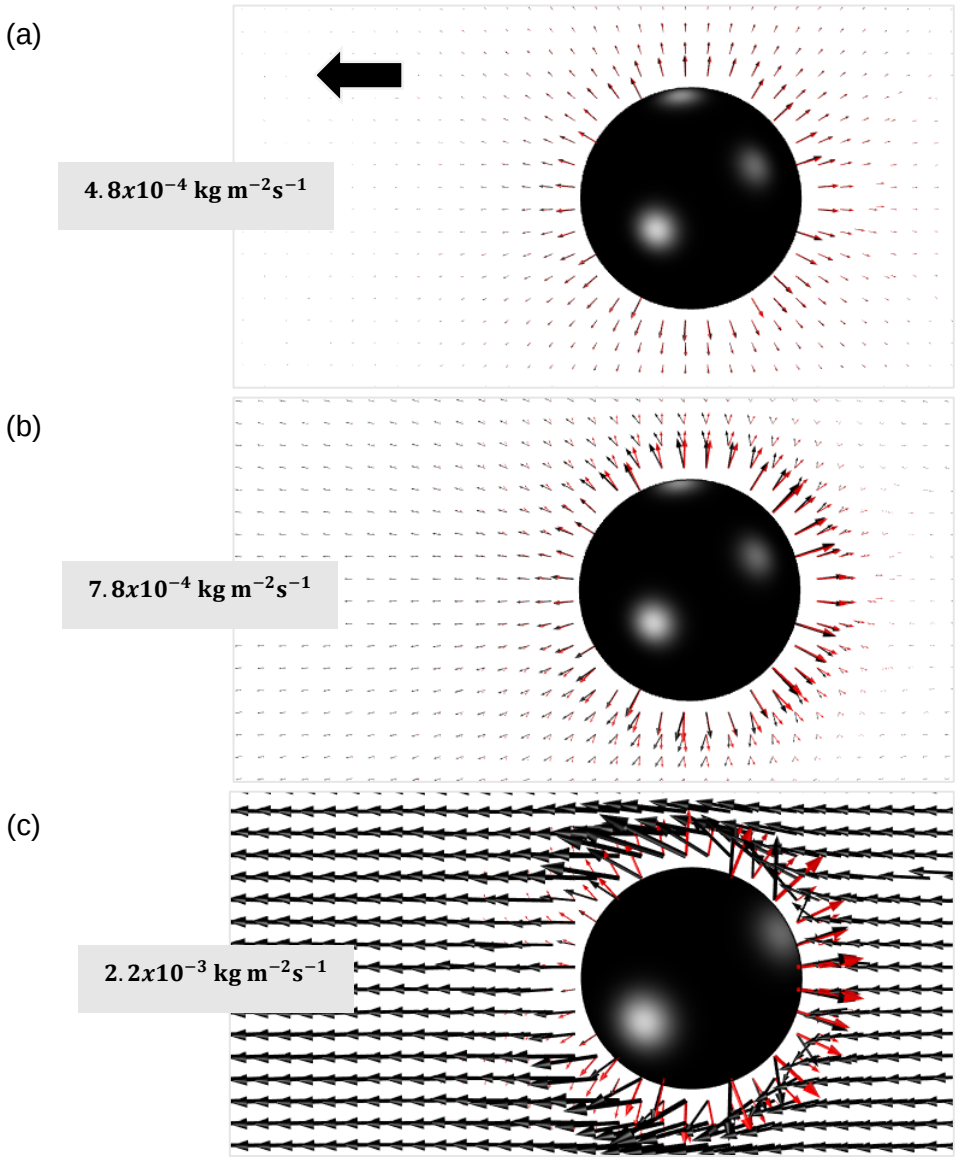

Figure 5-8: Diffusive flux (overlaid red arrows) and total flux (overlaid black arrows) plots after 300 s around the droplet (black solid circles), at (a) 0.02 m/s, (b) 0.2 m/s and (c) 2.0 m/s of the air speeds. The flux arrows are normalised to the same scale in all plots. The black solid arrow represents the airflow direction.

To do that, the sessile droplet evaporation model, presented in Chapter 3, is adopted here to simulate the evaporation of a flat circle of water with same radius of the sessile droplet, $R_c = 10^{-3}$ mm, at the lowest and highest air speeds (0.02 and 2.0 m/s) to represent approximately the evaporation of a droplet when it is almost flattened (i.e., at the latter stages of evaporation course). In this case, as the height of the flat circle is negligible therefore, no-slip boundary condition, i.e. $\mathbf{u} = 0$, is applied to the surface of the flat circle of water as no deformation occurs at this surface. Note that, Appendix B provides a theoretical analysis for the appropriate boundary condition applying on the surface of the flat circle of water. It shows that no-slip boundary condition is more reliable under conditions considered. Further, the surface of water circle is divided into two parts 'upstream' and 'downstream' related to the airflow direction as shown in the schematic illustration of the flat circle of water in Figure 5-9. Therefore, at each case of air speed, the evaporation rate at 300 s is calculated separately at these parts of the water circle to compare them with those (i.e., at the upstream and downstream parts) for the sessile water droplet evaporation case.

The numerical observations for the evaporation rates of water circle and sessile water droplet models are shown in Figure 5-9. Generally, it is very clear to see the difference in the evaporation rate trend with time between flat circle of water and sessile water droplet cases since, unlike for the sessile droplet case, the evaporation rate of water circle is almost constant, which it agrees well with what is observed previously in the literature for droplet evaporation with smaller contact angle [57, 89]. Again, higher evaporation rate is observed for both cases considered at the higher air speed compared to the lower air speed as a result of the strong effect of airflow in pushing the diffusive water vapour away from the droplet.

Further, it can be seen from Figure 5-9 that the evaporation rate of the upstream part of the flat circle and sessile droplet is higher than that of the downstream parts for both air speeds. This indicates the effect of water vapour transported from the upstream part in increasing the vapour levels around the downstream part of the flat circle and sessile droplet, and hence reducing the evaporation rate as a result of the reduction in the driving force of evaporation i.e., concentration gradient of water vapour. For the sessile droplet, the difference in the evaporation

rates between the upstream and downstream parts decreases with time due to the reduction of the role of airflow as the droplet height decreased, and hence less amount of water vapour transported from the upstream part towards the downstream part of the droplet. In addition, at 0.02 m/s, this difference initially is less than in the case of 2.0 m/s, which is attributed to the large amount of water vapour transported downstream in the case of higher air speed, and hence lower evaporative flux in the downstream area of the droplet.

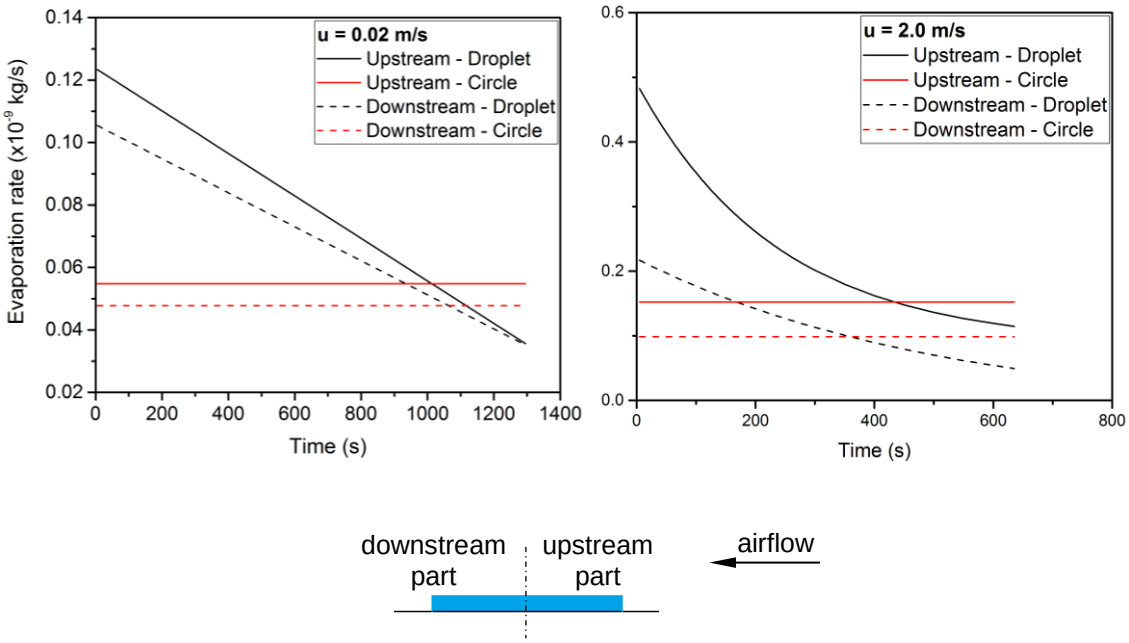

Figure 5-9: The evaporation rates of the upstream and downstream parts of water circle and sessile water droplet at 300 s, and at air speeds of 0.02 m/s and 2.0 m/s. Here, the schematic illustration of the flat circle of water shows the upstream and downstream parts related to the direction of the airflow.

Other findings can be observed from Figure 5-9 which the curve of the evaporation rate of the upstream part of the sessile droplet meets at some point the line of the evaporation rate of the upstream part of the flat circle of water, and same for the downstream parts. This point represents approximately the final time of the droplet evaporation i.e., when droplet completely evaporates. Although these times do not match exactly those calculated from Equation (5.3) because of being the flat circle of water evaporation model does not represent the actual situation of the sessile droplet evaporation, they give a good indication to the

importance of the comparison of the evaporation of the flat circle and the sessile droplet. As a result of the flat circle of water evaporation, it is very easy to conclude that the geometrical shape of the droplet has a slight effect in reducing the evaporation rate of the downstream part of the droplet since the great effect is due to the downstream water vapour transported from the upstream part of the droplet.

Recall that, in the present model, the droplet free surface is not constrained to be spherical cap, but is free to deform in response to the air flow and local evaporation rate. Despite the airflow and the non-uniform evaporative flux distributions on the droplet surface, especially at the highest airflow velocity – see Figure 5-10, it was found that deviations from a spherical cap shape were negligible under the conditions considered. Figure 5-10 shows the droplet free surface profile predicted by the present model at 20 s and 300 s after the initial state of evaporation compared to that determined using the geometric shape of a sessile droplet presented in Chapter 4, see Figure 4-1. Using the quadratic formula, the height of a general point on the sphere surface can be calculated by:

$$z = H - R + \sqrt{R^2 - x^2} \tag{5.6}$$

where, $R = {R_d}^2 + H^2/2H$, R_d is the contact radius of the sessile droplet and H is the droplet height at x = 0. Hence the spherical cap quasi-steady approach would be justified in future convection studies under similar conditions.

Given these results, it is clear to expect that droplets placed perpendicular or parallel to the airflow will experience rather different interactions. Figure 5-5 shows that perpendicular droplets placed sufficiently far apart can be expected to become effectively independent for sufficiently large air speeds, but droplets aligned parallel will inevitably be linked through the downstream vapour transport, as shown in Figure 5-7. These cases are considered and discussed separately in the next chapter.

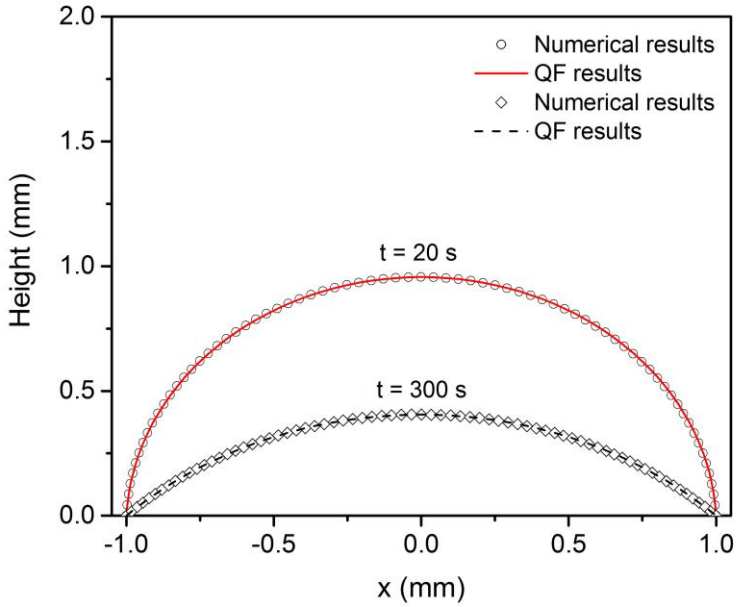

Figure 5-10: The profiles of the droplet free surface at 20 s and 300 s, and at 2.0 m/s of airflow velocity. Here, 'QF' represents results of using the quadratic formula.

5.3 Conclusions

After validation the numerical model, described in Chapter 3, against published experimental data, demonstrated in Chapter 4, the model was used to explore the influence of providing a gentle forced airflow on the evaporative behaviour, and hence the evaporation rate of an isolated single sessile water droplet in comparison with the evaporation of same droplet under natural convective environment.

Numerical results of the temporal evolution of the droplet volume show that the reduction of the droplet volume with time under various of air speeds can be well fitted by an exponential form of equation. This equation represents the droplet volume as a function of the air speed and time. The lifetime of the droplet as a function of the air speed is also constructed which decreases rapidly as the air speeds is increased as a result of accelerating the evaporation rate. Further, as a comparison with previous theoretical studies presented by Ranz and Marshall, Danberg, and Baines and James, new correlations of the evaporation rate of an isolated single sessile droplet under forced airflow are identified from the finite

element results for the initial and final values of the Sherwood as a function of the Reynolds and Schmidt numbers $Sh_i = 1.91 + 0.473Re^{0.478}Sc^{1/3}$ and $Sh_f = 0.67 + 0.035Re^{0.665}Sc^{1/3}$, respectively.

As expected and has been seen previously in the literature, the evaporation of a droplet open to the atmosphere is lower than in the case of presence a gentle forced airflow because of sweeping the diffusive vapour away from the droplet. This leads to reduce the concentration level of water vapour around the droplet, and hence increase the concentration gradient driving evaporation process. In addition, as the speed of the airflow is increased, the influence of the droplet evaporation on the surrounding environment reduces as the diffusive water vapour starts to concentrate around the droplet unlike in the natural environment case since it spreads outward to the surrounding as a result of absence the forced airflow. Under the forced air flow, a remarkable enhancement in the evaporation rate of the droplet is observed in comparison to the natural convection case since 12%, 46% and 91% increase in the evaporation rate at 0.02 m/s, 0.2 m/s and 2.0 m/s of the air speed, respectively. Moreover, the forced air convection is able to deviate the direction of the convective flux from the diffusive flux at the higher levels of air speeds whilst they are mostly identical at the lower air speed.

Further analysis on the downstream advection, results reveal that the downstream water vapour transported from the upstream area of the droplet is more influential on the downstream area of the droplet than the geometrical shape of the droplet itself, and this influence decreases gradually with time as a result of the reduction of the role of airflow as the droplet height decreased. Finally, given these results, an expectation of the evaporation of droplets placed perpendicular or parallel to the airflow can be concluded.

Chapter 6 Forced convection effects on the evaporation of interacting neighbouring sessile droplets

6.1 Introduction

Previously in Chapter 5, the evaporation of an isolated single sessile droplet under a forced convective environment is discussed extensively to examine the effect of the forced airflow on the evaporative behaviour of the droplet in comparison with the evaporation of same droplet under natural convective environment.

As mentioned previously in the literature review of Chapter 2, practical applications involve multiple droplets simultaneously evaporating in proximity to each other therefore, an interaction between those adjacent droplets will be generated. This interaction plays an important role in changing the behaviour of the evaporation process, hydrodynamics inside and outside the evaporating droplets, and hence the deposition patterns of the solid particles on substrates.

In this chapter, our attention will be directed towards understanding more complicated problems such the evaporation of a pair of pinned sessile water droplets at different arrangements and under convective environments. Unlike in the natural convective environment, where the arrangement of the droplets has no effect on the evaporative behaviour of the droplets, there is a significant effect when a forced airflow is directed towards the droplets. Therefore, two droplet configurations are considered in this chapter to study how the evaporative behaviour of the two droplets is influenced by the droplets orientation relative to the airflow direction. In addition, the influence of the separation distance between the pair of droplets and the air speed in reducing the interaction effects and isolating the droplets from each other are considered as important parameters discussed in this chapter. Further, results of the isolated single droplet observed in Chapter 5 is also considered here for comparison .

6.2 The mathematical model

Here, attention is focused on the effect of the surrounding air environment (i.e. natural and forced convective environments) on the evaporative behaviour of two neighbouring pinned sessile water droplets under isothermal conditions in which thermal effects are neglected. The mathematical model described in detail in Chapter 3 is adopted here to investigate the evaporation process of these two neighbouring pinned sessile water droplets under the above surrounding environments. Further, the same geometrical functions used in building the geometry of a single droplet model are also considered here to build the geometry of the two droplets evaporation model.

However, as the two droplets evaporate close to each other in same surrounding environment, both of them will affect each other through the diffused water vapour from each one via evaporation. Consequently, the local total evaporative flux from each droplet will be determined based on the saturation concentration along the surface of each droplet and the concentration field influenced by the neighbouring droplet (see equation 3.5). The free surface of each droplet deforms according to the local total mass flux of each droplet.

6.2.1 Representation of the geometric model

To study the evaporation of a pair of 1 mm-radius sessile water droplets subjected to a gentle forced airflow, two droplet configurations are considered in which the droplets are positioned along a line either perpendicular, see Figure 6-1 (a), or parallel to the flow, see Figure 6-1 (b). Further, the two droplets are separated with a varied distance (S = 0.5, 1.5, 3.0, 5 and 6 mm) to study the effects of droplet separation on the evaporation and interaction of the droplets. Three air stream velocities (U = 0.02, 0.2 and 2.0 m/s) are used to investigate the role of the forced convection on the evaporative behaviour of this pair of droplets. Further, using the separation between droplets as a characteristic length and the range of the air speeds quoted correspond to the average speed of the flow, the Péclet number, $Pe = US/D_v$, varies from approximately 0.4 to 240. For comparison, the evaporation of the same droplets in an open natural convective environment is also considered in this chapter as shown in Figure 6-2.

As mentioned previously in Chapter 4, the hemisphere physical domain with implemented infinite element domain approach is selected to investigate the evaporation of the two droplets under natural convective environment, see Figure 6-2, while a rectangular physical domain is utilized for the forced convection case, see Figure 6-1. All the physical properties of the two fluids listed in Chapter 3 (Table 3-1) are used in these computer simulations.

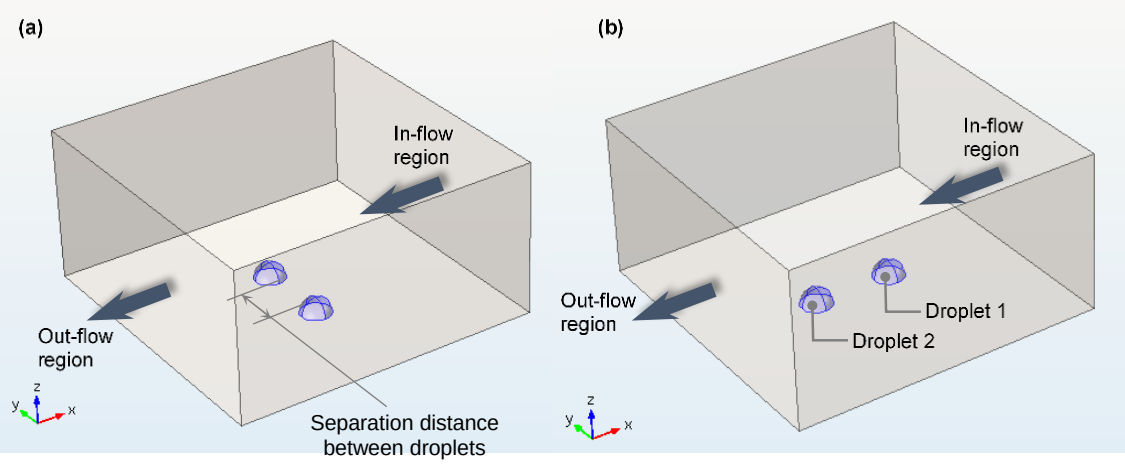

Figure 6-1. Illustration of the model for the forced convection flow in the case of: (a) perpendicular, and (b) parallel neighbouring droplets arrangement.

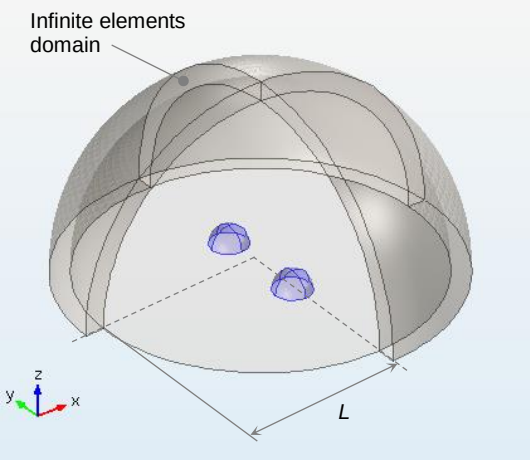

Figure 6-2. Schematic of the isothermal specific physical domain for natural convective environment surrounding two neighbouring sessile droplets.

6.3 Droplets aligned perpendicular to the flow

The isothermal diffusion-convection model, presented in Chapter 3, coupled with moving boundaries is adopted in all computer simulations to study the evaporation of two perpendicular neighbouring pinned water droplets (R_d = 1.0 mm and θ = 90°) in a specified isothermal physical domain under a forced convective environment. The evaporation of those droplets under a natural convective environment is also studied as a reference case to which the behaviour of the forced convective environment can be compared. The influence of the distribution of the vapour concentration has been studied by varying the separation distance between the droplets, and the velocity of the air stream. In addition, the behaviour of the two neighbouring droplets has been also compared to the behaviour of the isolated single droplet observed in Chapter 5.

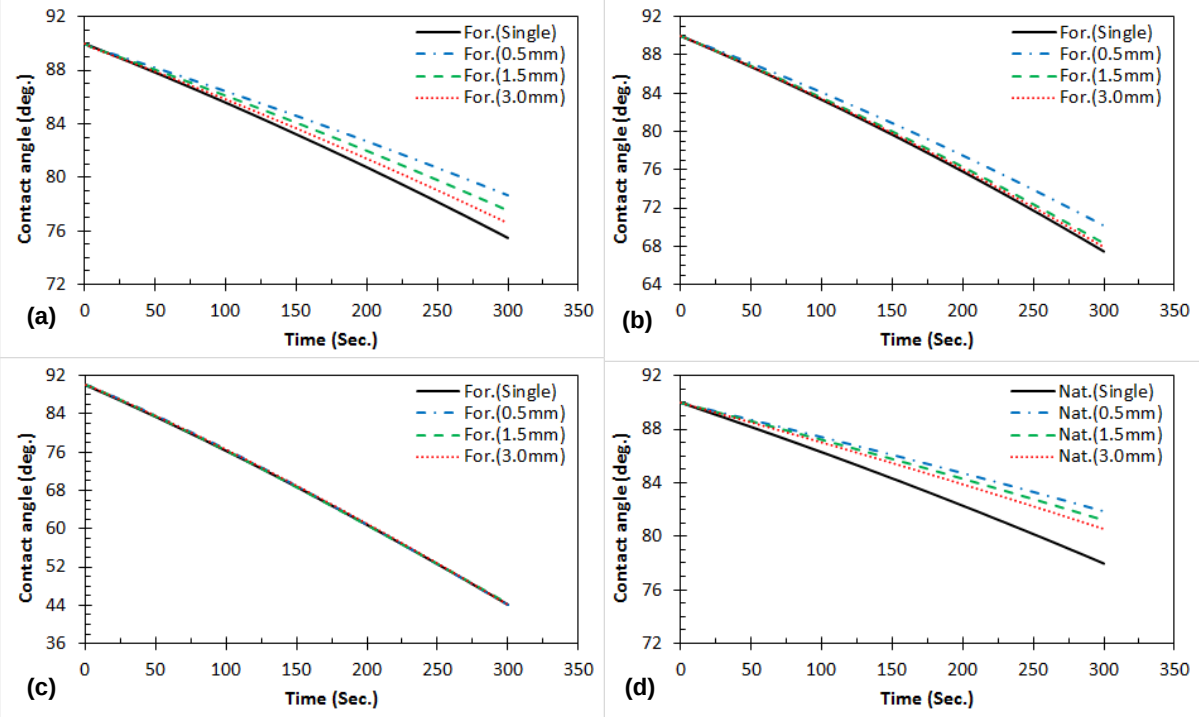

Figure 6-3. Evolutions of the contact angles of neighbouring perpendicular droplets in comparison with the isolated single droplet for various separation distances under the effect of: (a, b, c) forced convection with U = 0.02, 0.2 and 2 m/s, respectively, and (d) natural convection.

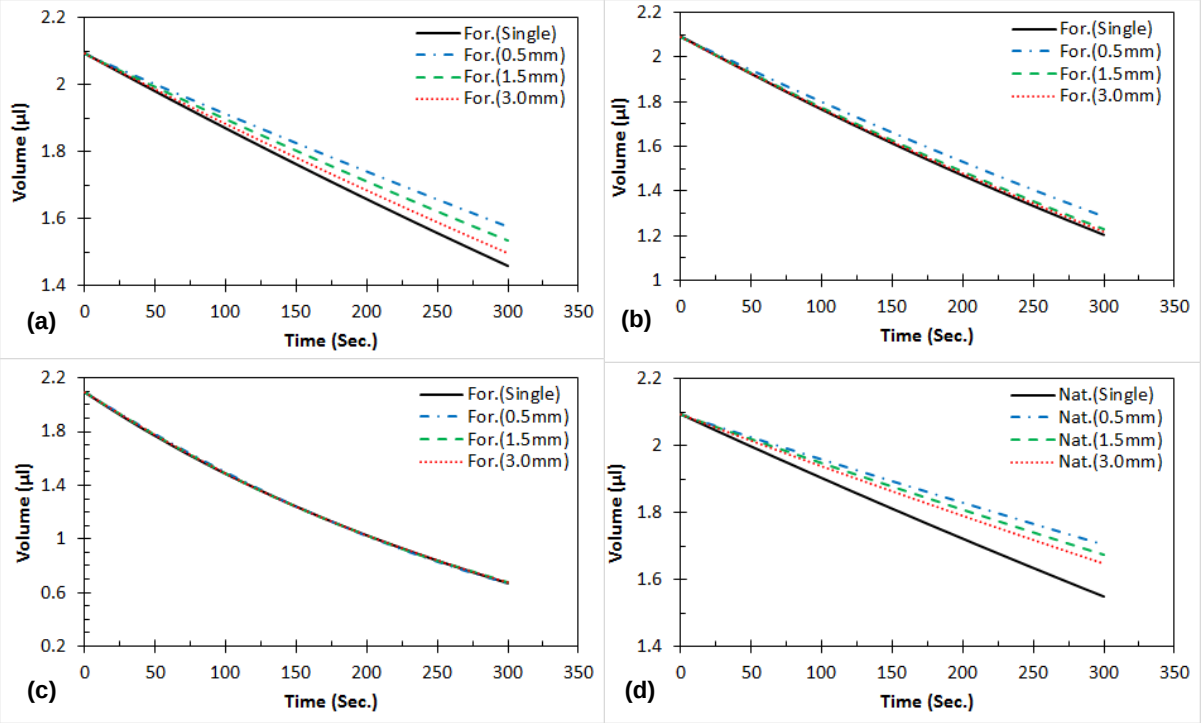

Figure 6-4. Evolutions of the volume of neighbouring perpendicular droplets in comparison with the isolated single droplet for various separation distances under the effect of: (a, b, c) forced convection with U = 0.02, 0.2 and 2 m/s, respectively, and (d) natural convection.

Figure 6-3 and Figure 6-4 show the temporal evolution of the droplet profiles (in terms of contact angle and volume) due to the changing flow pattern over the neighbouring evaporating droplets, the velocity of the air stream, and the separation distance between those droplets. The temporal evolution of the isolated single droplet profiles (the black solid lines) are also illustrated in Figure 6-3 and Figure 6-4. Generally, it can be seen from Figure 6-3 and Figure 6-4 that the decrease of contact angle and volume with time for the forced convective environment is faster than in the natural convective environment for same separation distance. This variation is due to increasing rates of evaporation of the droplets with increasing air stream velocity, as a result of larger concentration gradients near the droplets. However, the variations of contact angle and volume with time for the perpendicular droplets are slower than for the isolated single droplet under natural convective environment as shown in Figure 6-3 (d) and Figure 6-4 (d). This is due to the absence of an effective

evaporation source near the droplet for the isolated single droplet case as it is for the neighbouring perpendicular droplets. As the air speed is increased, Figure 6-3 (a, b) and Figure 6-4 (a, b), the behaviour of two perpendicular droplets starts to be close to that for the single droplet as a result of pushing the diffusive water vapour away from the gap between droplets until droplets become effectively isolated from each other (i.e. behave as the isolated single droplet) at the higher air speed as shown in Figure 6-3 (c) and Figure 6-4 (c).

At the lowest air speed (U = 0.02 m/s), the separation of the two droplets has a significant effect, with droplets close together (S=0.5 mm) taking about 20% longer to reach the same contact angle and volume than droplets 3.0 mm apart but it is still not sufficient to reach the behaviour of the single droplet, see Figure 6-3 (a) and Figure 6-4 (a). At this speed the effect of the droplet separation on the time to evaporate is roughly linear, which agrees well with the single droplet behaviour under the lower air speeds. Increasing the air speed tenfold to U=0.2 m/s, Figure 6-3 (b) and Figure 6-4 (b) show that the effect of the droplet separation is reduced, with droplets in closest proximity now taking about 10% longer to reach the same volume as those furthest apart (S = 3.0 mm). Moreover, the behaviour of droplets at intermediate separation is very close to that of the furthest droplets which is almost identical to the behaviour of the single droplet; the effect of separation falls off more quickly. This is consistent with the increasing strength of the advection downstream, acting to deplete the vapour levels in the region between droplets. At the fastest air speed considered (U = 2.0 m/s), droplets become effectively isolated from each other, as the downstream advection dominates the mass transport, and the contact angle and volume curves in Figure 6-3 (c) and Figure 6-4 (c) are practically indistinguishable. This indicates that the higher air speed is able to eliminate the interaction effect between droplets even for droplets very close to each other.

For the natural convective cases shown in Figure 6-3 (d) and Figure 6-4 (d), the lack of assistive forced convection means that evaporation is a little slower than in the corresponding low-speed forced convection situations, but the effect of the droplet separation is very similar. The closest droplets again take about 20% longer to reach a given state of evaporation than droplets furthest apart. Increasing the separation distance increases the evaporation rate of droplets,

since the water vapour concentration in the region between droplets is reduced, as has previously been observed by Pradhan and Panigrahi [32, 33].

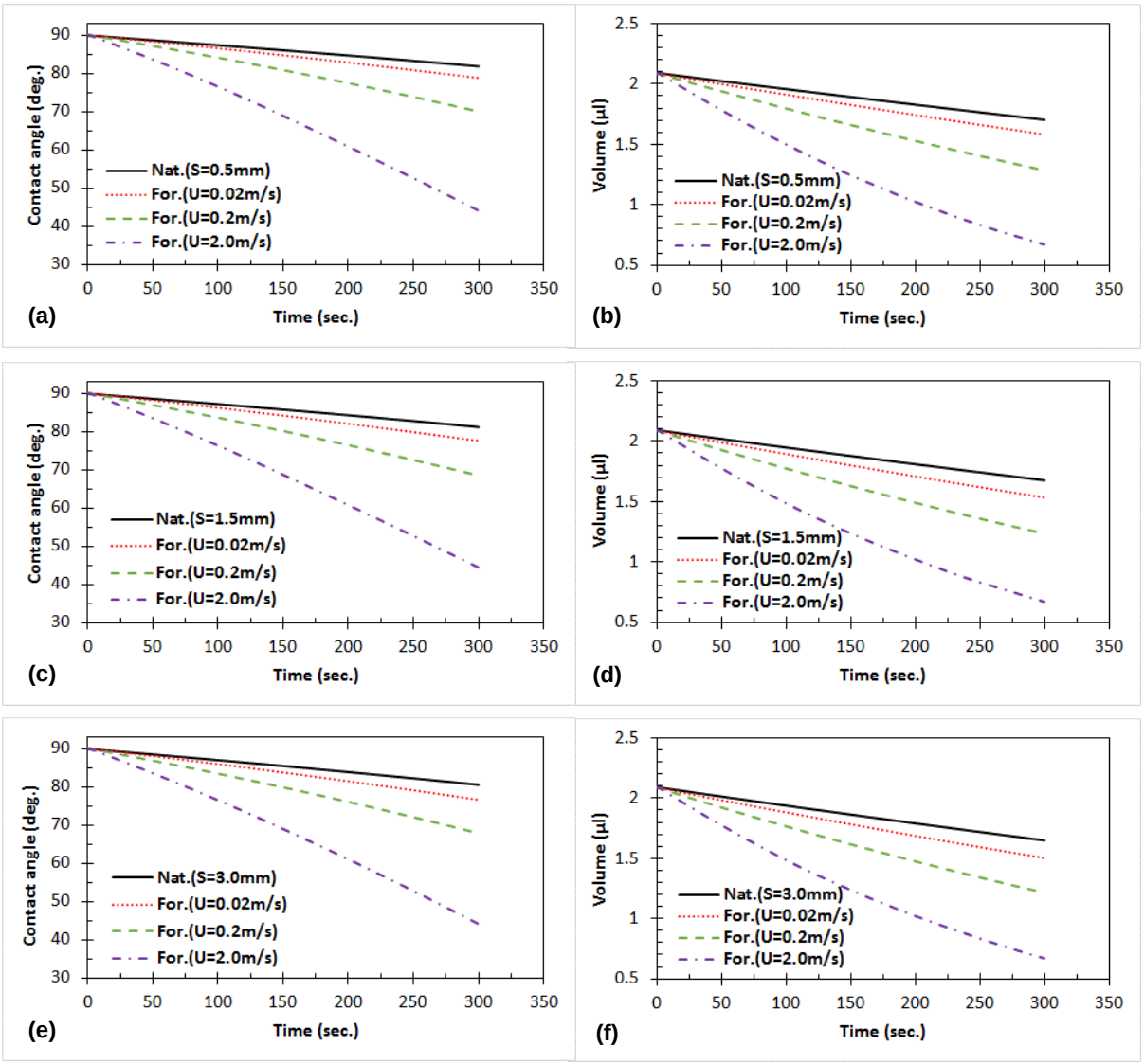

Figure 6-5. The effect of the air stream velocity on the evolution of perpendicular droplets' profile: (a, c and e) contact angle, and (b, d and f) droplets' volume at various separation distances S=0.5, 1.5 and 3.0 mm comparison to the natural convection case.

To compare the effects of natural and forced convection on evaporation rates of droplets more easily, Figure 6-5 plots the temporal evolution of the contact angle and volume for droplets separated by 0.5, 1.5 and 3.0 mm. Clearly the forced convection has a strong effect in increasing the evaporation rate of droplets when droplets are arranged on a line perpendicular to the flow, Figure 6-1 (a). From

Figure 6-5, it is easy to notice how the effect of the separation distance reduces significantly with increasing velocity of the air flow compared to the natural convection case, where the separation distance is the only influential parameter in the absence of the advection flow. Moreover, with an air stream of 2.0 m/s, for example, the droplets evaporate roughly five times faster than under natural convection alone, as the result of the strong effect of the air stream in pushing the diffusive water vapour away from droplets, and hence increasing the concentration gradient in the gap between droplets.

On further analysis of Figure 6-4 and Figure 6-5 (b, d and f), the volume evolution curves can all be very well represented by the same functional form as for the isolated single sessile droplet evaporation under forced convective environment discussed previously in Chapter 5, namely and shown in Figure 6-6

$$V(u,s,t) = V_o - \varphi_1(1 - e^{\omega_1 t}) \tag{6.1}$$

here $V(u,s,t)$ is the droplet volume at time t, and any velocity and droplet distance. The evolution curves of the droplet volume and fitting lines for all range of separation distances and airflow velocities considered for the perpendicular droplets arrangement are presented in Appendix C. Due to the complex dependence of evaporation rate on droplet spacing, air speed and time, it was found not to be possible to identify a relationship among all these three variables. Therefore, fitting coefficients φ_1 and ω_1 in Equation (6.1) are listed in Table 6-1 and Table 6-2 based on the airflow velocity and droplet separation distance. Based on these coefficients and Equation (6.1), the droplet liftimes can be estimated by the same fanctional form used for the single droplet, see equation (5.3). The lifetimes of the neighbouring perpendicular droplets are listed in Table 6-3 based on the airflow velocity and droplet separation distance.

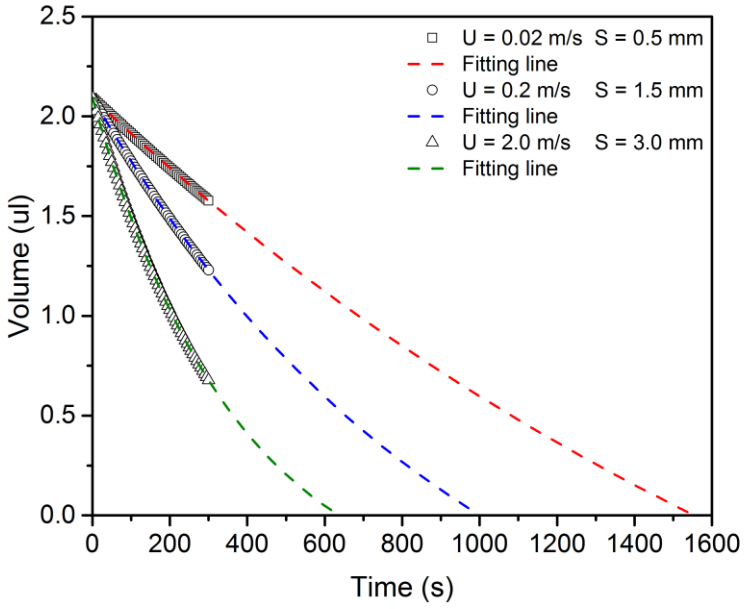

Figure 6-6: Evolutions of the volume of neighbouring perpendicular droplets and the fitting lines for various separation distances and air speeds.

Table 6-1: Fitting coefficient $\boldsymbol{\varphi_1}$ in equation (6.1) at various droplet separation distances and airflow velocities for the perpendicular droplets compared to the isolated single droplet.

S (mm) / U (m/s)	0.5	1.5	3	Single droplet
0.02	4.41×10^{-9}	4.14×10^{-9}	4.00×10^{-9}	3.92×10^{-9}
0.2	3.57×10^{-9}	3.26×10^{-9}	3.24×10^{-9}	3.31×10^{-9}
2	2.58×10^{-9}	2.56×10^{-9}	2.55×10^{-9}	2.55×10^{-9}

Table 6-2: Fitting coefficient $\boldsymbol{\omega_1}$ in equation (6.1) at various droplet separation distances and airflow velocities for the perpendicular droplets compared to the isolated single droplet.

S (mm) / U (m/s)	0.5	1.5	3	Single droplet
0.02	-4.14×10^{-4}	-4.83×10^{-4}	-5.353×10^{-4}	-5.89×10^{-4}
0.2	-8.56×10^{-4}	-0.00102	-0.00105	-0.00105
2	-0.00259	-0.00266	-0.0027	-0.0027

Table 6-3: The lifetimes of the neighbouring perpendicular droplets (in sec.) under forced airflow condition compared to the isolated single droplet lifetime.

S (mm) / U (m/s)	0.5	1.5	3	Single droplet
0.02	1556.4	1459.7	1383.3	1295.2
0.2	1030.7	1006.9	989.8	957.6
2	644.3	640.1	637.2	636.9

The presence of another droplet close to an evaporating droplet leads to an increase in the density of water vapour in the gap between the two droplets compared to the surrounding atmosphere. Hence the evaporative flux through the droplet surfaces at this region becomes lower than at the rest of the droplet surfaces because of the reduction of the driving force for evaporation, i.e. concentration gradient, as shown in Figure 6-7 (a). As expected, increasing the separation distance leads to a reduced interaction between droplets and hence increase in the evaporative flux at the region between droplets, as a result of the increase of the driving force for evaporation there, Figure 6-7 (b, c). These predicted results agree well with previous numerical works considering evaporation under natural convection conditions. Note that, with further increase in the separation distance, the evaporative flux through the droplet surface near to the gap between droplets will be enhanced to reach the behaviour of the single droplet evaporation illustrated previously in Chapter 5. Hence, the fitting coefficients in Table 6-1 and Table 6-2 tend towards the corresponding values for a single droplet. In addition, Table 6-3 shows how does the lifetime of prependicular droplets tends towards the lifetime of the single droplet as the separation distance between the two droplets is increased, particularly at the highest air speed.

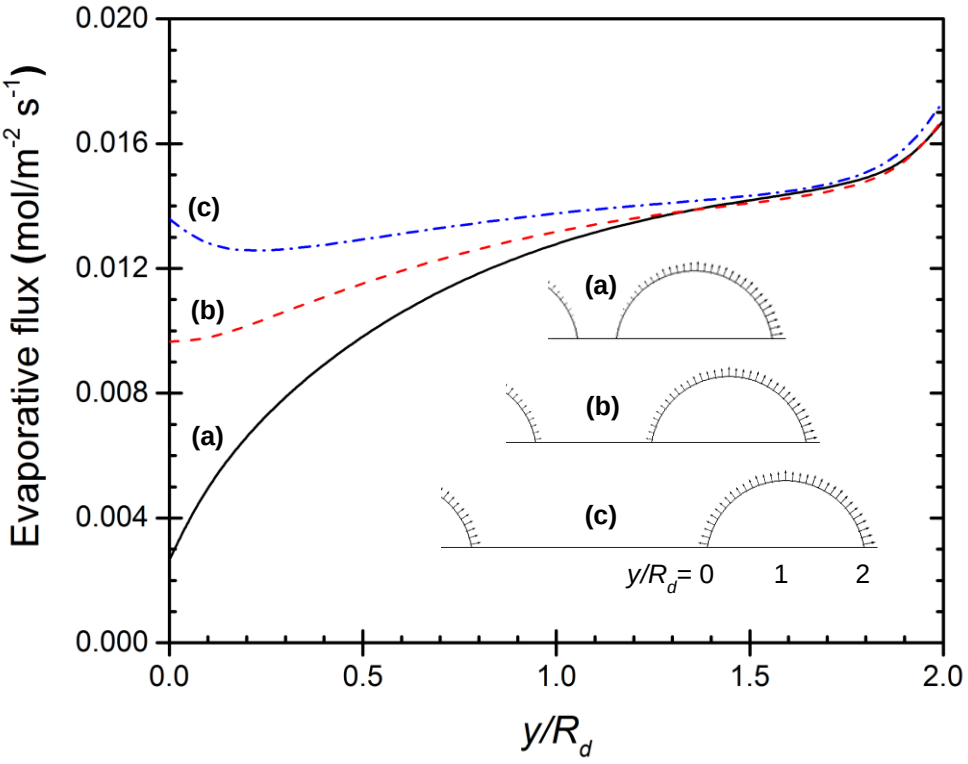

Figure 6-7: Evaporative flux along the perpendicular droplet free surfaces at t = 300s and at (a) 0.5 mm, (b) 1.5 mm and (c) 3.0 mm separation distance under natural convection. Note that the coordinate origin has been shifted to place y = 0 at the left-hand edge of the right-hand droplet. The velocity arrows are normalised to the same scale in all plots.

As noted above, the concentration field between droplets will be affected by the air stream. When it acts perpendicular to the line joining the droplet centres, Figure 6-2 (a), it transports water vapour away from both droplets equally, resulting in larger concentration gradients and consequently higher evaporative flux in the region between droplets, see Figure 6-8 (b-c). For sufficiently high speed, the distribution of the evaporative flux around each droplet becomes almost symmetrical, indicating that droplets are effectively decoupled. This is clearly seen in Figure 6-8 (d), where large fluxes occur between droplets in the high speed case, even for smaller droplet separation (0.5 mm).

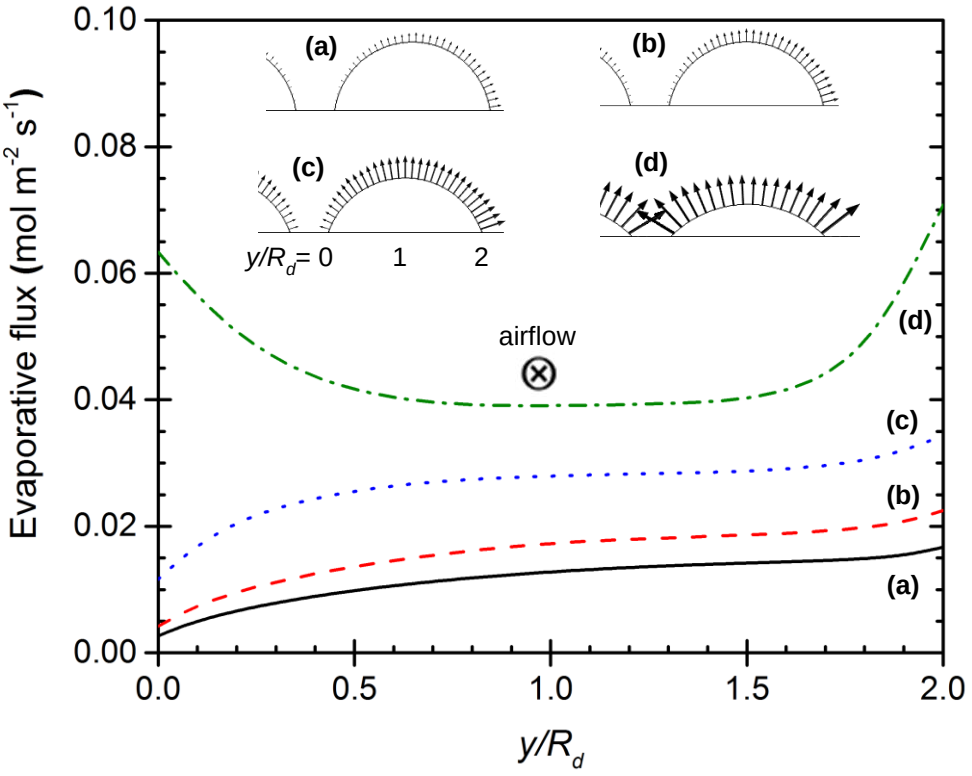

Figure 6-8: Evaporative flux along the perpendicular droplet free surfaces at t = 300s and separation 0.5 mm under (a) natural convection, and forced convection at air speeds (b) 0.02 m/s, (c) 0.2 m/s and (d) 2.0 m/s. The flow direction is into the page. Note that the coordinate origin has been shifted to place y = 0 at the left-hand edge of the right-hand droplet. The velocity arrows are normalised to the same scale in all plots.

Further, the almost symmetrical distribution of the evaporative flux also appears in several cases as shown in Figure 6-9 (d) and Figure 6-10 (c, d). This is also an indication of the importance of the forced air flow in enhancing the evaporation process of interacting droplets via reducing the density of the diffusive water vapour in the gap between those droplets. Furthermore, the significant difference in the droplet height as a result of the faster evaporation at higher speeds is also apparent in the inset vector plots of Figure 6-8, Figure 6-9 and Figure 6-10.

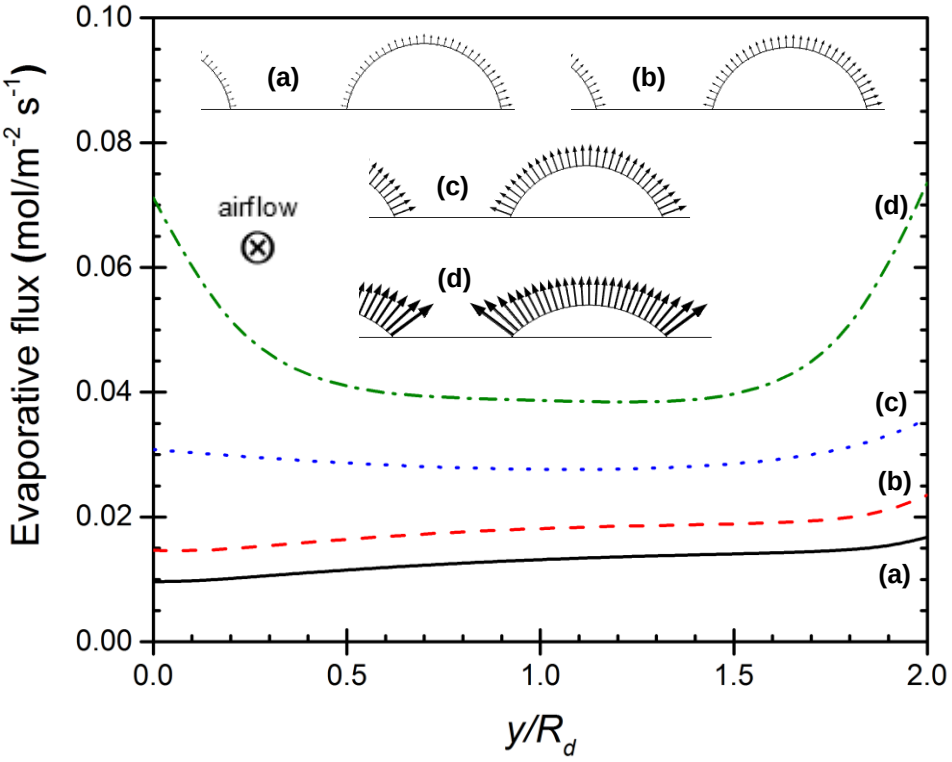

Figure 6-9: Evaporative flux along the perpendicular droplet free surfaces at t = 300s and separation 1.5 mm under (a) natural convection, and forced convection at air speeds (b) 0.02 m/s, (c) 0.2 m/s and (d) 2.0 m/s. The flow direction is into the page. Note that the coordinate origin has been shifted to place y = 0 at the left-hand edge of the right-hand droplet. The velocity arrows are normalised to the same scale in all plots.

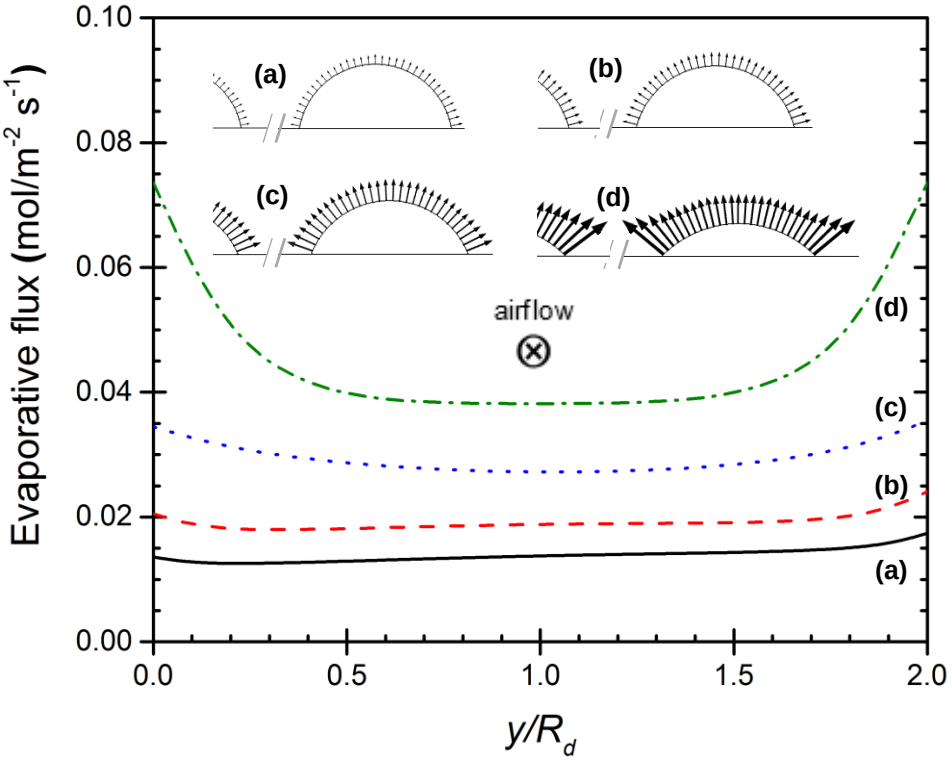

Figure 6-10: Evaporative flux along the perpendicular droplet free surfaces at t = 300s and separation 3.0 mm under (a) natural convection, and forced convection at air speeds (b) 0.02 m/s, (c) 0.2 m/s and (d) 2.0 m/s. The flow direction is into the page. Note that the coordinate origin has been shifted to place y = 0 at the left-hand edge of the right-hand droplet. The velocity arrows are normalised to the same scale in all plots.

To demonstrate clearly the effects of both forced convection and droplet separation distances, Figure 6-11 (b-d) shows concentration contours in a vertical plane containing both droplet centres, with a view looking along the direction of flow, for various air speeds and droplet separation distances. For comparison, Figure 6-11 (a) shows corresponding contours under natural convection. It can be seen from Figure 6-11 (a) that the infinite element domain approach, i.e. the dark blue region, is very effective in representing the outer boundaries surrounding the evaporating droplets without any negative effects on the accuracy of the numerical results. For natural convection case, although increasing the separation distance reduces noticeably the interaction between

droplets via their shared vapour space, there is still an elevated concentration level, and consequently a lower concentration gradient, between droplets compared to the regions to the left and right of the droplet pair – see the rightmost image in Figure 6-11 (a).

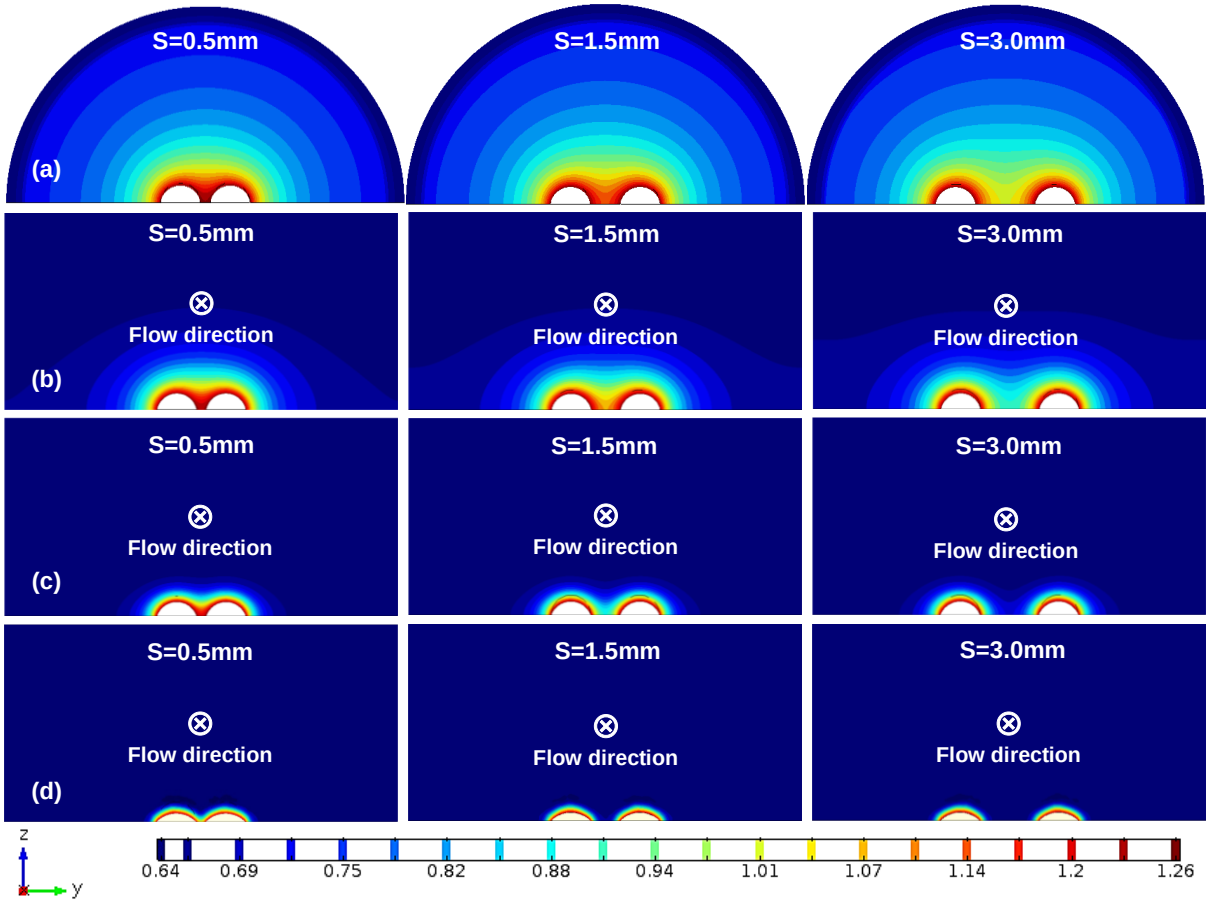

Figure 6-11. Contour plot of the vapour concentration distribution above the two perpendicular neighbouring evaporating droplets at time 300s for various separation distances (S = 0.5, 1.5 and 3.0mm), and under the effect of: (a) natural convection, and (b, c, d) forced convection with U = 0.02, 0.2 and 2 m/s, respectively. The colour bar represents the vapour concentration in mol/m^3.

With a slight air stream, U=0.02 m/s, passing over the two droplets as shown in Figure 6-11 (b), the overall variation in concentration field is more tightly focused around the droplet pair as a result of the downstream transport of water vapour. In-plane concentration gradients are therefore enhanced, leading to the increase in evaporation rate noted above. Increasing the separation of droplets now has a

more significant effect in lowering the vapour concentration between droplets, but this low speed is insufficient to isolate droplets from each other completely. With increase the air speed tenfold to U=0.2 m/s, the water vapour concentration in the region between the two droplets is still influential in decoupling the two droplets from each other, as shown in Figure 6-11 (c). As the air speed increases to the highest level, Figure 6-11 (d), the in-plane variation in concentration becomes ever more focused around droplets, and droplets become effectively isolated from each other. Hence the evaporation curves in Figure 6-3 (c) and Figure 6-4 (c) are barely distinguishable.

Although the air stream helps to reduce the build-up of vapour concentration between droplets, it does introduce a wake of higher concentration behind droplets, as suggested in Figure 5-5 and Figure 5-7 in Chapter 5, and shown more clearly in the full top-view contour plots of Figure 6-12 and in the zone of influence around the two droplets at various separation distances and air speeds, see Figure 6-13. As expected previously, perpendicular droplets can be effectively independent when sufficiently far apart and for large air speed as shown clearly in Figure 6-12 (c) and Figure 6-13 (c). Further, the wake in vapour concentration reduces concentration gradients in the downstream direction. While this is not particularly an issue for droplets arranged perpendicular to the flow, it becomes more important when droplets are arranged in a line parallel to the flow, as discussed in the next section.

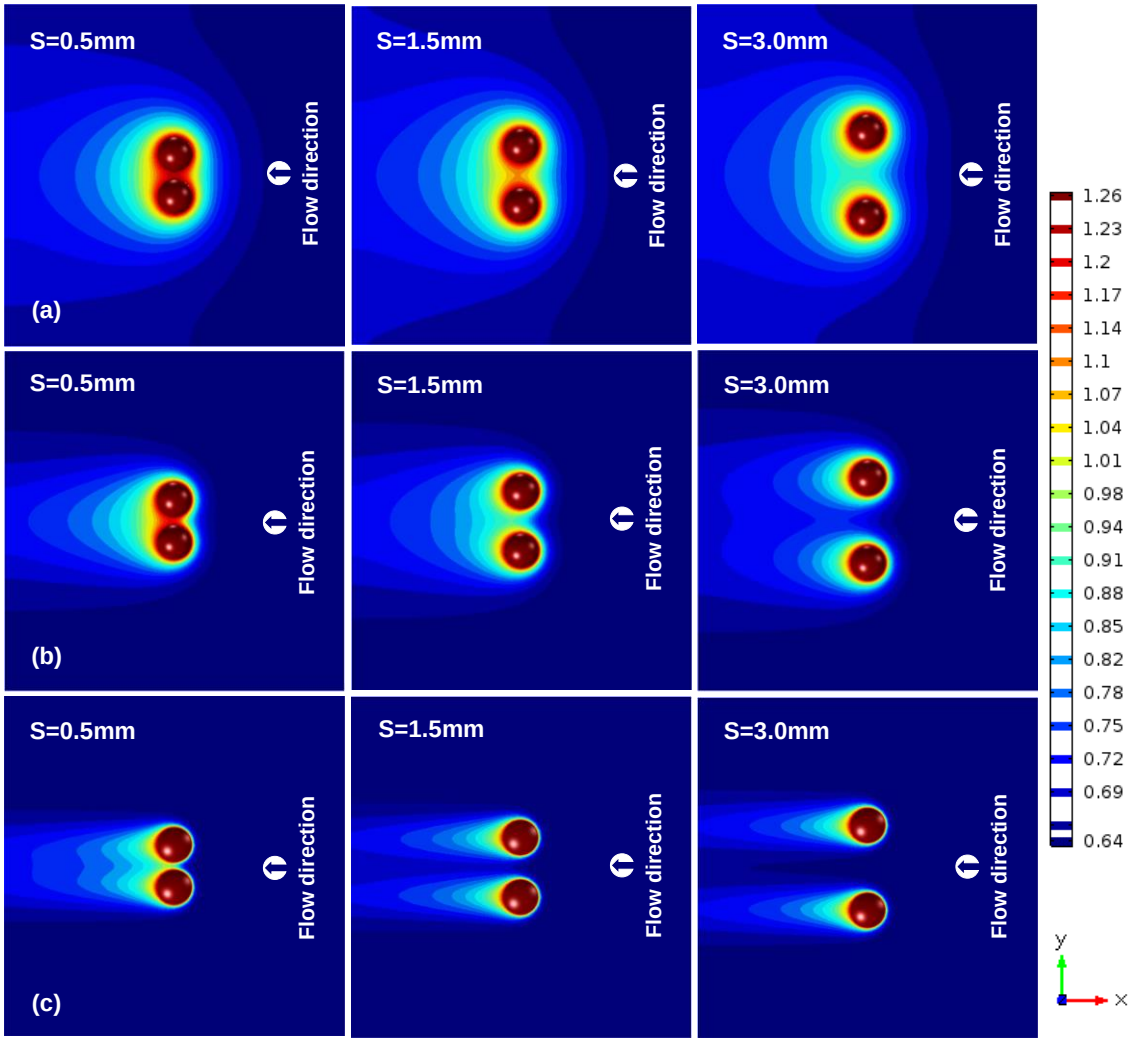

Figure 6-12: Contour plots of the vapour concentration distribution over the bottom surface of the domain at time 300s for two perpendicularly arranged neighbouring evaporating droplets at various separation distances (S = 0.5, 1.5 and 3.0mm) and under the effect of forced convection with: (a, b, c) U = 0.02, 0.2 and 2 m/s, respectively. The colour bar represents the vapour concentration in mol/m^3.

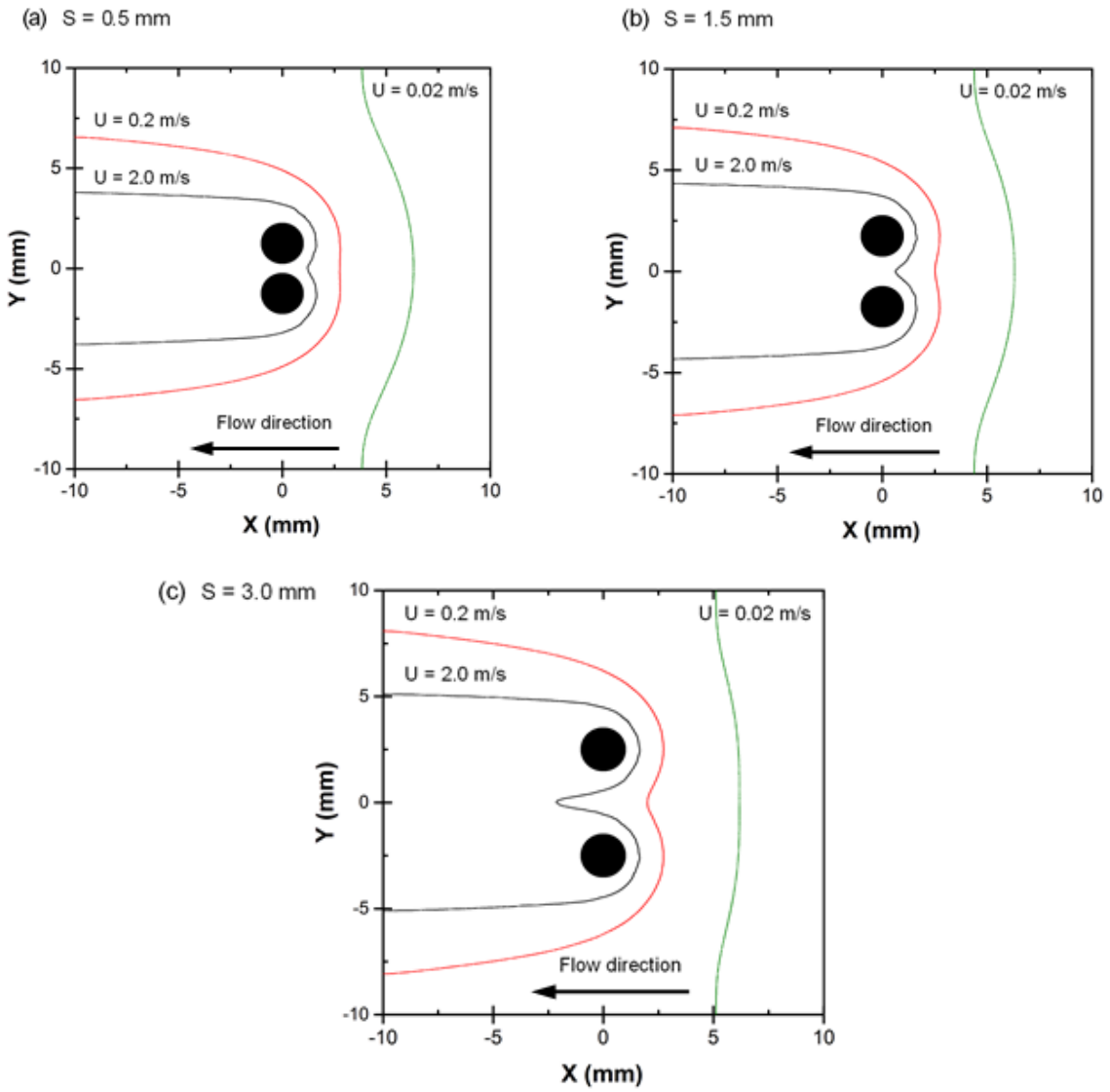

Figure 6-13: Zone of influence around the two perpendicular droplet after 300 s from the initial state and at separation distance (a) S = 0.5 mm, (b) S = 1.5 mm and (c) S = 3.0 mm, and various air speeds. The plot is defined by contours along which the vapour concentration is 1% higher than the ambient (inlet) concentration. The two black circles represent the two droplets. Contours are plotted on the plane of the solid surface.

6.4 Droplets aligned parallel to the flow

Unlike the evaporation behaviour in the perpendicular droplets arrangement, when droplets are arranged in parallel with the air flow, i.e. when one droplet is directly downstream of the other, as shown in Figure 6-2 (b), droplets are no longer exposed to the same air stream as the air steam passing the downstream droplet has high levels of water vapour transported from the upstream droplet. Hence the evaporation behaviour in this case is different because the second droplet, i.e. downstream droplet, evaporates in the lee of the first droplet, i.e. upstream droplet, where conditions are influenced not only by the partial shielding effect of the first droplet but also by the downstream transport of water vapour evaporating from the first droplet. The elevated vapour concentration around the second droplet causes a decrease in the concentration gradients driving evaporation and the second droplet therefore evaporates more slowly than the first droplet as shown in Figure 6-14, which illustrates the evolution profiles of each droplet (in terms of contact angle and volume) in comparison with the isolated single droplet. Note that, the phrase ‘shielding effect’ is used here to represent the hydrodynamic sheltering effect of an obstacle/droplet on a parallel droplet. This term ‘shielding’ is also used in purely diffusive studies (i.e. without forced convection) to describe the interaction between droplets via the vapour space between them. Unlike to the observations in Figure 6-3 (c) and Figure 6-4 (c) for the perpendicular droplets arrangement, it can be noticed that the two parallel droplets at 300 s are still not isolated from each other even at larger separation distance and higher air speed, Figure 6-14 (e and f).

On further analysis of Figure 6-14, it can be seen that the influence of the upstream droplet on the downstream droplet increases as the airflow velocity is increased for same separation distance, which is clearly shown in the difference of the volume of the upstream and downstream droplets. This can be attributed to the increasing of the evaporation rate of the upstream droplet as the airflow velocity is increased, and hence increase the water vapour transported from the upstream droplet. From Figure 6-15, which shows the volume evolution profile of each droplet at the lowest and highest air speeds and at various separation distances, one can notice that the separation distance generally has a slight role in reducing the interaction between the two parallel droplets as it is for the

perpendicular droplets case as a result of the downstream transport of water vapour evaporating from the upstream droplet which links the two droplets together.

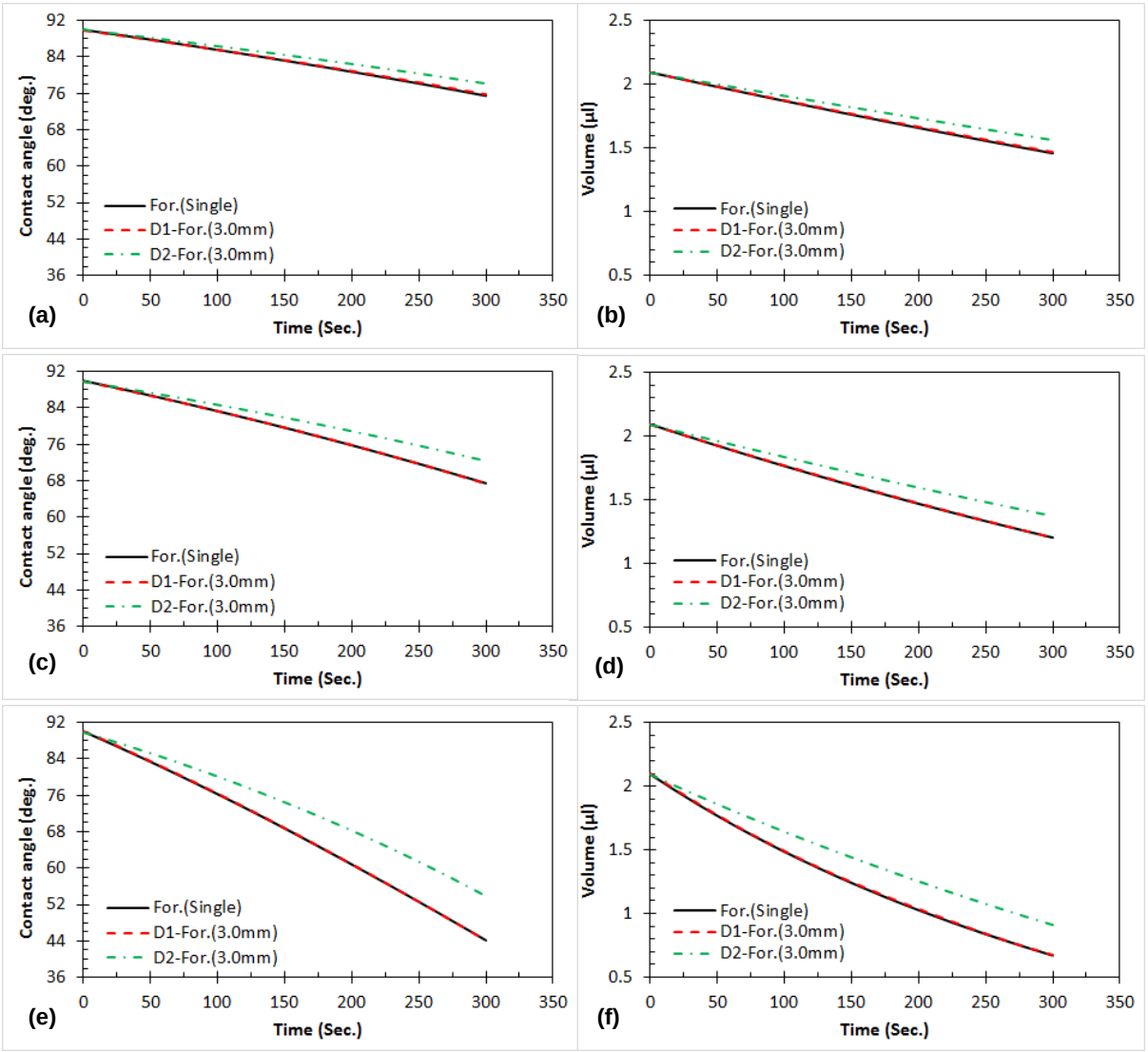

Figure 6-14**.** The evolution profiles of (a, c and e) contact angle and (b, d and f) droplet volume for each droplet in a parallel arrangement at U = 0.02, 0.2 and 2.0 m/s, and at 3.0 mm separation distance compared to isolated single droplet (solid black line). Here, D1 and D2 represent the upstream and downstream droplets, respectively.

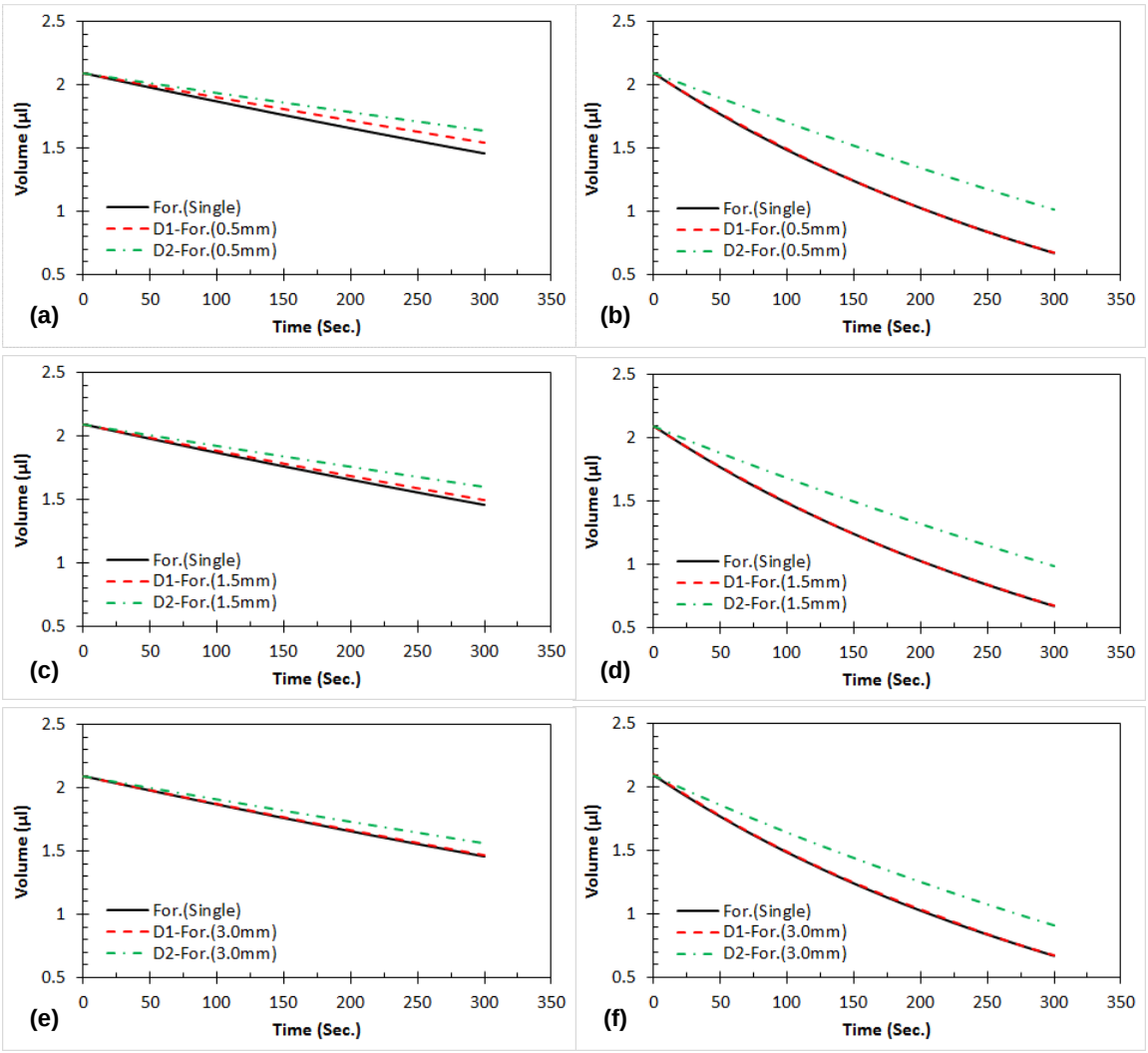

Figure 6-15: The evolution profiles of droplet volume at (a, c and e) U = 0.02 m/s and (b, d and f) U = 2.0 m/s for each droplet in a parallel arrangement, and at 0.5 mm, 1.5 mm and 3.0 mm separation distance compared to isolated single droplet (solid black line).

Moreover, it is easy to see from Figure 6-14 and Figure 6-15 that the first droplet is more influenced by the separation distance than the second droplet, where shorter distance is needed for the first droplet to reach the behaviour of the isolated single droplet even at the lower air speed. Unlike the first droplet, longer distance is needed for the second droplet to reach the behaviour of the isolated single droplet due to its influenced by the downstream transport water vapour from the first droplet. Further numerical results for the evolution of the parallel droplets' volume at the range of separation distance and airflow velocity

considered for this case of droplets arrangement are presented in Appendix C. As a comparison, the first droplet in the parallel arrangement evaporates slightly more quickly than the perpendicularly arranged droplets at the same air speed, see Figure 6-3 and Figure 6-4. This can be attributed to the fact that with the neighbouring droplet on the downstream side, the advective flow now directly opposes the upstream diffusive flux (and the Stefan flow) from the second droplet and the effect of the latter is therefore correspondingly reduced.

Figure 6-16 shows how the contact angles and volumes of the two parallel droplets reduce over time for the slowest air speed and different separations between the droplets. Again, the upstream droplet evaporates slightly faster than the parallel droplets (compare Figure 6-4 (a) for the perpendicular droplets arrangement), and increasing the separation accelerates the evaporation of both droplets. However, the key observation is that increasing the separation distance does very little to reduce the difference in evaporation rate of the two droplets. At the separations considered here, the downstream droplet is still influenced by the downstream vapour transport from the upstream droplet, and it is much more difficult to decouple droplets. This is considered further later in this section.

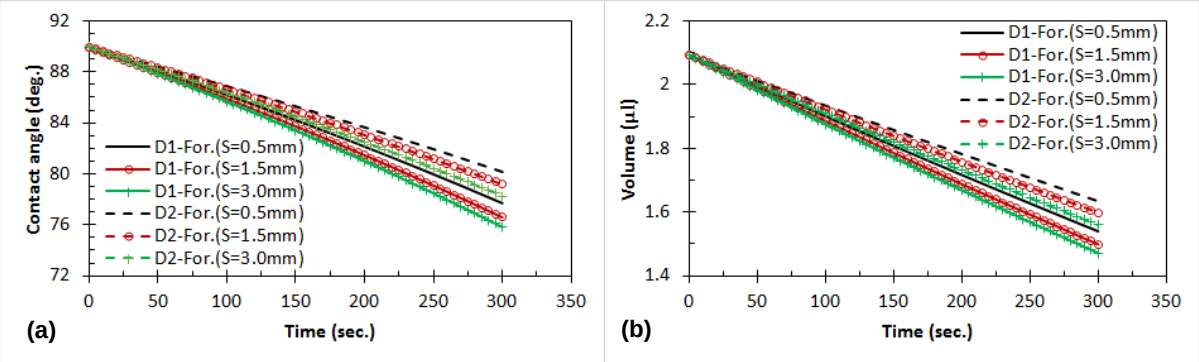

Figure 6-16. Evolutions of (a) contact angle (b) volume of neighbouring parallel droplets for various separation distances and under the effect of forced convection at U = 0.02 m/s.

As for the perpendicular droplets arrangement, from the droplet volume evolution plots, Figure 6-14 (b, d and f), Figure 6-15 and Figure 6-16 (b), it is clear to notice that the variation of the upstream and downstream droplets volume with time are almost identical to the same functional form as for the isolated single sessile

droplet evaporation under forced convective environment discussed previously in Chapter 5, namely and shown in Figure 6-17

$$V(u,s,t) = V_o - \varphi_2(1 - e^{\omega_2 t}) \tag{6.2}$$

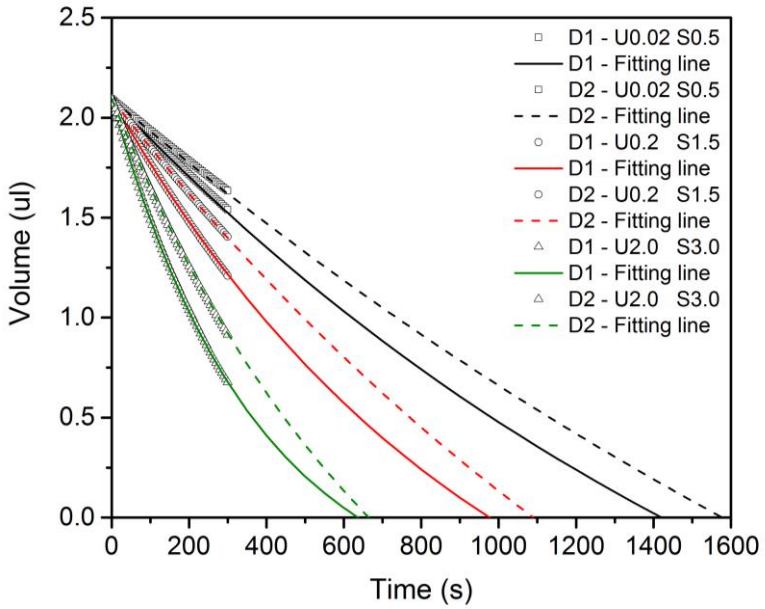

Figure 6-17: Evolutions of the volume of neighbouring parallel droplets and the fitting lines for various separation distances and air speeds.

Again, it is very difficult to find a relationship among the evaporation rate of droplets, droplets spacing, air speed and time therefore, fitting coefficients φ_2 and ω_2 in Equation (6.2) for parallel droplets arrangement are listed in Table 6-4 and Table 6-5 based on the airflow velocity and droplet separation distance. As for perpendicular droplets, parallel droplet lifetimes can be estimated based on these fitting coefficients and equation (6.2), and using the same fanctional form for the single droplet, as shown in Table 6-6. The evolution of parallel droplet volumes and fitting line for other cases of separation distance considered here are presented in Appendix C in which it is clear to notice that it is very easy to decople the first droplet from the upstream diffusive flux from the second droplet with either slower air speed and larger separation distance or higher air speed and smaller separation distance. Unlike the first droplet, further separation distance is needed to isolate the second droplet from the first one even at the higher air speed.

Table 6-4: Fitting coefficient φ_2 in equation (6.2) at various droplet separation distances and airflow velocities for the parallel droplets compared to the isolated single droplet.

U (m/s) \ S (mm)		0.5	1.5	3	Single droplet
0.02	D1	4.18×10^{-9}	4.06×10^{-9}	3.94×10^{-9}	3.92×10^{-9}
0.2		3.88×10^{-9}	3.30×10^{-9}	3.31×10^{-9}	3.31×10^{-9}
2		2.59×10^{-9}	2.55×10^{-9}	2.55×10^{-9}	2.55×10^{-9}
0.02	D2	5.80×10^{-9}	5.54×10^{-9}	5.26×10^{-9}	
0.2		5.70×10^{-9}	4.98×10^{-9}	4.73×10^{-9}	
2		4.63×10^{-9}	4.20×10^{-9}	3.58×10^{-9}	

Table 6-5: Fitting coefficient ω_2 in equation (6.2) at various droplet separation distances and airflow velocities for the parallel droplets compared to the isolated single droplet.

U (m/s) \ S (mm)		0.5	1.5	3	Single droplet
0.02	D1	-4.88×10^{-4}	-5.30×10^{-4}	-5.77×10^{-4}	-5.89×10^{-4}
0.2		-7.87×10^{-4}	-0.00103	-0.00104	-0.00105
2		-0.00259	-0.0027	-0.0027	-0.0027
0.02	D2	-2.84×10^{-4}	-3.17×10^{-4}	-3.58×10^{-4}	
0.2		-4.13×10^{-4}	-5.01×10^{-5}	-5.56×10^{-5}	
2		-8.71×10^{-5}	-0.00103	-0.00132	

Table 6-6: The lifetimes of the neighbouring parallel droplets (in sec.) under forced airflow condition compared to the isolated single droplet lifetime. Here, D1 and D2 represent the upstream and downstream droplets, respectively.

U (m/s) \ S (mm)		0.5	1.5	3	Single droplet
0.02	D1	1421.6	1368.6	1313.9	1295.2
0.2		985.6	977.2	961.9	957.6
2		639.3	638.2	637.5	636.9
0.02	D2	1578.0	1497.2	1419.7	
0.2		1108.5	1090.0	1051.2	
2		691.2	682.7	664.7	

Figure 6-18 illustrates the asymmetry of the concentration field surrounding the droplets in the parallel configuration. The plane shown is a vertical plane through the droplet centres. Note that the contour levels and colour scale match those in Figure 6-11, allowing a direct comparison with the corresponding natural convection cases in Figure 6-11 (a). Clearly, the water vapour transported away from the first droplet overlaps the second evaporating droplet which consequently decreases the concentration gradient above that droplet and hence decreases the evaporation rate there.

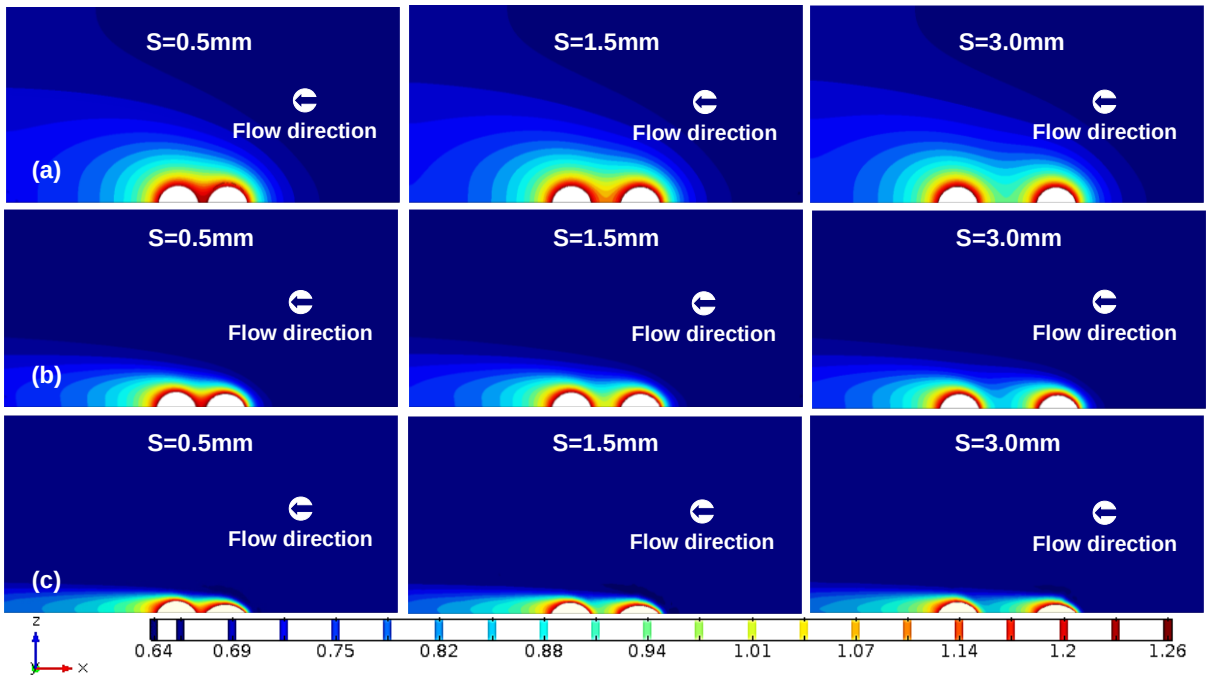

Figure 6-18. Contour plot of the vapour concentration distribution above the two parallel neighbouring evaporating droplets at time 300s for various separation distances (S = 0.5, 1.5 and 3.0mm), and under effect of forced convective environment with: (a, b, c) U = 0.02, 0.2 and 2 m/s, respectively. The colour bar represent the vapour concentration in mol/m^3.

For a more quantitative view, Figure 6-19 plots the concentration along horizontal lines within the centre plane, located at various heights above the substrate, for the medium speed and two separations. The solid curve corresponds to the horizontal line closest to the droplet surfaces, and clearly shows the difference in vapour concentration levels above each droplet (identified by the thick solid bars). Recall that at each droplet surface, the concentration is equal to the saturation

concentration, which is 0.023 kg m^{-3}. At this speed, the concentration profile upstream of the leading (right-hand) droplet, and over the upstream half of that droplet, looks the same in each case, and is hence effectively independent of the droplet separation. The large concentration gradient there indicates a region of high flux and is discussed in more detail below. These profiles also clearly show the elevated concentration levels above the downstream droplet and in the gap between the droplets, even as the droplet spacing is increased. Appendix C also illustrates the concentration profiles above the upstream and downstream droplets for other separation distances and air speeds considered here.

The evaporation fluxes from the droplet surfaces corresponding to the conditions in Figure 6-18 and Figure 6-19 are quantified and illustrated in Figure 6-20, Figure 6-21 and Figure 6-22, again at t = 300s. Note that in order to compare the flux curves for droplets at different separations, the graphs are constructed such that in each plot, the downstream droplet occupies the range $-2 \leq x/R_d \leq 0$ and the upstream droplet occupies $0 \leq x/R_d \leq 2$.

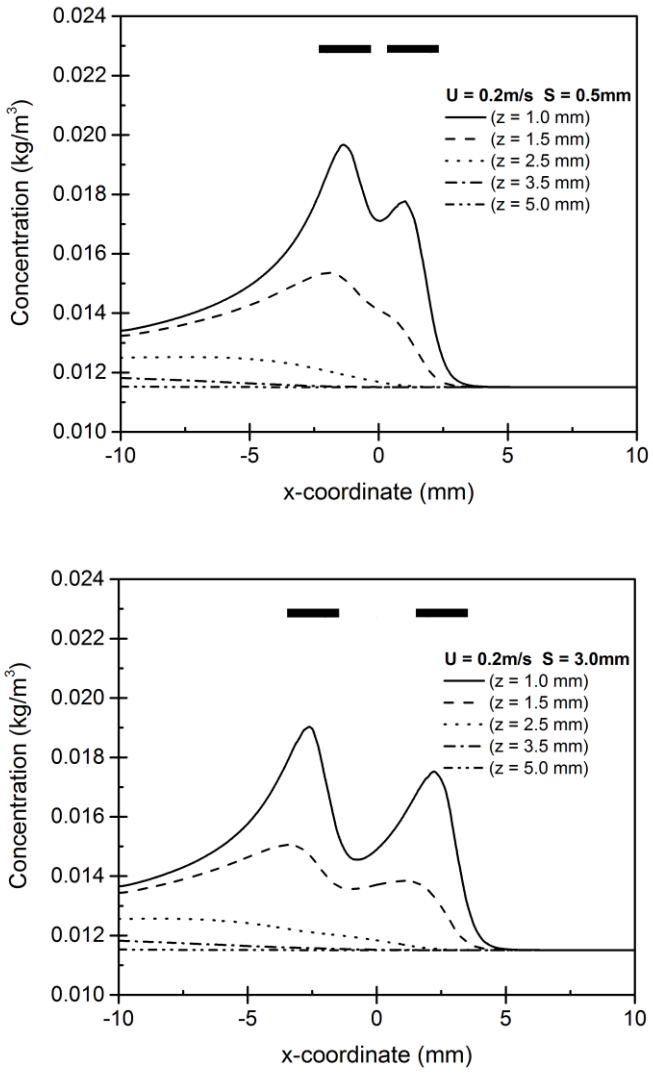

Figure 6-19: Concentration levels along horizontal lines (i.e. duct's length) located in the y = 0 centre plane and at various heights above the substrate, at *t* = 300s. The positions of the parallel droplets are indicated by the thick horizontal bars. The flow is from right to left.

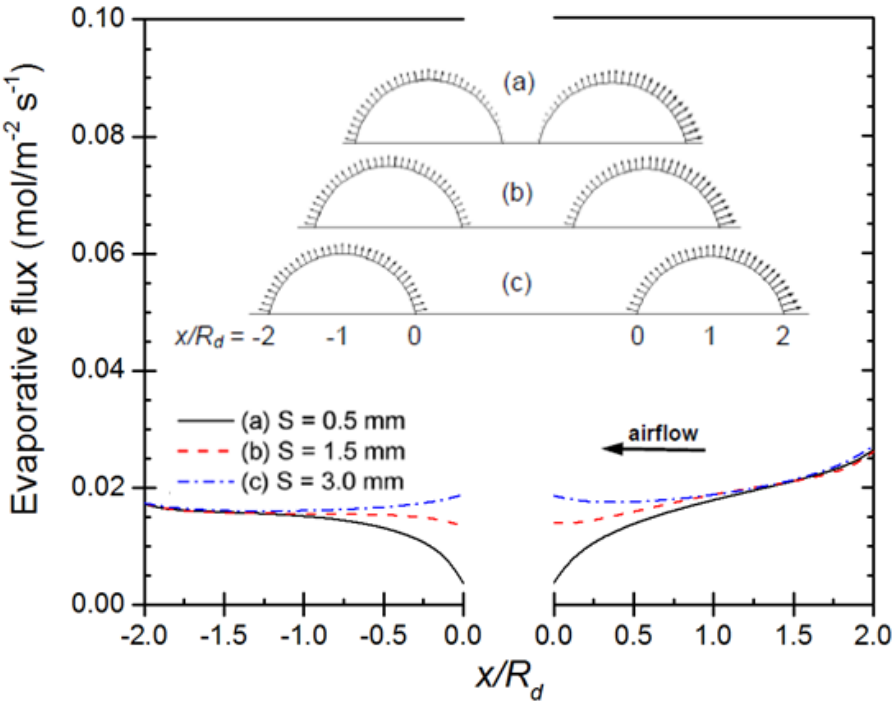

Figure 6-20: Evaporative flux at 300 s along the free surface of the droplets aligned parallel to an air flow of speed 0.02 m/s and various separation distances. The velocity arrows are normalised to the same scale in all plots.

These plots clearly show the enhanced evaporation on the upstream (right-hand) side of the leading droplet, as a result of the continuous transport of water vapour away from this region and the arrival of fresh air from the inlet. For U = 0.2 and 2.0 m/s (Figure 6-21 and Figure 6-22), the flux leaving the upstream part of the leading droplet is independent of the droplet separation, as expected from Figure 6-19, while for U = 0.02 m/s (Figure 6-20) there is a small influence of the droplet separation on the upstream flux. This is consistent with the 'zone of influence' idea of Figure 5-5, discussed in Chapter 5, applied to the downstream droplet.

The downstream parts of the leading droplet surface experience a significantly lower flux than the upstream parts. However, for the highest air speed (Figure 6-22), the flux even in this downstream part of the leading droplet is independent of the droplet separation. This indicates that the reduction in flux from the downstream half of the leading droplet is entirely due to the presence of vapour transported from the upstream half of the same droplet. At lower speeds,

the flux from the downstream parts of the leading droplet is influenced by the proximity of the second droplet (Figure 6-20, Figure 6-21) as a result of the effect of the upstream diffusive flux from the second droplet, as mentioned previously in this section.

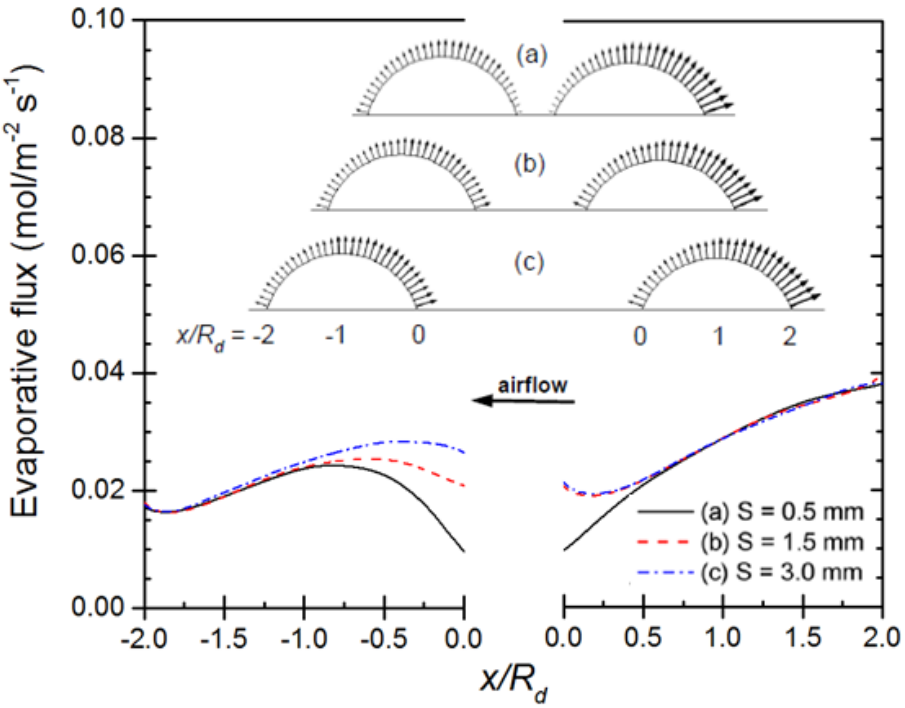

Figure 6-21: Evaporative flux at 300 s along the free surface of the droplets aligned parallel to an air flow of speed 0.2 m/s and various separation distances. The velocity arrows are normalised to the same scale in all plots.

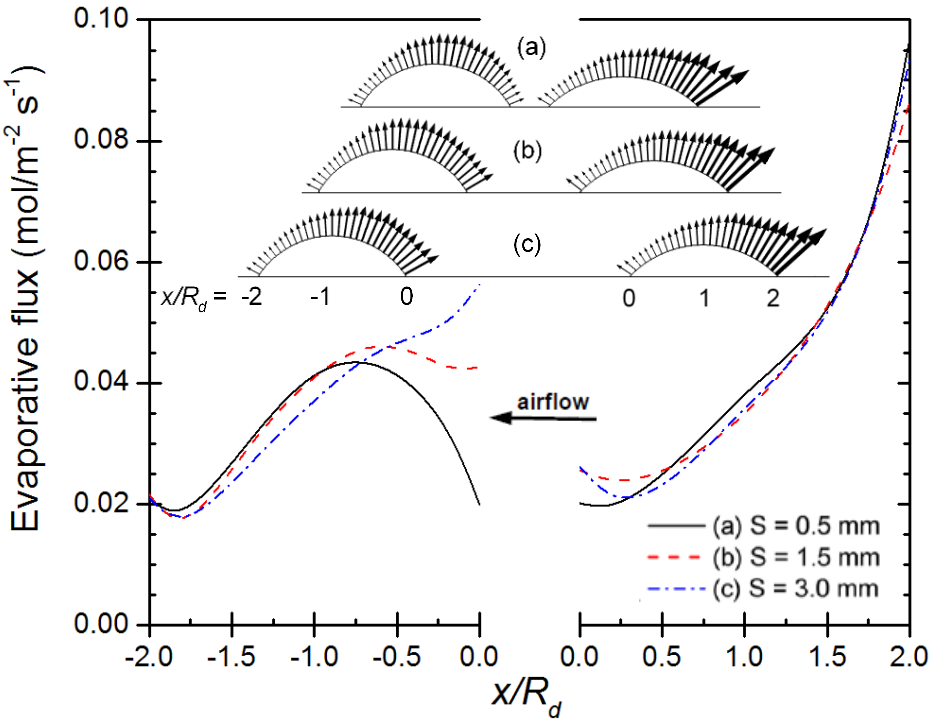

Figure 6-22: Evaporative flux at 300 s along the free surface of the droplets aligned parallel to an air flow of speed 2.0 m/s and various separation distances. The velocity arrows are normalised to the same scale in all plots.

As in the parallel droplet arrangement, the sharp drop in evaporative flux in the region between the droplets is also clearly seen in these figures. Unlike in the perpendicular droplet configuration, in the parallel case, the air flows *across* the gap between the droplets rather than *through* it. Hence it is less effective in flushing vapour out of the gap the vapour concentration is therefore higher in the gap between droplets. Correspondingly the evaporative fluxes are generally a little lower near $x/R_d = 0$ in Figures 20-22 than near $y/R_d = 0$ in Figure 6-8 and Figure 6-9, especially for higher speeds in Figure 6-10.

Focusing now on the downstream droplet, at low speed and small separation, the flux pattern looks very similar to the natural convection case – compare Figure 6-20 (a) with Figure 6-7 (for S = 0.5 mm) – with evaporation occurring more rapidly on the downstream than the upstream side of the droplet. As the gap is opened up, the interaction between the droplets diminishes and, despite being exposed to the water vapour transported downstream from the leading droplet, the downstream droplet evaporates marginally more rapidly through its

upstream surface. Note that the evaporation fluxes into the gap from each droplet are roughly the same at this low speed (the flux curves meet at $x/R_d = 0$).

At higher air speed (Figure 6-21), the flux distribution around the downstream droplet looks quite different. At small droplet separation, the flux is still small near the solid surface between the droplets, but the surface of the droplet upstream of its apex exhibits enhanced evaporation and indeed the maximum local evaporation rate for this droplet occurs there. This is consistent with that area being the part of the droplet most exposed to the overlying air flow. As the separation is increased, more of the downstream droplet becomes exposed to the passing air flow, and the flux through the upstream surface increases accordingly. Eventually a situation is reached where, near the solid surface between the droplets, the upwind flux from the second droplet exceeds the downwind flux from the first droplet – see curve (c) and vector plot (c) in Figure 6-21. As the droplet separation increases, the flux distribution on the downstream droplet surface looks similar to that on the upstream droplet. However the magnitude of the flux is always lower on the downstream droplet due to the concentration of water vapour transported downwind from the upstream droplet. For the highest speed considered (Figure 6-22), the flux distributions are similar to those in Figure 6-21 but rather more exaggerated as a result of the faster air flow enhancing evaporation. At high air speed and sufficient separation, the droplets show a similar behaviour, but with higher flux from the upstream droplet exposed to the advancing low-concentration air.

The vector plots in Figures. 6-20 – 6-22 (and the contour plots in Figure 6-18) also illustrate the difference in the upstream and downstream droplet volumes after 300s as a result of the inhibiting effect of the water vapour transported downstream from the leading droplet. Unlike in the perpendicular droplet arrangement, where the combination of air speed and separation can effectively decouple the vapour spaces around the droplets (Figure 6-11 and Figure 6-12), in the parallel arrangement, the two droplets remain coupled by the downstream advection from the first droplet. This is shown very clearly in the overhead views of the concentration field presented in Figure 6-23 and in the zone of influence around the two droplets at various separation distances and air speeds presented in Figure 6-24, and is discussed further in Section 6.5.

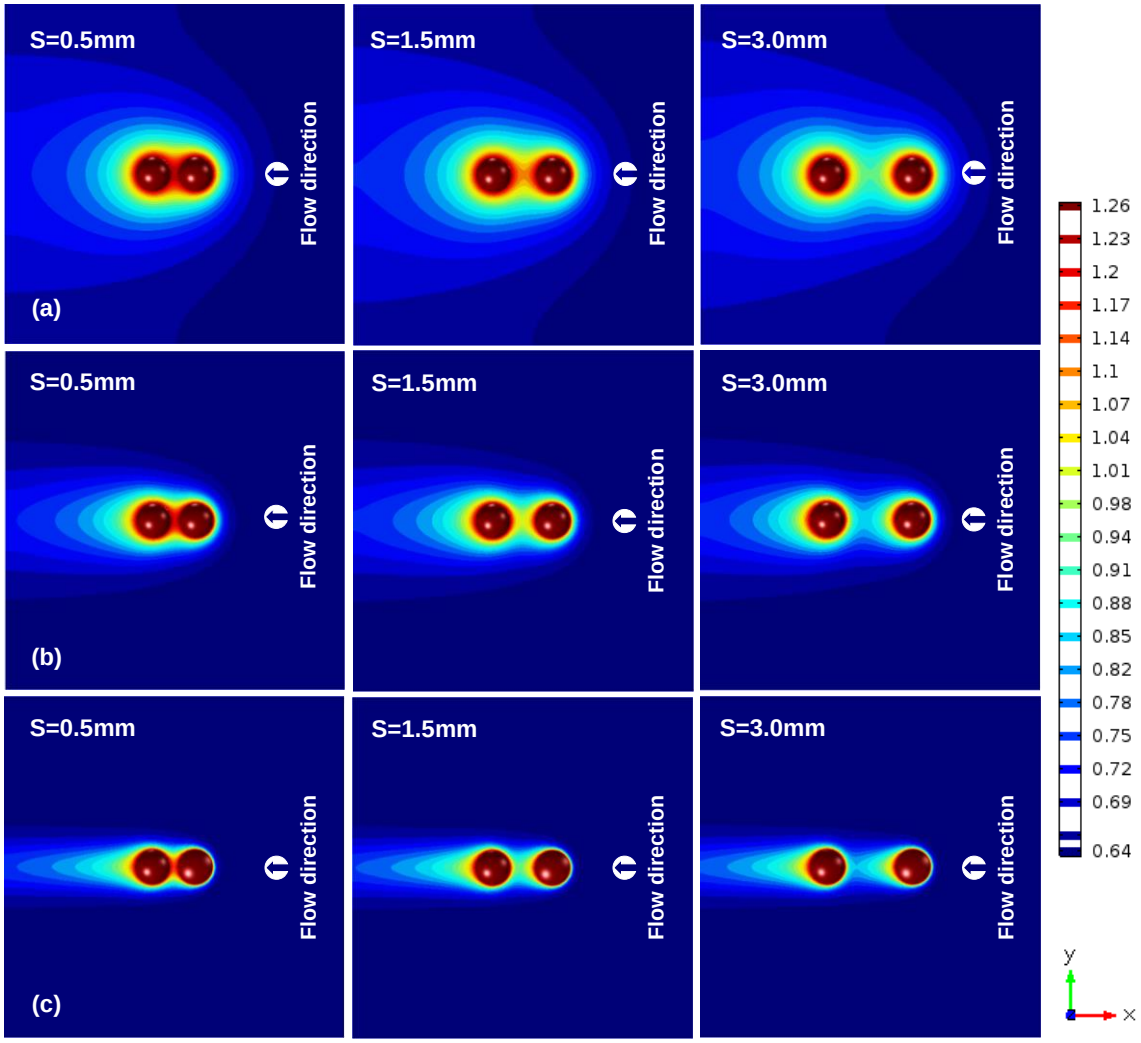

Figure 6-23. Contour plot of the vapour concentration distribution over the bottom surface of the domain at time 300s for two neighbouring evaporating droplets arranged parallel to the flow of speed (a, b, c) U = 0.02, 0.2 and 2 m/s, respectively and at various separation distances (S = 0.5, 1.5 and 3.0mm). The colour bar represents the vapour concentration in mol/m^3.

Although droplet pairs with different contact angles have not been explicitly investigated in this study, the above results allow some expected behaviour to be inferred. For droplets arranged parallel to the air flow, having an initially smaller upstream droplet would expose more of the downstream droplet to the air flow, leading to faster evaporation of that droplet.

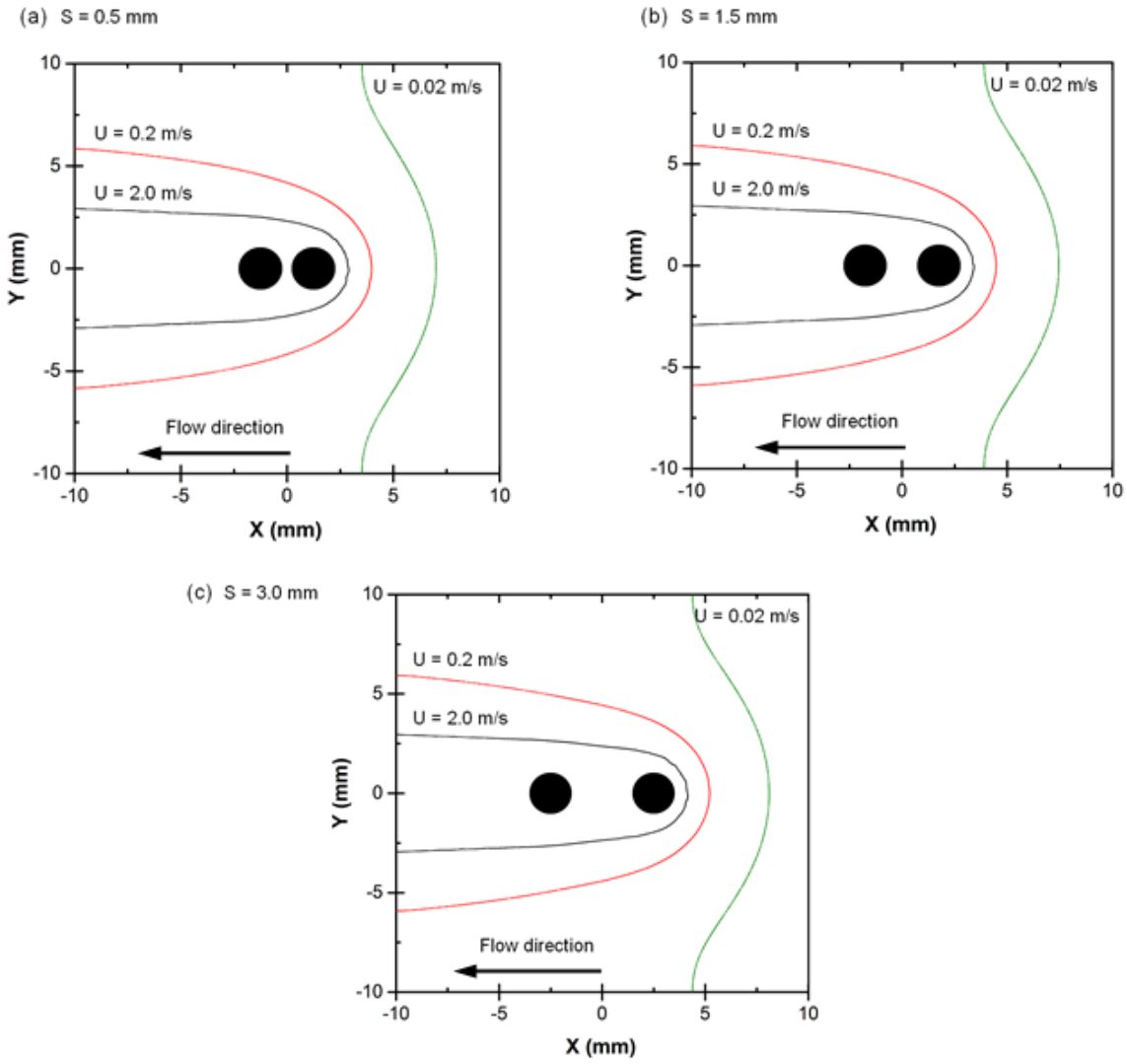

Figure 6-24: Zone of influence around the two parallel droplets after 300 s from the initial state and at separation distance (a) S = 0.5 mm, (b) S = 1.5 mm and (c) S = 3.0 mm, and various air speeds. The plot is defined by contours along which the vapour concentration is 1% higher than the ambient (inlet) concentration. The two black circles represent the two droplets. Contours are plotted on the plane of the solid surface.

The smaller upstream droplet would also experience a slightly lower local air speed as a result of it smaller protrusion into the parabolic laminar velocity profile. These effects would likely result in a smaller difference in the instantaneous evaporation rates of the two droplets, though of course the smaller droplet would likely still have a shorter lifetime due to its smaller volume. Having an initially larger upstream droplet would produce more shielding of the downstream droplet

and higher concentrations around it, especially at small separations. This would be expected to leading to a greater difference in evaporation rate. Perhaps for a certain radius ratio the two droplets could exhibit the same total drying time.

From these observations, it seems that the evaporative behaviour of droplets in the parallel arrangement case is very complex, and further investigation is needed to see which the most influential parameters (the influence of hydrodynamic shielding as a result of the droplet shape or the water vapour transported downstream from the upstream droplet) affect the evaporation of the downstream droplet. Therefore, it is worth to provide a comprehensive understanding of how a droplet evaporation aligned parallel to another source of influence, e.g. source of liquid evaporation or an obstacle, behaves, and how the downstream convective flux affects the evaporative behaviour of this droplet. This is considered intensively in the next section.

6.5 Isolating upstream influences on droplet evaporation

In the previous section, we examined that a droplet evaporating on the downstream side of a neighbouring evaporating upstream droplet is not only affected by the downstream diffusive water vapour transported by the forced air convection from the upstream droplet but also by the hydrodynamic shielding effect of the upstream droplet. In this section, to explore comprehensively and separately whether the hydrodynamic shielding effects of the upstream droplet or the downstream water vapour transport from the upstream droplet are the most influential mechanisms on the evaporative behaviour of the downstream droplet therefore, two cases of the source of influences affecting the downstream droplet evaporation will be simulated here, as shown in Figure 6-25. Further, two separation distances (S=0.5 mm and S=3.0 mm), and two airflow velocities (U=0.02 m/s and U=2.0 m/s) are considered in these simulations, where S, here is the separation distance between the downstream droplet and the source of influence. The evaporation of the isolated single droplet under forced convective environment (studied previously in Chapter 5) is also considered here as a reference case to which the evaporative behaviour of the downstream droplet can be compared.

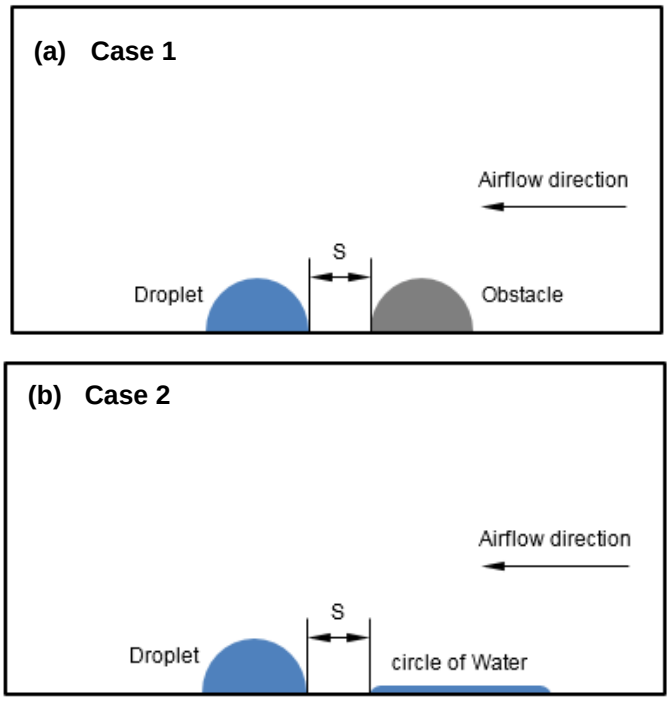

Figure 6-25: A side view of the computational domain – showing different sources of influence: (a) a hemispherical solid obstacle and (b) a circular layer of water aligned parallel in front of a single droplet subjected to airflow.

In case 1, which illustrates the hydrodynamic shielding effects on the downstream droplet evaporation, a hemispherical solid obstacle with same radius of the sessile droplet is used as shown in Figure 6-25 (a), since no-slip and no-flux boundary conditions are applied on the surface of the this solid obstacle. On other side, in case 2, which focuses on the vapour concentration increase effect, different scenario is represented since a source of evaporation (i.e. a circular layer of water with no-slip boundary condition at the surface of water layer, as described in Chapter 5 and Appendix B, but with surface area equal to the surface area of the sessile droplet) is placed in the upstream region of the evaporating sessile droplet as shown in Figure 6-25 (b).

For the case 1 at 0.02 m/s and 0.5 mm, see curve (b) and vector plot (b) in Figure 6-26, the evaporative flux along the droplet free surface, as expected, is obviously affected by the presence of the solid obstacle with very small separation distance, particularly the first quarter part of the sessile droplet since the evaporative flux is lower than for the single sessile droplet case, curve (a) and vector plot (a) of Figure 6-26. This can be attributed to the fact that the solid

obstacle shades the upstream part of the droplet at which a small amount of airflow reaches this part of the droplet. Consequently, the diffused water vapour could not be swept completely away from this part of the droplet rising the concentration levels of water vapour there, and hence decreasing the concentration gradient driving evaporation. With larger separation distance (3.0 mm), as shown in curve (c) and vector plot (c) in Figure 6-26, the flux pattern looks very similar to that for the single droplet since a significant increase in the evaporative flux is observed at the upstream part of the droplet because the airflow is able to sweep downstream water vapour, and hence increasing the driving force of the evaporative flux. At the downstream part of the droplet for both cases (b and c) of Figure 6-26 however, it seems that although increasing the separation distance enhances the evaporative flux at the upstream region of the droplet, the amount of water vapour transported downstream via the forced airflow is still able to affect the vapour space surrounding the downstream part of the droplet. Hence, more evaporative flux is observed at the downstream region of the droplet for 0.5 mm case compared with 3.0 mm case of the separation distance.

Figure 6-26 (d and e) shows the evaporative flux along the free surface of a droplet influenced by another source of evaporation. It is very clear to notice from curve (d) and vector plot (d) of Figure 6-26 that the water vapour transported from the water layer overlaps the sessile evaporating droplet which consequently increases the concentration levels of water vapour in the gap between them, and hence decreases the concentration gradient driving evaporation. As the gap is opened up to 3.0 mm, see curve (e) and vector plot (e) - Figure 6-26, the interaction between the droplet and the water layer decreases, and hence the droplet evaporates rapidly through its upstream part (i.e., higher evaporative flux). Again, the downstream part of the droplet is still influenced by the water vapour transported from the upstream half of the droplet together with that transported from the water layer.

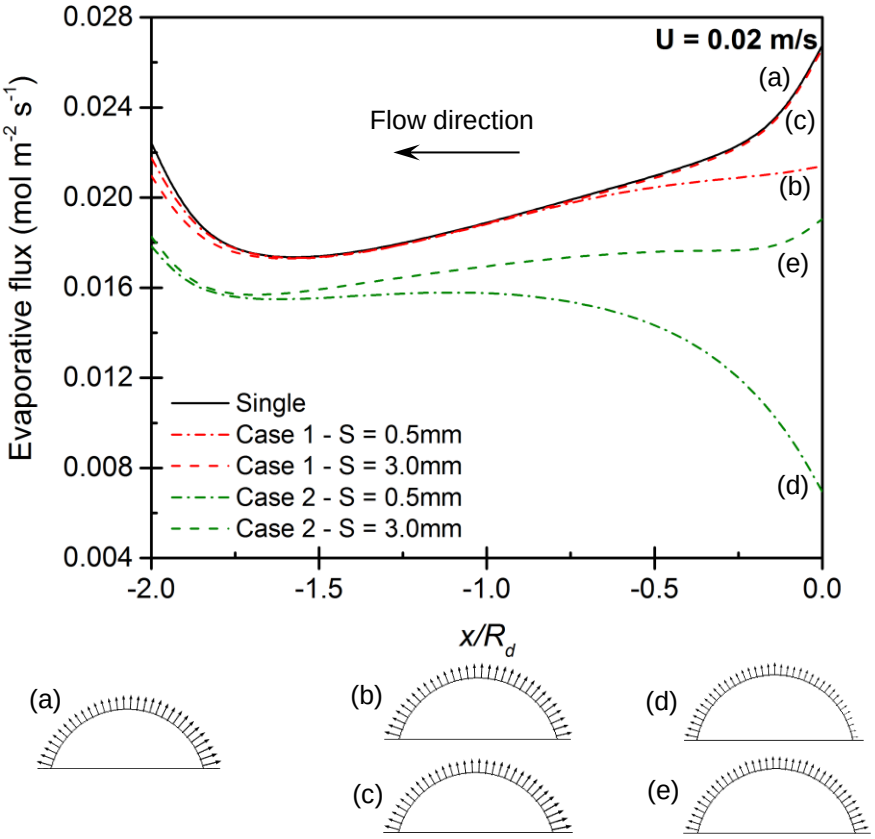

Figure 6-26: Evaporative flux along the droplet free surface at t = 300 s under 0.02 m/s of forced airflow, and at various situations; (a) single sessile droplet, (b, c) case 1 at 0.5 mm and 3.0 mm respectively, and (d, e) case 2 at 0.5 mm and 3.0 mm respectively. The coordinate origin of the single sessile droplet has been shifted to match the other cases of the droplet evaporation. The velocity arrows are normalised to the same scale in all plots.

At the higher air speed (2.0 m/s), Figure 6-27, the flux distribution around the droplet is quite different. For the solid obstacle case with small separation, curve (b) and vector plot (b) of Figure 6-27, the evaporative flux is still small in the gap region compared to that for the single droplet, see curve (a) and vector plot (a) in Figure 6-27. As the separation distance is increased, curve (c) and vector plot (c) - Figure 6-27, the droplet becomes more exposed to the passing airflow, and higher evaporative flux occurs accordingly through the upstream part of the droplet. Unlike for the lower air speed, the flux through the downstream part of

the droplet becomes more less than through the upstream part as a result of increasing the downstream water vapour transported from the upstream half of the droplet. Again, the droplet experiencing an upstream source of evaporation, the flux along the droplet free surface becomes less compared to the solid obstacle case under same conditions, as shown in Figure 6-27. At the higher air speed and small separation distance, curve (d) and vector plot (d) of Figure 6-27, lower evaporative flux is observed at the upstream part of the droplet as a result of decreasing the concentration gradient at the gap region. Further, a significant enhancing in the evaporative flux is noticed at the upstream apex of the droplet surface. This is consistent with that region being part of the droplet exposed to the most airflow and less downstream water vapour transported from the upstream regions. At the larger separation distance (3.0 mm), curve (e) and vector plot (e) - Figure 6-27, the flux pattern looks similar to that at the lower air speed, Figure 6-26 (e), but with higher levels of the evaporative flux around the droplet.

From Figure 6-26 and Figure 6-27, it is easy to observe the role of each source of influence on the evaporative behaviour of the evaporating droplet. At the lower speed, the influence of the evaporating water layer is more noticeable than the effects of the solid obstacle on the evaporative behaviour of the droplet in comparison with the single droplet evaporation. As the air speed is increased, the effects of both sources of influence are approximately same as a result of the great role of the faster airflow. Further, one can see the remarkable influence of the separation distance in reducing the interaction between the droplet and the influencing source at the lower air speed, while this role significantly decreases as the speed of the airflow is increased, particularly for the evaporating water layer case. In addition, at the lower air speed, with slightly further increase in the separation distance, the droplet can be isolated completely from the influence of the solid obstacle while, larger separation distance is needed to isolate the droplet completely from the influence of the evaporating water layer. Decoupling the droplet from the source of influence becomes more difficult with the higher air speed because of that they remain coupled by the downstream advection from the upstream influencing source, particularly for the evaporating water layer case.

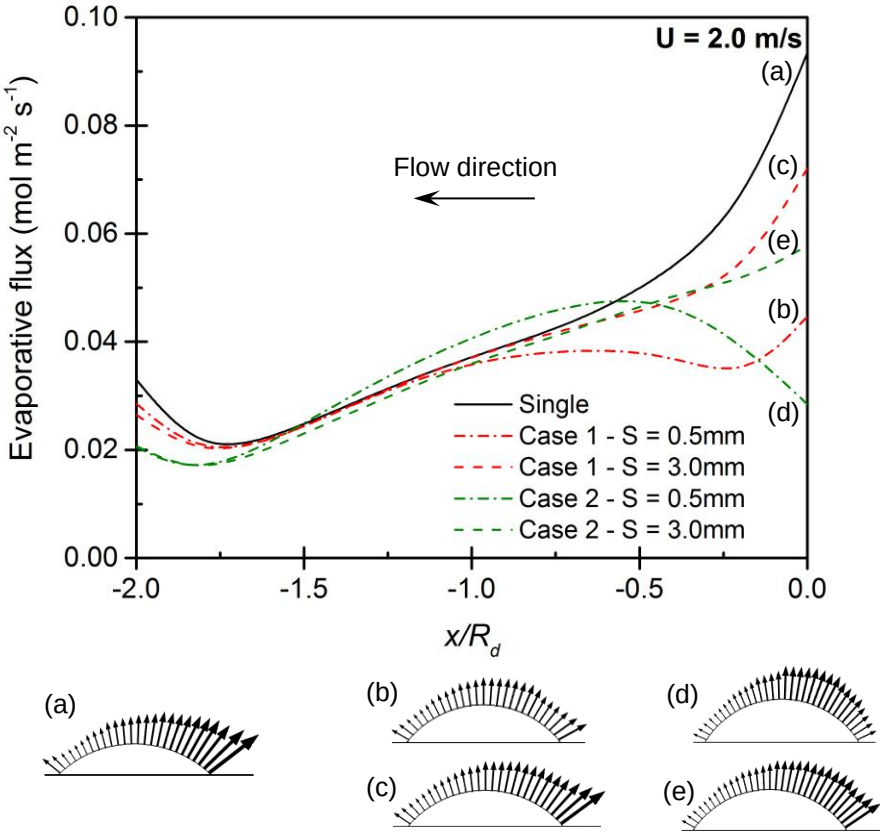

Figure 6-27: Evaporative flux along the droplet free surface at t = 300 s under 2.0 m/s of forced airflow, and at various situations; (a) single sessile droplet, (b, c) case 1 at 0.5 mm and 3.0 mm respectively, and (d, e) case 2 at 0.5 mm and 3.0 mm respectively. The coordinate origin of the single sessile droplet has been shifted to match the other cases of the droplet evaporation. The velocity arrows are normalised to the same scale in all plots.

For more qualitative view, Figure 6-28 and Figure 6-29, illustrate the concentration field surrounding the droplet in the vertical plane through the droplet centre under various air speeds and separation distances. Clearly, the presence of a solid obstacle upstream a droplet in the airflow with a small separation distance, see Figure 6-28 (a) helps in accumulating the diffusive water vapour through the upstream surface in the gap region leading to lowering the concentration gradient driving evaporation there even at the higher air speed, see Figure 6-29 (a). As the separation distance is increased, Figure 6-28 (b), the airflow with lower velocity is sufficient to sweep the water vapour diffused through

the upstream surface of the droplet downstream, and hence enhances the evaporation rate of the droplet. However, the solid obstacle still influences the advection airflow passing the droplet. Unlike the lower air speed, Figure 6-29 (b) shows that at the higher air speed, although the droplet is mostly decoupled from the solid obstacle, its presence has a great effect on the advection airflow passing the droplet, and hence lower evaporative flux through the upstream surface of the droplet, as shown previously in Figure 6-27 (c).

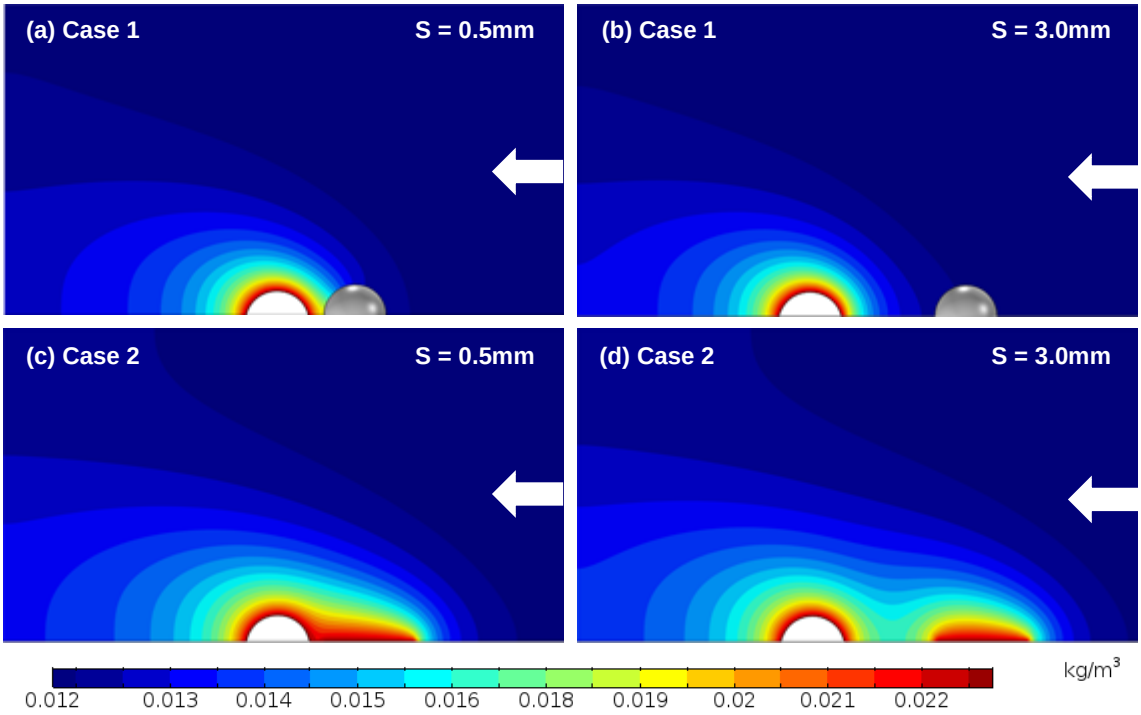

Figure 6-28: Contour plot of the vapour concentration distribution above the droplet at time 300 s, and under 0.02 m/s of the forced airflow and different sources of influence; (a, b) a solid obstacle with 0.5 mm and 3.0 mm, respectively, and (c, d) an evaporating water layer with 0.5 mm and 3.0 mm, respectively. The white arrow represents the airflow direction.

Focusing on the influence of the evaporating water layer on the droplet evaporation, Figure 6-28 (c) shows the higher level of the water vapour concentration in the gap region at the lower separation distance. Increasing the separation distance, Figure 6-28 (d), under same speed of the airflow helps significantly in reducing the interaction between the droplet and the water layer but the droplet is still coupled with the downstream water vapour transported from

evaporation of the water layer. However, it is clear to notice from Figure 6-29 (c and d) that increasing the air speed reduces the role of the separation distance in lowering the interaction in the gap region, and consequently larger distance is needed to diminish the interaction and isolate the droplet completely. Further analysis of the above findings, Figure 6-30 and Figure 6-31 show clearly the concentration field in the overhead view in which the combination effect of both air speed and separation distance, and the effect of the droplet evaporation under each case of the influencing sources on the surrounding as well, are presented.

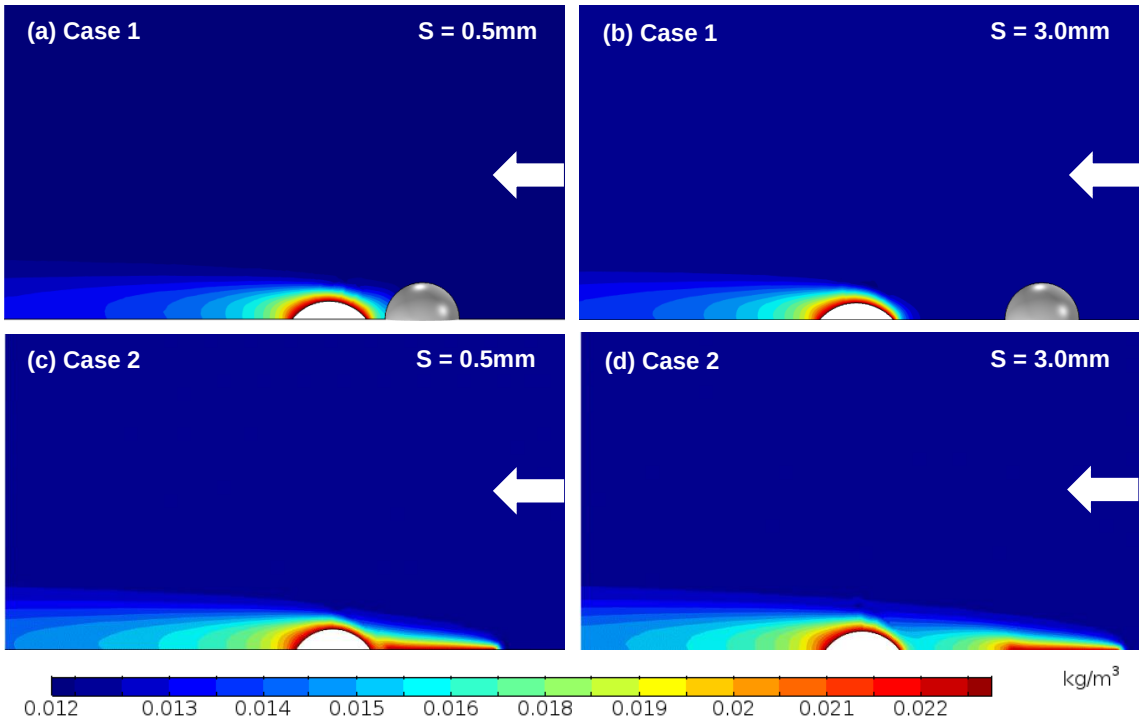

Figure 6-29: Contour plot of the vapour concentration distribution above the droplet at time 300 s, and under 2.0 m/s of the forced airflow and different sources of influence; (a, b) a solid obstacle with 0.5 mm and 3.0 mm, respectively, and (c, d) an evaporating water layer with 0.5 mm and 3.0 mm, respectively. The white arrow represents the airflow direction.

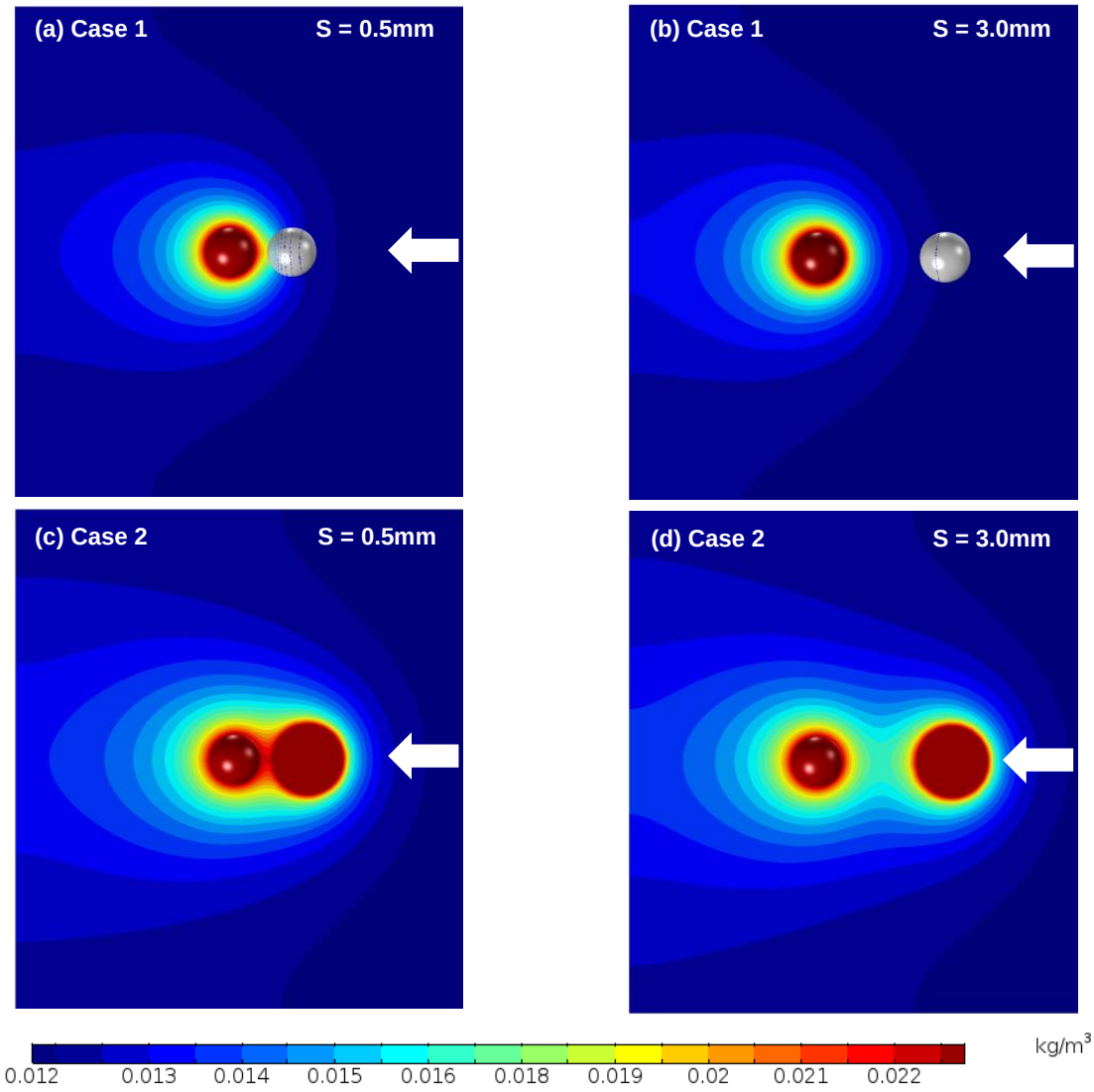

Figure 6-30: Contour plot of the vapour concentration distribution over the bottom surface of the domain at time 300 s for a droplet under 0.02 m/s of the forced airflow and different sources of influence; (a, b) a solid obstacle with 0.5 mm and 3.0 mm, respectively, and (c, d) an evaporating water layer with 0.5 mm and 3.0 mm, respectively. The white arrow represents the airflow direction.

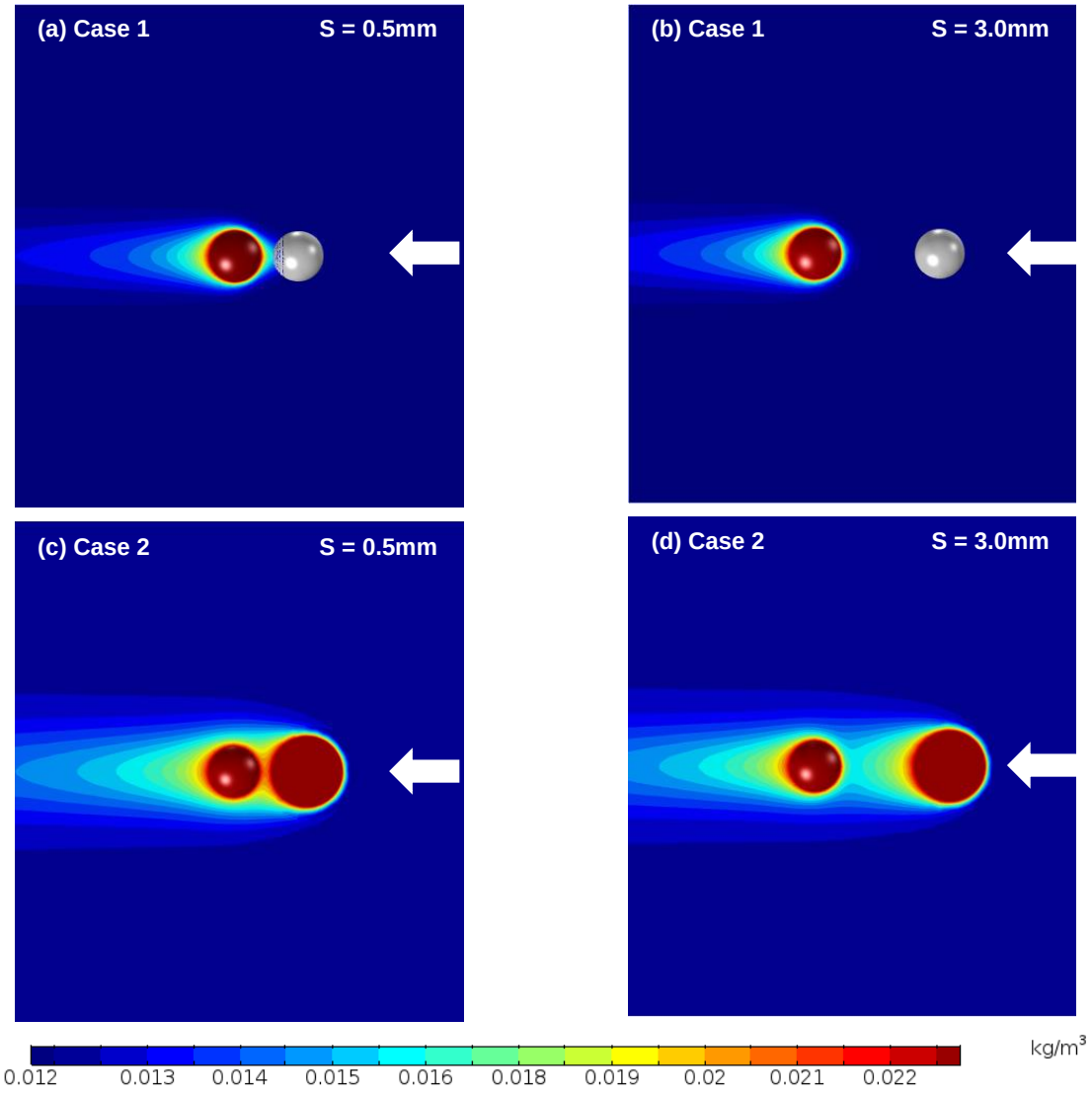

Figure 6-31: Contour plot of the vapour concentration distribution over the bottom surface of the domain at time 300 s for a droplet under 2.0 m/s of the forced airflow and different sources of influence; (a, b) a solid obstacle with 0.5 mm and 3.0 mm, respectively, and (c, d) an evaporating water layer with 0.5 mm and 3.0 mm, respectively. The white arrow represents the airflow direction.

For further comparison, Figure 6-32 shows a comparison of the evaporative flux along the droplet free surface for case 1 and 2 with the evaporative flux along the free surface of the downstream droplet for the parallel droplets arrangement –see Figure 6-20 and Figure 6-22. One can easily see that the evaporative flux for the parallel droplets case is lower than those for case 1 and 2 at the lower air speed, particularly through the upstream surface of the downstream droplet which is the

most influenced part by the upstream droplet effect, as observed previously. This can be attributed to the combination effects of the partial shielding effect of the upstream droplet and the downstream transport of water vapour evaporating from the upstream droplet on the downstream droplet. In addition, the flux distribution of the downstream droplet is similar to that for the case 2 as a result of the reduced role of the hydrodynamic shielding effect compared to the vapour concentration increase effect even at larger droplet distance. At the higher air speed (2.0 m/s), the flux distributions of all cases are almost similar as a result of the faster airflow enhancing evaporation. As a result, it seems that the downstream droplet is more influenced by the transported water vapour downstream from the upstream droplet than the hydrodynamic shielding effect of the upstream droplet.

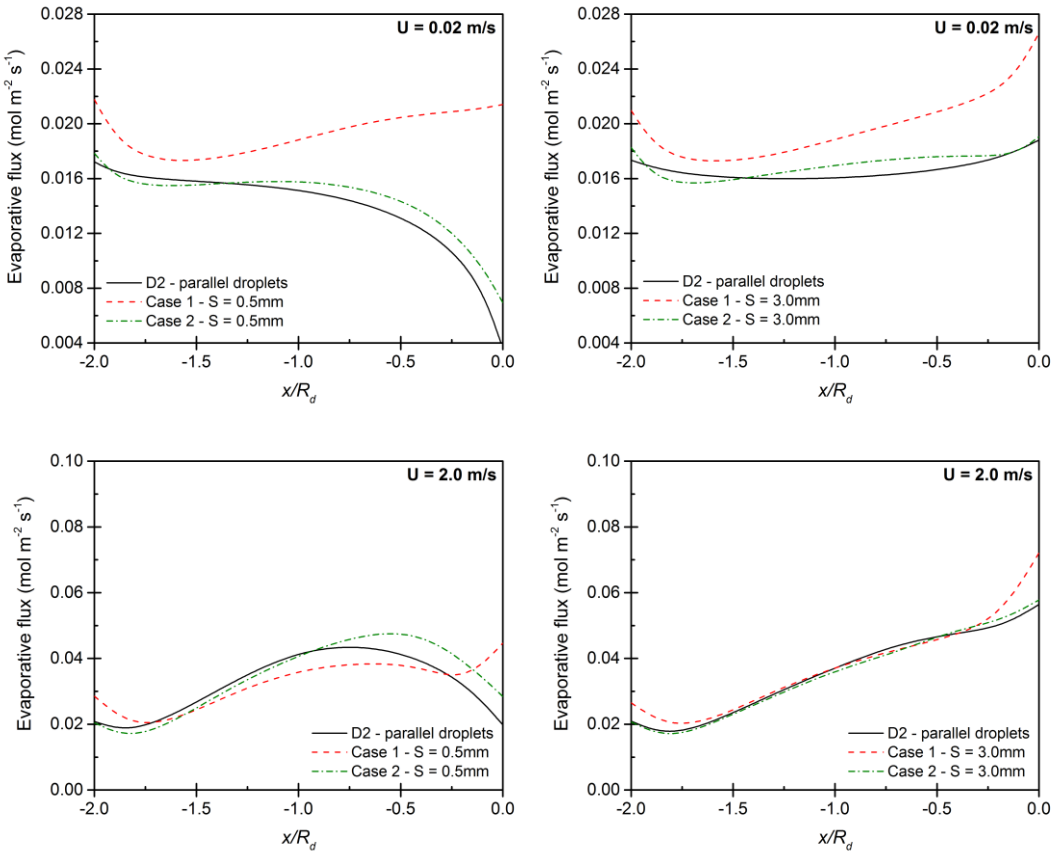

Figure 6-32: A comparison of the evaporative flux at t = 300 s along the droplet free surface under conditions of case 1 and 2 with that along the free surface of the downstream droplet (represented by D2) of parallel droplets arrangement, and at different air speeds and various separation distances.

6.6 Implications of arrays of evaporating droplets

Clearly the observations presented in this chapter have significance for the evaporation of arrays of droplets, particularly if achieving uniformity of evaporation behaviour across an array is important. Under a natural convection environment, the evaporation rate of the two droplets is sensitive to the separation of the droplets, varying linearly with separation for separations from a half to three times the droplet radius. For the smallest separation considered here, switching from natural convection to a 0.02 m/s forced airflow over the droplets resulted in a 30% increase in evaporation rate for droplets aligned perpendicular to the flow. For speeds of 0.2 m/s and 2 m/s, the evaporation rate increased by 91% and 158% respectively. Increasing the separation of the droplets produces further enhancement of the evaporation rate, especially at low air speed. The presence of the airflow sweeping vapour out of the region between the droplets means that a droplet separation can be reached where the droplets no longer influence each other.

However, the decoupling of the droplets by the forced convection is only really possible for the first row of droplets in an array, which could be aligned perpendicular to the airflow. For subsequent rows, the transport of the vapour evaporated from the first row would influence the vapour space around the downstream droplets over much longer distances. The downstream droplets would therefore evaporate more slowly. To give a quantitative indication of this effect, Figure 6-33 shows how much bigger the downstream droplet is compared to the upstream droplet in the two-droplets configuration parallel to the airflow, with the droplet separation range extended to larger separations. The difference in volume shown is after 300 s and is expressed as a percentage of the upstream droplet volume.

At low speed, the difference in volume is almost flat, with the downstream droplet approximately 5% bigger at this point in the droplet lifetime. At the medium speed, the size difference is larger and although it reduces slightly with separation distance, it levels off to a larger difference than the low speed case. This is because of the faster evaporation of the upstream droplet at higher speed leading to higher vapour concentration levels in the region downstream of the droplet and

hence slower evaporation of the other droplet. The difference in size is even more pronounced at the highest air speed but also shows a steeper variation with separation.

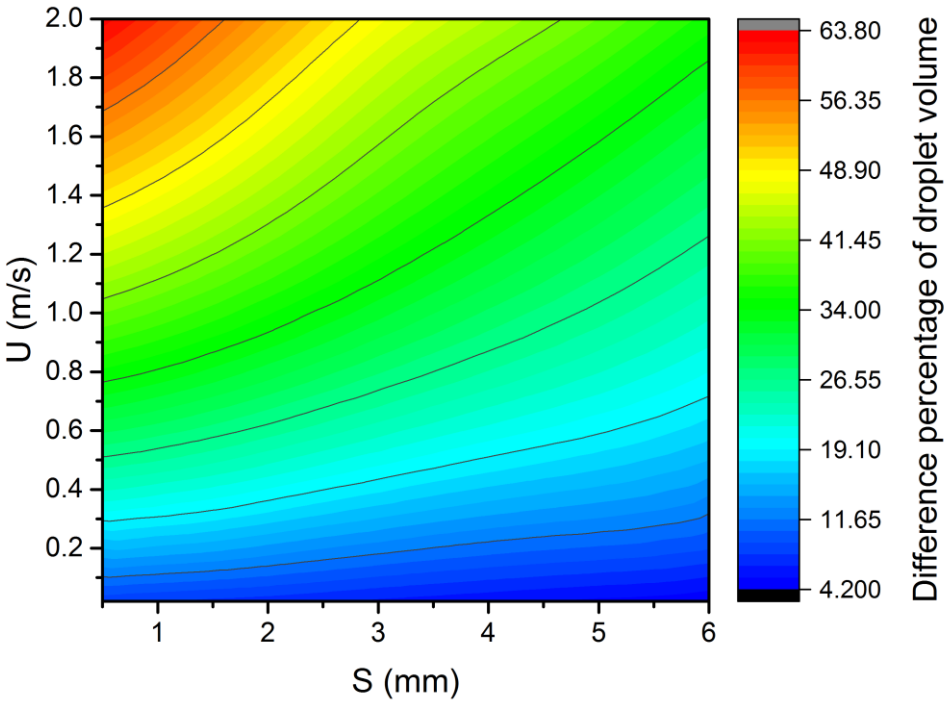

Figure 6-33: Difference in the volume of two parallel droplets after 300 s (as a percentage of the upstream droplet volume) as a function of the distance between the droplets.

Clearly the downstream influence of the leading droplet is felt over relatively large distances, as suggested by Figure 5-5 as shown in Chapter 5. Hence in a droplet array, the streamwise spacing of the droplets would need to be significantly longer than the transverse spacing if a reasonably uniform evaporation were required. In an array of several rows of droplets in a forced convective airflow, there would likely be a cumulative effect of a build-up of vapour concentration in the downstream direction, together with a reduction in the transverse dispersion of vapour because of the presence of more droplets along each row. It is expected that evaporation of the droplets would take place in the manner of an advancing front across the array.

6.7 Conclusions

As has been seen previously, under natural convection, evaporation of two neighbouring droplets is slower than an independent single droplet because of the raised vapour concentration levels in the region between the droplets, which reduces the local concentration gradient-driven evaporation rate near the facing parts of the droplet surfaces. Increasing the droplet separation hence speeds up the evaporation.

For droplets arranged perpendicular to the forced airflow, the behaviour at low speeds is (as expected) very similar to the natural convection case but evaporation is slightly accelerated. Increasing the flow speed has a strong effect on the evaporation rate, with an airflow of 2.0 m/s producing approximately five times faster evaporation than the natural convection case. The forced convection also effectively decouples the two droplets at sufficiently high speed or droplet separation, since the vapour in the region between the droplets is swept sufficiently quickly downstream.

For droplets arranged parallel to the airflow, the upstream droplet evaporates significantly more quickly than the downstream droplet, especially at higher air speeds, and more quickly than the corresponding perpendicularly arranged droplets. At sufficiently high speed or separation, the downstream advection dominates upstream diffusion and Stefan flow, and the interaction between the droplets becomes effectively one-way, with the upstream droplet becoming independent of the downstream but the evaporation of the downstream droplet being slowed by the downstream vapour transport from the leading droplet.

For perpendicular and parallel droplets arrangements, the variations of the droplet volumes with time are almost identical to the same trend of the isolated single droplet under the forced convection condition represented by the exponential form of equation.

Further analysis of the downstream advection results reveal that droplet evaporation is more influenced by the downstream water vapour transported from another upstream source of evaporation than the shielding effect arising from the presence a solid obstacle upstream the droplet. Moreover, a small distance from the upstream influencing source might be sufficient to diminish the interaction in

the gap region, particularly at the lower air speed. At the higher air speed, the droplet remains coupled with the upstream influencing source by the downstream advection, and larger separation distance is needed to isolate the droplet completely.

The behaviour of the pairs of droplets in response to forced convection considered here has implications for the evaporation of arrays of droplets assisted by airflow. The analysis of the perpendicular and parallel droplets provides a starting point for optimisation of droplet array configurations in order to create efficient systems for evaporating multiple droplets simultaneously.

Chapter 7 Internal dynamics and concentration distribution in salt solution droplets evaporating under forced convection

7.1 Introduction

To this point, previous chapters focused on the evaporative behaviour and hence the evaporation rate of a pair of neighbouring droplets under the effect of a gentle forced airflow, without specifically considering the internal dynamics within the droplets, and how this airflow affects these dynamics compared to droplet evaporation under a natural convective environment.

In recent decades, the dynamics inside multiple droplets evaporating close to each other in arrays has become a key topic of interest in many industrial and scientific applications. This continues to drive the need for a comprehensive understanding of this fundamental phenomenon.

Experimental and numerical observations in the literature of Chapter 2 show that the dynamics inside droplets having pinned contact lines depend on the evaporation conditions and the environment surrounding the droplets [130]. An outward flow towards the edge of the droplet producing a ring-like deposit is observed, which is caused by either the replenishment of liquid loss in this area or by edge enhanced evaporation [127, 130]. In contrast, a flow towards the centre of the droplet inhibiting the ring-like deposit is generated due to either centre enhanced evaporation or surface tension gradients causing Marangoni flow [129].

In parallel, another flow pattern is observed inside evaporating droplets of aqueous solution. Kang et al. [283], Savino and Monti [284], Lee et al. [285], and Pradhan and Panigrahi [33, 80] found that due to the concentration gradient inside the droplet, a recirculating flow mechanism caused by buoyancy driven convection is induced where the liquid moves along the droplet surface towards the contact line and towards the droplet apex in the centre region of the droplet. Further observations reveal that this internal flow field is significantly affected by the solute concentration inside evaporating droplets [286].

As observed previously in Chapter 6 and in the literature in Chapter 2, the interaction between adjacent evaporating droplets, by its nature, affects the evaporation behaviour, and hence the flow pattern inside these droplets [32, 33, 287, 288]. In addition, since the flow convection around the droplets influences the evaporation rate of the droplets [184, 188], an under-estimation of the evaporation rate can be expected by neglecting the effect of this mechanism [275, 289]. At the same time, as the forced air convection affects the evaporative behaviour of the droplets [34, 236], it was found that it strongly influences the flow-field induced by Marangoni effects inside the droplet [246].

In this regard, despite all the previous work in the literature, even the most recent numerical studies [34] and [236], it appears that there are no prior detailed numerical studies of the effect of forced convection on the internal dynamics and species distributions within interacting neighbouring evaporating droplets. Therefore, this chapter focuses on the internal dynamics including the flow patterns and species distributions inside a regular array of multiple interacting droplets exposed to a forced air convection. To visualise the species distributions within droplets, the evaporation of salt solution droplets are simulated instead of pure water droplets since no significant flow field was observed experimentally for water droplets [283].

7.2 The mathematical model

7.2.1 Assumptions

The mathematical model is developed based on the fully-coupled transient model for the evaporation of neighbouring droplets exposed to a forced convection airflow described in Chapter 3. Due to the symmetry in modelling multiple pinned sessile droplets simultaneously evaporating in proximity to each other inside a semi-infinite physical domain, see Figure 7-1 (a), a unit flow is defined in the beginning of the numerical work in order to simplify the numerical simulations. The unit flow, as shown in Figure 7-1 (b), represents evaporation of two pinned sessile salt solution droplets aligned parallel with the airflow covering the area between lines A and B, with periodic conditions along the side boundaries of the unit flow. The mathematical model is formulated under the following assumptions:

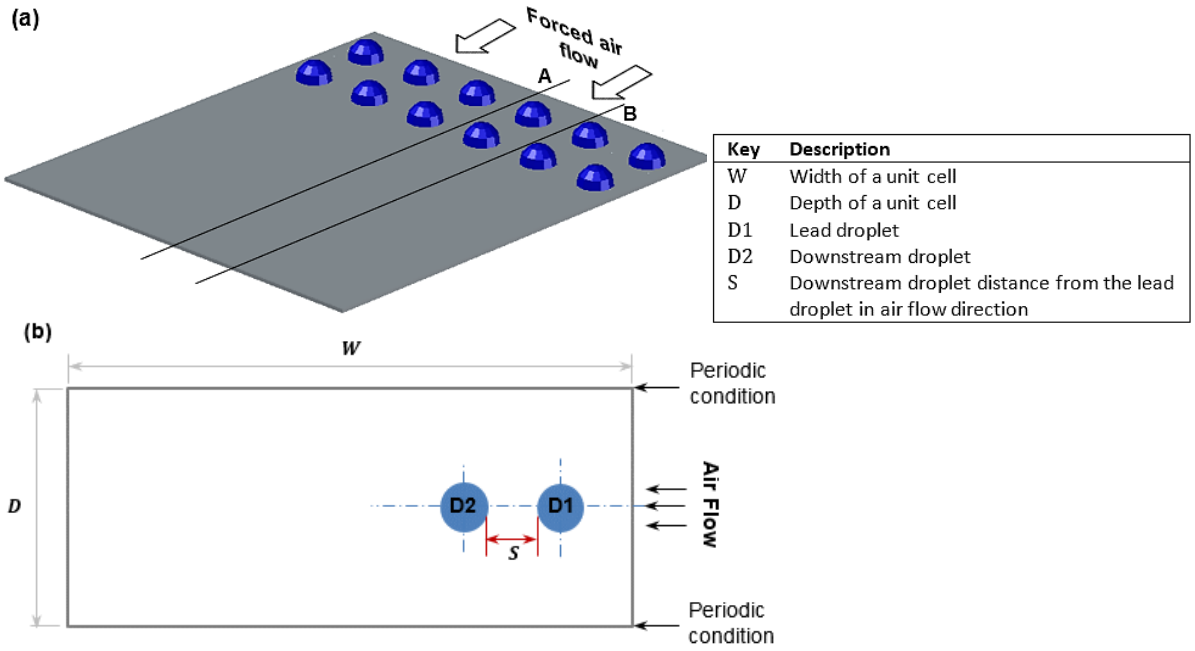

Key	Description
W	Width of a unit cell
D	Depth of a unit cell
D1	Lead droplet
D2	Downstream droplet
S	Downstream droplet distance from the lead droplet in air flow direction

Figure 7-1: (a) Schematic of a regular array of multiple sessile droplets. The area between lines A-B represents a unit flow. (b) A plan view of the unit flow which illustrates two neighbouring sessile droplets with parallel arrangement related to the air stream path inside a semi-infinite isothermal forced convective environment. The inserted table demonstrates the key descriptions of the samples mentioned in above schematics.

(1) Droplets of aqueous NaCl solution with initial volume 2.1 μL and 1 M concentration are used to investigate the effect of the forced convective environment on the solute distribution inside those droplets.

(2) Based on this type of salt solution droplets, the experimental observations of Kang et al. [283] show that the flow inside droplet is completely driven by convection due to solute concentration gradient (i.e. density difference) in the absence of an overlying airflow, and Marangoni effect due to surface tension gradient is negligible.

(3) The physical domain is assumed to be in thermal equilibrium, thus the energy equation is neglected.

(4) Both liquid and air are modelled as incompressible with Boussinesq approximation for buoyancy effects.

Regardless of the above, other assumptions and considerations are same as for water droplets evaporation model described previously in Chapter 3. Here, Figure 7-2 shows the corresponding 3D computational domain including the two parallel droplets.

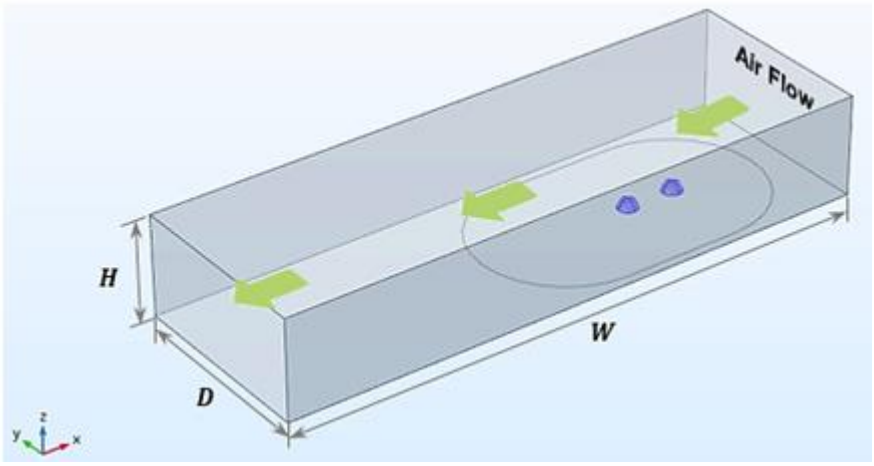

Figure 7-2: The modelled geometry of the unit flow in 3D.

7.2.2 Governing equations, initial and boundary conditions

Considering two pinned sessile aqueous NaCl solution droplets evaporating in an isothermal forced convective environment, and based on the above assumptions, the mass species, continuity and momentum equations govern the droplets evaporation through the system:

$$\frac{\partial c}{\partial t} + \mathbf{u}.\nabla c = \nabla.(D\nabla c) \tag{7.1}$$

$$\nabla.\mathbf{u} = 0 \tag{7.2}$$

$$\rho\left(\frac{\partial \mathbf{u}}{\partial t} + (\mathbf{u}.\nabla)\mathbf{u}\right) = \nabla.[-p\mathbf{I} + \mu(\nabla\mathbf{u} + (\nabla\mathbf{u})^{\mathrm{T}})] - \Delta\rho g\mathbf{k} \tag{7.3}$$

where c and D are the molar concentration field and diffusion coefficient, respectively, in the relevant fluid. At the initial time, the solute concentration, $\overline{c}_{sol}$, is uniform inside the droplets. During the evaporation, the solute concentration increases at the droplet free surfaces, and diffuses to the inner region of the droplets. Therefore, the increasing rate of the solute concentration inside the droplets is proportional to the local total molar flux at the droplet free surfaces, expressed as:

$$-D_{sol}\nabla\overline{c}.\mathbf{n} = -\frac{\overline{c}\,\mathbf{j}_{\Gamma}}{\boldsymbol{\rho_l}}M_{H_2O} \tag{7.4}$$

where $\overline{c}$ is the solute molar concentration and $M_{H_2O} = 0.018$ kg/mol is the molar mass of water. Due to considering the fluid motion in the surrounding air and within droplets, the local total molar flux, $\mathbf{j}_{\Gamma}$, from the droplet free surfaces combines the effects of water vapour transport both by diffusion and convection mass fluxes, expressed as:

$$\mathbf{j}_{\Gamma} = -D_v\nabla C + \mathbf{u}C \tag{7.5}$$

where C is the molar concentration of water vapour in the surrounding air. The diffusion of water vapour from the droplet free surfaces to the surrounding air is driven by the difference in the water vapour concentration at these surfaces and the surrounding air. The water vapour concentration is assumed to be saturated at the ambient temperature, $C_v = C_{sat}(T_{amb})$, while in the surrounding air the concentration is $C_{amb} = HC_{sat}(T_{amb})$. Due to the solute presence in the solution and based on Raoult's law, the water vapour concentration at the droplet free surfaces is adjusted to be $C_{\Gamma} = X_{solvent}C_v$, where $X_{solvent}$ is the mole fraction of solvent. The no-flux and no-slip conditions are applied, i.e. $\mathbf{n}\cdot\mathbf{j} = 0$, and $\mathbf{u} = \mathbf{0}$ at the unwetted solid surfaces (i.e. vapour-solid boundaries), and the wetted solid surfaces (i.e. liquid-solid boundaries) as well. The inlet boundary of the air stream is defined to be the surrounding air concentration, and at a specified average velocity with the entrance length, $L_{entr} = 0.06ReD_H$, as well to satisfy the fully developed laminar flow. At the outlet of the air stream, outflow, i.e. $-\mathbf{n}.D_v\nabla C = 0$, and atmospheric pressure conditions are applied. As noted above, a periodic condition is applied to the left and right side boundaries of the domain to represent the semi-infinite physical domain.

As described previously in Chapter 3, the velocity and stress conditions at the droplet free surfaces are:

$$\mathbf{u}_g - \mathbf{u}_l = M_{H_2O}\left({}^{1}/_{\rho_g} - {}^{1}/_{\rho_l}\right)(\mathbf{j}_{\Gamma}\cdot\mathbf{n})\mathbf{n} \tag{7.6}$$

$$\mathbf{n}\cdot\boldsymbol{\sigma}_g - \mathbf{n}\cdot\boldsymbol{\sigma}_l = \gamma(\nabla\cdot\mathbf{n})\mathbf{n} \tag{7.7}$$

and the free surface shape evolves according to the displaced rate of each mesh node lying on the droplet surfaces:

$$\dot{\mathbf{x}}_{\Gamma} = (\mathbf{u}_l \cdot \mathbf{n})\mathbf{n} - \frac{(\mathbf{j}_{\Gamma} \cdot \mathbf{n})M_{H_2O}}{\rho_l}\,\mathbf{n} \tag{7.8}$$

Forced convection is the dominant mechanism in the surrounding air domain while the flow inside the salt solution droplets is caused by buoyancy-driven flow due to the variation of the solution density arising from the solute concentration gradient inside the droplets. Thus, the Boussinesq approximation, $(\rho_s - \rho_{s,o})g$, is used to represent the solution density variation in the body force term, i.e. $\Delta\rho g$, where $\rho_s = \rho_{s,o}[1 + \beta(\overline{c} - \overline{c}_{sol})]$ is the solution density as a function of the solute concentration. Note that, the Boussinesq approximation is also used in the air domain for the natural convection condition, as discussed previously in Chapter 3.

7.2.3 Input and geometrical parameters

For droplets evaporating in an isothermal convection environment, the physical parameters of fluids used, which are summarised in Table 7-1 [33], are constant at the temperature of the surrounding environment, T_a, unless specified otherwise. As considered previously in Chapter 5, three average air stream velocities, $U_{a,avg} = 0.02, 0.2 \text{ and } 2.0\ \mathrm{m/s}$, are chosen to investigate clearly the role of the forced convection environment on the internal dynamics within droplets. These velocities satisfy the fully developed laminar flow, and do not displace the droplets along the solid surface at this range of droplets size and contact angle [263, 268].

To extend the investigation of the role of the droplet separation distance in reducing the interaction between the droplets under the forced convection environment, a wide range of droplet distances is considered here, where the downstream droplet is shifted away from the leading droplet with a distance, S, starting from 3 mm up to 9 mm while the leading droplet is fixed at a distance from the entrance of the air domain, see Figure 7-1 (b). To achieve that, the size of the computational domain (i.e., the size of the unit flow) is increased (i.e. $\mathrm{W60\ x\ D20\ x\ H10}\ mm$) to allow examining the range of the separation distances under the conditions considered, as illustrated in Figure 7-2.

Table 7-1: Main parameters used in the present numerical model [33]**.**

Parameter	Air	NaCl solution
Environmental temperature, T_a, [°C]	20.0	20.0
Relative humidity, H, [%]	60	
Contact angle, θ, [deg.]		90
Droplet radius, R_d, [mm]		1.0
Water vapour diffusion coefficient, D_v, [m^2/s]		2.423×10^{-5}
Solution diffusion coefficient, D_s, [m^2/s]		1.6×10^{-9}
Initial solution density, $\rho_{s,o}$, [kg/m^3]		1038
Initial solution concentration, c_{sol}, [mol/m^3]		1000
Saturated water vapour concentration, C_v, [mol/m^3]		0.96
Mole fraction of solvent, $X_{solvent}$		0.965
Solution expansion coefficient, β, [m^3/mol]		3.7×10^{-5}

7.2.4 Model validation against experimental studies

To validate the predictions of the adopted numerical method, a very recent experimental study of Pradhan and Panigrahi [33] is chosen for comparison. Their experiments were conducted at 20℃ ambient temperature and 60±5% relative humidity with two droplets of volume 0.7μL (contact line radius of 0.69 mm and contact angle of 90°) placed on a siliconized cover slip with a 0.26 mm of separation distance. The droplets used are aqueous NaCl solution with 1M concentration. All data available for the NaCl solution droplets in the experimental and numerical study of Pradhan and Panigrahi [33] such as droplets radius, contact angle, solute concentration and environment conditions, are used in the numerical models to achieve accurate comparison results.

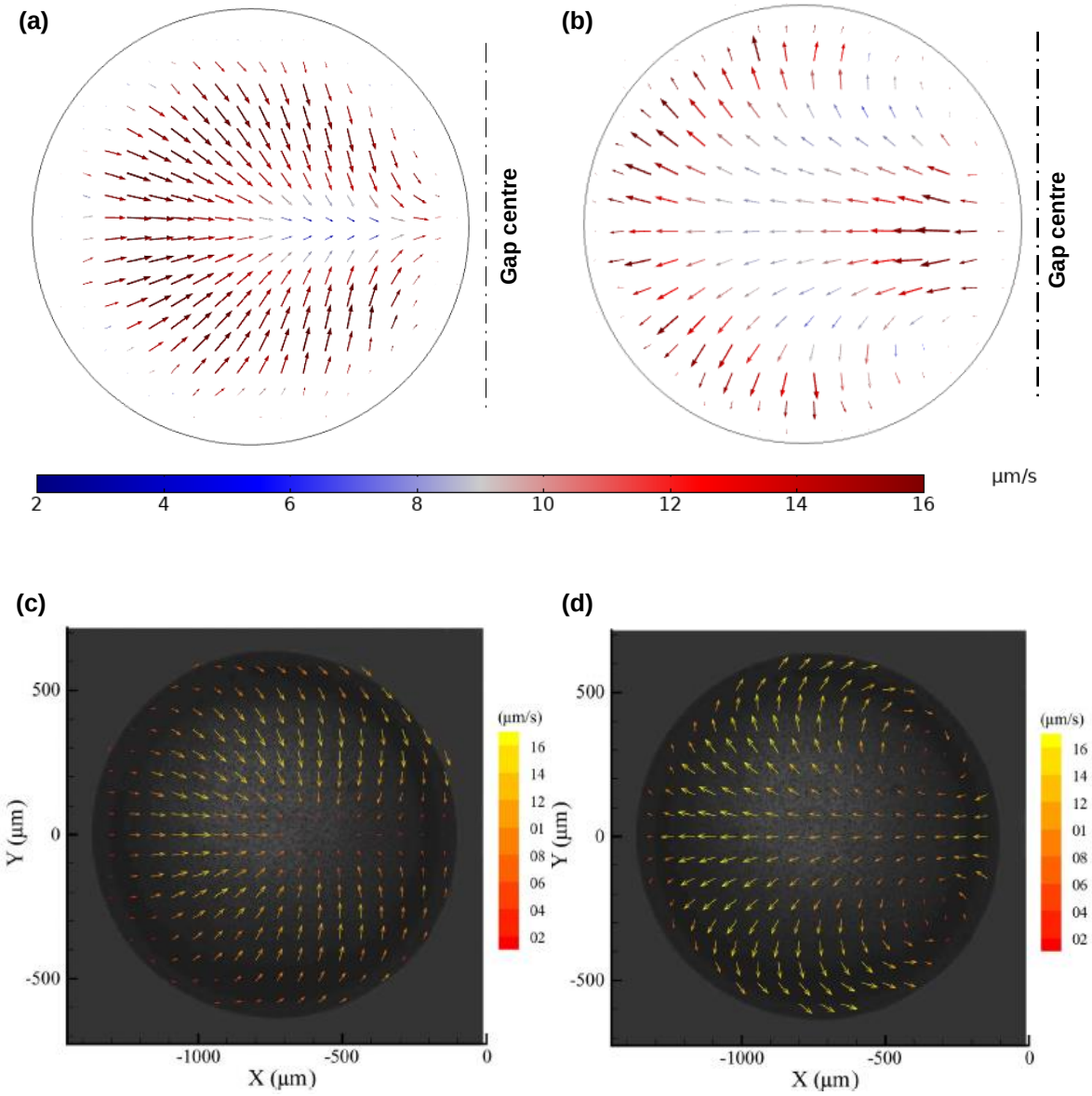

Figure 7-3: Comparison of the numerical results (a and b) with the experimental results of Pradhan and Panigrahi [33] (c and d) for the velocity vector field in horizontal planes inside the left-hand droplet of two adjacent droplets. The planes shown are at heights: (a and c) 50 μm and (b and d) 350 μm above the solid surface. Reprinted from ref. 31, Copyright (2020), with permission from Elsevier. License no. 4753641421455.

Figure 7-3 shows the comparison of the predicted results with the experimental results of Pradhan and Panigrahi for velocity vector field in horizontal planes at two different heights from the solid surface (i.e. 50 μm and 350 μm). Overall, it can be seen clearly that the simulation results are in a very good agreement with

their experimental observations, particularly at the height 350 μm from the solid surface as shown in Figure 7-3 (b and d). For the 50 μm height, see Figure 7-3 (a and c), there is a little difference in the flow field near the adjacent region between droplets since fluid flows towards the gap between droplets, as illustrated in Figure 7-3 (a). There is no clear reason for this behaviour except it might be due to the singularity at the contact line of the droplet.

7.3 Concentration distribution inside droplets under natural and forced convective environments

The developed isothermal diffusion-convection model, presented previously in this chapter, is used to study the internal dynamics and hence the distribution of the solute concentration within a pair of multiple salt solution droplets under forced convective environment and at various air speeds. Here, the evaporation of the droplets under a natural convective environment is considered as a baseline case, where the buoyant convection arising from density variations of fluids is considered both outside and inside the droplets. Figure 7-4 shows the distribution of the solute concentration at 300 s inside two droplets separated by a distance of 3 mm under different convective environments on a vertical plane passing through the droplet centres. It also illustrates a sketch of the flow patterns within the droplets, representing by the overlaid white arrows.

For natural convection, see Figure 7-4 (a), after the initiation of the evaporation process, the solute concentration increases at the droplet free surfaces due to liquid evaporation from these surfaces. As a result, a concentration gradient inside the droplets is created inducing buoyancy-driven natural convection (i.e., gravity-driven flow) inside the droplets, since an upward movement of the lighter fluid is observed along the droplet centres while the heavier fluid moves downwards along the droplet free surfaces. As observed previously in Chapter 6, the presence of an interacting neighbouring droplet reduces the evaporative flux in the gap between the droplets compared to the rest of the droplet surfaces, and hence lowers evaporation at this region. Consequently, an asymmetric distribution of the solute concentration arises about the z-axis where low solute

concentration is observable in the gap between the droplets compared to the farthest region of the droplets.

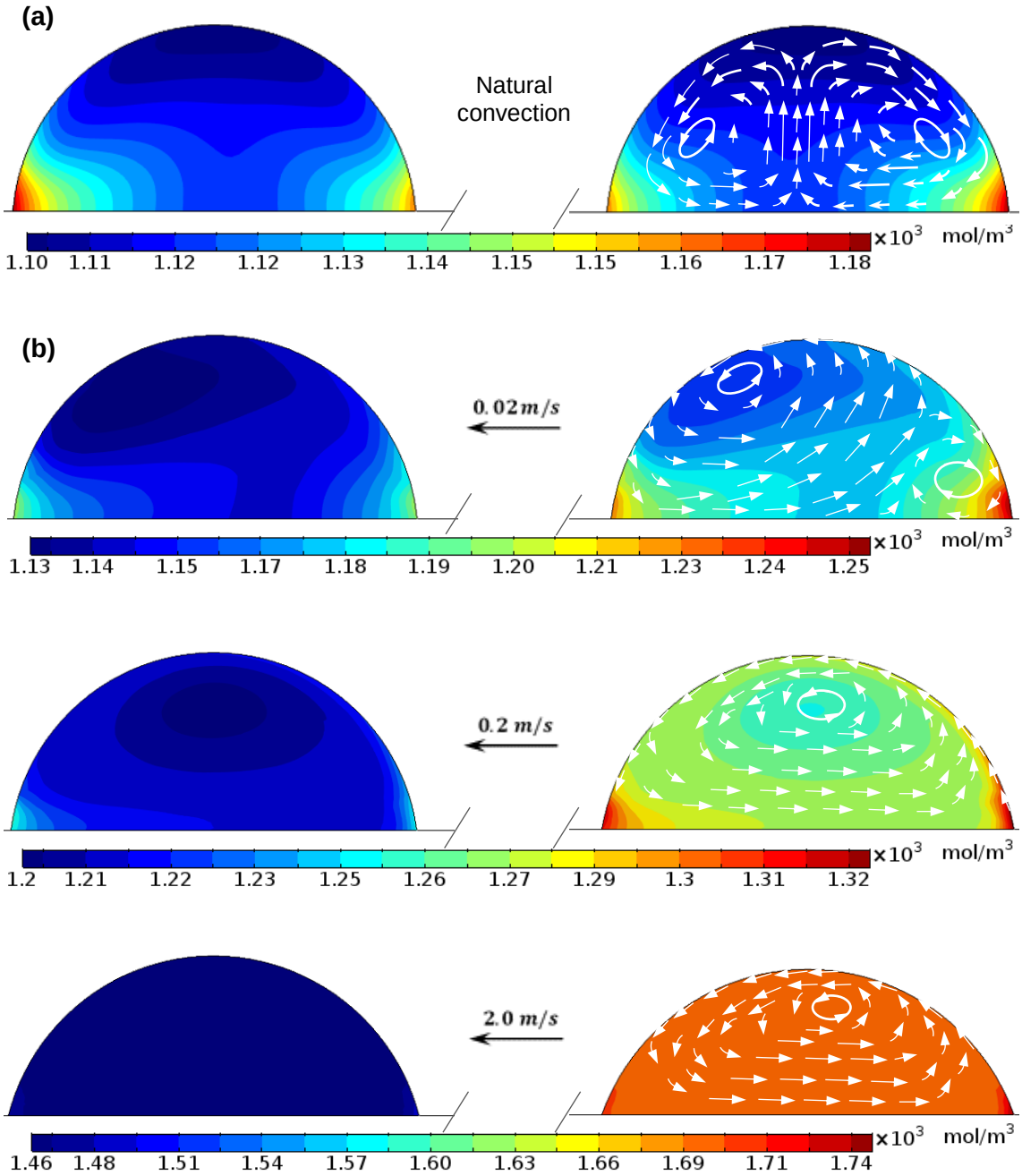

Figure 7-4: Contour plot of the solute concentration field (after 300 s) inside the droplets under (a) natural convection and (b) forced convection at various air speeds. The two droplets are separated by a distance, $S = 3.0\,mm$. The overlaid white arrows indicate the flow pattern but are not to scale.

Unlike the natural convection, in which the gravity-driven flow induced by the density increase with increasing salinity is the only mechanism controlling the internal dynamics within the droplets, the presence of a gentle force air convection gradually changes the flow and behaviour of the solute distribution inside droplets due to the shear-induced flow within the droplets arising from the passing air over the droplets as shown in Figure 7-4 (b), which illustrates the distribution of the solute concentration at various air stream velocities. Generally, it can be noticed from Figure 7-4 (b) that the solute concentration is higher near the upstream section of droplet surfaces, since the highest evaporative flux occurs at these regions. The solute concentration gradually decreases towards the apex region of the droplet surfaces, and then increases gradually towards the downstream contact-line regions, where there is also enhanced evaporation arising from the sharp gradients of the vapour concentration there. This can be attributed to the non-uniformity of the evaporative flux along droplet surfaces and effects of shear forces arising from the forced air convection which attempts to transfer the solute along the droplet surfaces.

At the lowest air speed, 0.02 m/s, the concentration distribution in the upstream droplet looks similar to that in droplets under natural convection, see Figure 7-4 (a), since the shear-induced flow is very small compared to the buoyancy-driven flow, and a clear non-uniformity in the solute distribution is observed. When the forced convection speed is increased tenfold to 0.2 m/s, the greater magnitude of the shear-driven circulation pushes the regions of non-uniform solute concentration closer to the contact lines. The average concentration level is also raised a little by the convection-enhanced evaporation. At the maximum speed considered, the shear-induced flow within the droplets dominates the gravity-driven flow, and is sufficient to ensure effective mixing of the solute inside the droplets. This results in much more uniform concentration fields in the two droplets (which is still observed when the contour scales are more focused than shown in Figure 7-4).

Considering the downstream droplet (left-hand droplet in Figure 7-4), it is very noticeable that the level of the solute concentration in the downstream droplet is significantly less than in the upstream droplet (right-hand droplet) at all air speeds

considered. This is because that the downstream water vapour transported from the upstream droplet increases the concentration levels of water vapour around the downstream droplet, and hence reduces the local concentration gradients and the associated evaporative flux, as observed previously in Chapter 6 for the parallel droplet arrangement section.

As expected, the faster air flow increases the evaporation rates of the droplets. However, there is a proportionally bigger increase in the evaporation rate of the upstream droplet, and consequently a proportionally bigger difference in the average concentration levels of the two droplets compared to the 0.2 m/s case. While the upstream droplet is exposed to ‘fresh’ air, the downstream droplet sits in the wake of the upstream droplet and consequently experiences both a shielding effect and raised surrounding vapour levels from the downstream water vapour transport, as mentioned previously in Chapter 6.

In parallel to the above findings, Figure 7-5 shows a similar illustration of Figure 7-4 in an attempt to reveal differences in the average concentration levels in the droplets at different environments, i.e. natural and forced convection. Here, a common scale of the solute concentration level is used in Figure 7-5. As can be seen in the natural convection environment, Figure 7-5 (a), the concentration levels in the two droplets are almost the same because of the symmetric water vapour space surrounding the two droplets. The presence of a gentle airflow at low speed, i.e. 0.02 m/s in Figure 7-5 (b), passing over these droplets increases slightly the differences in the concentration level inside the two droplets, which is consistent with the above observations. Again, this can be attributed to the downstream water vapour transported from the upstream droplet which influences the vapour space surrounding the downstream droplet, and hence the concentration gradients driving evaporation. At the highest air speed considered, the downstream transport strongly affects the downstream droplet evaporation, and hence larger differences in the concentration levels are observable inside the two droplets. Moreover, Figure 7-5 shows clearly the differences in the droplet size, which correspond to the higher concentrations as a result of faster evaporation.

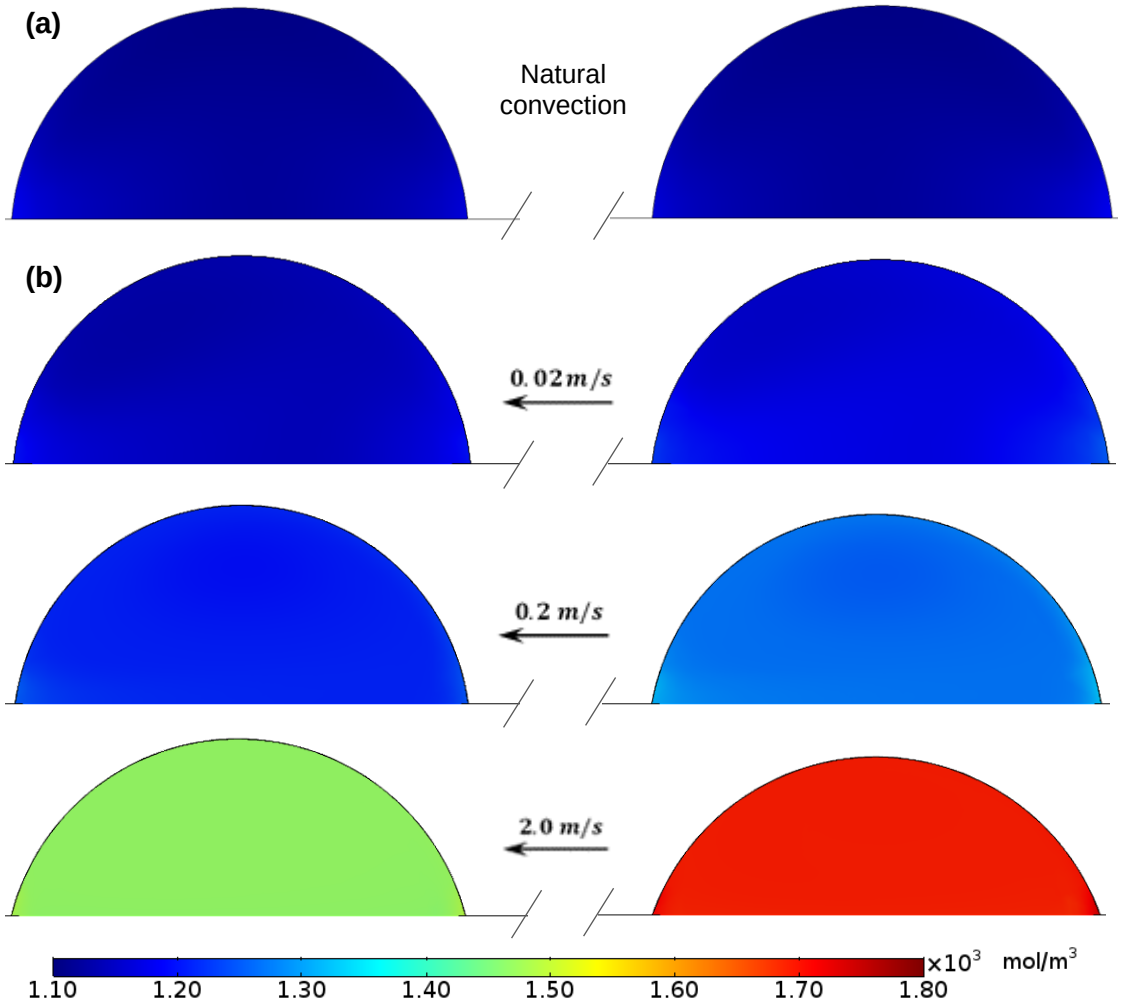

Figure 7-5: Contour plot of the solute concentration field (after 300 s) inside the droplets under different conditions: (a) natural convection and (b) forced convection at various air speeds. The two droplets are separated with a distance, $S = 3.0\ mm$. Note that an average concentration scale is used.

7.4 Flow field inside the droplets

As mentioned previously, the flow inside the droplets is due to the buoyancy-driven natural convection caused by the gradient of the solute concentration inside the droplets during evaporation. As noticed from Figure 7-6, which shows the velocity vector fields in the streamwise vertical plane through the centre of the droplets under different convective environments, the flow fields inside the

two droplets change significantly by switching from natural convection to the forced convection conditions.

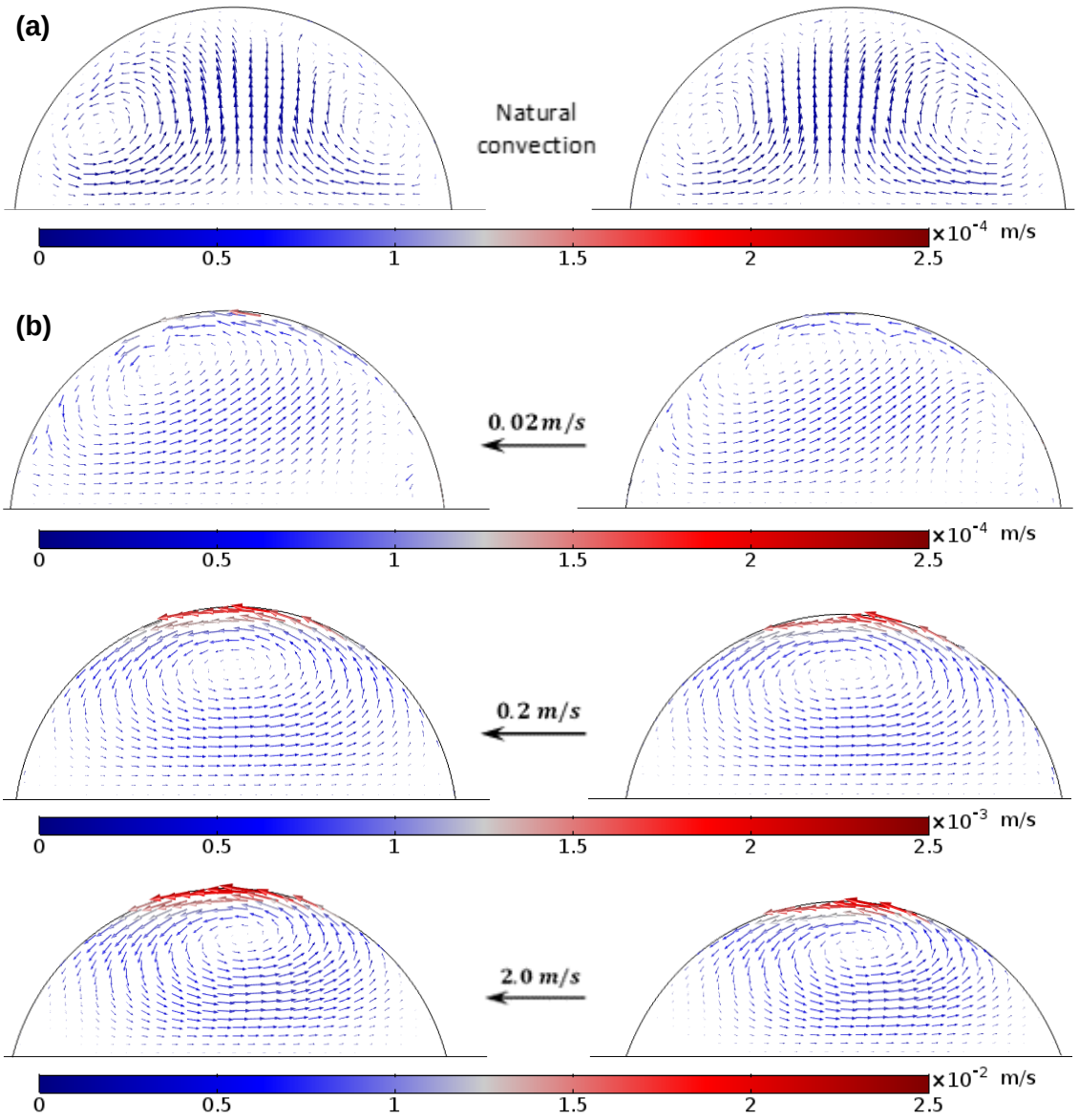

Figure 7-6: Velocity vector field in a streamwise vertical section through the centre of the droplets exposed to different environments (a) natural convection and (b) forced convection at various air speeds, considering the gravity effects within the droplets. The droplets are placed at separation distance, $S = 3\ mm$.

For natural convection, see Figure 7-6 (a), the flow fields are the same in the two droplets as water vapour space surrounding the two droplets is symmetric about the vertical z-axis between the two droplets. However, the flow behaviour is not symmetrical in each droplet as a result of the asymmetric solute distribution inside the droplet due to the presence of the interacting neighbouring droplet. Note that, the velocity vector field for natural convection is scaled by 2.5 more than actual scale to match the scale for the forced convection condition. Again, fluid with higher solute concentration moves downwards along the droplet free surfaces while the lighter fluid moves upwards along the droplet centres. Hence, an outward movement of fluid at the apex of the droplets and an inward flow near the solid surface are observable within the droplets, which is consistent with previous experimental and numerical predictions available in the literature [33, 283].

The shear-induced flow within droplets resulting from the presence of a gentle forced air convection passing over the droplets changes the flow behaviour inside the droplets, see Figure 7-6 (b). As can be seen at the lowest air speed considered, the centres of the two circulations produced within the droplets due the buoyant convection, Figure 7-6 (a), are shifted, inducing a circulation flow pattern within the droplets instead. Hence, a non-structured pattern of the velocity vector field is observed as a result of the competition between the buoyancy-driven flow and shear-induced circulation inside the droplets. As the air speed increased tenfold to 0.2 m/s, a very pronounced circulation flow pattern is observable within the droplets, and hence a structured pattern of the velocity vector is also produced within the droplets. At the highest air speed considered, the flow pattern becomes more structured since the shear-induced flow becomes more dominant, and the buoyancy-driven flow will be mostly negligible.

On further analysis of Figure 7-6, one can notice that the magnitude of the velocity vectors in the central region of the droplets and at the droplet apexes increases with increase the airflow velocity as a result of increasing the magnitude of the shear-induced flow inside the droplets. Note the difference in order of magnitude of the scale bars ($\times 10^{-4}$, $\times 10^{-3}$ and $\times 10^{-2}$ m/s). In each case the maximum speed of the flow inside the droplets induced by the passing air is approximately 1% of the air speed.

7.5 Internal dynamics inside the droplets under zero-gravity environment

The previous sections illustrated the distributions of the solute concentration and the flow patterns inside the droplets under different convective environments, i.e. natural and forced convection. The predictions show that under natural convection, the solute concentration gradient inside the droplets induces gravity-driven flow while a shear-induced flow caused by the passing forced air convection is produced inside the droplets as well. At some environments such as space station environments, i.e. zero-gravity environments, the gravity effects are negligible there and consequently, no-convection is observable both outside and inside the evaporating droplets in the absence of an external source of convection. Hence, the solute distribution and flow pattern inside the droplet become different from when the gravity effects are considered. In this section therefore, the evaporation of salt solution droplets under such environment is performed to provide a clear understanding of the role of the gravity in changing the internal dynamics inside the droplets. Here, the convection mass transfer effects and the body force terms are neglected from Equations (7.1) and (7.3), respectively, and the droplet evaporation is driven only by diffusion.

Figure 7-7 shows the distribution of the solute concentration at 300 s inside the droplets separated by a distance of 3 mm in a vertical plane containing both droplet centres under zero-gravity effect condition. The solute distribution inside the droplets under normal-gravity environment (i.e. natural convection), discussed in previous sections, is also illustrated in Figure 7-7 as a reference case for comparison. For zero-gravity condition, a different pattern of the solute concentration field is found inside the droplet as shown in Figure 7-7 (a) compared to the distribution pattern within the droplets under normal-gravity condition, Figure 7-7 (b). An almost concentric pattern of the solute distribution is created inside the droplets with slight change in the solute concentration along the droplet free surfaces with time, as a result of the diffusion of water vapour through the droplet free surfaces via evaporation. In addition, a little increase in the average concentration levels between the two cases is observed due to the role of the gravity effects within the droplets. Again, the presence of an interacting

neighbouring droplet leads to reduction in the solute concentration in the gap between the droplets, and non-uniform distribution of solute concentration is observable within the droplets. Further, no flow pattern is observed within droplets under zero-gravity condition compared with the flow pattern observable within droplets, as illustrated by the overlaid white arrows, in the normal-gravity condition.

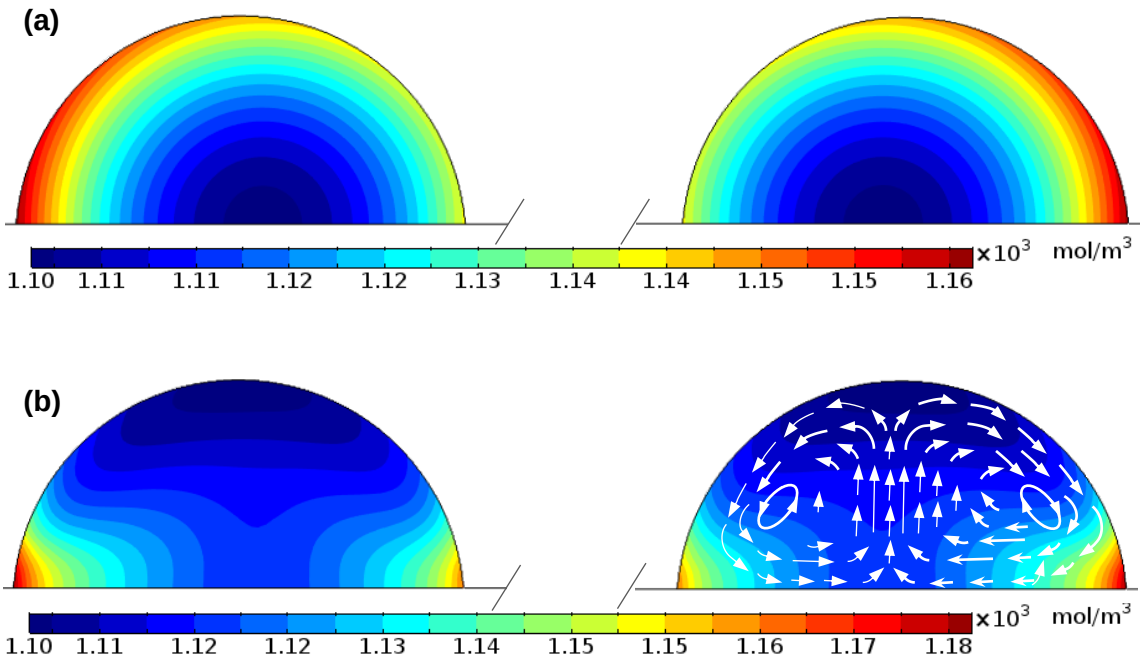

Figure 7-7: Contour plot of the solute concentration field (after 300 s) inside the droplets under natural convection with different conditions: (a) zero-gravity condition; (b) normal-gravity condition. The two droplets are separated by a distance, $S = 3.0\,mm$. The overlaid white arrows indicate the flow pattern but are not to scale.

Further qualitative comparison, Figure 7-8 shows the distribution of the solute concentration (after 300 s) on the vertical centre plane passing through the upstream and downstream droplets, with view looking perpendicular to the direction of flow, at 3 mm separation distance and under various air stream velocities. Here, the gravity-driven flow inside the droplets is neglected as considering the space station conditions (zero-gravity environment) while the forced air convection still drives the flow in the surrounding air domain.

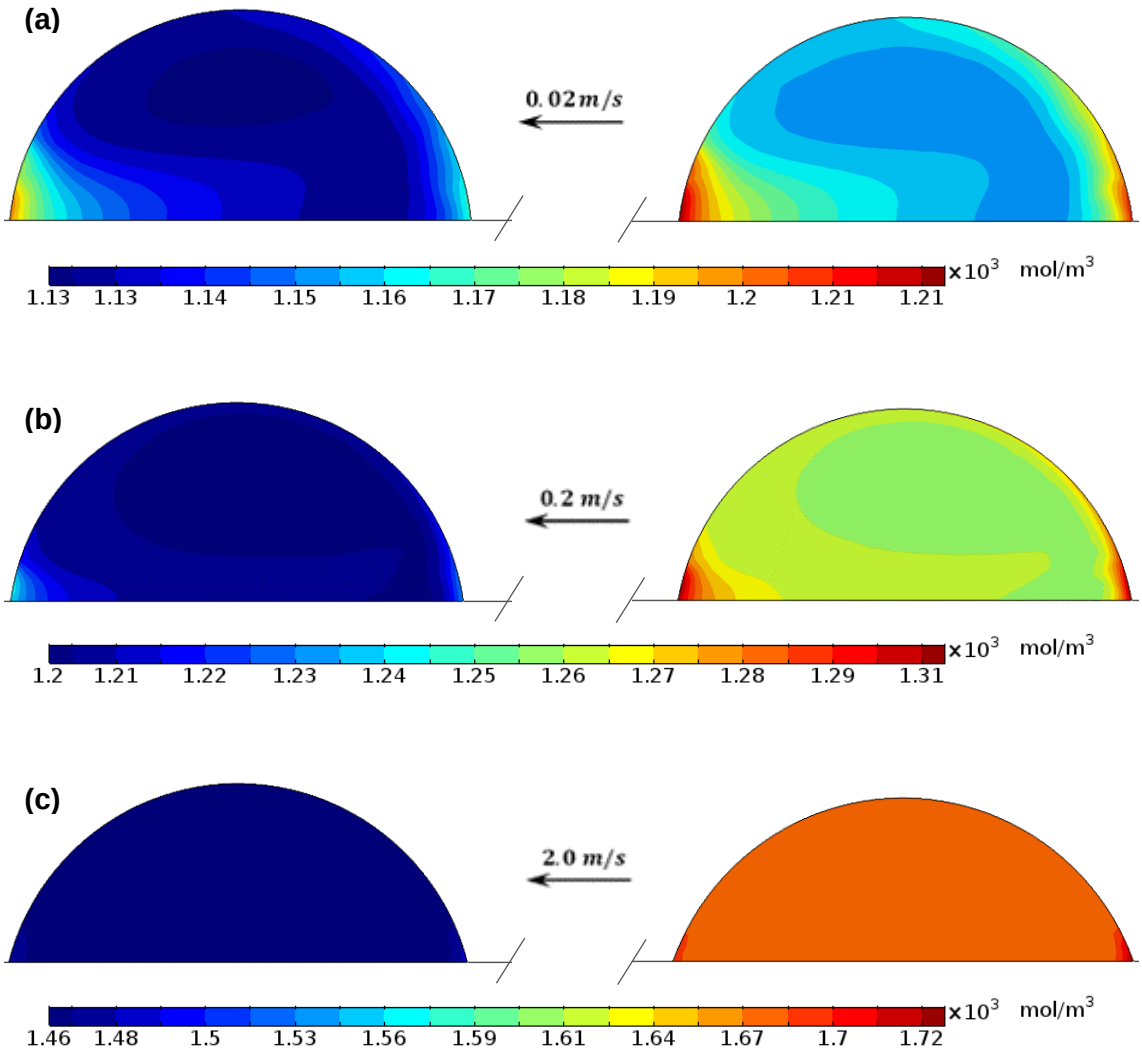

Figure 7-8: Contour plot of the solute concentration field (after 300 s) inside the droplets under forced convection, and at various air speeds: (a) 0.02 m/s, (b) 0.2 m/s, and (c) 2.0 m/s. The two droplets are separated with a distance, $S = 3.0\ mm$. Here, the zero-gravity condition is considered.

It is very clear to observe the differences in the solute distribution inside the droplets compared to the results of Figure 7-4. As there is a competition inside the droplets between the buoyancy-driven flow and shear-induced flow when gravity effects are considered, the shear-induced circulation arising from the passing air is the only mechanism drives the flow within the droplets in the zero-

gravity environments. This is very noticeable at the lower air speeds, 0.02 m/s and 0.2 m/s in Figure 7-4 (b) and Figure 7-8 (a and b), that the shear-induced flow is still insufficient to mix the solute effectively inside the droplets. At the highest air speed considered, 2.0 m/s in Figure 7-4 (b) and Figure 7-8 (c), there is no noticeable difference in the solute distribution between the two cases and uniform distribution of the solute inside the droplets as a result of the sufficient role of the shear-induced circulation to ensure effective mixing of the solute within the droplets.

Further comparison with the results of considering the gravity effects inside the droplets shown in Figure 7-6 (b), Figure 7-9 shows the velocity vector field inside the upstream droplet when zero-gravity condition is considered. It can be seen clearly that the flow pattern is more structured than within the droplets in Figure 7-6 (b) at the lowest air speed considered. This can be attributed to the absence of the competition with the gravity-driven flow as the shear-induced flow is the only mechanism controls the flow pattern inside the droplets. As the air speed is increased to 0.2 m/s, there is a little increase in the magnitude of the velocity vector in the central region of the droplet as the gravity effects are still negligible within the droplets. At the highest air speed considered, as the shear-induced flow becomes more stronger, there is no noticeable change in the flow pattern whether the gravity effects are considered or not inside the droplets. Again, the same difference in order of magnitude of the scale bars is noticed in Figure 7-9 as it is in Figure 7-6, and the maximum speed of the flow inside the droplets in each case is approximately 1% of the air speed.

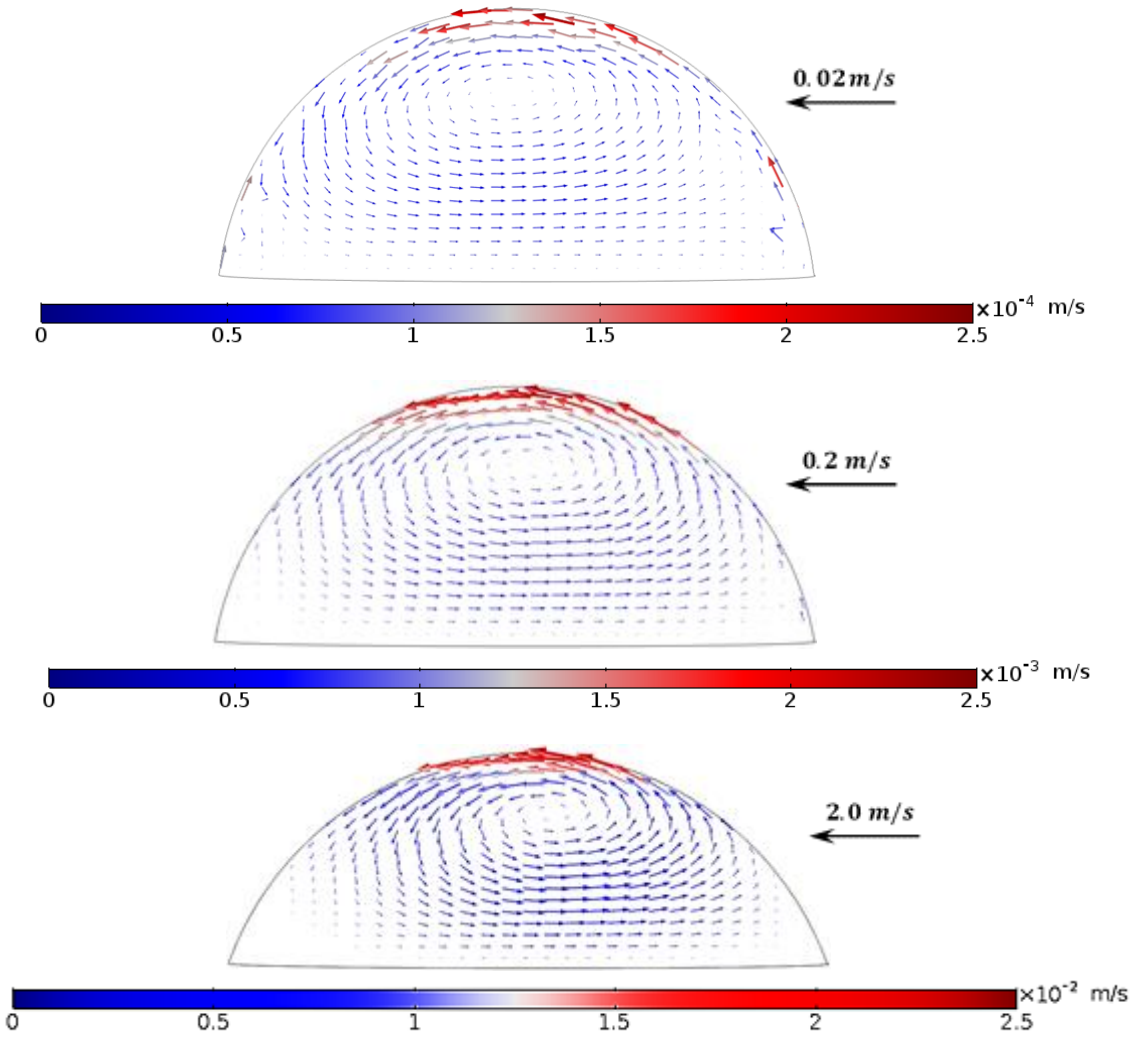

Figure 7-9: Velocity vector field in a streamwise vertical section through the centre of the upstream droplet exposed to various air speeds in the case of zero-gravity condition considered. The separation distance between the upstream and downstream droplets is 3 mm.

7.6 Solute distribution on the solid surfaces inside the droplets

To give a clear idea of the influence of the forced air convection on the solute distribution pattern on the solid surface inside the droplets, Figure 7-10 illustrates an overhead view of the solute concentration field and the corresponding flow field, as represented by the overlaid arrows, at 300 s on the solid surface inside the two droplets and at different surrounding environments, i.e. natural and forced convection. Note that the flow field inside the droplets is constructed in a parallel

plane to the solid surface with a height of 50 μm as there is no flow field on the solid surface, since the no-slip boundary condition applies there. In addition, the gravity effects are now included again in this section.

As mentioned previously, in the natural convective environment, an asymmetric solute distribution and hence flow pattern are induced within the droplets due to the low solute concentration convected towards the gap between the two droplets compared to the rest regions of the droplets, as a result of the lower evaporative flux at this region, as shown in Figure 7-10 (a). Again, the flow fields are the same in the two droplets with an inward flow near the solid surface, which agrees well with the previous results in this chapter.

For the forced air convection, as observed previously in Chapter 6, the two droplets are no longer exposed to the same air stream since the downstream droplet evaporates in the lee of the upstream droplet. Hence, different levels of the solute concentration on the solid surfaces are noticeable inside the two droplets. Further, the presence of the forced air convection changes the internal dynamics inside the droplets and hence the solute distribution on the solid surface compared to the natural convection case, as shown in Figure 7-10 (b). In addition, higher solute concentration on the upstream section of the solid surface is noticed compared to the downstream section of the solid surface as a result of the highest evaporative flux there.

At the lower speed, 0.02 m/s in Figure 7-10 (b), it can be seen clearly that due to the contribution effects of both the gravity-driven flow and shear-induced circulation inside the droplets a non-uniform distribution of the solute concentration is observed within the droplets. The movement of the velocity vector field towards the upstream section of the droplets is more than in the natural convection case due to the role of the shear-induced circulation inside the droplets arising from the passing air. As the air speed is increased to 0.2 m/s, the role of the gravity-driven flow becomes less compared to the shear-induced circulation, and hence more uniformity in the solute distribution is observed on the sold surfaces, particularly on the side of the solid surfaces.

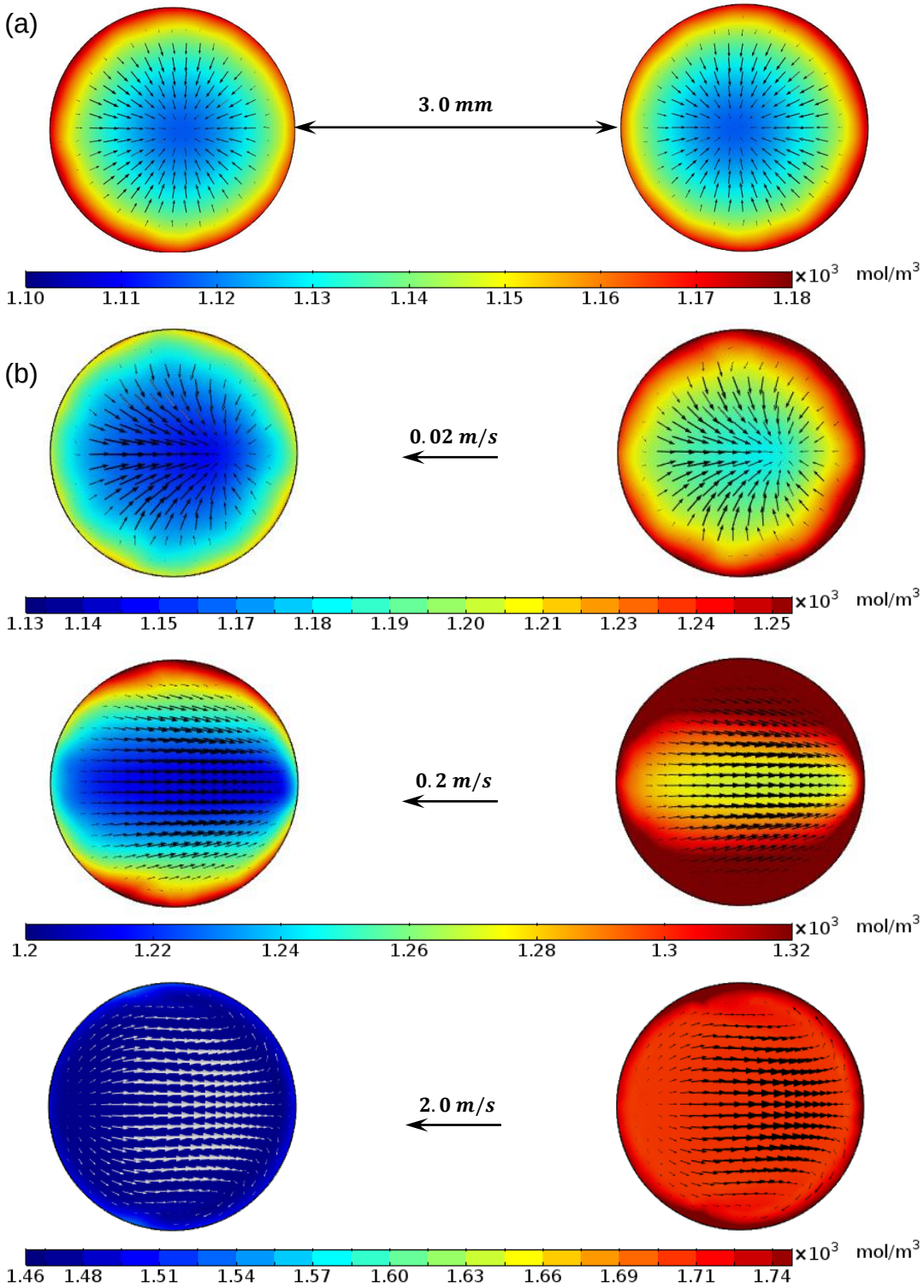

Figure 7-10: The solute concentration distribution on the solid surface (after 300s) within droplets in the case of: (a) natural convective environment; (b) forced convective environment at various air speeds, and at separation distance, $S = 3\,mm$. The overlaid arrows indicate the flow field on a plane parallel to the solid surface with a height of 50 μm.

At the highest air speed considered in Figure 7-10 (b), the distribution of the solute concentration becomes much more uniform on the solid surfaces due to the dominant effect of the shear-induced circulation compared to the gravity-driven flow which is mostly negligible. The great role of the shear-induced circulation inside the droplets is able to ensure sufficient mixing of the solute within the two droplets. However, one can notice a small region of non-uniform distribution of the solute concentration near the downstream section of the droplets. This can be attributed to the presence of a weak circulation flow at this region which is clearly shown in Figure 7-11. Figure 7-11 illustrates the resulting velocity vector field on the free surface of the upstream droplet at the highest air speed. On further analysis of Figure 7-11, it is very clear to see the structured pattern on the velocity field on the droplet free surface as a result of the great value of the shear-induced flow caused by the forced air flow compared to other mechanisms considered i.e., Stefan flow.

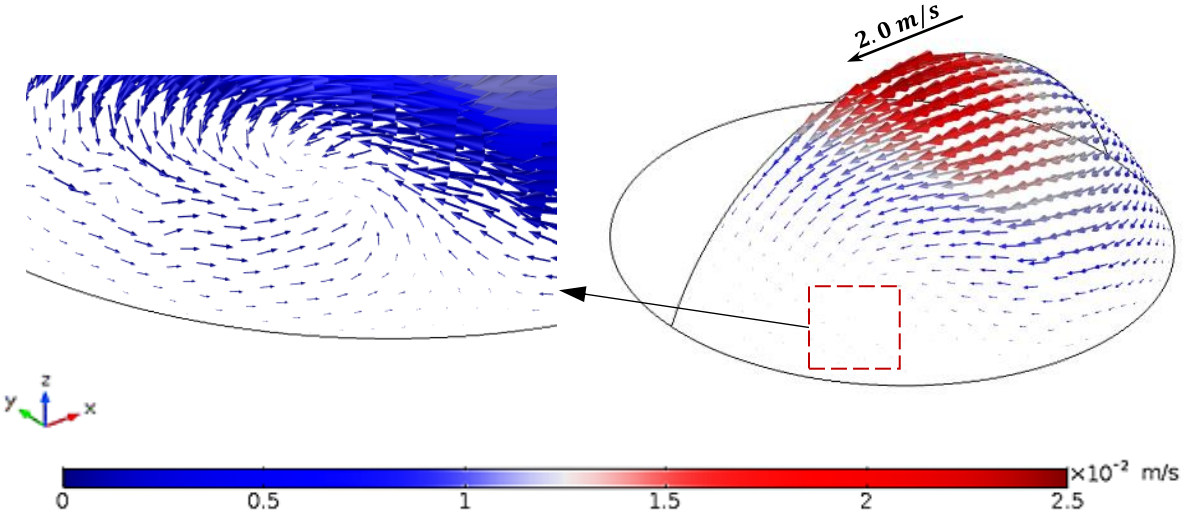

Figure 7-11: 3D view of the velocity vector field on the free surface of the upstream droplet at $2.0\ m/s$ air speed and 3.0mm separation distance. The scale of the velocity vector field in the inserted plot is increased to 6 times.

7.7 Effect of droplet separation

The previous observations, discussed in Chapter 6, showed that when a droplet evaporates in the lee of an upstream droplet under a forced air convection, the separation distance between those droplets plays a slight role in reducing the influence of the downstream water vapour transported from the upstream droplet via the passing air compared to other droplets arrangements. This role decreases as the air stream velocity is increased, and therefore larger separation distances are needed to reduce this interaction, particularly at higher air speeds. As mentioned earlier in this chapter, a range of droplet separations, i.e., 3 mm up to 9 mm, is considered here for the purpose of investigating this effect.

Given the clear differences in evaporation rates and associated solute concentration levels inside the droplets, a natural question to ask is how does the larger droplet separation affect this difference? Figure 7-12 shows an extended version of Figure 7-5 in an attempt to create a parameter space ‘map’ illustrating the effects of both air speed and droplet separation distance on the solute concentration levels inside the upstream and downstream droplets. The top row corresponds to the separation considered earlier in this chapter, and the air flow is from right to left. Note that a common scale of the solute concentration level is used. Clearly this does not allow simultaneous detailed observation of the uniformity of solute concentration within individual droplets, but it is effective in revealing differences in the average solute concentration levels inside the droplets. As noted earlier, higher air speeds produce better uniformity in individual droplets, and this is true at all separations.

As can be seen in Figure 7-12, increasing the separation of the droplets does help to reduce the difference in the solute concentration levels (indicative of evaporation rates) inside the pairs of droplets at a given air speed. At the lowest air speed, 0.02 m/s, the solute concentration levels are almost the same inside the two droplets as a result of the downstream advection from the upstream droplet being still insufficient to affect the downstream droplet significantly. As the air stream velocity is increased to 0.2 m/s, the difference in the solute concentration levels is increased due to increase in the influence of the downstream water vapour transported from the leading droplet. At the highest air

speed considered, however, the strong downstream transport of water vapour from the upstream droplet is still able to influence the vapour space surrounding the downstream droplet, and hence the concentration gradients driving evaporation, even at the largest separation distance considered. Hence, a great difference in the solute concentration levels inside the droplets is observed at the highest air speed.

Clearly, for parallel droplets arrangement, the downstream advection from the upstream droplet is still able to influence the evaporative behaviour and hence internal dynamics inside the downstream droplet, particularly at higher air speeds, and even at larger droplet distances. Therefore, different droplet arrangements should be considered within an array of multiple droplets evaporation, which will be discussed further in the next chapter.

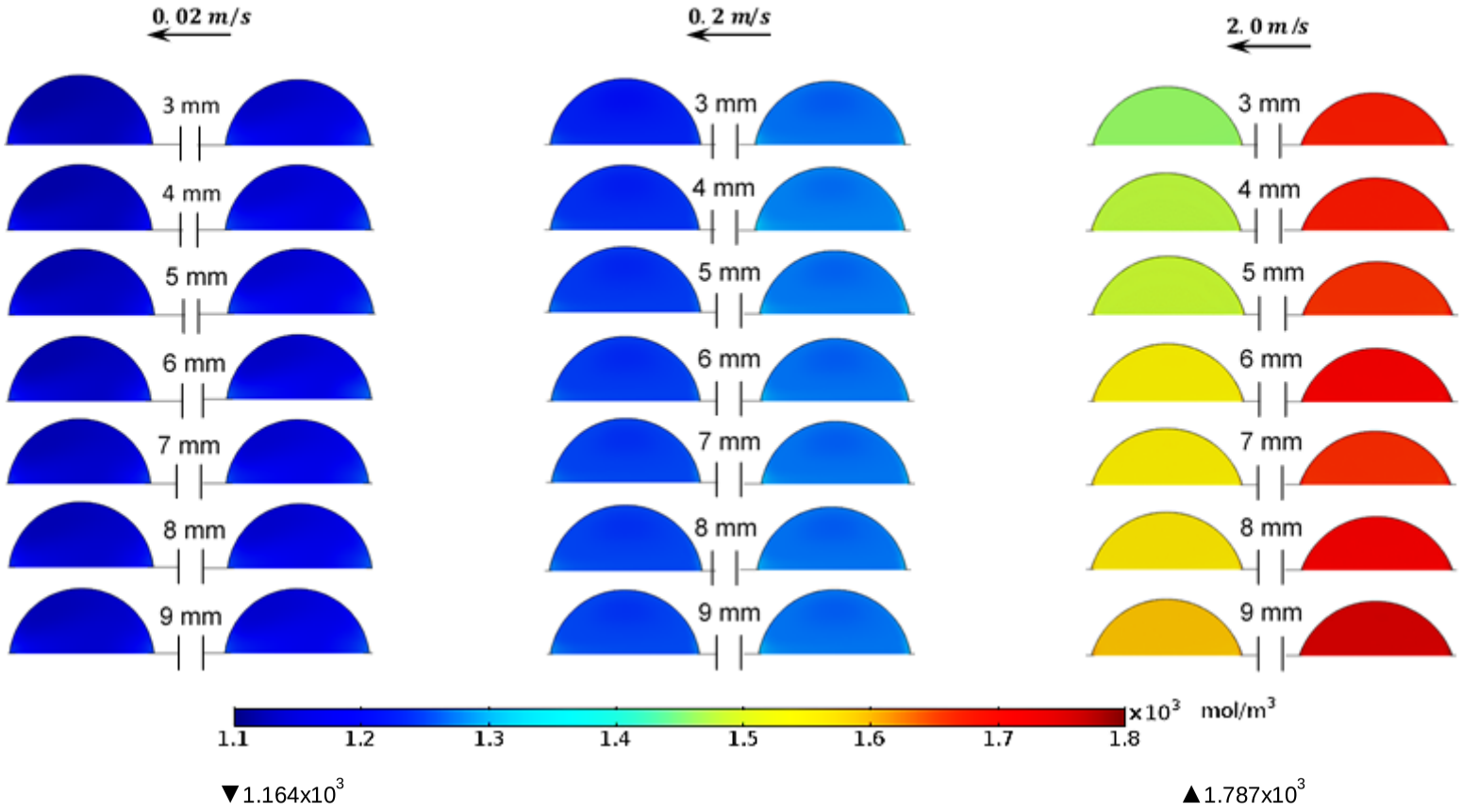

Figure 7-12: A parameter 'map' showing the effects of forced convection speed and droplet separation on the concentration levels in each droplet after 300 s of evaporation. The symbols ▼ and ▲ represent the overall minimum and maximum values of solute concentration (in mol/m^3), respectively.

7.8 Conclusions

The developed numerical model is adopted to study the evaporation process of multiple salt solution droplets, and examine the internal dynamics inside the droplets under various air convection speeds and droplet separation distances.

Numerical observations for the distribution of the solute concentration inside the droplets show that the passing air convection over the droplets causes a shear-induced circulation inside the droplets unlike the natural convection in which increasing density with increasing salinity induces a gravity-driven flow inside the droplets. Hence, fluid with higher solute concentration moves downwards along the droplet free surfaces while the lighter fluid moves upwards along the droplet centres. As a result, a clear non-uniformity in the solute distribution is observed within the droplets, particularly at the lower air speed. As the air speed is increased, the greater magnitude of the shear-driven circulation pushes the regions of non-uniform solute concentration closer to the contact lines until the highest air speed, where much more uniform concentration fields are observable inside the droplets as a result of the dominance of the shear-induced flow over the gravity-driven flow which is mostly insufficient. Further, the maximum speed of circulation flow pattern inside the droplets caused by the forced air convection passing the evaporating droplets is approximately 1% of the forced air speed.

Considering the presence of an interacting neighbouring droplet in the natural convection case, the distribution of the solute concentration is symmetric around the vertical z-axis between the droplets since the water vapour space surrounding each droplet is similar while an asymmetric distribution in the individual droplet is observed around the central vertical axis inside the droplets due to the interaction in the gap between the droplets. Unlike the natural convection, in the forced convection case, the solute concentration level in the downstream droplet is less than in the upstream droplet due the downstream water vapour transported from the upstream droplet.

For zero-gravity environment, results show different patterns of the solute distribution inside the droplets compared to the normal-gravity environment since an almost concentric pattern of the solute distribution is found inside the droplets

with a slight change in the solute concentration along the droplet free surfaces with time. Moreover, a small difference in the solute distribution is observable inside the droplets exposed to a slower airflow in the zero-gravity environment compared to that in the normal-gravity environment as a result of the absence of buoyancy-driven flow with the shear-induced flow arising from the passing air in driving the solute distribution pattern within the droplets. At the higher air speed, as the shear-induced circulation becomes dominant, there is no noticeable difference in the solute distribution between the normal-gravity and zero-gravity environments.

Observations also show different patterns of the solute distribution on the solid surfaces within the droplets corresponding to the convection environment considered. An asymmetric solute distribution inside the droplets with less concentration near the gap region is observed in the natural convection condition, while higher solute concentration on the upstream section of the solid surface compared to the downstream section is observed in the lower speeds of the forced convection. At the highest air speed, a much more uniform distribution of the solute on the solid surfaces arises due to the dominant effect of the shear-induced circulation inside the droplets.

Finally, the numerical results reveal that the larger separation distance between the parallel droplets is still unable to eliminate the influence of the downstream advection from the upstream droplet on the evaporative behaviour and hence internal dynamics inside the downstream droplet, particularly at the higher air speeds, while the separation distance has an influential effect in the lower level of air speeds.

Chapter 8 Effects of staggered droplet placements

8.1 Introduction

As noted earlier in this thesis, the evaporation of an array of multiple sessile droplets on a semi-infinite solid surface is a fundamental process involved in many scientific and practical applications such as protein-crystal-growth [290], DNA/RNA microarrays [291], ink-jet printing [21], biomedical and pharmaceuticals [16, 164]. Understanding experimentally the internal dynamics, including the fluid flow pattern and concentration field inside such array of droplets is a considerable challenge and difficult because of many hydrodynamics which are mutually coupled. Therefore, a numerical modelling is desirable, which can provide a quicker and cheaper approach to investigate new ideas before doing experiments, and the capability to 'steer' experiments efficiently [236, 292].

The previous chapter examined the influence of the forced air convection on the evaporation of salt solution droplets. The droplets were arranged such that the downstream droplet lies directly behind the upstream droplet with respect to the direction of the airflow. Hence, the second droplet is placed only downstream of the leading droplet with a given distance. However, results showed that the second droplet remains coupled with the first droplet by the downstream vapour transport from the leading droplet even at large droplet separations.

This chapter, therefore, focuses more on expanding previous predictions by staggering the position of the downstream droplet with respect to the upstream droplet, so that it is displaced both laterally and downstream as shown in Figure 8-1. The effect of such droplet arrangements on the solute distribution on solid surfaces, the evaporative behaviour of the downstream droplet, and the concentration field around the droplets and across the array are investigated as well in this chapter. For achieving the goal of this chapter, the mathematical model and numerical approach used here are the same as described in Chapters 3 and 7, with fluid properties the same as given in Chapter 7, see Table 7-1.

Key	Description
W	Width of a unit cell
D	Depth of a unit cell
D1	Lead droplet
D2	Downstream droplet
S	Downstream droplet distance from the lead droplet in air flow direction

Key	Description
W	Width of a unit cell
D	Depth of a unit cell
D1	Upstream droplet
D2	Downstream droplet
S_D	Downstream droplet distance
S_L	Lateral droplet distance

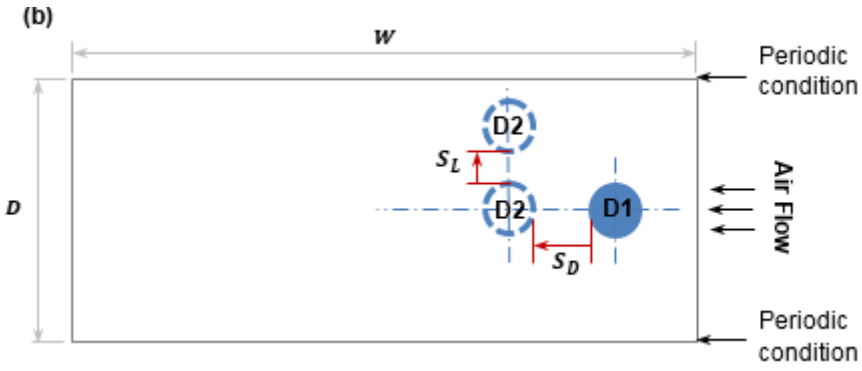

Figure 8-1: (a) Schematic of a regular array of multiple sessile droplets. The area between lines A-B represents a unit flow defined in Chapter 7. (b) A plan view of the unit flow which illustrates two neighbouring sessile droplets with staggered arrangements related to the air stream path inside a semi-infinite isothermal forced convective environment. Here, D1 and D2 represent the upstream and downstream droplets, respectively.

8.2 Input and geometrical parameters

Here, as used in Chapter 7, droplets of aqueous NaCl solution with initial volume 2.1 µL (i.e., contact radius, $R_d = 1mm$, and contact angle, $\theta = 90^{\circ}$) and 1 M concentration are used in the current numerical work to investigate the evaporation of these droplets under an isothermal forced airflow. The models are run for a period of 300 s.

Figure 8-1 illustrates the three-dimensional diagram of the regular array of multiple sessile droplets, and the plan view of the unit flow, which is defined to represent two droplets aligned parallel with the airflow and sitting on a semi-infinite solid surface. Here, as considered previously in Chapter 7, three average air stream velocities, $U_{a,avg} = 0.02, 0.2 \text{ and } 2.0 \text{ m/s}$, are chosen to investigate

clearly the effects of the staggered droplet placements under a forced convective environment on the internal dynamics within droplets and evaporative behaviour of the droplets. This range of air stream velocities satisfies the fully developed laminar flow, and do not displace the droplets along the solid surface at this range of droplets size and contact angle [263, 268].

As in Chapter 7, the position of the upstream droplet is fixed at a distance from the entrance of the air stream while the downstream droplet is positioned downstream of the leading droplet by a 'downstream distance' S_D, which is varied from 3 mm to 9 mm. In order to investigate the possibility of different configurations of droplets arrangements, at each value of S_D, the downstream droplet is also shifted laterally, i.e., perpendicular to the airflow, by a 'lateral distance' S_L, as illustrated in Figure 8-1 (b). The lateral distance should be reasonable such that the downstream droplet would not be influenced by a neighbour droplet in the next unit flow.

8.3 Concentration field surrounding the droplets

In the previous chapter, it has been demonstrated that increasing the separation distance between the droplets from 3 mm to 9 mm in the airflow direction is not sufficient to eliminate the influence of the downstream water vapour transported from the upstream droplet on the downstream droplet, particularly at higher air speeds. Hence, the downstream droplet is still coupled by the downstream advection from the lead droplet. This indicates the need of further larger downstream distances or different droplet arrangement configurations to achieve this aim.

Figure 8-2 shows overhead contour plots of the concentration field surrounding the upstream and downstream droplets at the lowest air speed considered, 0.02 m/s, and for various lateral and downstream droplet distances. Generally, it can be seen clearly that as the downstream droplet is shifted laterally, more of the downstream droplet becomes exposed to the passing airflow, and the evaporation rate increases accordingly. In addition, as the lateral separation distance between the droplets, S_L, is increased from 1 mm to 5 mm at a given downstream distance, S_D - see each row of Figure 8-2, the shielding effect of the

upstream droplet on the downstream droplet decreases. This can be attributed to the fact that the combination of air speed and lateral distance can effectively reduce the vapour concentration around the droplets, as observed previously in Chapter 6 for the perpendicular droplet arrangement. Alternatively, increasing the downstream separation distance at a given lateral distance, as illustrated in each column of Figure 8-2, has a more significant effect in lowering the vapour concentration between the droplets, but it is still insufficient to isolate the droplets. Thus, the two droplets remain coupled by the downstream advection from the upstream droplet. Further, it is very easy to notice that at the largest lateral distance considered, $S_L = 5\,\mathrm{mm}$, although the downstream droplet is still overwhelmed by the diffused water vapour transported from the upstream droplet, the interaction between the droplets is reduced significantly, particularly at the largest downstream distance $S_D = 9\,\mathrm{mm}$, as shown in the third column of Figure 8-2.

It is worth recalling that periodic conditions are applied in this problem, to represent the transverse array of droplets shown in Figure 8-1 (b). As observed from Figure 8-2, at the lowest air speed, there is a noticeable transverse diffusive transport of water vapour, which will affect the evaporation rates of the droplets in the domain, particularly at small domain widths. This transversal effect of the diffusive transport water vapour increases significantly as the lateral distance is increased, and hence the droplets in the domain will be coupled together by the diffusive transport within the array.

For the middle and highest air speeds considered, the observed results show that although the 1 mm lateral distance does help in reducing the interaction between the droplets, the downstream droplet is still coupled by the downstream advection from the leading droplet even at the largest downstream distance considered. Further, its effects are very similar for zero lateral distance, i.e., the two droplets are aligned parallel on a line passing through the centre of the two droplets, as illustrated previously in Chapter 7. Therefore, the 3 mm and 5 mm lateral separation distances are considered only to illustrate the concentration field surrounding the upstream and downstream droplets at 0.2 m/s and 2.0 m/s air speed, while the downstream distance varies from 3 mm to 9 mm, as shown in Figure 8-3 and Figure 8-4.

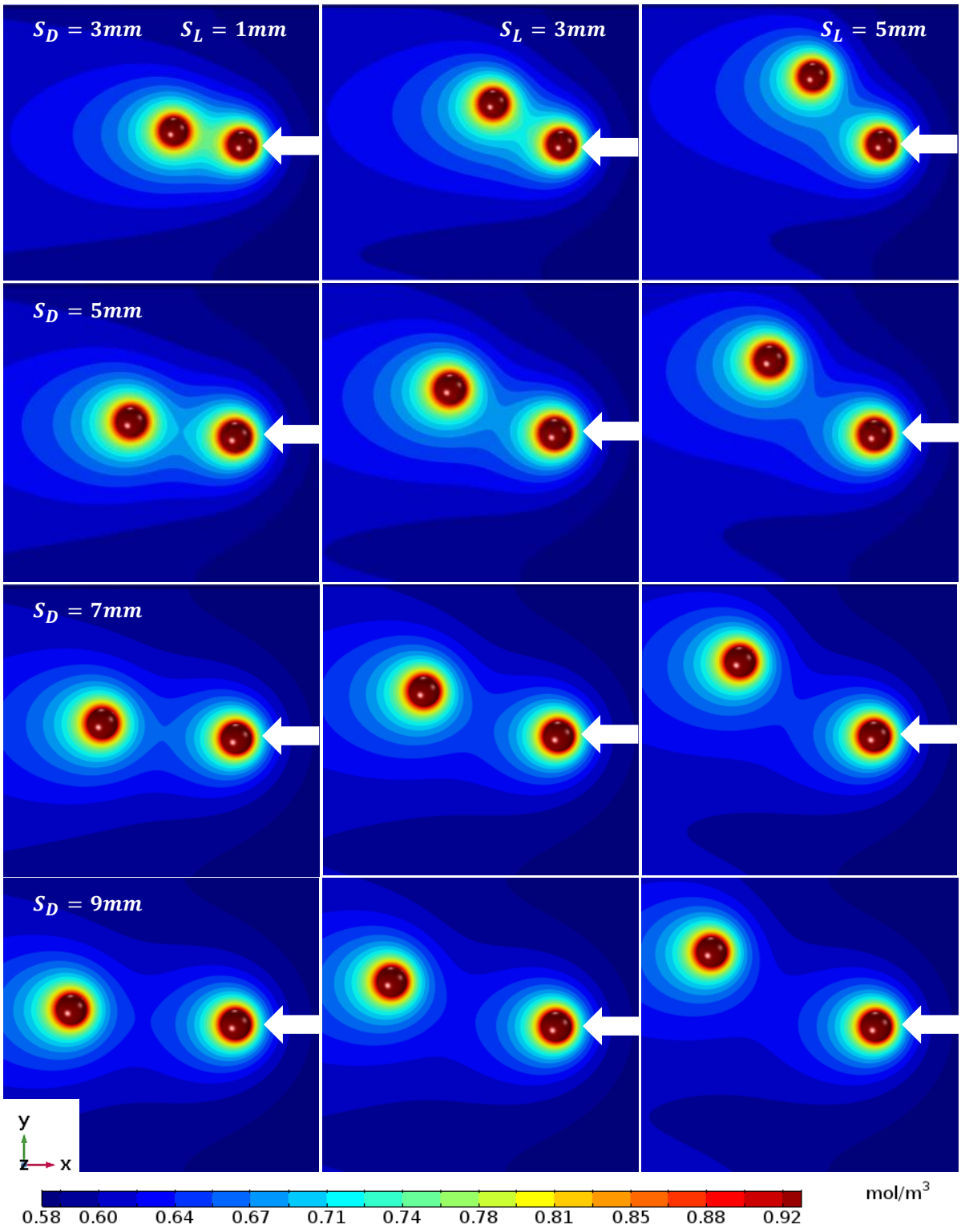

Figure 8-2: Contour plot of water vapour concentration on the bottom surface of the domain (after 300 s) at 0.02 m/s air speed and different downstream distances, S_D. The first, second and third columns are for S_L of 1, 3, 5 mm, respectively. The white arrow represents the direction of airflow.

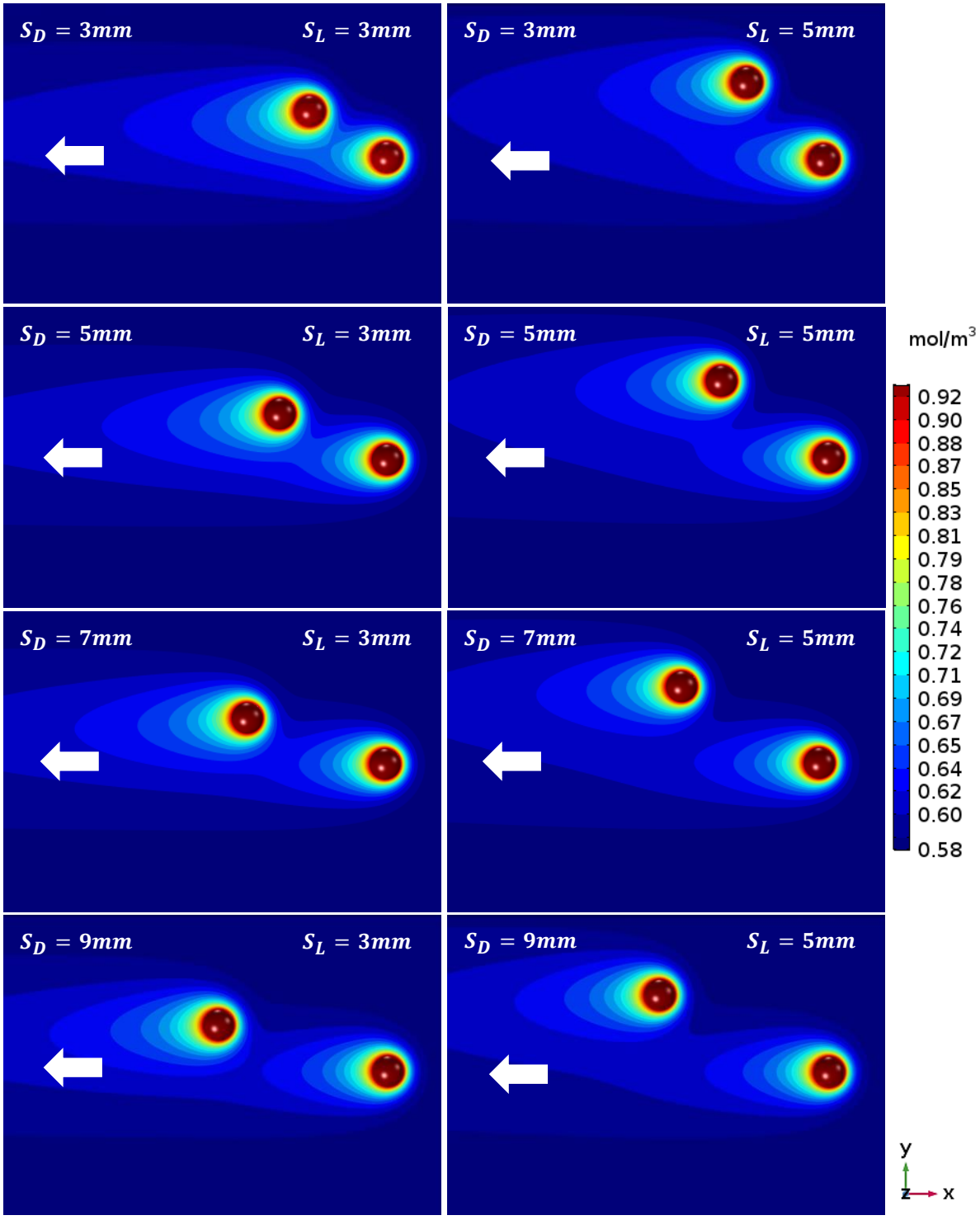

Figure 8-3: Contour plot of water vapour concentration on the bottom surface of the domain (after 300 s) at 0.2 m/s air speed for varying separation distances of S_D and S_L. The white arrow represents the direction of airflow.

As can be noticed from Figure 8-3, increasing the air speed tenfold to 0.2 m/s has a significant role in focusing the variation in concentration around the droplets, particularly at 5 mm lateral distance, and further reduction in the interaction between the droplets can be achieved by increasing the downstream distance as well. Unlike that observation, the downstream droplet is still coupled strongly by the downstream advection from the upstream droplet at 3 mm lateral distance even with larger separation of the downstream distance. However, this level of air speed is still uninfluential in decoupling the droplets from each other completely even with this wide range of the droplet separations. On further analysis of Figure 8-3, it is very clear to see the reduction in the transverse diffusive transport of water vapour within the domain, with the result that larger lateral distance can be achieved at this range of the air speed and domain width.

As the air speed increases to the highest level considered, see Figure 8-4, the interaction between the droplets decreases significantly, and the variation in concentration becomes ever more focused around the droplets. Hence, the droplets at 3 mm lateral distance become effectively isolated from each other, particularly at the largest downstream distance considered. Figure 8-4 also shows that at this level of the air speed, the droplets can also be isolated from each other with a small downstream distance when the downstream droplet is shifted laterally with 5 mm since there is no observable interaction between the droplets. Again, on further analysis of Figure 8-4, one can notice that there is no noticeable effect of the transverse diffusive transport of water vapour within the domain, and hence there is no effect on the evaporation rates of the droplets in the domain.

For a more visual depiction of the transverse diffusive transport of water vapour within the domain, Figure 8-5 shows 3D views of the vapour concentration field plotted on the bottom surfaces of the domain, the droplet surfaces and on the vertical plane representing the periodic conditions at different air speeds and droplet distances. The vapour concentration field in the case of zero lateral distance is also illustrated for comparison. Note that, for clarity, a selection of different concentration values of water vapour are chosen for the contours on the vertical planes in each plot.

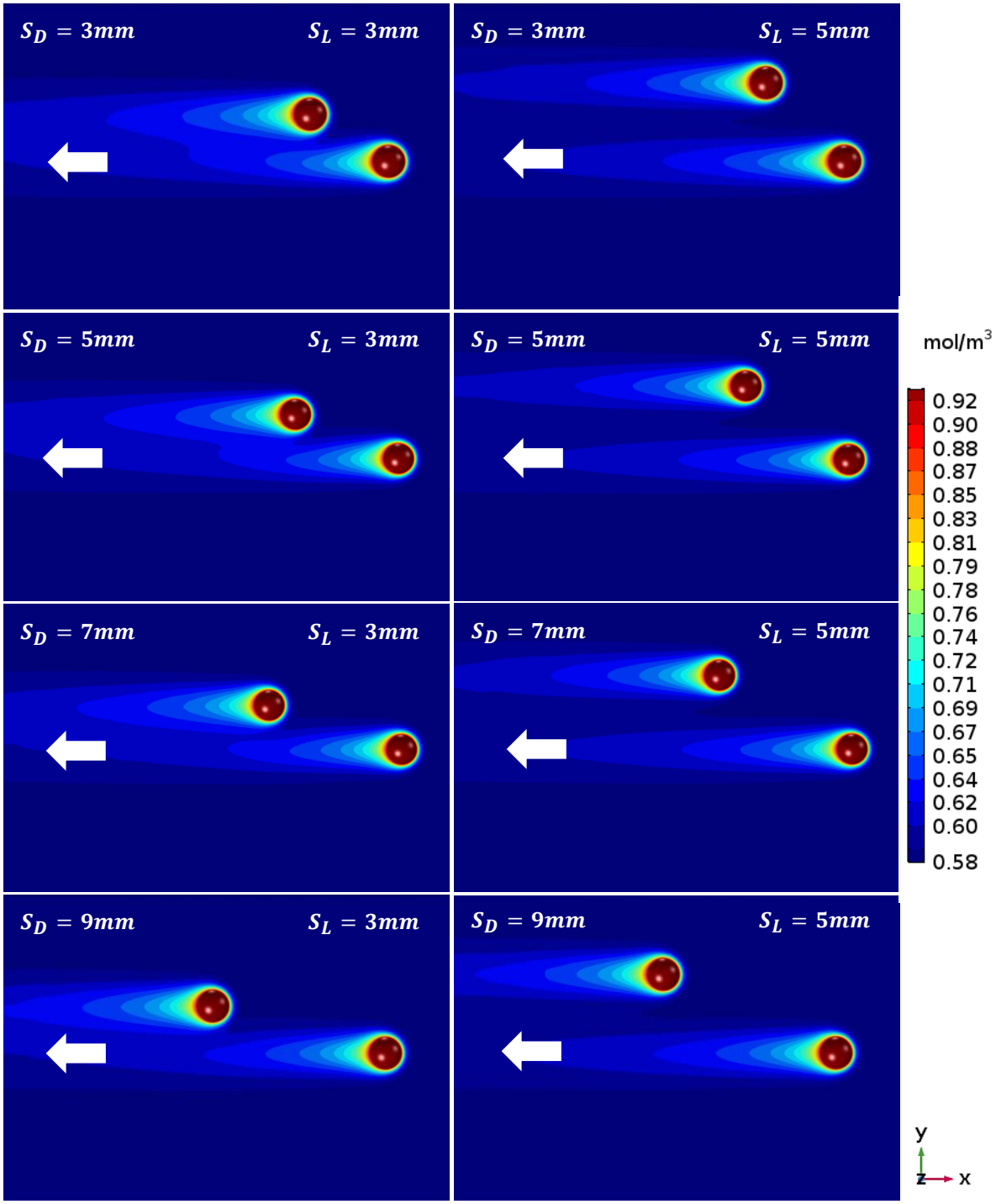

Figure 8-4: Contour plot of water vapour concentration on the bottom surface of the domain (after 300 s) at 2.0 m/s air speed for varying separation distances of S_D and S_L. The white arrow represents the direction of airflow.

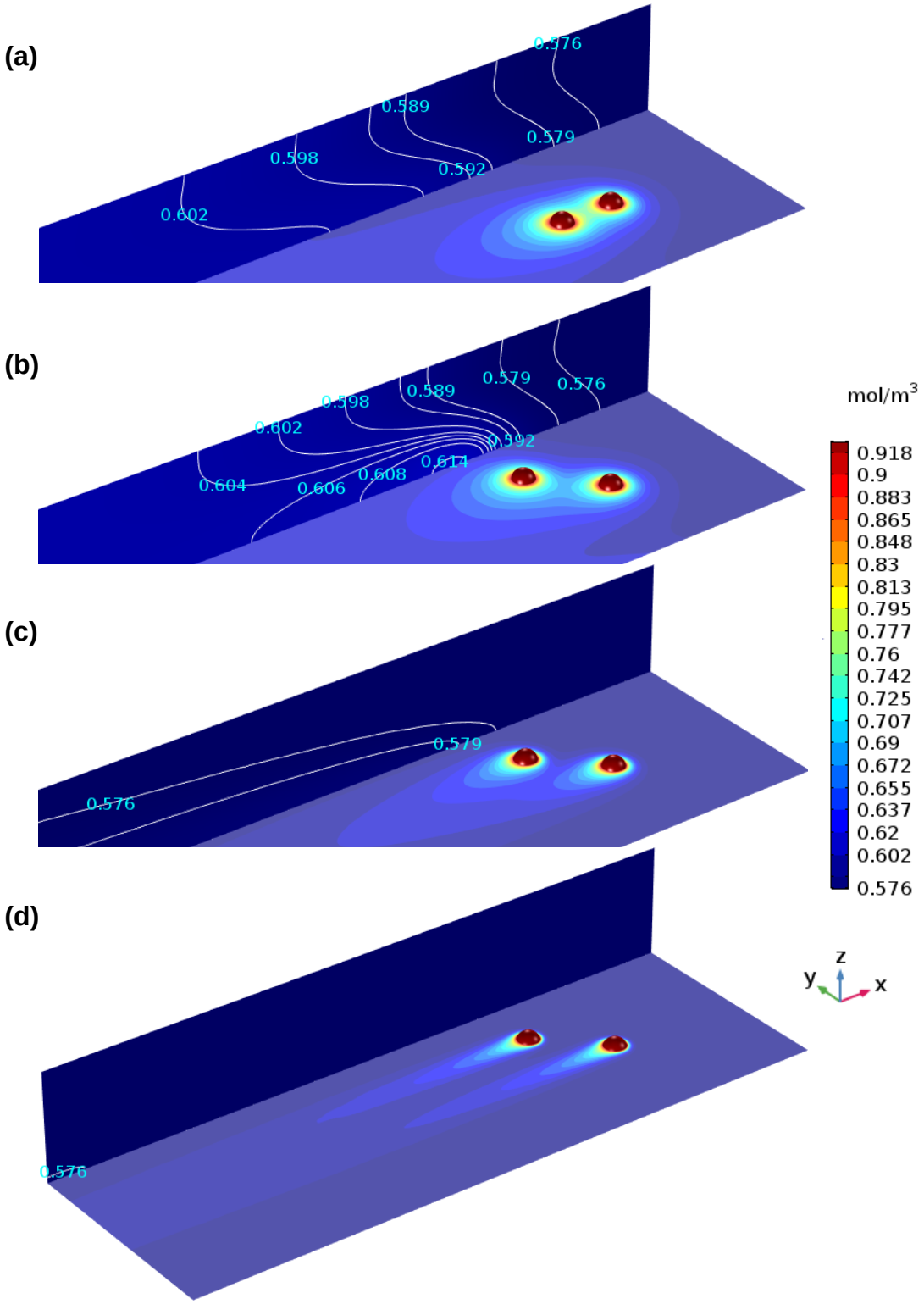

Figure 8-5: Vapour concentration field on the bottom surface of the domain, droplet surfaces and on the vertical periodic plane at 3 mm downstream distance and at (a) zero lateral distance at 0.02 m/s air speed. (b, c, d) 5 mm lateral distance and at 0.02 m/s, 0.2 m/s and 2.0 m/s air speed, respectively.

These 3D plots clearly show how at low speed, when the zero lateral distance is considered as shown in Figure 8-5 (a), the transverse diffusive transport of water vapour in such droplet arrangement strongly affects the evaporation rates of the droplets in the whole domain. This effect increases significantly at this range of air speed as the lateral distance is increased, see Figure 8-5 (b). Increasing the air speed tenfold to 0.2 m/s, see Figure 8-5 (c), has a significant role in reducing the effect of the transverse diffusive transport of water vapour within the domain, but it still slightly affects the evaporation rates of the droplets in the domain when farther lateral distance is considered. At the highest air speed, the transverse diffusive transport of water vapour within the array becomes negligible, as shown in Figure 8-5 (d), and no longer affects the droplet evaporation rates in the domain even with farther lateral distance.

8.4 Solute distribution on the solid surfaces inside the droplets

As observed previously in Chapter 7, when the droplets are aligned parallel on the same line passing through their centre, i.e. zero lateral distance, the distribution of the solute concentration on the solid surface within the downstream droplet is strongly influenced by the vapour transported from the upstream droplet and the partial shielding effect of the upstream droplet, in addition to the shear-induced circulation caused by the passing air over the droplets and the buoyancy-driven flow due to the increase in density with increasing salinity. Further, the previous observations revealed how increasing the downstream distance helps in reducing this interaction between the downstream and upstream droplets, particularly at the low level of the air speed, while there is no significant effect of increasing the downstream distance at the higher level of the air speed.

The distribution of the solute within the droplets, however, becomes different when the downstream droplet is shifted laterally from the centre of the upstream droplet, as shown in Figure 8-1 (b), in which the downstream droplet is no longer exposed completely to the downstream advection from the upstream droplet, i.e. there is an asymmetric effect of the downstream advection along the downstream droplet centre perpendicular to the airflow. Consequently, the upstream droplet shields part of the downstream droplet while the rest of the downstream droplet

is exposed to fresh air leading to more solute concentration at this region of the droplet.

Figure 8-6, Figure 8-7 and Figure 8-8 effectively form a parameter ‘map’ illustrating the solute distribution on the solid surface of the downstream droplet after 300 s of the evaporation course in the lowest, middle and highest air speeds considered, respectively, and at different downstream, S_D, and lateral, S_L, distances. These figures also show the corresponding velocity vector fields inside the downstream droplet, represented by the overlaid black arrows, on a parallel plane 50 μm above the solid surface. Note that the scale bars in these three figures are the same as in the corresponding figure in Chapter 7 for zero lateral distance ($S_L = 0$), Figure 7-10 (b), for ease of comparison. Further, the solute distribution inside the upstream droplet for each case of the air speeds is not presented here since only slight differences in the concentration distribution within the upstream droplet are seen when changing the position of the downstream droplet. The solute distributions within the upstream droplet remain essentially the same as in the zero lateral distance case, Figure 7-10 (b).

Generally, from Figure 8-6, Figure 8-7 and Figure 8-8, one can easily notice that increasing the downstream distance at a given lateral distance, $S_L \neq 0$, has a significant role in reducing the shielding effect of the upstream droplet on the downstream droplet at the lowest air speed as a result of the less effect of the advection flow. As the air speed is increased, the effect of the downstream distance decreases until it becomes insignificant at the highest level of the air speed, which agrees well with previous predictions illustrated in Chapter 6 and 7. In parallel, increasing the lateral distance at a given downstream distance has a great influence compared with increasing the downstream distance as a result of the contribution of both air speed and separation in reducing the vapour concentration around the downstream droplet, and the increased exposure to airflow due to the lateral displacement.

Considering the lowest air speed, see Figure 8-6, it is very clear to observe that at any downstream distance of the downstream droplet, the solute distribution on the solid surface is asymmetric fore-and-aft as a result of the non-uniformity of the evaporative flux fore-and-aft arising from the downstream vapour transported from the upstream droplet, but mostly laterally symmetric despite the asymmetry

in the droplet configurations. This is also evident from the velocity fields within the droplet since again asymmetric pattern of the velocity vector is noticed fore

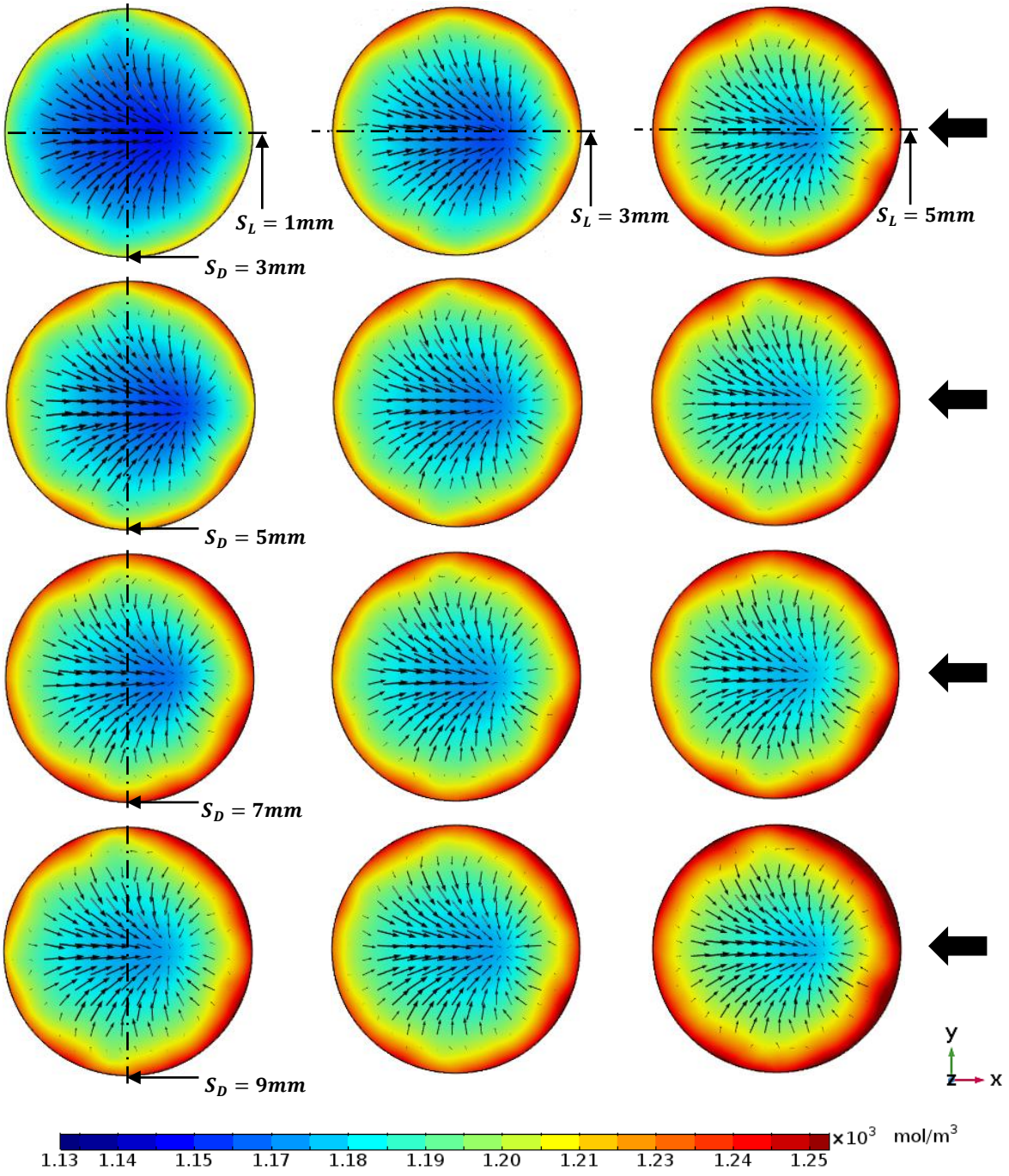

Figure 8-6: The solute concentration distribution on the solid surface inside the downstream droplet (after 300 s) at 0.02 m/s air speed and various downstream and lateral distances. The overlaid black arrows indicate the flow field on a plane parallel to the solid surface with a height of 50 μm. The black solid arrow represents the flow direction.

and aft while it is laterally symmetric within the droplet. Moreover, although the solute distribution inside the downstream droplet at largest downstream and lateral distances considered, Figure 8-6, is almost similar to the solute distribution pattern inside the upstream droplet at this level of the air speed, the solute distribution is still non-uniform on the solid surface due to insufficient effect of the shear-induced circulation compared to the buoyancy-driven flow, as mentioned previously in Chapter 7. Despite the significant role of the lateral distance in reducing the interaction between the droplets, the downstream water vapour transported from the upstream droplet still affects the vapour space around the downstream droplet as a result of insufficient forced air convection.

Increasing the air speed to 0.2 m/s, as shown in Figure 8-7, increases the effect of the lateral distance in depleting water vapour concentration levels in the region between the droplets due to increasing strength of the advection flow in flushing water vapour out of the gap between the droplets. Hence, a similar solute distribution inside the upstream droplet can be observed inside the downstream droplet with either smaller lateral and larger downstream distances or larger lateral and smaller downstream distances, as shown in the second column and first rows of Figure 8-7, respectively. On further analysis of Figure 8-7, the lateral symmetric in the solute distribution and velocity field inside the downstream droplet is more than that found in the lowest level of the air speed. This can be attributed again to the strong effect of the air convection in pushing water vapour away from the region between the droplets. Again, as mentioned in Chapter 7, more uniformity in the solute distribution is observed on the sold surface of the droplets as a result the buoyancy-driven flow becoming less significant compared to the shear-induced circulation. Consequently, reverse flow of the velocity vector related to airflow is noticed near the droplet solid surface arising from the shear-induced circulation.

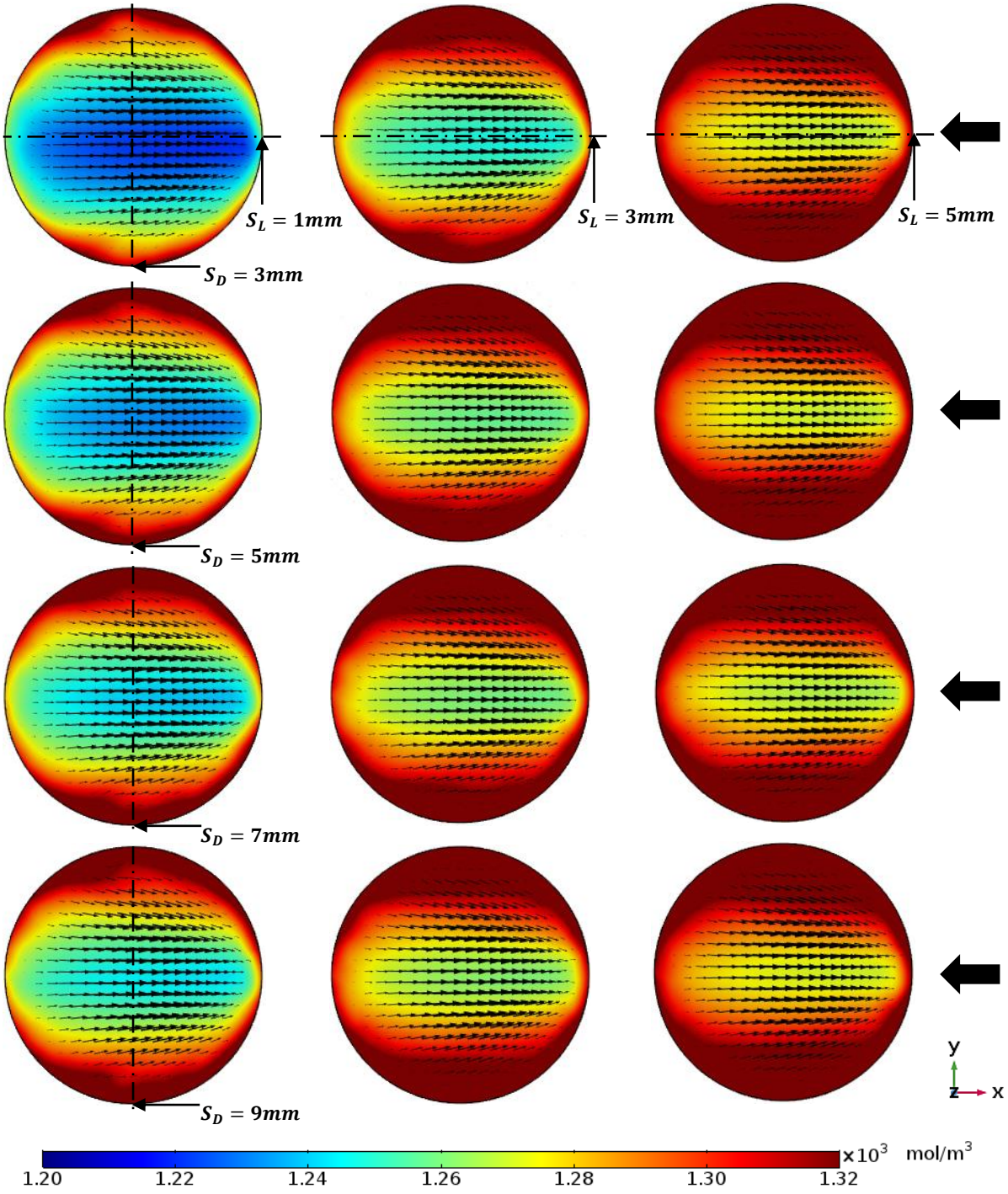

Figure 8-7: The solute concentration distribution on the solid surface inside the downstream droplet (after 300 s) at 0.2 m/s air speed and various downstream and lateral distances. The overlaid black arrows indicate the flow field on a plane parallel to the solid surface with a height of 50 μm. The black solid arrow represents the flow direction.

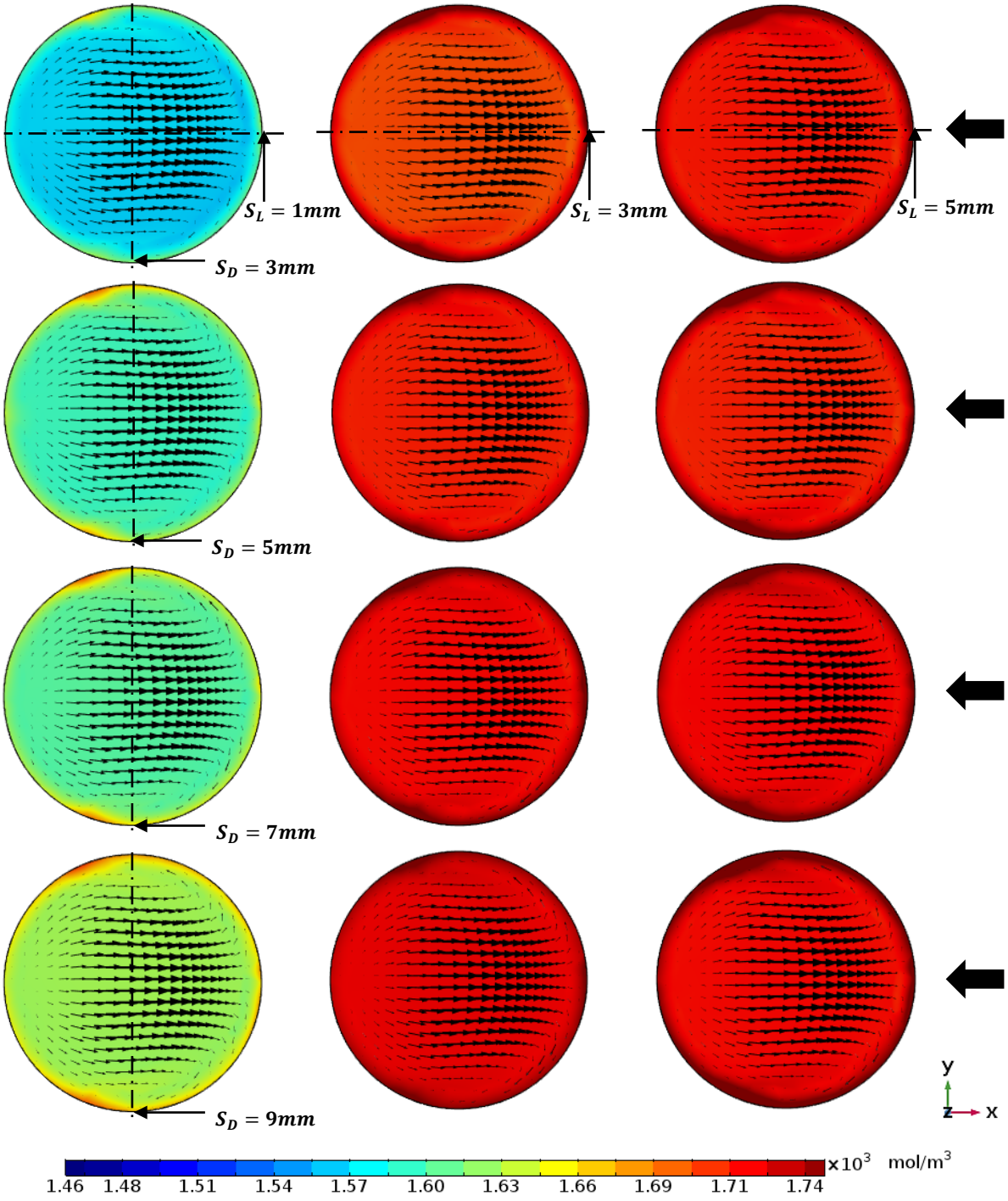

Figure 8-8: The solute concentration distribution on the solid surface inside the downstream droplet (after 300 s) at 2.0 m/s air speed and various downstream and lateral distances. The overlaid black arrows indicate the flow field on a plane parallel to the solid surface with a height of 50 μm. The black solid arrow represents the flow direction.

At the highest air speed considered, see Figure 8-8, it is easy to see the uninfluential role of the downstream distance compared to the great effect of the lateral distance in reducing the interaction between droplets due to increase the influence of the downstream vapour transported from the upstream droplet. As a result of increasing the influence of the lateral distance, the solute distribution within the downstream droplet becomes similar to that in the upstream droplet even at smaller downstream and lateral distances, as shown clearly in the first droplets of the second column of Figure 8-8. More lateral symmetry in the solute distribution and velocity field can be seen inside the droplets due to the dominance of the advection flow over the diffusive mass transport. Furthermore, much more uniformity in the solute distribution is observable on the solid surface of the droplets as the shear-induced circulation dominates the buoyancy-driven flow, and it is able to ensure sufficient mixing of the solute within the droplets, as mentioned previously in Chapter 7.

8.5 Flux field surrounding the droplets

As mentioned previously in Chapter 6 and 7, and observed earlier in this chapter, the downstream droplet is influenced by both the hydrodynamic shielding effects and downstream advection of the upstream droplet, and they would be affected strongly by three essential parameters, which are the speed of the airflow, the separation distance between the droplets and the droplet arrangements, i.e. parallel or perpendicular configurations. Observations revealed that the downstream droplet remains coupled with the upstream droplet by the downstream transport of water vapour even at larger separation distance while a small droplet distance with sufficient air speed are enough to isolate the perpendicular droplets.

It is worth considering the flux fields surrounding the droplets, as illustrated previously in Chapter 5 for an isolated single sessile droplet, and focusing on the gap between the droplets under the conditions considered. Figure 8-9, Figure 8-10 and Figure 8-11 therefore, show the vector fields of the diffusive flux and total flux around the droplets on a horizontal plane raised by 50 μm from the solid surface, and at a downstream separation of 3 mm with various air speeds

and different lateral distances. Note that the arrow scales are different in the three figures, but are the same in each sub-plot of each figure. The corresponding fluxes are indicated by the scale arrow in each figure.

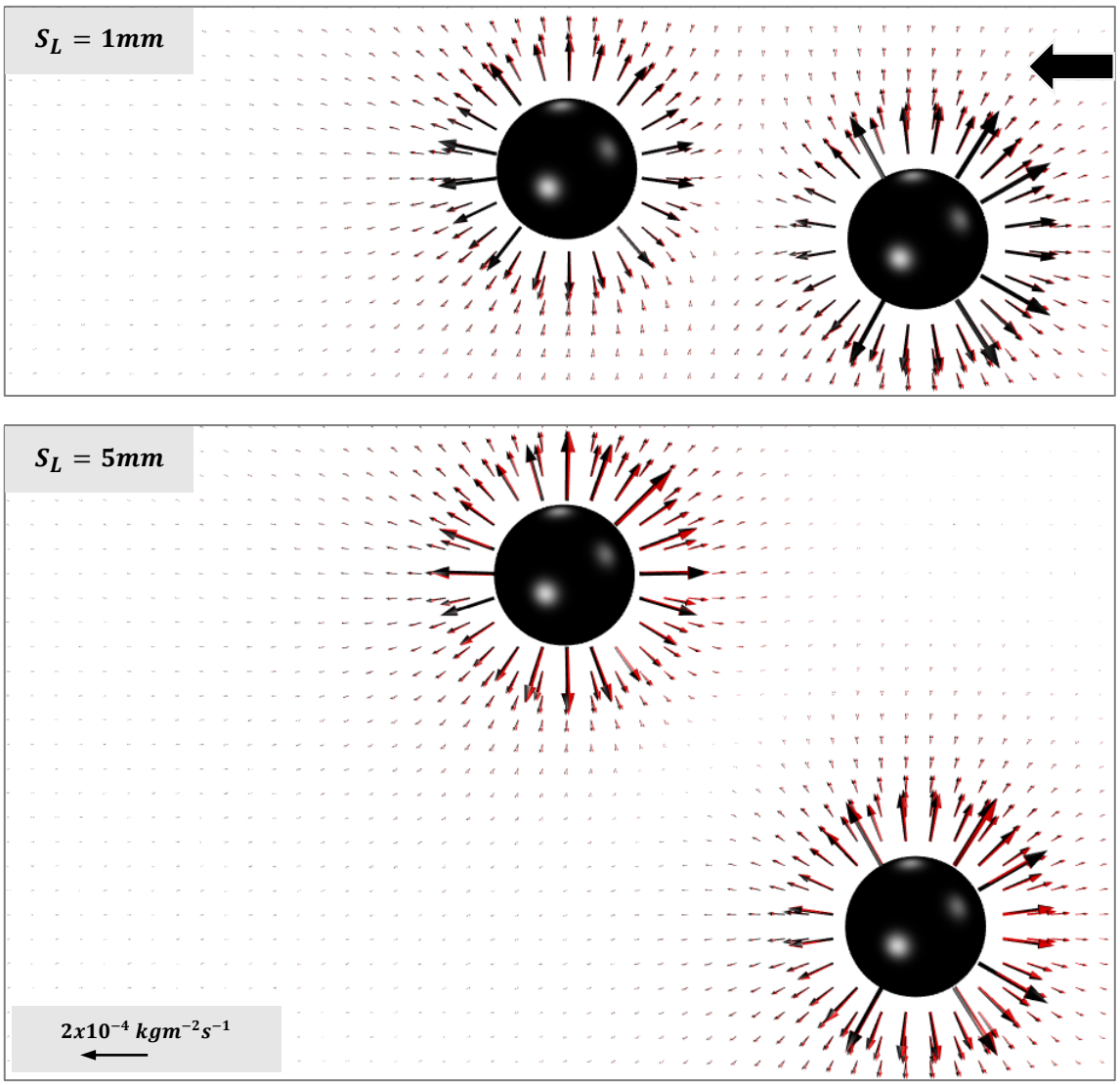

Figure 8-9: Diffusive flux (overlaid red arrows) and total flux (black arrows) plots after 300 s around the droplets (black solid circles), at 0.02 m/s air speed, and for $S_D = 3mm$ and different lateral distances. The black solid arrow represents the airflow direction.

For the lowest air speed, Figure 8-9, similar to what is observed from Figure 5-8 (a), higher diffusive flux (overlaid red arrows) around the droplets compared to the total flux (overlaid black arrows) is noticed as an indication of the lower convective flux arising from the lower air speed. Again, the direction of the total

flux arrows are almost identical to that of the diffusive flux due to the lower influence of the forced air convection. Focusing now on the gap between the droplets, lower flux is observable near the downstream part of the leading droplet compared to the upstream part and even to that in the upstream part of the downstream droplet. This can be attributed, as mentioned in Chapter 6, to the influence of the upstream diffusive flux and Stefan flow from the downstream droplet, which opposes the lower advection flow in the gap between the droplets, in addition to the downstream water vapour transported from the upstream half of the same droplet. At the smaller lateral offset, the downstream droplet is mostly overwhelmed by the downstream advection from the upstream droplet, as illustrated previously in Figure 8-2, and hence the flux around the downstream droplet is mostly less than in the upstream droplet. As the lateral offset increased, a part of the downstream droplet exposes to more airflow, hence enhancing the diffusive flux there compared to the nearest parts to the upstream droplet, and hence laterally asymmetric pattern of the flux is observed.

As the air speed increased tenfold to 0.2 m/s, see Figure 8-10 and Figure 5-8 (b), the convective flux becomes more influential since the direction of the total flux vector is no longer identical with the vector of the diffusive flux. As can be seen in the gap between the droplets that the upstream diffusive flux and Stefan flow from the downstream droplet are still influential at this level of the air speed, where the flux in the downstream part of the leading droplet is still lower than in the upstream part, and it is even independent of the droplet separation, which is also similar to 0.02 m/s air speed case shown in Figure 8-2. Furthermore, the flux of the downstream droplet is still lower than that of the upstream droplet at the smaller lateral offset while it is almost similar to the upstream droplet at the larger lateral distance as a result of the reduction in the interaction between the droplet as shown in Figure 8-3.

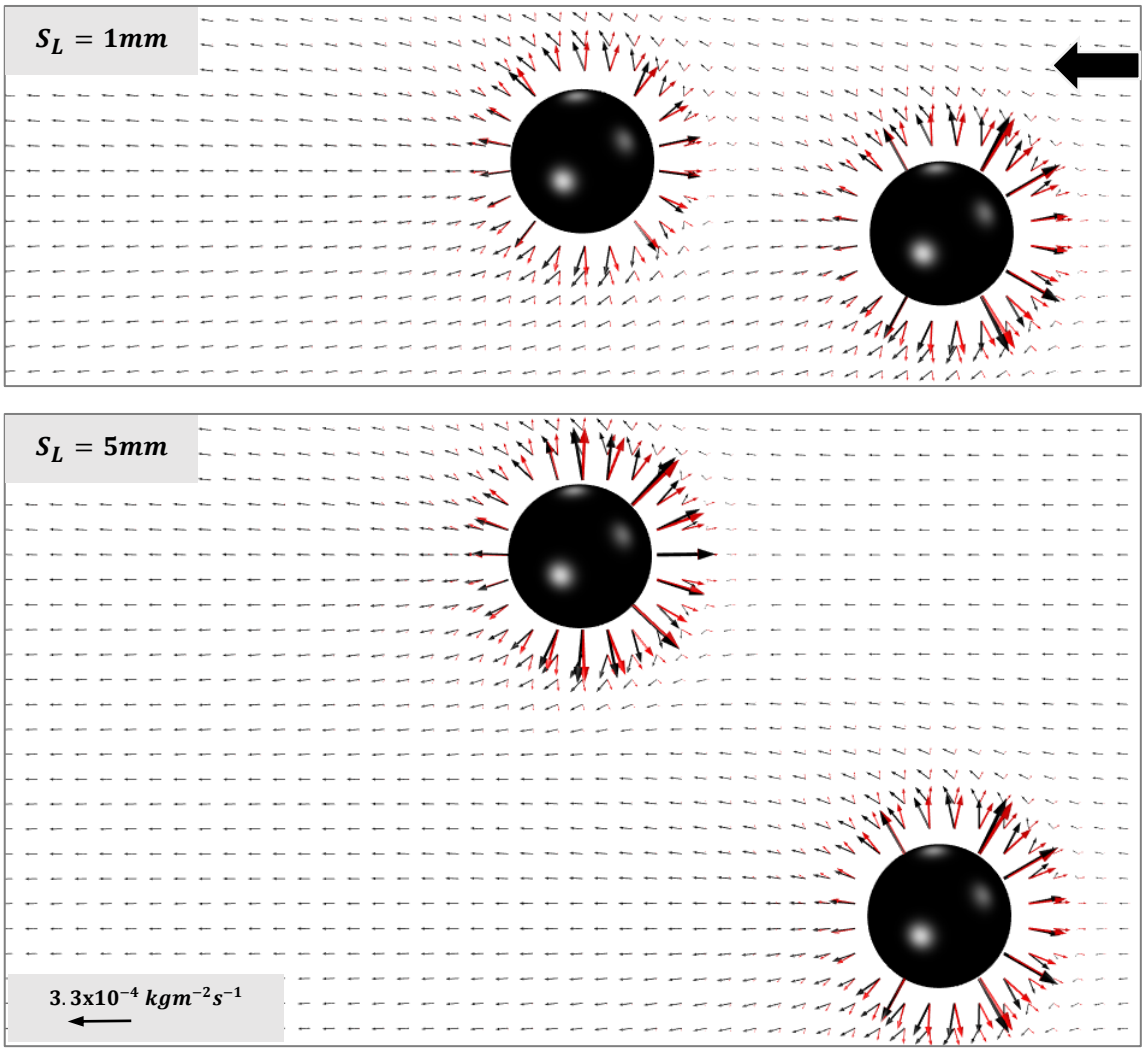

Figure 8-10: Diffusive flux (overlaid red arrows) and total flux (black arrows) plots after 300 s around the droplets (black solid circles), at 0.2 m/s air speed, and for $S_D = 3mm$ and different lateral distances. The black solid arrow represents the airflow direction.

Since the forced convection strength is high at the highest air speed considered, the total flux is shifted significantly from the direction of the diffusive flux where the convective flux becomes dominant over the diffusive flux, as shown in Figure 8-11 (focusing on the dashed box) and Figure 5-8 (c). Further, the downstream part of the leading droplet still experiences a significantly lower flux than the upstream part, which is entirely due to the presence of water vapour sweeping from the upstream half of the same droplet via the airflow passing over the droplets. Focusing on the downstream droplet at the largest lateral distance, the flux field is similar to that around the upstream droplet compared to the

smaller lateral distance condition, resulting in decoupling the droplets from each other at this level of the air speed.

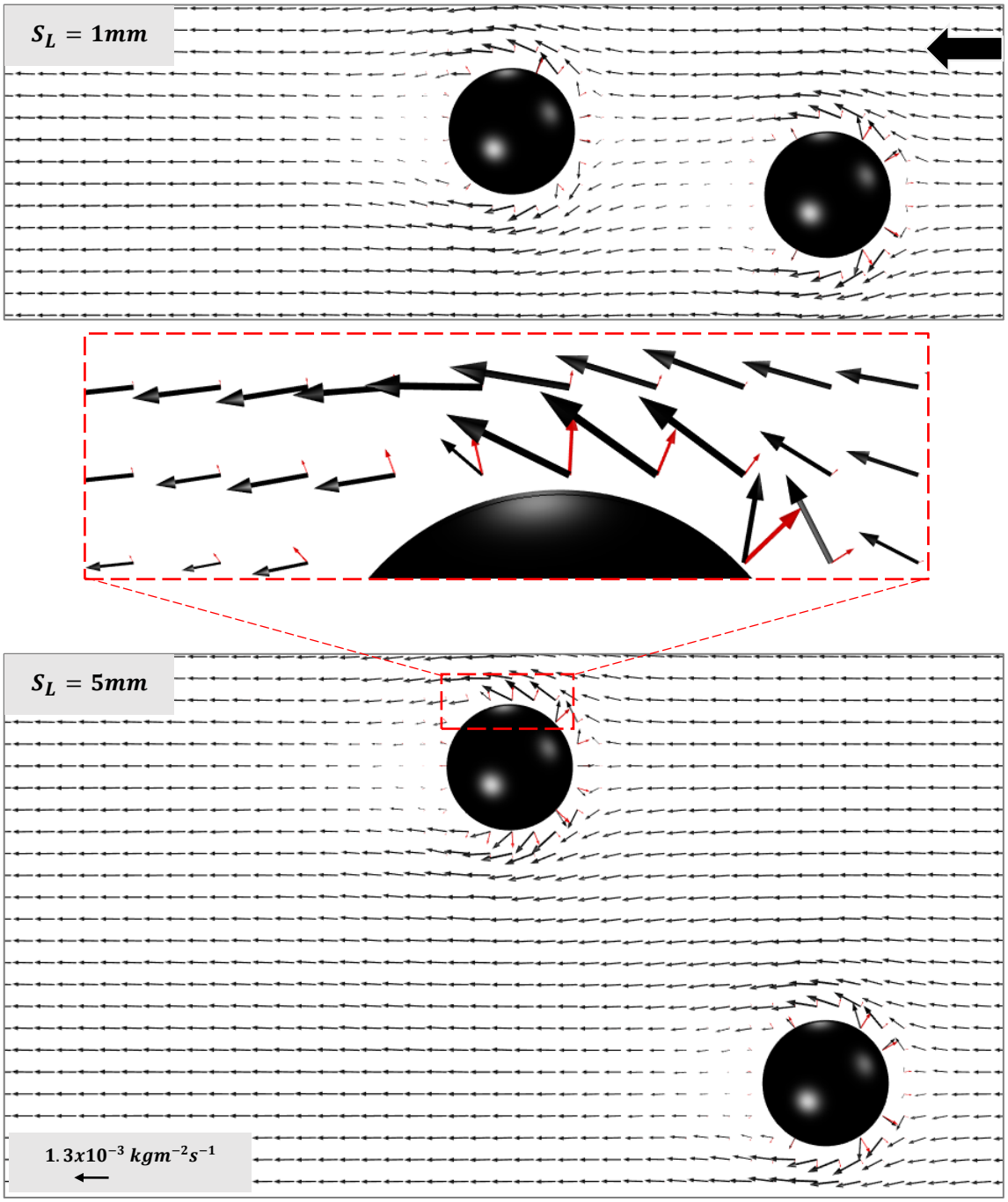

Figure 8-11: Diffusive flux (overlaid red arrows) and total flux (black arrows) plots after 300 s around the droplets (black solid circles), at 2.0 m/s air speed, and for $S_D = 3mm$ and different lateral distances. The dashed box shows the fluxes around the furthest part of the downstream droplet. The black solid arrow represents the airflow direction.

8.6 Effect of droplet configuration in enhancing droplet evaporation rates

As mentioned previously in Chapter 6, achieving uniformity of evaporation behaviour across an array of multiple droplets is important for optimising a sufficient system for appropriate applications therefore, the evaporative behaviour of the downstream droplet should be compared to the upstream droplet within the array to achieve this goal.

A more quantitative measure of the effect of droplet arrangement on the evaporation rates of the downstream droplet compared to the upstream droplet for various air speeds is illustrated in Figure 8-12. As expected, the evaporative behaviour of the upstream droplet, here represented by D1, is weakly dependent of both droplet separations (i.e., downstream and lateral distances) except at the lower air speed considered here, see Figure 8-12 (a), since it is affected slightly by the upstream diffusive flux and the Stefan flow from the downstream droplet, which dominate the downstream advection. Further enhancement in the evaporation rate of the upstream droplet is noticed as the air speed is increased.

Unlike the leading droplet, the second droplet, represented by D2, is significantly affected by increasing the downstream distance when the two droplets are aligned parallel on the same line, $S_L = 0$ mm, as a result of reducing the downstream advection from the leading droplet, but increasing the downstream distance is still insufficient in reducing the difference in the evaporation rate of the two droplets, as mentioned previously in Chapter 6 and illustrated clearly in Figure 8-12. As the lateral distance increased to 1 mm, a slight enhancing in the evaporation rate is observed at the lowest air speed, which is not sufficient in flushing water vapour out of the gap between the droplets whereas, further increase in the downstream droplet evaporation rate is noticeable at this distance as the air speed is increased, see Figure 8-12 (b and c).

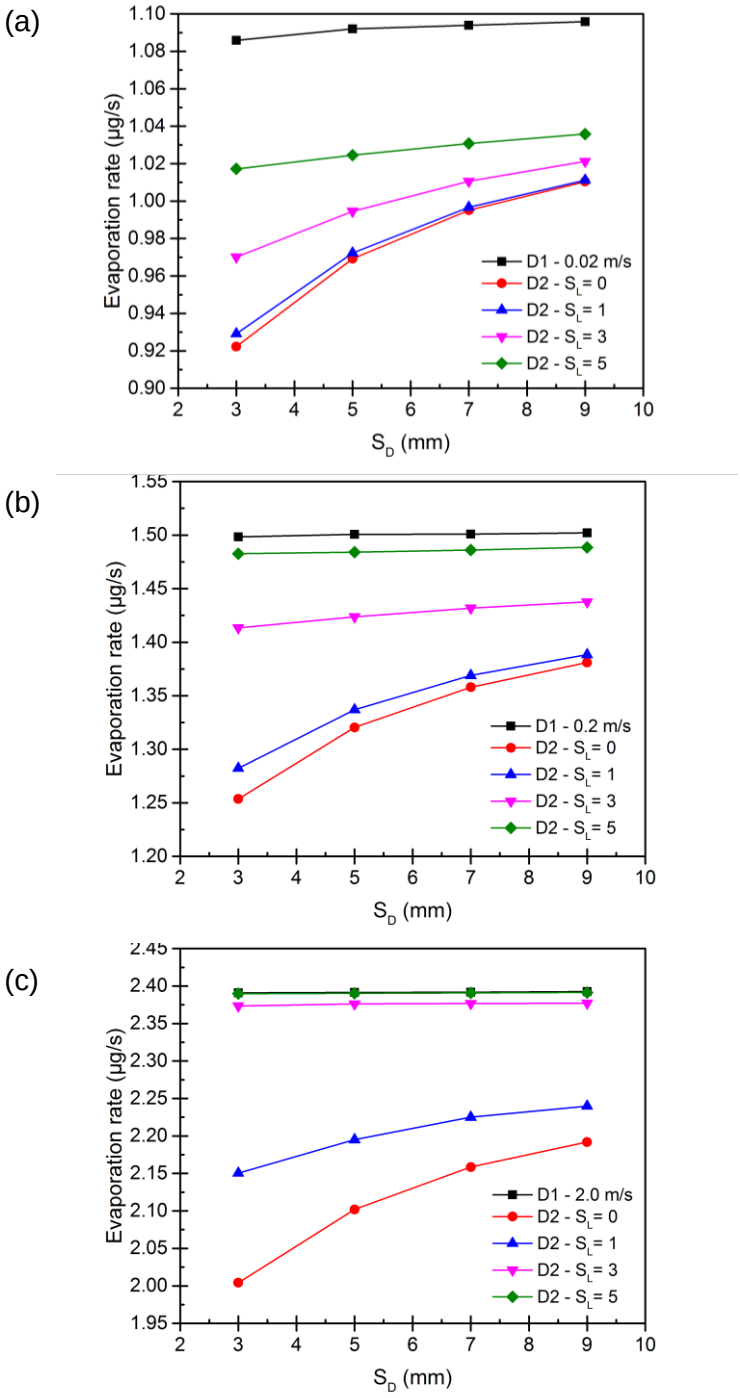

Figure 8-12: Evaporation rates of the upstream (D1) and downstream (D2) droplets after 300 s of the evaporation course at (a) 0.02 m/s, (b) 0.2 m/s and (c) 2.0 m/s air speed, and different downstream and lateral distances.

At the lowest air speed, Figure 8-12 (a), increasing the lateral distance further, i.e., 3 mm and 5 mm, is still insufficient to eliminate the interaction effects between the droplets even at the furthest downstream distance, and hence the droplets remain coupled by the downstream advection from the leading droplet. For the

medium air speed, see Figure 8-12 (b), increasing the downstream distance does very little to reduce the interaction between the droplets at 3 mm lateral distance, and hence increases the evaporation rate of the second droplet while there is no remarkable increase in the evaporation rate at the largest lateral distance as the downstream distance is increased. As a result, although the largest lateral distance does help in reducing the difference in the evaporation rates of the droplets the downstream droplet is still influenced slightly by the water vapour transported from the upstream droplet.

At the highest velocity of the airflow, Figure 8-12 (c), it seems that the downstream advection from the leading droplet still influences the downstream droplet a bit at 3 mm lateral distance and even for droplets very far from each other. With further increase in the lateral offset, $S_L = 5$ mm, it is very clear to see that the evaporation rate curves for the downstream and upstream droplets are practically indistinguishable, which indicates that this droplet arrangement at this level of the air speed are able to deplete water vapour completely in the gap between the droplets and even for droplets very close to each other.

However, as mentioned previously in Chapter 6, the decoupling of the droplets by the forced air convection is not possible for the subsequent rows of droplets when they are aligned parallel to the airflow due to the transport of water vapour diffused from the first row. As observed earlier, the decoupling of the droplets is only possible if the subsequent rows are shifted laterally from the first row. Therefore, in parallel to the above, Figure 8-13 provides a more quantitative measure of the effect of air speed and droplet configuration by plotting, as a function of the downstream and lateral distances, the percentage difference in the volume of the two droplets after 300 s of the evaporation process, i.e., as a proportion of the upstream droplet volume.

Generally, following the trends of the curves in Figure 8-13 shows clearly that longer downstream spacing of the droplets would be needed to eliminate the influence of the downstream transport at the smaller transverse spacing, and a much longer spacing is needed as the air speed is increased. Furthermore, it is very clear to notice that the second droplet is more sensitive to the transverse spacing than the downstream droplet separation at the lower air speed as shown in Figure 8-13 (a). This sensitive of the downstream droplet increases as the air

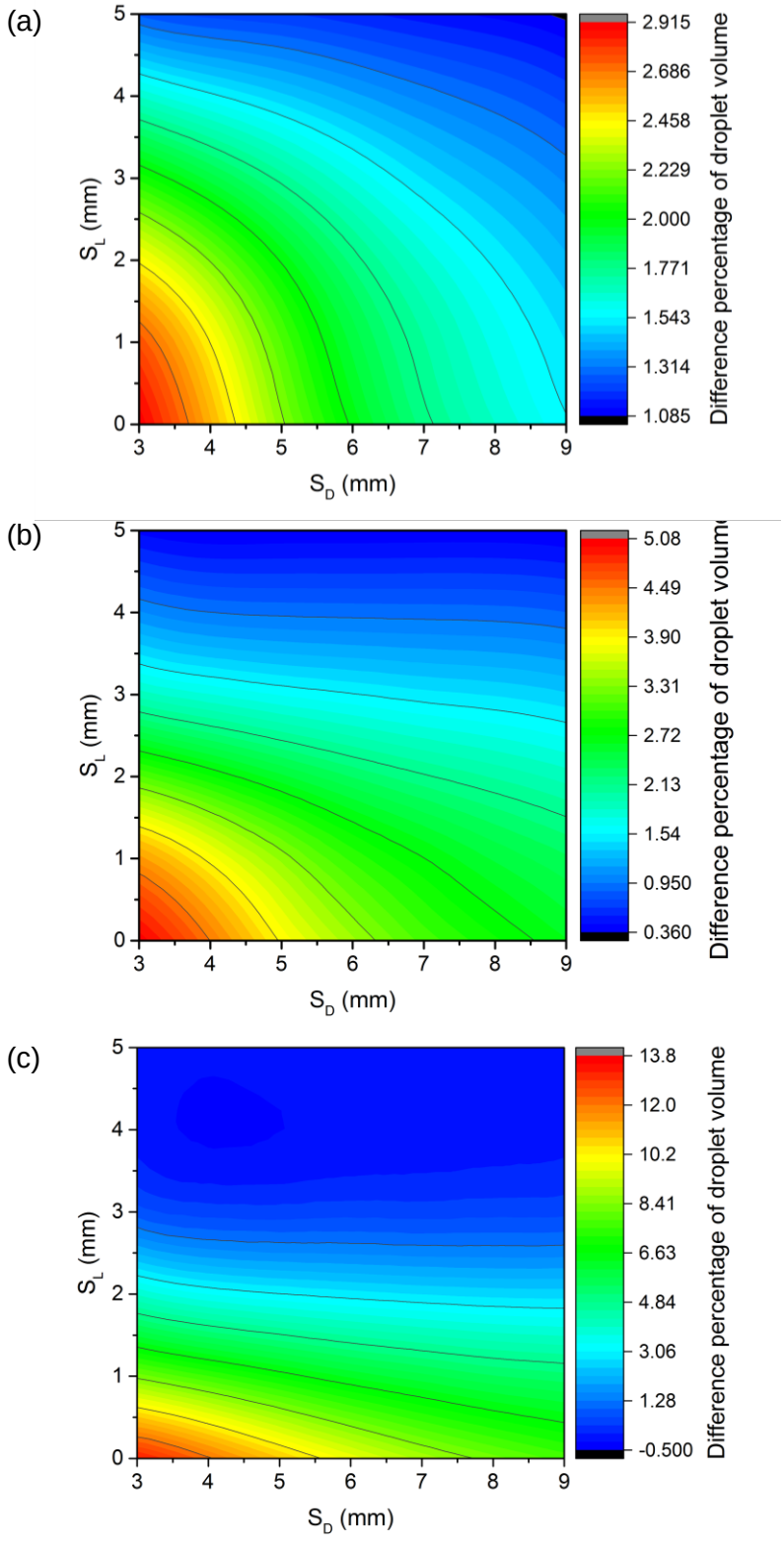

Figure 8-13: Difference in the volume of two droplets after 300 s (as a percentage of the upstream droplet volume) as a function of the downstream and lateral distances, and at (a) 0.02 m/s, (b) 0.2 m/s and (c) 2.0 m/s air speed.

speed is increased, see Figure 8-13 (b and c), which indicates that the transverse spacing becomes more effective with increasing the velocity of the airflow. At low speed, the difference in volume is more pronounced at all droplet arrangements due to the higher vapour concentration levels in the region downstream of the leading droplet, and hence slower evaporation of the second droplet. This difference levels off significantly to smaller level at the medium speed, and it is almost flat at the highest air speed.

8.7 Conclusions

As has been seen in this chapter compared to what is observed previously in Chapter 6 and 7, the shifting of the downstream droplet laterally from the upstream droplet increases its exposure to the fresh airflow, and hence accelerates its evaporation as a result of reducing the levels of the vapour concentration around the droplet. In addition, the lateral offset increases the possibility of pushing water vapour transported downstream from the leading droplet away from the space around the downstream droplet, particularly at higher air speeds unlike the downstream spacing in which the second droplet remains influenced by the downstream transport from the first droplet.

For the lower air speeds, findings revealed that the largest lateral distance considered here is insufficient to eliminate water vapour effectively in the gap between the droplets even at larger downstream spacing therefore, much larger lateral distance would be needed and consequently increasing the transverse diffusive transport of water vapour within the array. At the highest level of the air speed, the staggered droplet configuration has a significant role in depleting the vapour levels in the region between the droplets, and hence isolating the droplets effectively from each other without affecting the evaporation of other droplets in the array by the transverse dispersion of water vapour.

Focusing on the solute distribution on the solid surface inside the droplets under the droplet arrangements considered, the key observation is that increasing the lateral offset is more influential than the downstream distance on distributing the solute on the solid surface at all levels of air speeds due to the contribution of both air speed and separation in reducing the downstream advection from the

upstream droplet. The solute distribution is asymmetric fore-and-aft whilst mostly laterally symmetric, despite the asymmetry in the droplet configurations. Further, similar solute distribution in the leading droplet with much more uniformity can be achieved in the second droplet with increasing the lateral offset and air speed.

Observations revealed that the upstream diffusive flux and Stefan flow from the downstream droplet affect the flux fields in the region between the droplets at lower levels of air speed whilst it is affected entirely by the vapour transported from the leading droplet when the air speed is increased to the highest level. In addition, increasing the lateral distance is able to produce a laterally symmetric flux fields around the downstream droplet and even similar to that around the upstream droplet with sufficient air speed.

Finally, in an array of multiple droplets in a forced convection airflow, it can be deduced that both the lateral and downstream distances contribute together with the velocity of airflow in reducing the interaction in the gap between the droplets, and hence achieving uniformity of the evaporation behaviour across the array to create efficient systems for appropriate applications.

Chapter 9 Conclusions

9.1 Introduction

The main aim of the present work was to obtain a detailed understanding of how arrays of multiple droplets simultaneously evaporating in proximity to each other under different convective environments, i.e. natural and forced convection, and mutually influence the drying dynamics, particularly the uniformity and quality of the solid products deposited on surfaces. The aim of this thesis was achieved through developing a 3D transient diffusion-convection model fully coupled with the Arbitrary Lagrangian-Eulerian finite element method via COMSOL Multiphysics®. In addition, the aim of the current numerical study was carried out through four crucial parts;

- The evaporation of an isolated single sessile water droplet under a forced air convection.
- The evaporation of a pair of sessile water droplets aligned either perpendicular or parallel to the forced air convection, and at various droplet distances.
- The influence of the forced airflow on the internal dynamics inside salt solution droplets.
- The influence of staggered droplet displacements on the evaporative behaviour of an array of multiple salt solution droplets under a forced air convection.

The evaporation of droplets in an open natural convection environment using an ‘Infinite Element Domain’ approach was also performed as a reference case for comparison. This approach consists of applying an outer coordinate-stretching layer to the hemispherical computational domain, seemingly for the first time in this field of research, to incorporate far-field boundary conditions appropriately without the need for huge computational domain.

9.2 Significance of the droplet array evaporation

As has been seen in the literature, evaporation of sessile droplets occurs in a number of natural and engineered systems. Evaporation of sessile sweat droplets from the skin surface to control the temperature of the human body is a good example of natural phase-change cooling systems, involving multiple sessile droplets simultaneously evaporating in close proximity to each other. This fundamental natural process can be exploited in thermal management systems in which the temperature of substrates can be regulated via the evaporation of those droplets in a way that ensures uniform evaporative behaviour across the system. Spray coating, 3D printing, condensation, and the manufacture of hi-resolution displays are also very important engineered applications, which involve a number of droplets of industrial liquids interacting amongst each other, which leads to non-uniform deposits of solid products on surfaces. Further, such systems are very complex and involves many interacting physical mechanisms therefore, understanding these physical mechanisms individually allows identification of the most influential mechanisms controlling the deposition patterns of solid particles on surfaces.

However, introducing a better theoretical understanding of the evaporation of arrays of multiple droplets, particularly under the forced convective environment, through studying the underlying physics of the evaporation of an isolated single sessile droplet, and developing the knowledge to understand the evaporation of a pair of sessile droplets under different droplet configurations is the appropriate way to understand and optimise these processes before doing experiments or fabricating device components.

Therefore, the present numerical work is a motivation for providing a clear picture of the nature of interacting physical mechanisms during the evaporation of such array of droplets to guide experimental developments.

9.3 Key conclusions

As mentioned previously, the present theoretical study was achieved through four crucial parts therefore, the key observations of these four numerical studies will be summarised as follow:

1. The temporal evolution of the droplet volume decreases exponentially with time under the forced convection condition unlike the linear variation of the droplet volume during the droplet evaporation in an open natural convection environment.
2. The evaporation rate of an isolated single sessile droplet under forced airflow can be determined by correlations for initial and final Sherwood number in terms of Reynolds and Schmidt numbers, $Sh_i = 1.91 + 0.4734Re^{0.478}Sc^{1/3}$ and $Sh_f = 0.67 + 0.035Re^{0.665}Sc^{1/3}$ for a range of an average air speed between 0 to 2 m/s.
3. An enhancement in the evaporation rate of the droplet compared to the natural convection case is noticed by providing a gentle forced air convection as a result of pushing the vapour away from the droplet surface, and hence increases the concentration gradient-driven evaporation process.
4. Unlike the evaporation of interacting neighbouring droplets at a given separation distance and under the natural convection environment, where the raised vapour concentration levels in the gap between the droplets leads to slow the evaporation process, the combination of air speed and droplet separation in the perpendicular droplets can effectively decouple the vapour around the droplets whilst the parallel droplets remain coupled by the downstream advection from the leading droplet.
5. The variations of the volume of perpendicular and parallel droplets with time are almost identical to the same trend of the isolated single droplet assisted by airflow.
6. The downstream droplet is more influenced by the downstream advection from the upstream droplet than the hydrodynamic shielding effects of the upstream droplet.

7. The forced convective airflow over sessile droplets produces a circulation flow inside the droplets with a maximum speed approximately 1% of the air speed whilst the increase in density with increasing salinity induces a buoyancy-driven flow inside the droplets in the natural convective environment. In contrast, an almost concentric pattern of the solute distribution is induced inside the droplets as zero-gravity environment is considered.
8. As air speed is increased, the shear-induced circulation becomes sufficient to mix the solution effectively, producing much more uniform concentration distributions inside the droplets. Strong variations in concentration still exist near contact lines, but these regions become more localised as air speed increases.
9. The larger downstream spacing between the parallel droplets is unable to eliminate the influence of the downstream advection from the upstream droplet therefore, staggered droplet arrangement is needed for this purpose.
10. The shifting of the downstream droplet laterally from the leading droplet increases the ability of pushing the downstream vapour transported from the upstream droplet away from the downstream droplet, particularly at the higher levels of the air speed. Hence, more uniform distribution of the solute is observable inside the second droplet.
11. Although increasing the lateral offset is more influential in reducing the interaction between droplets than the downstream distance, increasing the lateral distance increases the transverse diffusive transport of water vapour within the domain, and hence affects the evaporation rates of droplets across the array, particularly at the lower levels of the air speed.
12. A uniform evaporative behaviour of the droplets across the array can be achieved at sufficient lateral and downstream distances with sufficient air speed.

9.4 Limitation of the present work

As mentioned previously in earlier chapters, the present work is computational, and coupled physics models available within COMSOL Multiphysics® are used to simulate the evaporation process of multiple interacting neighbouring droplets. Further, the simulations are 3D and time-dependent with multiple free surfaces, and hence mesh movement and adaption. This leads to very high memory requirements, and consequently the simulations were restricted to what is available in institutional resources to implement these simulations in addition to the limited time available in HPC machines and number of mesh elements that can be used. All these restrictions created practical limitations on this work. For instance, it would have been interesting to investigate the evaporative behaviour, internal dynamics and solid particles deposition on solid surfaces at the later stages of the evaporation course and after the liquid drying stage under conditions considered here.

In this work, only pure liquids or liquid solutions have been considered. However, in some practical applications, droplets are likely to be colloidal suspensions, which would require more sophisticated modelling of the solid content, especially in the later stages of droplet evaporation. Further, the key assumptions have been considered in this work are that the droplet evaporates under the constant contact radius regime, where the contact line of the droplet is pinned during the evaporation course, without any displacement or movement of the droplet on solid surfaces under the effect of the convection airflow. Therefore, the laminar flow model was the appropriate adopted model under these conditions. The isothermal condition is also the key assumption considered in this work based on the type of liquids used. Thus, the evaporative cooling effect, temperature gradient driven Marangoni effect were not investigated in the present numerical work.

In parallel, modelling multiple droplets, e.g., three parallel droplets or four staggered droplets, to investigate how the build-up of vapour concentration affects other droplets in the downstream direction in such droplet arrangements, was also very difficult under constraints available. Hence, modelling a pair of multiple droplets in a laminar air convection environment was the alternative

appropriate way to predict results of such complex systems. Moreover, it would have been interesting to utilise the present numerical model in a real practical application such as spray cooling or thermal management systems to prove the capability of the adopted mothed in solving such real complex applications.

9.5 Suggestions for future work

Based on the numerical observations of the evaporation of pinned sessile droplets under a laminar forced air convection, the following suggestions can be considered as recommended future work;

1. Investigate numerically the evaporation of unpinned sessile droplets under laminar forced air convection.
2. Develop the numerical model to study the evaporation of both pinned and unpinned sessile droplets under a turbulent forced air convection.
3. Extend the present study, if possible, to cover the evaporative behaviour and internal dynamics inside the droplets at later stages of the evaporation course to introduce a better understanding of the drying process.
4. Develop the numerical model to consider the droplet evaporation under non-isothermal forced convective environment.
5. Extend the study to investigate the effect of using different structures of substrates and different liquids on the evaporative behaviour of the droplets under the forced convective environment.
6. Exploit the numerical model, if possible, in applications such as phase-change cooling system, inkjet printing and spray coating.

List of References

1. Cutnell, J.D. and W.J. Kenneth, *Essentials of Physics*. 2006: Wiley Publishing.
2. Erbil, H.Y., *Evaporation of pure liquid sessile and spherical suspended drops: A review.* Advances in Colloid and Interface Science, 2012. **170**(1–2): pp. 67-86.
3. Liu, H., *Science and engineering of droplets: fundamentals and applications*. 2000, Norwich, N.Y;Park Ridge, N.J;: Noyes Publications.
4. Chen, R., et al., *Blood drop patterns: Formation and applications.* Advances in Colloid and Interface Science, 2016. **231**: pp. 1-14.
5. Czerwiec, T., et al., *Thermal management of metallic surfaces: evaporation of sessile water droplets on polished and patterned stainless steel*, in *IOP Conference Series: Materials Science and Engineering*. 2017, IOP Publishing Ltd. pp. 1-10.
6. Chen, X., Z. Ding, and R. Liu, *Spreading of Annular Droplets on a Horizontal Fiber.* Microgravity Science and Technology, 2018. **30**(3): pp. 143-153.
7. Thiele, U., *Patterned deposition at moving contact lines.* Advances in Colloid and Interface Science, 2014. **206**: pp. 399-413.
8. Ito, A., et al., *Medical application of functionalized magnetic nanoparticles.* Journal of Bioscience and Bioengineering, 2005. **100**(1): pp. 1-11.
9. Dunnill, P. and M. Lilly, *Purification of enzymes using magnetic bio-affinity materials.* Biotechnology and bioengineering, 1974. **16**(7): pp. 987-990.
10. Šafařík, I. and M. Šafaříková, *Use of magnetic techniques for the isolation of cells.* Journal of Chromatography B: Biomedical Sciences and Applications, 1999. **722**(1–2): pp. 33-53.
11. Saiyed, Z., S. Telang, and C. Ramchand, *Application of magnetic techniques in the field of drug discovery and biomedicine.* BioMagnetic Research and Technology, 2003. **1**(1): pp. 1-8.

12. Setchell, C.H., *Magnetic separations in biotechnology—a review.* Journal of Chemical Technology and Biotechnology. Biotechnology, 1985. **35**(3): pp. 175-182.

13. Gulka, C.P., et al., *Coffee Rings as Low-Resource Diagnostics: Detection of the Malaria Biomarker Plasmodium falciparum Histidine-Rich Protein-II Using a Surface-Coupled Ring of Ni(II)NTA Gold-Plated Polystyrene Particles.* ACS Applied Materials & Interfaces, 2014. **6**(9): pp. 6257-6263.

14. Lanotte, L., et al., *Role of red cells and plasma composition on blood sessile droplet evaporation.* Physical Review E, 2017. **96**(5): pp. 053114-053121.

15. Bahmani, L., M. Neysari, and M. Maleki, *The study of drying and pattern formation of whole human blood drops and the effect of thalassaemia and neonatal jaundice on the patterns.* Colloids and Surfaces A: Physicochemical and Engineering Aspects, 2017. **513**: pp. 66-75.

16. Vehring, R., *Pharmaceutical Particle Engineering via Spray Drying.* Pharmaceutical Research, 2008. **25**(5): pp. 999-1022.

17. Dinh, N.T., et al., *High-resolution inkjet printing of conductive carbon nanotube twin lines utilizing evaporation-driven self-assembly.* Carbon, 2016. **96**: pp. 382-393.

18. Bhatt, N.H., et al., *Enhancement of heat transfer rate of high mass flux spray cooling by ethanol-water and ethanol-tween20-water solution at very high initial surface temperature.* International Journal of Heat and Mass Transfer, 2017. **110**: pp. 330-347.

19. Swartz, M., et al., *An Overview of Corona Charged Aerosol Detection in Pharmaceutical Analysis*. 2009: Synomics Pharma, White Paper. pp. 1-12.

20. Zhang, L., et al., *Inkjet Printing High-Resolution, Large-Area Graphene Patterns by Coffee-Ring Lithography.* Advanced Materials, 2012. **24**(3): pp. 436-440.

21. Park, J. and J. Moon, *Control of Colloidal Particle Deposit Patterns within Picoliter Droplets Ejected by Ink-Jet Printing.* Langmuir, 2006. **22**(8): pp. 3506-3513.

22. Filik, J. and N. Stone, *Drop coating deposition Raman spectroscopy of protein mixtures.* Analyst, 2007. **132**(6): pp. 544-550.

23. Shimoni, A., S. Azoubel, and S. Magdassi, *Inkjet printing of flexible high-performance carbon nanotube transparent conductive films by "coffee ring effect".* Nanoscale, 2014. **6**(19): pp. 1184-1189.

24. Hiroshi, O. and K. Nobuhiro, *New Fabrication Method for Poly(vinyl alcohol)/Liquid Crystal Composite Films with Controlled Droplet Size.* Japanese Journal of Applied Physics, 1995. **34**(1A-Part 2): pp. L54-L56.

25. Ueda, T., et al., *Growth of GaAs microcrystal by Ga droplet formation and successive As supply with low-pressure metalorganic chemical vapor deposition.* Journal of Crystal Growth, 1994. **145**(1–4): pp. 707-713.

26. Lefebvre, A.H., *Atomization and sprays*. 1989, New York: Hemisphere Publishing Corp.

27. Yang, J., L.C. Chow, and M.R. Pais, *Nucleate Boiling Heat Transfer in Spray Cooling.* Journal of Heat Transfer, 1996. **118**(3): pp. 668-671.

28. Jafari, M. 2014. *Analysis of heat transfer in spray cooling systems using numerical simulations.* Master Thesis, University of Windsor.

29. Kim, J., *Spray cooling heat transfer: The state of the art.* International Journal of Heat and Fluid Flow, 2007. **28**(4): pp. 753-767.

30. Zhibin, Y., et al., eds. *Spray Cooling*. Two Phase Flow, Phase Change and Numerical Modeling, ed. A. Amimul. September 26, 2011 InTech. 596.

31. Deegan, R.D., et al., *Contact line deposits in an evaporating drop.* Physical Review E, 2000. **62**(1): pp. 756-765.

32. Pradhan, T.K. and P.K. Panigrahi, *Deposition pattern of interacting droplets.* Colloids and Surfaces A: Physicochemical and Engineering Aspects, 2015. **482**: pp. 562-567.

33. Pradhan, T.K. and P.K. Panigrahi, *Influence of an adjacent droplet on fluid convection inside an evaporating droplet of binary mixture.* Colloids and Surfaces A: Physicochemical and Engineering Aspects, 2016. **500**: pp. 154-165.

34. Doursat, C., et al., *Droplet evaporation on a solid surface exposed to forced convection: Experiments, simulation and dimensional analysis.* International Journal of Heat and Mass Transfer, 2017. **113**: pp. 1234-1245.

35. Çengel, Y.A., *Introduction to thermodynamics and heat transfer*. 2nd ed. 2008, New York, NY: McGraw-Hill Higher Education.

36. Yu, J. and H. Wang, *A molecular dynamics investigation on evaporation of thin liquid films.* International Journal of Heat and Mass Transfer, 2012. **55**(4): pp. 1218-1225.

37. Ghasemi, H. and C.A. Ward, *Energy Transport by Thermocapillary Convection during Sessile-Water-Droplet Evaporation.* Physical Review Letters, 2010. **105**(13): pp. 136102-136105.

38. Incropera, F.P., et al., *Principles of heat and mass transfer*. 7th ed. 2013, New York, NY: Wiley. 1048.

39. Mugele, F. and J.-C. Baret, *Electrowetting: from basics to applications.* Journal of Physics: Condensed Matter, 2005. **17**(28): pp. R705-R774.

40. Sazhin, S.S., *Advanced models of fuel droplet heating and evaporation.* Progress in Energy and Combustion Science, 2006. **32**(2): pp. 162-214.

41. Yildirim Erbil, H., *Control of stain geometry by drop evaporation of surfactant containing dispersions.* Advances in Colloid and Interface Science, 2015. **222**: pp. 275-290.

42. Eral, H.B., D.J.C.M. 't Mannetje, and J.M. Oh, *Contact angle hysteresis: a review of fundamentals and applications.* Colloid and Polymer Science, 2013. **291**(2): pp. 247-260.

43. Sefiane, K., *Patterns from drying drops.* Advances in Colloid and Interface Science, 2014. **206**: pp. 372-381.

44. Larson, R.G., *Transport and deposition patterns in drying sessile droplets.* AIChE Journal, 2014. **60**(5): pp. 1538-1571.

45. Kovalchuk, N.M., A. Trybala, and V.M. Starov, *Evaporation of sessile droplets.* Current Opinion in Colloid & Interface Science, 2014. **19**(4): pp. 336-342.

46. Askounis, A., et al., *Effect of particle geometry on triple line motion of nano-fluid drops and deposit nano-structuring.* Advances in Colloid and Interface Science, 2015. **222**: pp. 44-57.

47. Zhong, X., A. Crivoi, and F. Duan, *Sessile nanofluid droplet drying.* Advances in Colloid and Interface Science, 2015. **217**: pp. 13-30.

48. Garcia-Cordero, J.L. and Z.H. Fan, *Sessile droplets for chemical and biological assays.* Lab on a Chip, 2017. **17**(13): pp. 2150-2166.

49. Brutin, D. and V. Starov, *Recent advances in droplet wetting and evaporation.* Chemical Society Reviews, 2018. **47**(2): pp. 558-585.

50. Mampallil, D. and H.B. Eral, *A review on suppression and utilization of the coffee-ring effect.* Advances in Colloid and Interface Science, 2018. **252**: pp. 38-54.

51. Breitenbach, J., I.V. Roisman, and C. Tropea, *From drop impact physics to spray cooling models: a critical review.* Experiments in Fluids, 2018. **59**(3): pp. 1-21.

52. Dhar, P., *Thermofluidic Transport in Droplets under Electromagnetic Stimulus: A Comprehensive Review.* Journal of the Indian Institute of Science, 2018. **99**(1): pp. 105-119.

53. Mahmud, M.A. 2015. *Analysis of heat transfer and fluid flow in an evaporating sessile droplet for evaporative cooling applications.* Master of Applied Science, University of Ontario Institute of Technology.

54. Froessling, N., *On the evaporation of falling drops*. 1968, Army Biological Labs Frederick MD.

55. Johansen Crosby, E., *Spray Drying Handbook.* Drying Technology, 1989. **7**(2): pp. 419-425.

56. Ranz, W. and W. Marshall, *Evaporation from drops.* Chem. Eng. Prog, 1952. **48**(3): pp. 141-146.

57. Picknett, R.G. and R. Bexon, *The evaporation of sessile or pendant drops in still air.* Journal of Colloid And Interface Science, 1977. **61**(2): pp. 336-350.

58. Kinzer, G.D. and R. Gunn, *The Evaporation, Temperature and Thermal Relaxation-Time of Freely Falling Waterdrops.* Journal of Meteorology, 1951. **8**(2): pp. 71-83.

59. Bhardwaj, R., J.P. Longtin, and D. Attinger, *Interfacial temperature measurements, high-speed visualization and finite-element simulations of droplet impact and evaporation on a solid surface.* International Journal of Heat and Mass Transfer, 2010. **53**(19–20): pp. 3733-3744.

60. Fuchs, N.A., ed. *Evaporation and droplet growth in gaseous media*. ed. J.M. Pratt. 1959, Pergamon Press: New York.

61. Kukkonen, J., T. Vesala, and M. Kulmala, *The interdependence of evaporation and settling for airborne freely falling droplets.* Journal of Aerosol Science, 1989. **20**(7): pp. 749-763.

62. Maxwell, J.C., *Collected scientific papers*. Vol. 2. 1890, Cambridge: CUP. 625.

63. Brenn, G., et al., *Evaporation of acoustically levitated multi-component liquid droplets.* International Journal of Heat and Mass Transfer, 2007. **50**(25–26): pp. 5073-5086.

64. Imaoka, R.T. and W.A. Sirignano, *Vaporization and combustion in three-dimensional droplet arrays.* Proceedings of the Combustion Institute, 2005. **30**(2): pp. 1981-1989.

65. Sazhin, S.S., et al., *A simplified model for bi-component droplet heating and evaporation.* International Journal of Heat and Mass Transfer, 2010. **53**(21–22): pp. 4495-4505.

66. Gudris , N. and L. Kulikowa *The evaporation of small drops of water. Z*. Phys., 1924. **25**: pp. 121-132.

67. Nestle, R.Z., *Vaporisation phenomena in mercury particles.* Z Physik, 1932. **77**: pp. 174-197.

68. Woodland, D.J. and E.J. Mack, *The effect of curvature of surface on surface energy. Rate of evaporation of liquid droplets. Thickness of saturated vapor films.* Journal of the American Chemical Society, 1933. **55**(8): pp. 3149-3161.

69. Shereshefsky, J.L. and S. Steckler, *A Study of the Evaporation of Small Drops and of the Relationship Between Surface Tension and Curvature.* The Journal of Chemical Physics, 1936. **4**(2): pp. 108-115.

70. Spalding, D., *Experiments on the burning and extinction of liquid fuel spheres.* Fuel, 1953. **32**(2): pp. 169-185.

71. Williams, A., *Combustion of sprays of liquid fuels*. 1976, London, UK: Elek Science. 132.

72. Law, C.K., *Recent advances in droplet vaporization and combustion.* Progress in Energy and Combustion Science, 1982. **8**(3): pp. 171-201.

73. Zhifu, Z., et al., *Evaluation of Evaporation Models for Single Moving Droplet with a High Evaporation Rate.* Powder Technology, 2013. **240**: pp. 95-102.

74. Agrawal, M., et al., *Nonspherical liquid droplet falling in air.* Physical Review E, 2017. **95**(3): pp. 033111-033119.

75. Ranz, W. and W.R. Marshall, *Evaporation from drops: Part 1.* Chem. Eng. Prog, 1952. **48**(3): pp. 141-146.

76. Ranz, W. and W.R. Marshall, *Evaporation from drops: Part 2.* Chem. Eng. Prog, 1952. **48**(3): pp. 141-146.

77. Langstroth, G.O., C.H.H. Diehl, and E.J. Winhold, *The evaporation of droplets in still air.* Canadian Journal of Research, 1950. **28a**(6): pp. 580-595.

78. Godsave, G.A.E., *Studies of the combustion of drops in a fuel spray—the burning of single drops of fuel.* Symposium (International) on Combustion, 1953. **4**(1): pp. 818-830.

79. Rossow, V.J., *Boundary-layer stability diagrams for electrically conducting fluids in the presence of a magnetic field*. 1958: US Government Printing Office. pp. 1-16.

80. Pradhan, T.K. and P.K. Panigrahi, *Evaporation induced natural convection inside a droplet of aqueous solution placed on a superhydrophobic surface.* Colloids and Surfaces A: Physicochemical and Engineering Aspects, 2017. **530**: pp. 1-12.

81. Jaiswal, V., et al., *Ionic solubility and solutal advection governed augmented evaporation kinetics of salt solution pendant droplets.* Physics of Fluids, 2018. **30**(1): pp. 012113-012125.

82. Walls, D.J., E. Meiburg, and G.G. Fuller, *The shape evolution of liquid droplets in miscible environments.* Journal of Fluid Mechanics, 2018. **852**: pp. 422-452.

83. Somwanshi, P.M., K. Muralidhar, and S. Khandekar, *Coalescence dynamics of sessile and pendant liquid drops placed on a hydrophobic surface.* Physics of Fluids, 2018. **30**(9): pp. 092103-092116.

84. Sterlyagov, A.N., et al., *Experimental study of the evaporation of suspended droplets of a water-ethanol solution.* Journal of Physics: Conference Series, 2018. **1128**: pp. 1-5.

85. Li, W., et al., *Pattern Formation in Drying Sessile and Pendant Droplet: Interactions of Gravity Settling, Interface Shrinkage, and Capillary Flow.* Langmuir, 2019. **35**(1): pp. 113-119.

86. Young, T., *An Essay on the Cohesion of Fluids.* Philosophical Transactions of the Royal Society of London, 1805. **95**: pp. 65-87.

87. Mampallil, D., *Some physics inside drying droplets.* Resonance, 2014. **19**(2): pp. 123-134.

88. Birdi, K.S., D.T. Vu, and A. Winter, *A study of the evaporation rates of small water drops placed on a solid surface.* The Journal of Physical Chemistry, 1989. **93**(9): pp. 3702-3703.

89. Hu, H. and R.G. Larson, *Evaporation of a Sessile Droplet on a Substrate.* The Journal of Physical Chemistry B, 2002. **106**(6): pp. 1334-1344.

90. Sefiane, K. and L. Tadrist, *Experimental investigation of the de-pinning phenomenon on rough surfaces of volatile drops.* International Communications in Heat and Mass Transfer, 2006. **33**(4): pp. 482-490.

91. Stauber, J.M., et al., *On the lifetimes of evaporating droplets.* Journal of Fluid Mechanics, 2014. **744**: pp. 1-12.

92. Fang, X., et al., *Factors Controlling the Drop Evaporation Constant.* The Journal of Physical Chemistry B, 2005. **109**(43): pp. 20554-20557.

93. Zhang, B.J., et al., *Biologically inspired tunable hydrophilic/hydrophobic surfaces: a copper oxide self-assembly multitier approach.* Bioinspiration & Biomimetics, 2012. **7**(3): pp. 1-13.

94. Cachile, M., O. Bénichou, and A.M. Cazabat, *Evaporating Droplets of Completely Wetting Liquids.* Langmuir, 2002. **18**(21): pp. 7985-7990.

95. Cachile, M., et al., *Evaporating Droplets.* Langmuir, 2002. **18**(21): pp. 8070-8078.

96. Poulard, C., O. Bénichou, and A.M. Cazabat, *Freely Receding Evaporating Droplets.* Langmuir, 2003. **19**(21): pp. 8828-8834.

97. Guena, G., C. Poulard, and A.M. Cazabat, *The dynamics of evaporating sessile droplets.* Colloid Journal, 2007. **69**(1): pp. 1-8.

98. Haley, P.J. and M.J. Miksis, *The effect of the contact line on droplet spreading.* Journal of Fluid Mechanics, 1991. **223**: pp. 57-81.

99. Lee, K.S., et al., *Spreading and evaporation of sessile droplets: Universal behaviour in the case of complete wetting.* Colloids and Surfaces A: Physicochemical and Engineering Aspects, 2008. **323**(1–3): pp. 63-72.

100. Shahidzadeh-Bonn, N., et al., *Evaporating droplets.* Journal of Fluid Mechanics, 2006. **549**: pp. 307-313.

101. Maatar, A., et al., *Transient effects on sessile droplet evaporation of volatile liquids.* International Journal of Heat and Mass Transfer, 2015. **86**: pp. 212-220.

102. Schweigler, K.M., et al., *Experimental and numerical investigation of drop evaporation depending on the shape of the liquid/gas interface.*

International Journal of Heat and Mass Transfer, 2017. **105**(Supplement C): pp. 655-663.

103. Dunn, G.J., et al., *A mathematical model for the evaporation of a thin sessile liquid droplet: Comparison between experiment and theory.* Colloids and Surfaces A: Physicochemical and Engineering Aspects, 2008. **323**(1–3): pp. 50-55.

104. Sefiane, K., et al., *On the effect of the atmosphere on the evaporation of sessile droplets of water.* Physics of Fluids, 2009. **21**(6): pp. 062101-062109.

105. François, B., I. François, and H.A. Stone, *Coffee-stain growth dynamics on dry and wet surfaces.* Journal of Physics: Condensed Matter, 2016. **29**(7): pp. 1-12.

106. Sefiane, K., *Effect of nonionic surfactant on wetting behavior of an evaporating drop under a reduced pressure environment.* Journal of Colloid and Interface Science, 2004. **272**(2): pp. 411-419.

107. David, S., K. Sefiane, and L. Tadrist, *Experimental investigation of the effect of thermal properties of the substrate in the wetting and evaporation of sessile drops.* Colloids and Surfaces A: Physicochemical and Engineering Aspects, 2007. **298**(1–2): pp. 108-114.

108. Dunn, G.J., et al., *The strong influence of substrate conductivity on droplet evaporation.* Journal of Fluid Mechanics, 2009. **623**: pp. 329-351.

109. Nagornov, O. and N. Starostin. *Influence of substrate properties on evaporation of the sessile drop*. in *Advances in Engineering Mechanics and Materials*. 2014. Santorini Island, Greece.

110. Bazargan, V. and B. Stoeber, *Effect of substrate conductivity on the evaporation of small sessile droplets.* Physical Review E, 2016. **94**(3): pp. 033103-033107.

111. Li, Y., et al., *Investigation of evaporation process of water droplet on different material surfaces*, in *Chemeca 2016: Chemical Engineering-Regeneration, Recovery and Reinvention*. 2016: Melbourne, Australia. pp. 1085-1095.

112. Barash, L.Y., *Dependence of fluid flows in an evaporating sessile droplet on the characteristics of the substrate.* International Journal of Heat and Mass Transfer, 2015. **84**: pp. 419-426.

113. Zhu, S., et al., *Superspreading of water—silicone surfactant on hydrophobic surfaces.* Colloids and Surfaces A: Physicochemical and Engineering Aspects, 1994. **90**(1): pp. 63-78.

114. Misyura, S.Y., *Contact angle and droplet heat transfer during evaporation on structured and smooth surfaces of heated wall.* Applied Surface Science, 2017. **414**: pp. 188-196.

115. Misyura, S.Y., *Contact angle and droplet evaporation on the smooth and structured wall surface in a wide range of droplet diameters.* Applied Thermal Engineering, 2017. **113**(Supplement C): pp. 472-480.

116. Stauber, J.M., et al., *Evaporation of Droplets on Strongly Hydrophobic Substrates.* Langmuir, 2015. **31**(12): pp. 3653-3660.

117. He, M., D. Liao, and H. Qiu, *Multicomponent Droplet Evaporation on Chemical Micro-Patterned Surfaces.* Scientific Reports, 2017. **7**: pp. 1-12.

118. Semenov, A.A. and D.V. Zaitsev, *The drop evaporation on a heated substrate with single wall nanotubes coating.* Journal of Physics: Conference Series, 2017. **925**: pp. 1-5.

119. Dhar, P., et al., *Superhydrophobic Surface Curvature Dependence of Internal Advection Dynamics within Sessile Droplets.* Langmuir, 2019. **35**(6): pp. 2326-2333.

120. Dash, S. and S.V. Garimella, *Droplet evaporation on heated hydrophobic and superhydrophobic surfaces.* Physical Review E, 2014. **89**(4): pp. 042402-042409.

121. Gao, M., et al., *An experimental investigation of sessile droplets evaporation on hydrophilic and hydrophobic heating surface with constant heat flux.* International Communications in Heat and Mass Transfer, 2017. **88**(Supplement C): pp. 262-268.

122. McHale, G., et al., *Analysis of Droplet Evaporation on a Superhydrophobic Surface.* Langmuir, 2005. **21**(24): pp. 11053-11060.

123. Duursma, G.R., K. Sefiane, and S. David, *Advancing and receding contact lines on patterned structured surfaces.* Chemical Engineering Research and Design, 2010. **88**(5–6): pp. 737-743.

124. Zhang, Y., et al., *Enhanced Coffee-Ring Effect via Substrate Roughness in Evaporation of Colloidal Droplets.* Advances in Condensed Matter Physics, 2018. **2018**: pp. 1-9.

125. Handscomb, C.S. 2009. *Simulating droplet drying and particle formation in spray towers.* Ph.D. Thesis, University of Cambridge.

126. Elimelech, M., *Particle deposition and aggregation: measurement, modelling, and simulation*. Vol. Pbk. 1998, Oxford England: Butterworth-Heinemann.

127. Deegan, R.D., et al., *Capillary flow as the cause of ring stains from dried liquid drops.* Nature, 1997. **389**(6653): pp. 827-829.

128. Deegan, R.D., *Pattern formation in drying drops.* Physical Review E, 2000. **61**(1): pp. 475-485.

129. Hu, H. and R.G. Larson, *Marangoni Effect Reverses Coffee-Ring Depositions.* The Journal of Physical Chemistry B, 2006. **110**(14): pp. 7090-7094.

130. Fischer, B.J., *Particle Convection in an Evaporating Colloidal Droplet.* Langmuir, 2002. **18**(1): pp. 60-67.

131. Popov, Y.O., *Evaporative deposition patterns: Spatial dimensions of the deposit.* Physical Review E, 2005. **71**(3): pp. 036313-036329.

132. Kim, J.Y. and B.M. Weon, *Evaporation of strong coffee drops.* Applied Physics Letters, 2018. **113**(18): pp. 183704-183708.

133. Starov, V. and K. Sefiane, *On evaporation rate and interfacial temperature of volatile sessile drops.* Colloids and Surfaces A: Physicochemical and Engineering Aspects, 2009. **333**(1–3): pp. 170-174.

134. Steinchen, A. and K. Sefiane, *Self-organised marangoni motion at evaporating drops or in capillary menisci – thermohydrodynamical model.* Journal of Non-Equilibrium Thermodynamics, 2005. **30**(1): pp. 39-51.

135. Hu, H. and R.G. Larson, *Analysis of the Effects of Marangoni Stresses on the Microflow in an Evaporating Sessile Droplet.* Langmuir, 2005. **21**(9): pp. 3972-3980.

136. Hu, H. and R.G. Larson, *Analysis of the Microfluid Flow in an Evaporating Sessile Droplet.* Langmuir, 2005. **21**(9): pp. 3963-3971.

137. Xu, X. and J. Luo, *Marangoni flow in an evaporating water droplet.* Applied Physics Letters, 2007. **91**(12): pp. 124102-124104.

138. Christy, J.R.E., K. Sefiane, and E. Munro, *A Study of the Velocity Field during Evaporation of Sessile Water and Water/Ethanol Drops.* Journal of Bionic Engineering, 2010. **7**(4): pp. 321-328.

139. Tseng, Y.-T., et al., *Fundamental studies on micro-droplet movement by Marangoni and capillary effects.* Sensors and Actuators A: Physical, 2004. **114**(2–3): pp. 292-301.

140. Widjaja, E. and M.T. Harris, *Particle deposition study during sessile drop evaporation.* AIChE Journal, 2008. **54**(9): pp. 2250-2260.

141. Xu, X., et al., *Linear growth of colloidal rings at the edge of drying droplets.* Colloids and Surfaces A: Physicochemical and Engineering Aspects, 2014. **447**: pp. 28-31.

142. Uno, K., et al., *Particle adsorption in evaporating droplets of polymer latex dispersions on hydrophilic and hydrophobic surfaces.* Colloid and Polymer Science, 1998. **276**(9): pp. 810-815.

143. Girard, F. and M. Antoni, *Influence of Substrate Heating on the Evaporation Dynamics of Pinned Water Droplets.* Langmuir, 2008. **24**(20): pp. 11342-11345.

144. Patil, N.D., et al., *Effects of Substrate Heating and Wettability on Evaporation Dynamics and Deposition Patterns for a Sessile Water Droplet Containing Colloidal Particles.* Langmuir, 2016. **32**(45): pp. 11958-11972.

145. Chen, L. and J.R.G. Evans, *Drying of colloidal droplets on superhydrophobic surfaces.* Journal of Colloid and Interface Science, 2010. **351**(1): pp. 283-287.

146. Al-Sharafi, A., et al., *Heat transfer characteristics and internal fluidity of a sessile droplet on hydrophilic and hydrophobic surfaces.* Applied Thermal Engineering, 2016. **108**(Supplement C): pp. 628-640.

147. Shmuylovich, L., A.Q. Shen, and H.A. Stone, *Surface Morphology of Drying Latex Films: Multiple Ring Formation.* Langmuir, 2002. **18**(9): pp. 3441-3445.

148. Bardakov, R.N., Y.D. Chashechkin, and V.V. Shabalin, *Hydrodynamics of a drying multicomponent liquid droplet.* Fluid Dynamics, 2010. **45**(5): pp. 803-816.

149. Nikolov, A.D., et al., *Superspreading driven by Marangoni flow.* Advances in Colloid and Interface Science, 2002. **96**(1–3): pp. 325-338.

150. Chengara, A., A. Nikolov, and D. Wasan, *Surface tension gradient driven spreading of trisiloxane surfactant solution on hydrophobic solid.* Colloids and Surfaces A: Physicochemical and Engineering Aspects, 2002. **206**(1–3): pp. 31-39.

151. Parsa, M., S. Harmand, and K. Sefiane, *Mechanisms of pattern formation from dried sessile drops.* Advances in Colloid and Interface Science, 2018. **254**: pp. 22-47.

152. Trokhymchuk, A., et al., *A Simple Calculation of Structural and Depletion Forces for Fluids/Suspensions Confined in a Film.* Langmuir, 2001. **17**(16): pp. 4940-4947.

153. Wasan, D., A. Nikolov, and B. Moudgil, *Colloidal dispersions: Structure, stability and geometric confinement.* Powder Technology, 2005. **153**(3): pp. 135-141.

154. Vafaei, S., et al., *Effect of nanoparticles on sessile droplet contact angle.* Nanotechnology, 2006. **17**(10): pp. 2523-2527.

155. Sefiane, K. and R. Bennacer, *Nanofluids droplets evaporation kinetics and wetting dynamics on rough heated substrates.* Advances in Colloid and Interface Science, 2009. **147–148**: pp. 263-271.

156. Dan, B., et al., *Templating of Self-Alignment Patterns of Anisotropic Gold Nanoparticles on Ordered SWNT Macrostructures.* ACS Applied Materials & Interfaces, 2011. **3**(9): pp. 3718-3724.

157. Darwich, S., et al., *Nanobubble and nanodroplet template growth of particle nanorings versus nanoholes in drying nanofluids and polymer films.* Nanoscale, 2011. **3**(3): pp. 1211-1217.

158. Chon, C.H., et al., *Effect of Nanoparticle Sizes and Number Densities on the Evaporation and Dryout Characteristics for Strongly Pinned Nanofluid Droplets.* Langmuir, 2007. **23**(6): pp. 2953-2960.

159. Zhong, X., H. Xie, and F. Duan, *Deposition patterns from evaporating sessile droplets with suspended mixtures of multi-sized and multi-species hydrophilic and non-adsorbing nanoparticles.* Applied Thermal Engineering, 2016. **111**: pp. 1565-1572.

160. Zhang, J., F. Leroy, and F. Müller-Plathe, *Evaporation of Nanodroplets on Heated Substrates: A Molecular Dynamics Simulation Study.* Langmuir, 2013. **29**(31): pp. 9770-9782.

161. Zhang, J., et al., *Formation of coffee-stain patterns at the nanoscale: The role of nanoparticle solubility and solvent evaporation rate.* The Journal of Chemical Physics, 2017. **146**(11): pp. 114503-114513.

162. Wray, A.W., et al., *Electrostatic Suppression of the "Coffee Stain Effect".* Langmuir, 2014. **30**(20): pp. 5849-5858.

163. Wray, A.W., et al., *Electrostatic Suppression of the "Coffee-stain Effect".* Procedia IUTAM, 2015. **15**: pp. 172-177.

164. Sefiane, K., *On the Formation of Regular Patterns from Drying Droplets and Their Potential Use for Bio-Medical Applications.* Journal of Bionic Engineering, 2010. **7**: pp. S82-S93.

165. Huang, D., L. Ma, and X. Xu, *The capillary outward flow inside pinned drying droplets.* International Journal of Heat and Mass Transfer, 2015. **83**: pp. 307-310.

166. Crivoi, A. and F. Duan, *Effect of Surfactant on the Drying Patterns of Graphite Nanofluid Droplets.* The Journal of Physical Chemistry B, 2013. **117**(19): pp. 5932-5938.

167. Crivoi, A. and F. Duan, *Elimination of the Coffee-Ring Effect by Promoting Particle Adsorption and Long-Range Interaction.* Langmuir, 2013. **29**(39): pp. 12067-12074.

168. Cui, L., et al., *Suppression of the coffee ring effect by hydrosoluble polymer additives.* ACS Applied Materials and Interfaces, 2012. **4**(5): pp. 2775-2780.

169. Morales, V.L., et al., *Surfactant-Mediated Control of Colloid Pattern Assembly and Attachment Strength in Evaporating Droplets.* Langmuir, 2013. **29**(6): pp. 1831-1840.

170. Cui, L., et al., *Avoiding coffee ring structure based on hydrophobic silicon pillar arrays during single-drop evaporation.* Soft Matter, 2012. **8**(40): pp. 10448-10456.

171. Weon, B.M. and J.H. Je, *Capillary force repels coffee-ring effect.* Physical Review E, 2010. **82**(1): pp. 015305-015308.

172. Bansal, L., et al., *Suppression of coffee ring: (Particle) size matters.* Applied Physics Letters, 2018. **112**(21): pp. 211605-211609.

173. Pradhan, T. and P. Panigrahi, *Thermocapillary convection inside a stationary sessile water droplet on a horizontal surface with an imposed temperature gradient.* Experiments in Fluids, 2015. **56**(9): pp. 1-11.

174. Lebovka, N.I., et al., *Drying of sessile droplets of laponite-based aqueous nanofluids.* Colloids and Surfaces A: Physicochemical and Engineering Aspects, 2014. **462**: pp. 52-63.

175. Yunker, P.J., et al., *Suppression of the coffee-ring effect by shape-dependent capillary interactions.* Nature, 2011. **476**(7360): pp. 308-311.

176. Xu, T., M.L. Lam, and T.-H. Chen, *Discrete Element Model for Suppression of Coffee-Ring Effect.* Scientific Reports, 2017. **7**: pp. 1-10.

177. Thokchom, A.K., et al., *Analysis of fluid flow and particle transport in evaporating droplets exposed to infrared heating.* International Journal of Heat and Mass Transfer, 2014. **68**: pp. 67-77.

178. Eral, H.B., et al., *Suppressing the coffee stain effect: How to control colloidal self-assembly in evaporating drops using electrowetting.* Soft Matter, 2011. **7**(10): pp. 4954-4958.

179. Malinowski, R., et al., *Dynamic Control of Particle Deposition in Evaporating Droplets by an External Point Source of Vapor.* The Journal of Physical Chemistry Letters, 2018. **9**(3): pp. 659-664.

180. Yen, T.M., et al., *Reversing Coffee-Ring Effect by Laser-Induced Differential Evaporation.* Scientific Reports, 2018. **8**(1): pp. 1-11.

181. Semenov, S., et al., *Computer Simulations of Evaporation of Pinned Sessile Droplets: Influence of Kinetic Effects.* Langmuir, 2012. **28**(43): pp. 15203-15211.

182. Semenov, S., V.M. Starov, and R.G. Rubio, *Evaporation of pinned sessile microdroplets of water on a highly heat-conductive substrate: Computer simulations.* The European Physical Journal Special Topics, 2013. **219**(1): pp. 143-154.

183. Carrier, O., et al., *Evaporation of water: evaporation rate and collective effects.* Journal of Fluid Mechanics, 2016. **798**: pp. 774-786.

184. Kelly-Zion, P.L., et al., *Evaporation of sessile drops under combined diffusion and natural convection.* Colloids and Surfaces A: Physicochemical and Engineering Aspects, 2011. **381**(1–3): pp. 31-36.

185. Carle, F., et al., *Contribution of convective transport to evaporation of sessile droplets: Empirical model.* International Journal of Thermal Sciences, 2016. **101**: pp. 35-47.

186. Gogos, G., S. Soh, and D.N. Pope, *Effects of gravity and ambient pressure on liquid fuel droplet evaporation.* International Journal of Heat and Mass Transfer, 2003. **46**(2): pp. 283-296.

187. Kelly-Zion, P.L., et al., *Evaporation rates of pure hydrocarbon liquids under the influences of natural convection and diffusion.* International Journal of Heat and Mass Transfer, 2009. **52**(13–14): pp. 3305-3313.

188. Ait Saada, M., S. Chikh, and L. Tadrist, *Numerical investigation of heat and mass transfer of an evaporating sessile drop on a horizontal surface.* Physics of Fluids, 2010. **22**(11): pp. 112115-112127.

189. Sill, B.L., *Free and Forced Convection Effects on Evaporation.* Journal of Hydraulic Engineering, 1983. **109**(9): pp. 1216-1231.

190. Zhang, H., *Evaporation of a suspended droplet in forced convective high-pressure environments.* Combustion Science and Technology, 2003. **175**(12): pp. 2237-2268.

191. Gan, Y. and L. Qiao, *Evaporation characteristics of fuel droplets with the addition of nanoparticles under natural and forced convections.* International Journal of Heat and Mass Transfer, 2011. **54**(23–24): pp. 4913-4922.

192. Garner, F.H. and R.W. Grafton, *Mass Transfer in Fluid Flow from a Solid Sphere.* Proceedings of the Royal Society of London. Series A, Mathematical and Physical Sciences, 1954. **224**(1156): pp. 64-82.

193. Garner, F.H. and R.B. Keey, *Mass-transfer from single solid spheres—I: Transfer at low Reynolds numbers.* Chemical Engineering Science, 1958. **9**(2): pp. 119-129.

194. Baines, W.D. and D.F. James, *Evaporation of a droplet on a surface.* Industrial & Engineering Chemistry Research, 1994. **33**(2): pp. 411-416.

195. Danberg, J.E., *Evaporation into Couette flow*. 2008, Science Applications International Corp (SAIC) Abingdon MD.

196. Danberg, J.E., *Mass Remaining During Evaporation of Sessile Drop*. 2008, Science Applications International Corp (SAIC) Abingdon MD.

197. Buffone, C., *Evaporating sessile drops subject to crosswind.* International Journal of Thermal Sciences, 2019. **144**: pp. 1-10.

198. Labowsky, M., *The effects of nearest neighbor interactions on the evaporation rate of cloud particles.* Chemical Engineering Science, 1976. **31**(9): pp. 803-813.

199. Labowsky, M., *A Formalism for Calculating the Evaporation Rates of Rapidly Evaporating Interacting Particles.* Combustion Science and Technology, 1978. **18**(3-4): pp. 145-151.

200. Labowsky, M., *Calculation of the Burning Rates of Interacting Fuel Droplets†.* Combustion Science and Technology, 1980. **22**(5-6): pp. 217-226.

201. Twardus, E.M. and T.A. Brzustowski, *The interaction between two burning fuel droplets.* Archiwum Termodynamiki Spalania, 1977. **8**(3): pp. 347-358.

202. Umemura, A., S. Ogawa, and N. Oshima, *Analysis of the interaction between two burning droplets.* Combustion and Flame, 1981. **41**: pp. 45-55.

203. Carles, P. and A.M. Cazabat, *Spreading involving the marangoni effect: Some preliminary results.* Colloids and Surfaces, 1989. **41**: pp. 97-105.

204. Chen, L. and J.R.G. Evans, *Arched Structures Created by Colloidal Droplets as They Dry.* Langmuir, 2009. **25**(19): pp. 11299-11301.

205. Cira, N.J., A. Benusiglio, and M. Prakash, *Vapour-mediated sensing and motility in two-component droplets.* Nature, 2015. **519**(7544): pp. 446-450.

206. Shaikeea, A.J.D. and S. Basu, *Evaporating sessile droplet pair: Insights into contact line motion, flow transitions and emergence of universal vaporisation pattern.* Applied Physics Letters, 2016. **108**(24): pp. 244102-244106.

207. Laghezza, G., et al., *Collective and convective effects compete in patterns of dissolving surface droplets.* Soft Matter, 2016. **12**(26): pp. 5787-5796.

208. Shaikeea, A.J.D. and S. Basu, *Insight into the Evaporation Dynamics of a Pair of Sessile Droplets on a Hydrophobic Substrate.* Langmuir, 2016. **32**(5): pp. 1309-1318.

209. Khilifi, D., et al., *Study of the phenomenon of the interaction between sessile drops during evaporation.* Thermal Science, 2019. **23**(No. 2B): pp. 1105-1114.

210. Hegde, O., et al., *Controlling self-assembly and buckling in nano fluid droplets through vapour mediated interaction of adjacent droplets.* Journal of Colloid and Interface Science, 2019. **541**: pp. 348-355.

211. Hatte, S., et al., *Universal evaporation dynamics of ordered arrays of sessile droplets.* Journal of Fluid Mechanics, 2019. **866**: pp. 61-81.

212. Girard, F., et al., *Influence of heating temperature and relative humidity in the evaporation of pinned droplets.* Colloids and Surfaces A: Physicochemical and Engineering Aspects, 2008. **323**(1–3): pp. 36-49.

213. Sobac, B. and D. Brutin, *Thermal effects of the substrate on water droplet evaporation.* Physical Review E, 2012. **86**(2): pp. 021602-021611.

214. Xu, X. and L. Ma, *Analysis of the effects of evaporative cooling on the evaporation of liquid droplets using a combined field approach.* Scientific Reports, 2015. **5**: pp. 1-6.

215. Wang, Y., et al., *Combined effects of underlying substrate and evaporative cooling on the evaporation of sessile liquid droplets.* Soft Matter, 2015. **11**(28): pp. 5632-5640.

216. Dunn, G.J., et al., *Evaporation of a thin droplet on a thin substrate with a high thermal resistance.* Physics of Fluids, 2009. **21**(5): pp. 52101-52107.

217. Hu, D., H. Wu, and Z. Liu, *Effect of liquid–vapor interface area on the evaporation rate of small sessile droplets.* International Journal of Thermal Sciences, 2014. **84**: pp. 300-308.

218. Kumar, M. and R. Bhardwaj, *A combined computational and experimental investigation on evaporation of a sessile water droplet on a heated hydrophilic substrate.* International Journal of Heat and Mass Transfer, 2018. **122**: pp. 1223-1238.

219. Nguyen, T.A.H., S.R. Biggs, and A.V. Nguyen, *Analytical Model for Diffusive Evaporation of Sessile Droplets Coupled with Interfacial Cooling Effect.* Langmuir, 2018. **34**(23): pp. 6955-6962.

220. Tran, H.V., et al., *On the predictions for diffusion-driven evaporation of sessile droplets with interface cooling.* Chemical Engineering Science, 2018. **177**: pp. 417-421.

221. Schofield, F.G.H., et al., *The lifetimes of evaporating sessile droplets are significantly extended by strong thermal effects.* Journal of Fluid Mechanics, 2018. **851**: pp. 231-244.

222. Ruiz, O.E. and W.Z. Black, *Evaporation of water droplets placed on a heated horizontal surface.* Journal of Heat Transfer-Transactions of The ASME, 2002. **124**(5): pp. 854-863.

223. Girard, F., et al., *Evaporation and Marangoni Driven Convection in Small Heated Water Droplets.* Langmuir, 2006. **22**(26): pp. 11085-11091.

224. Girard, F., M. Antoni, and K. Sefiane, *On the Effect of Marangoni Flow on Evaporation Rates of Heated Water Drops.* Langmuir, 2008. **24**(17): pp. 9207-9210.

225. Widjaja, E. and M.T. Harris, *Numerical study of vapor phase-diffusion driven sessile drop evaporation.* Computers & Chemical Engineering, 2008. **32**(10): pp. 2169-2178.

226. Lopes, M.C., et al., *Influence of the substrate thermal properties on sessile droplet evaporation: Effect of transient heat transport.* Colloids and Surfaces A: Physicochemical and Engineering Aspects, 2013. **432**: pp. 64-70.

227. Diddens, C., *Detailed finite element method modeling of evaporating multi-component droplets.* Journal of Computational Physics, 2017. **340**: pp. 670-687.

228. Chen, X., et al., *Thermal effects of substrate on Marangoni flow in droplet evaporation: Response surface and sensitivity analysis.* International Journal of Heat and Mass Transfer, 2017. **113**: pp. 354-365.

229. Bin, L., et al., *Transient Effects in Evaporating Sessile Drops: With and Without Heating.* Journal of Heat Transfer, 2016. **138**(9): pp. 091009-0910015.

230. Yang, K., F. Hong, and P. Cheng, *A fully coupled numerical simulation of sessile droplet evaporation using Arbitrary Lagrangian–Eulerian formulation.* International Journal of Heat and Mass Transfer, 2014. **70**: pp. 409-420.

231. Chen, Y.H., et al., *Transient effects and mass convection in sessile droplet evaporation: The role of liquid and substrate thermophysical properties.* International Journal of Heat and Mass Transfer, 2017. **108, Part B**: pp. 2072-2087.

232. Dell'Aversana, P., J.R. Banavar, and J. Koplik, *Suppression of coalescence by shear and temperature gradients.* Physics of Fluids, 1996. **8**(1): pp. 15-28.

233. Borcia, R. and M. Bestehorn, *Partial Coalescence of Sessile Drops with Different Miscible Liquids.* Langmuir, 2013. **29**(14): pp. 4426-4429.

234. Sellier, M., V. Nock, and C. Verdier, *Self-propelling, coalescing droplets.* International Journal of Multiphase Flow, 2011. **37**(5): pp. 462-468.

235. Sellier, M., et al., *Droplet actuation induced by coalescence: Experimental evidences and phenomenological modeling.* The European Physical Journal Special Topics, 2013. **219**(1): pp. 131-141.

236. Chakraborty, S., M.A. Rosen, and B.D. MacDonald, *Analysis and feasibility of an evaporative cooling system with diffusion-based sessile droplet evaporation for cooling microprocessors.* Applied Thermal Engineering, 2017. **125**: pp. 104-110.

237. Wray, A.W., B.R. Duffy, and S.K. Wilson, *Competitive evaporation of multiple sessile droplets.* Journal of Fluid Mechanics, 2019. **884**: pp. 1-19.

238. Misyura, S.Y., *Evaporation and heat and mass transfer of a sessile drop of aqueous salt solution on heated wall.* International Journal of Heat and Mass Transfer, 2018. **116**(Supplement C): pp. 667-674.

239. Strizhak, P.A., et al., *The role of convection in gas and liquid phases at droplet evaporation.* International Journal of Thermal Sciences, 2018. **134**: pp. 421-439.

240. Volkov, R.S., et al., *The influence of key factors on the heat and mass transfer of a sessile droplet.* Experimental Thermal and Fluid Science, 2018. **99**: pp. 59-70.

241. Zhang, H. 2000. *Evaporation of a spherical moving fuel droplet over a wide range of ambient pressures within a nitrogen environment.* Ph.D. thesis, University of Nebraska - Lincoln.

242. Navaz, H.K., E. Chan, and B. Markicevic, *Convective evaporation model of sessile droplets in a turbulent flow—comparison with wind tunnel data.* International Journal of Thermal Sciences, 2008. **47**(8): pp. 963-971.

243. Vik, T. and B.A. Pettersson Reif, *Modeling the evaporation from a thin liquid surface beneath a turbulent boundary layer.* International Journal of Thermal Sciences, 2011. **50**(12): pp. 2311-2317.

244. Raimundo, A.M., et al., *Wind tunnel measurements and numerical simulations of water evaporation in forced convection airflow.* International Journal of Thermal Sciences, 2014. **86**: pp. 28-40.

245. Shang, X., Z. Luo, and B. Bai, *Numerical simulation of dynamic behavior of compound droplets on solid surface in shear flow by front-tracing method.* Chemical Engineering Science, 2019. **193**: pp. 325-335.

246. Raghuram, S., et al., *Numerical study of Marangoni convection during transient evaporation of two-component droplet under forced convective environment.* International Journal of Heat and Mass Transfer, 2012. **55**(25–26): pp. 7949-7957.

247. Ljung, A.-L. and S.T. Lundström, *Evaporation of a sessile water droplet subjected to forced convection in humid environment.* Drying Technology, 2018. **37**(1): pp. 129-138.

248. Tal, R., D.N. Lee, and W.A. Sirignano, *Heat and momentum transfer around a pair of spheres in viscous flow.* International Journal of Heat and Mass Transfer, 1984. **27**(11): pp. 1953-1962.

249. Raju, M.S. and W.A. Sirignano, *Interaction between two vaporizing droplets in an intermediate Reynolds number flow.* Physics of Fluids A: Fluid Dynamics, 1990. **2**(10): pp. 1780-1796.

250. Liang, S.C., T. Hong, and L.S. Fan, *Effects of particle arrangements on the drag force of a particle in the intermediate flow regime.* International Journal of Multiphase Flow, 1996. **22**(2): pp. 285-306.

251. Yoon, D.-H. and K.-S. Yang, *Flow-induced forces on two nearby spheres.* Physics of Fluids, 2007. **19**(9): pp. 098103-098106.

252. Kishore, N., *Flow and Drag Phenomena of Tandem Spheroid Particles at Finite Reynolds Numbers.* Industrial & Engineering Chemistry Research, 2012. **51**(7): pp. 3186-3196.

253. Hooshanginejad, A. and S. Lee, *Droplet depinning in a wake.* Physical Review Fluids, 2017. **2**(3): pp. 031601-031610.

254. Razzaghi, A., S.A. Banitabaei, and A. Amirfazli, *Shedding of multiple sessile droplets by an airflow.* Physics of Fluids, 2018. **30**(8): pp. 087104-087112.

255. Hari, B. and A. Dhir, *Computational Fluid Dynamics and Multiphysics*, in *Introduction to Software for Chemical Engineers*, M.M. Martín, Editor. 2015, Taylor & Francis Group. pp. 604-654.

256. Semenov, S., et al., *Instantaneous distribution of fluxes in the course of evaporation of sessile liquid droplets: Computer simulations.* Colloids and Surfaces A: Physicochemical and Engineering Aspects, 2010. **372**(1–3): pp. 127-134.

257. Pradhan, T.K. and P.K. Panigrahi, *Evaporation-induced natural convection of a liquid slug of binary mixture inside a microchannel: effect of confinement.* Microfluidics and Nanofluidics, 2016. **20**(8): pp. 1-14.

258. Hu, D. and H. Wu, *Numerical study and predictions of evolution behaviors of evaporating pinned droplets based on a comprehensive model.* International Journal of Thermal Sciences, 2015. **96**: pp. 149-159.

259. Brutin, D., *Droplet wetting and evaporation: from pure to complex fluids*. 2015, Amsterdam: Academic Press is an imprint of Elsevier.

260. Lide, D.R. and T.J. Bruno, *CRC Handbook of Chemistry and Physics*. 2012-2013, Boca Raton: CRC Press.

261. Gelderblom, H., et al., *How water droplets evaporate on a superhydrophobic substrate.* Physical Review E, 2011. **83**(2): pp. 026306-026311.

262. Ait Saada, M., S. Chikh, and L. Tadrist, *Evaporation of a sessile drop with pinned or receding contact line on a substrate with different thermophysical properties.* International Journal of Heat and Mass Transfer, 2013. **58**(1): pp. 197-208.

263. Fan, J., M.C.T. Wilson, and N. Kapur, *Displacement of liquid droplets on a surface by a shearing air flow.* Journal of Colloid and Interface Science, 2011. **356**(1): pp. 286-292.

264. Dash, S. and S.V. Garimella, *Droplet Evaporation Dynamics on a Superhydrophobic Surface with Negligible Hysteresis.* Langmuir, 2013. **29**(34): pp. 10785-10795.

265. Monteith, J. and M. Unsworth, *Principles of Environmental Physics*. 2007: Academic Press. 1-418.

266. Shirani, E. and S. Masoomi, *Deformation of a Droplet in a Channel Flow.* Journal of Fuel Cell Science and Technology, 2008. **5**(4): pp. 041008-041015.

267. Isachenko, E.A., E.V. Orlik, and E.F. Bykovskaya, *Water droplet evaporation and dynamics in a mini-channel under action of the gas flow.* Journal of Physics: Conference Series, 2016. **754**(4): pp. 1-6.

268. Isachenko, E. and E. Orlik, *The effect of surface temperature on dynamics of water droplet in minichannel with gas flow.* EPJ Web Conference, 2017. **159**: pp. 1-6.

269. Barwari, B., S. Burgmann, and U. Janoske, *Deformation and movement of adhering droplets in shear flow*, in *5th International Conference on Experimental Fluid Mechanics*. 2018: Munich, Germany.

270. Burgmann, S., B. Barwari, and U. Janoske, *Oscillation of adhering droplets in shear flow*, in *5th International Conference on Experimental Fluid Mechanics*. 2018: Munich, Germany.

271. *COMSOL Multiphysics Reference guide V.5.3*. 2015, Burlington, MA, USA

272. Bhardwaj, R., *Analysis of an Evaporating Sessile Droplet on a Non-Wetted Surface.* Colloid and Interface Science Communications, 2018. **24**: pp. 49-53.

273. Lide, D.R. and W.M. Haynes, *CRC Handbook of Chemistry and Physics : A Ready-Reference Book of Chemical and Physical Data*. 2009, Boca Raton, Fla: CRC.

274. Kelly-Zion, P.L., J. Batra, and C.J. Pursell, *Correlation for the convective and diffusive evaporation of a sessile drop.* International Journal of Heat and Mass Transfer, 2013. **64**: pp. 278-285.

275. Misyura, S.Y., *Free convection and vapor diffusion of droplet aqueous solutions.* Chemical Engineering Research and Design, 2017. **126**(Supplement C): pp. 153-160.

276. Pham, T. and S. Kumar, *Drying of Droplets of Colloidal Suspensions on Rough Substrates.* Langmuir, 2017. **33**(38): pp. 10061-10076.

277. Martin, C., et al. *Assessing Quasi-Steady State in Evaporation of Sessile Drops by Diffusion Models*. in *APS Meeting Abstracts*. 2017.

278. Masoudi, S. and H.C. Kuhlmann, *Axisymmetric buoyant–thermocapillary flow in sessile and hanging droplets.* Journal of Fluid Mechanics, 2017. **826**: pp. 1066-1095.

279. Ljung, A.-L. and T.S. Lundström, *Heat and mass transfer boundary conditions at the surface of a heated sessile droplet.* Heat and Mass Transfer, 2017. **53**(12): pp. 3581-3591.

280. Misyura, S.Y., *Non-isothermal evaporation in a sessile droplet of water-salt solution.* International Journal of Thermal Sciences, 2018. **124**(Supplement C): pp. 76-84.

281. Qin, T. and R.O. Grigoriev, *A numerical study of buoyancy-Marangoni convection of volatile binary fluids in confined geometries.* International Journal of Heat and Mass Transfer, 2018. **127**: pp. 308-320.

282. Razzaghi, A. and A. Amirfazli, *Shedding of a pair of sessile droplets.* International Journal of Multiphase Flow, 2018. **110**: pp. 59-68.

283. Kang, K.H., et al., *Evaporation-induced saline Rayleigh convection inside a colloidal droplet.* Physics of Fluids, 2013. **25**(4): pp. 042001-042022.

284. Savino, R. and R. Monti, *Buoyancy and surface-tension-driven convection in hanging-drop protein crystallizer.* Journal of Crystal Growth, 1996. **165**(3): pp. 308-318.

285. Lee, S.J., J. Hong, and Y.-S. Choi, *Evaporation-Induced Flows inside a Confined Droplet of Diluted Saline Solution.* Langmuir, 2014. **30**(26): pp. 7710-7715.

286. Xu, G., et al., *Effect of Salt Concentration on the Motion of Particles near the Substrate in Drying Sessile Colloidal Droplets.* Langmuir, 2017. **33**(3): pp. 685-695.

287. Davoust, L. and J. Theisen, *Evaporation Rate of Drop Arrays within a Digital Microsystem.* Procedia Engineering, 2012. **47**: pp. 1-4.

288. Davoust, L. and J. Theisen, *Evaporation rate of drop arrays within a digital microfluidic system.* Sensors and Actuators B: Chemical, 2013. **189**: pp. 157-164.

289. Misyura, S.Y., *Evaporation of a sessile water drop and a drop of aqueous salt solution.* Scientific Reports, 2017. **7**(1): pp. 1-11.

290. Lin, H., et al., *Convective-diffusive transport in protein crystal growth.* Journal of Crystal Growth, 1995. **151**(1): pp. 153-162.

291. Schena, M., et al., *Quantitative Monitoring of Gene Expression Patterns with a Complementary DNA Microarray.* Science, 1995. **270**(5235): pp. 467-470.

292. Wilson, M.C.T. and K.J. Kubiak, *Simulation of Drops on Surfaces*, in *Fundamentals of Inkjet Printing*, S.D. Hoath, Editor. 2015.

Appendices

Appendix A Further results of Chapter 5

Further details of the fitting coefficients of Equations (5.2a) and (5.2b) including data and statistics of these fittings are provided in Table A-1.

Table A-1: Summary of the statistics for the logarithm, Equation (5.2a), and exponential, Equation (5.2b), fittings.

A			B		
α_A	Value	2.79427×10^{-9}	α_B	Value	-4.5341×10^{-4}
	Standard Error	6.9219×10^{-12}		Standard Error	1.3616×10^{-5}
β_A	Value	3.25023×10^{-10}	β_B	Value	-0.0015
	Standard Error	8.4426×10^{-12}		Standard Error	1.6189×10^{-5}
C_A	Value	0.01291	C_B	Value	0.58414
	Standard Error	0.00408		Standard Error	0.00901
Statistics	R-Square*	0.9979	Statistics	R-Square	0.9998
	Fit Status	Succeeded(100)		Fit Status	Succeeded(100)

* R-Square can be used to quantify how well a model fits the data, and should vary between 0 and 1. Generally, if it is close to 1, it indicates that the fitted line explains all the variability of the response data around its mean.

The influence of the evaporating isolated single sessile droplet on the surrounding environment, particularly the space downstream the droplet at different heights from the solid surface and at various airflow velocities is illustrated further in Figure A-1 and Figure A-2.

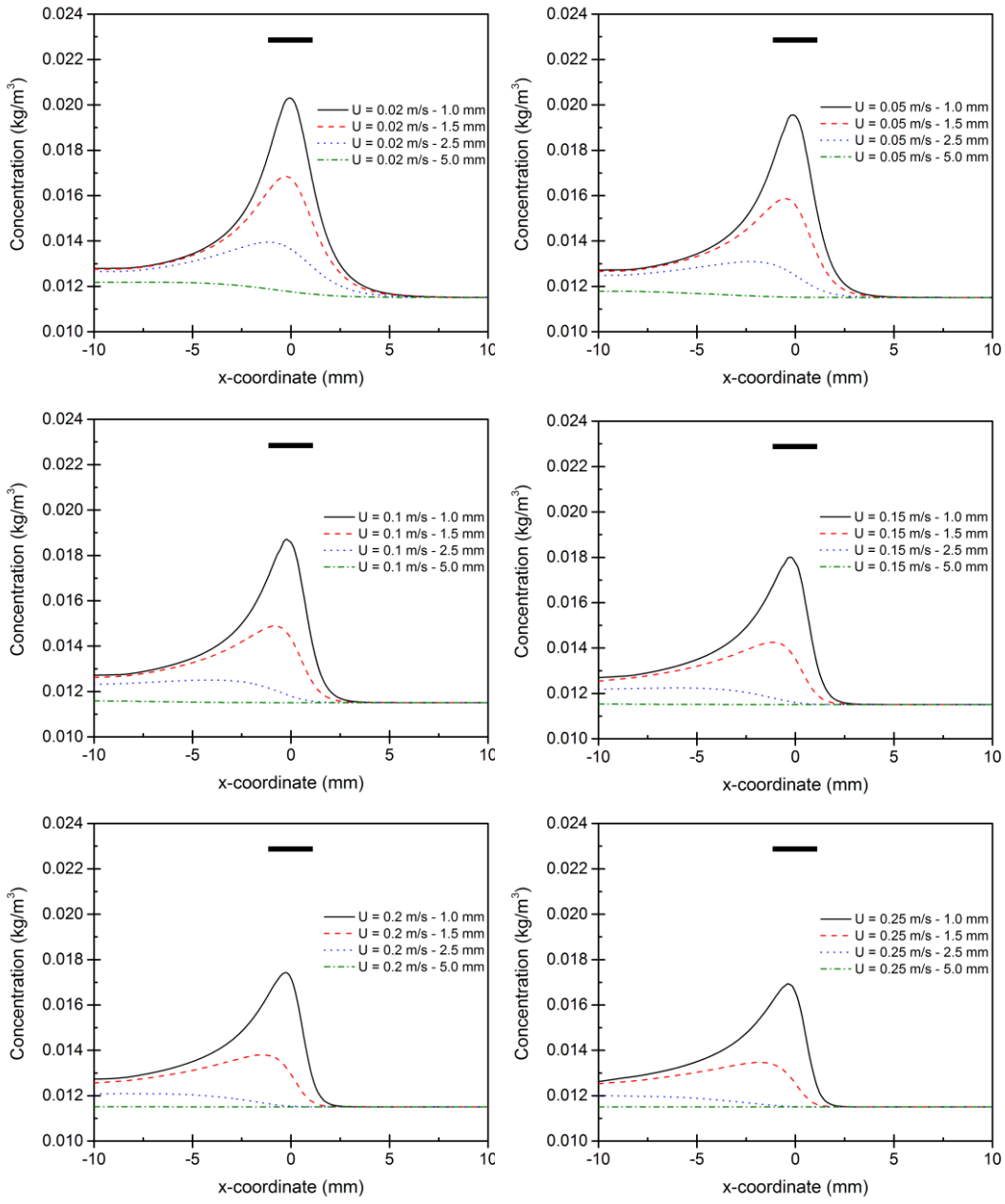

Figure A-1: Concentration levels along horizontal line located in the y = 0 centre plane and at different heights above the substrate, at *t* = 300s, and at various air speeds. The flow is from right to left. The position of the droplet is indicated by the thick horizontal black bar. (Continued)

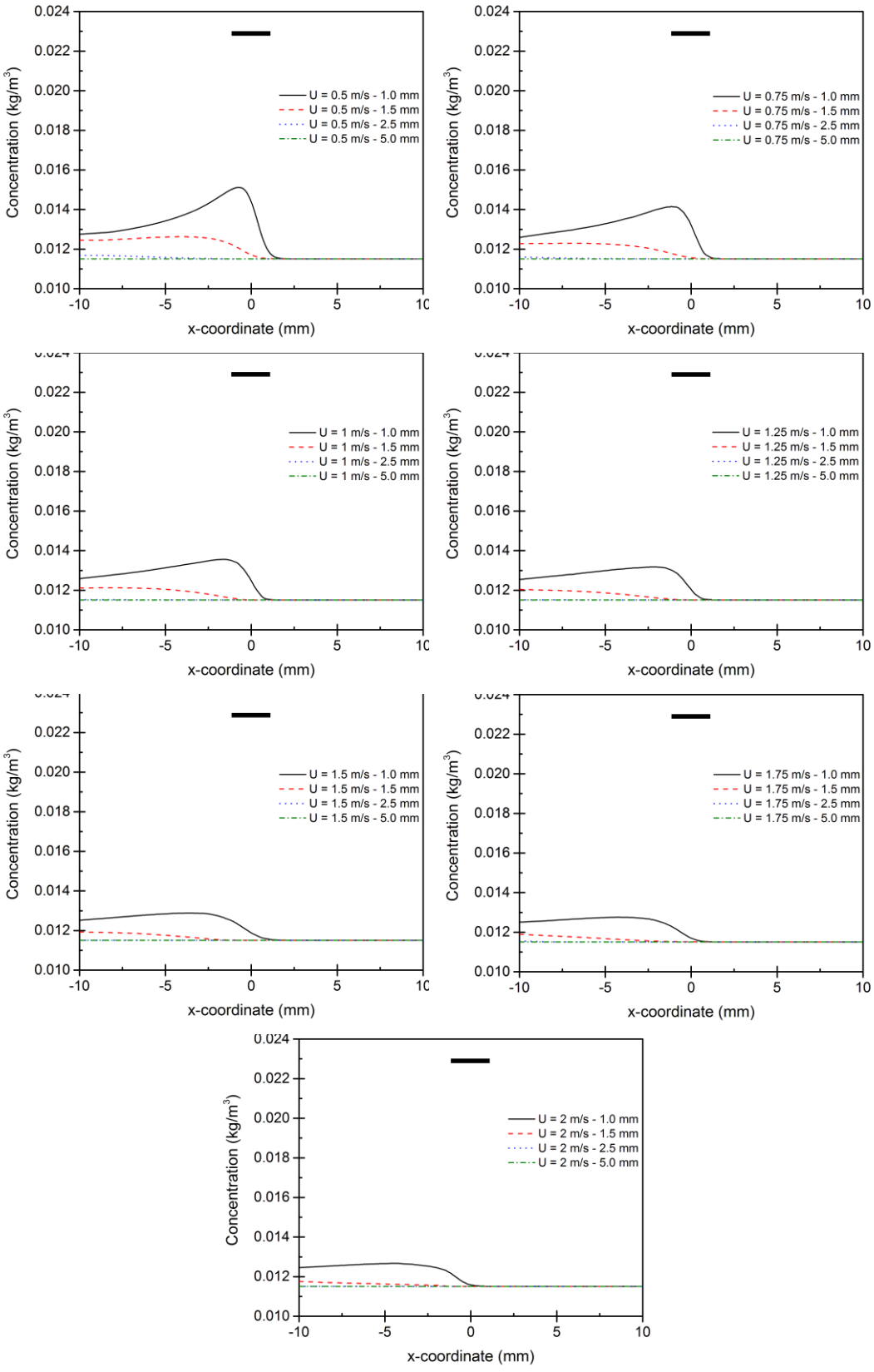

Figure A-2: Continued.

Appendix B Analysis study of 'no-slip' boundary condition

For the evaporation of a flat water circle under isothermal forced convection environment, discussed in Chapter 5, the evaporation of a water film with thickness (d) attached to a solid surface, with its other surface exposed to a non-saturated ambient air is considered here, as shown in Figure B-1, to analyse the reliable boundary condition applying on the surface of this water film. For unidirectional flow, the Navier-Stokes equations can be simplified as;

$$\mu \frac{d^2u}{dz^2} = \frac{dp}{dx} \tag{B.1}$$

By integrating Equation (B.1) twice, the velocity of air (at $z = H$) and the velocity of water (at $z = -d$) can be expressed as;

$$u_a = \frac{1}{2\mu_a}\frac{dp}{dx}H^2 + C_1H + C_2 = 0 \tag{B.2}$$

$$u_w = \frac{1}{2\mu_w}\frac{dp}{dx}d^2 - C_3d + C_4 = 0 \tag{B.3}$$

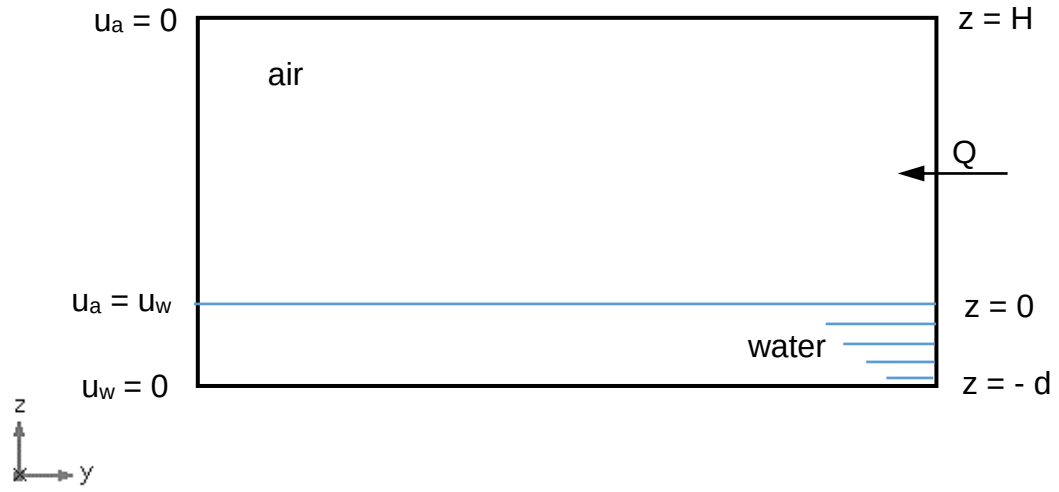

Figure B-1: Scheme of a water film evaporation to the ambient air.

At the water-air interface, $z = 0$, the stress in water side is the same as the stress in air side, and the velocity is also continuous at that interface since;

$$\mu_a \frac{du_a}{dz} = \mu_w \frac{du_w}{dz} \qquad \text{thus,} \qquad C_3 = \frac{\mu_a}{\mu_w} C_1 \tag{B.4}$$

$$u_a = u_w \qquad \text{thus,} \qquad C_2 = C_4 \tag{B.5}$$

By substituting C_2 and C_3 through Equations (B.2) and (B.3), and subtracting Equations (B.3) from Equations (B.2), an expression can be constructed;

$$\frac{1}{2\mu_a}\frac{dp}{dx}H^2 - \frac{1}{2\mu_w}\frac{dp}{dx}d^2 + C_1 H + C_1\frac{\mu_a}{\mu_w}d = 0 \tag{B.6}$$

$$C_1\left[H + \frac{\mu_a}{\mu_w}d\right] = -\frac{1}{2}\frac{dp}{dx}\left[\frac{H^2}{\mu_a} - \frac{d^2}{\mu_w}\right] \tag{B.7}$$

Thus,
$$C_1 = \frac{-\frac{1}{2}\frac{dp}{dx}\left[\frac{H^2}{\mu_a} - \frac{d^2}{\mu_w}\right]}{\left[H + \frac{\mu_a}{\mu_w}d\right]} = \frac{-\frac{1}{2\mu_a}\frac{dp}{dx}H\left[1 - \frac{\mu_a}{\mu_w}\left(\frac{d}{H}\right)^2\right]}{\left[1 + \frac{\mu_a}{\mu_w}\left(\frac{d}{H}\right)\right]} \tag{B.8}$$

Also,
$$C_2 = -\frac{1}{2\mu_a}\frac{dp}{dx}H^2 + \frac{\frac{1}{2}\frac{dp}{dx}H\left[\frac{H^2}{\mu_a} - \frac{d^2}{\mu_w}\right]}{\left[H + \frac{\mu_a}{\mu_w}d\right]} \tag{B.9}$$

$$C_2 = \frac{-\frac{1}{2}\frac{dp}{dx}\left[\frac{H^2}{\mu_a}\left(H + \frac{\mu_a}{\mu_w}d\right) - H\left(\frac{H^2}{\mu_a} - \frac{d^2}{\mu_w}\right)\right]}{\left[H + \frac{\mu_a}{\mu_w}d\right]} \quad \text{(B.10)}$$

Thus, $$C_2 = \frac{-\frac{1}{2}\frac{dp}{dx}\left[\frac{H^2 d}{\mu_w} + \frac{Hd^2}{\mu_w}\right]}{\left[H + \frac{\mu_a}{\mu_w}d\right]} = \frac{-\frac{1}{2\mu_w}\frac{dp}{dx}H^2\left[\frac{d}{H} + \left(\frac{d}{H}\right)^2\right]}{\left[1 + \frac{\mu_a}{\mu_w}\left(\frac{d}{H}\right)\right]} \quad \text{(B.11)}$$

By assuming, $\overline{\mu} = \frac{\mu_a}{\mu_w}$ and $\varepsilon = \frac{d}{H}$, Equations (B.8) and (B.11) can be written as;

$$C_1 = \frac{-\frac{1}{2\mu_a}\frac{dp}{dx}H\left[1 - \overline{\mu}\varepsilon^2\right]}{\left[1 + \overline{\mu}\varepsilon\right]} \quad \text{(B.12)}$$

$$C_2 = \frac{-\frac{1}{2\mu_w}\frac{dp}{dx}H^2\left[\varepsilon + \varepsilon^2\right]}{\left[1 + \overline{\mu}\varepsilon\right]} \quad \text{(B.13)}$$

The flow rate of air convection above water film, Q, can be obtained from;

$$Q = \int_0^H u_a dz = \overline{U}H \quad \text{(B.14)}$$

$$\frac{1}{6\mu_a}\frac{dp}{dx}H^2 + \frac{1}{2}HC_1 + C_2 = \overline{U} \quad \text{(B.15)}$$

By substituting C_1 and C_2, i.e., Equations (B.12) and (B.13), respectively through Equations (B.15), the pressure gradient in the flow direction can be expressed as;

$$\frac{1}{2}\frac{dp}{dx} = \frac{\overline{U}\left[1+\overline{\mu}\varepsilon\right]}{\frac{H^2}{3\mu_a}\left[1+\overline{\mu}\varepsilon\right]-\frac{H^2}{2\mu_a}\left[1-\overline{\mu}\varepsilon^2\right]-\frac{H^2}{\mu_w}\left[\varepsilon+\varepsilon^2\right]} \quad \text{(B.16)}$$

$$\frac{1}{2}\frac{dp}{dx} = \frac{\overline{U}\left[1+\overline{\mu}\varepsilon\right]}{\frac{H^2}{3\mu_a}\left[1+\overline{\mu}\varepsilon\right]-\frac{H^2}{2\mu_a}\left[1-\overline{\mu}\varepsilon^2\right]-\frac{H^2}{\mu_w}\left[\varepsilon+\varepsilon^2\right]} \quad \text{(B.16)}$$

As the slip speed at the surface of water film, $u_o(z=0) = C_2$ therefore, after substituting the pressure gradient terms in Equation (B.13) and simplifying the right-hand term, the slip speed can be expressed as;

$$u_o = \frac{6\overline{\mu}\overline{U}\left[\varepsilon-\varepsilon^2\right]}{1+4\overline{\mu}\varepsilon+3\overline{\mu}\varepsilon^2} \quad \text{(B.17)}$$

Now, as the two dimensionless factors $\overline{\mu}$ and ε tend to zero as a result of considering there is a great difference in the viscosity of both fluids and the thickness of water film is negligible, the slip speed at the film surface, in its turn, tends to zero as expressed below and shown in Figure B-2.

$$\lim_{\mu\to 0} u_o = 0 \quad \text{and} \quad \lim_{\varepsilon\to 0} u_o = 0 \quad \text{(B.18)}$$

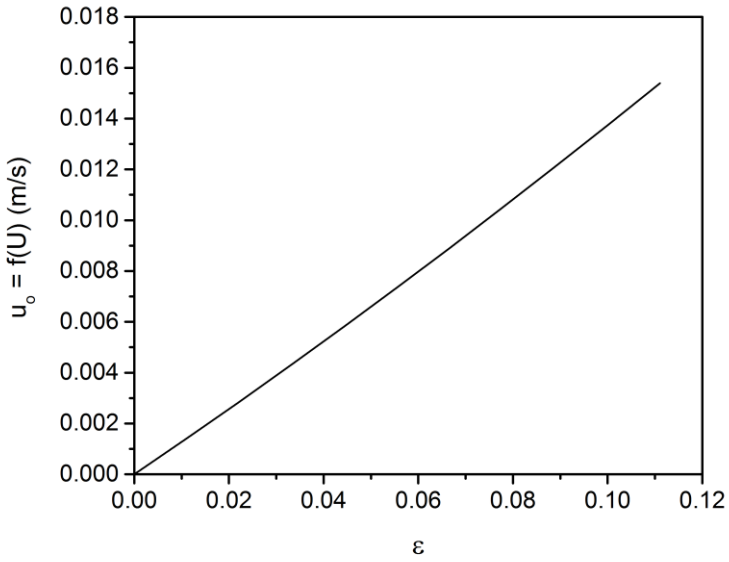

Figure B-2: The slip velocity at the surface of water film against the variation of the thickness of water film.

Appendix C Further results of the evaporation of interacting neighbouring sessile droplets

The evolution of the volume of perpendicular droplets with time and the curve fittings at various droplet distances and at 0.02 m/s, 0.2 m/s and 2.0 m/s air speed is illustrated in Figure C-1, Figure C-2 and Figure C-3, respectively.

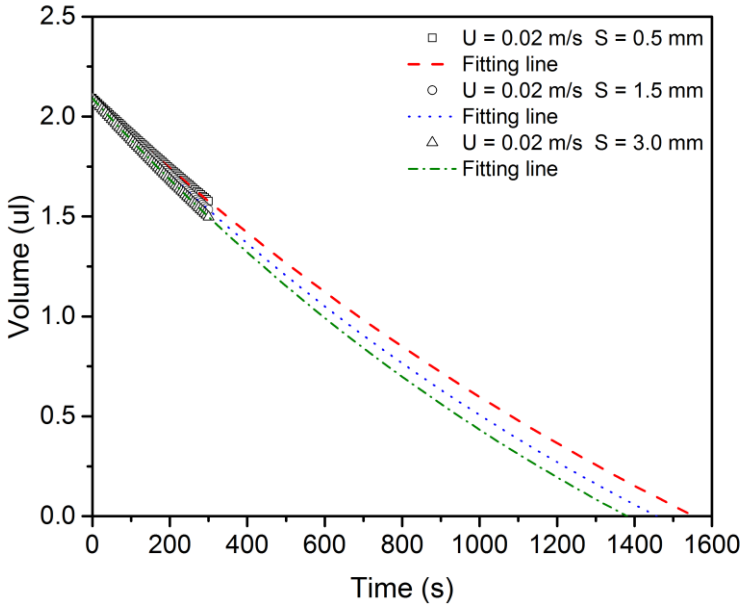

Figure C-1: Evolutions of the volume of neighbouring perpendicular droplets and the fitting lines for various separation distances and 0.02 m/s air speed.

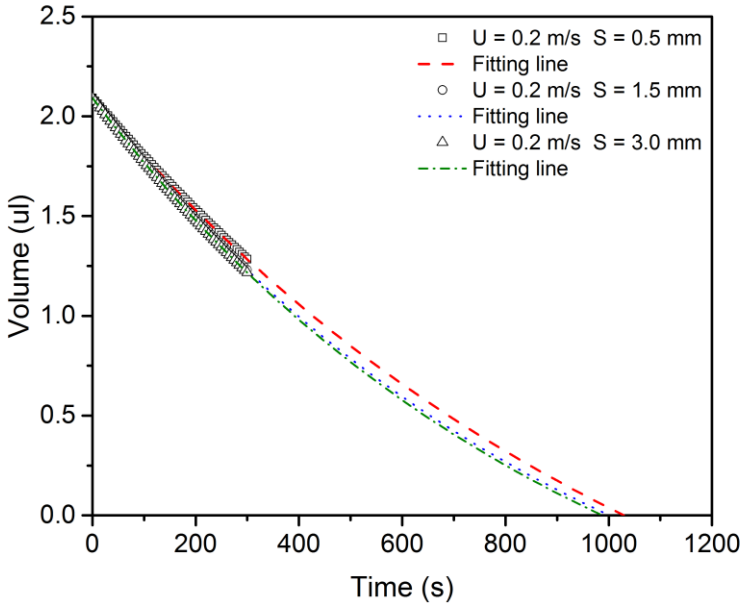

Figure C-2: Evolutions of the volume of neighbouring perpendicular droplets and the fitting lines for various separation distances and 0.2 m/s air speed.

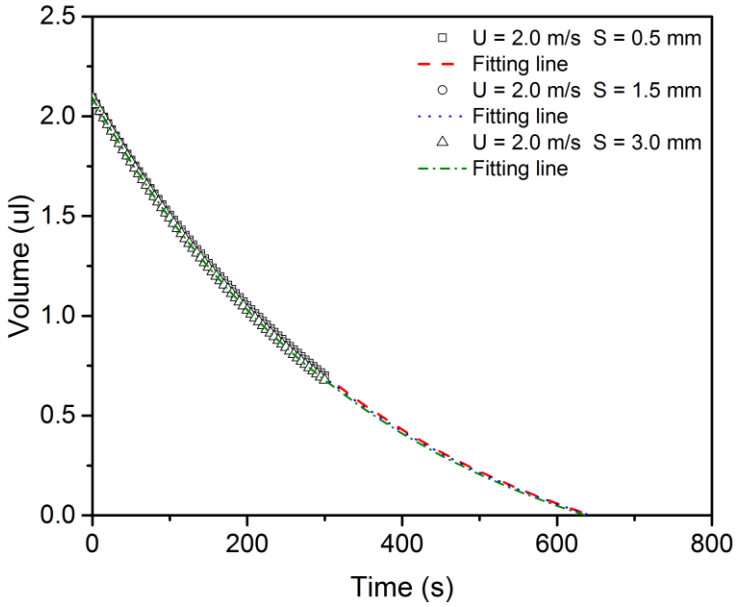

Figure C-3: Evolutions of the volume of neighbouring perpendicular droplets and the fitting lines for various separation distances and 2.0 m/s air speed.

The evolution profiles of the volume of parallel droplets (upstream and downstream droplets) at 300 s, and at various droplet distances considered for this droplets arrangement and at 0.02 m/s, 0.2 m/s and 2.0 m/s air speed are illustrated in Figure C-4, Figure C-5 and Figure C-6, respectively.

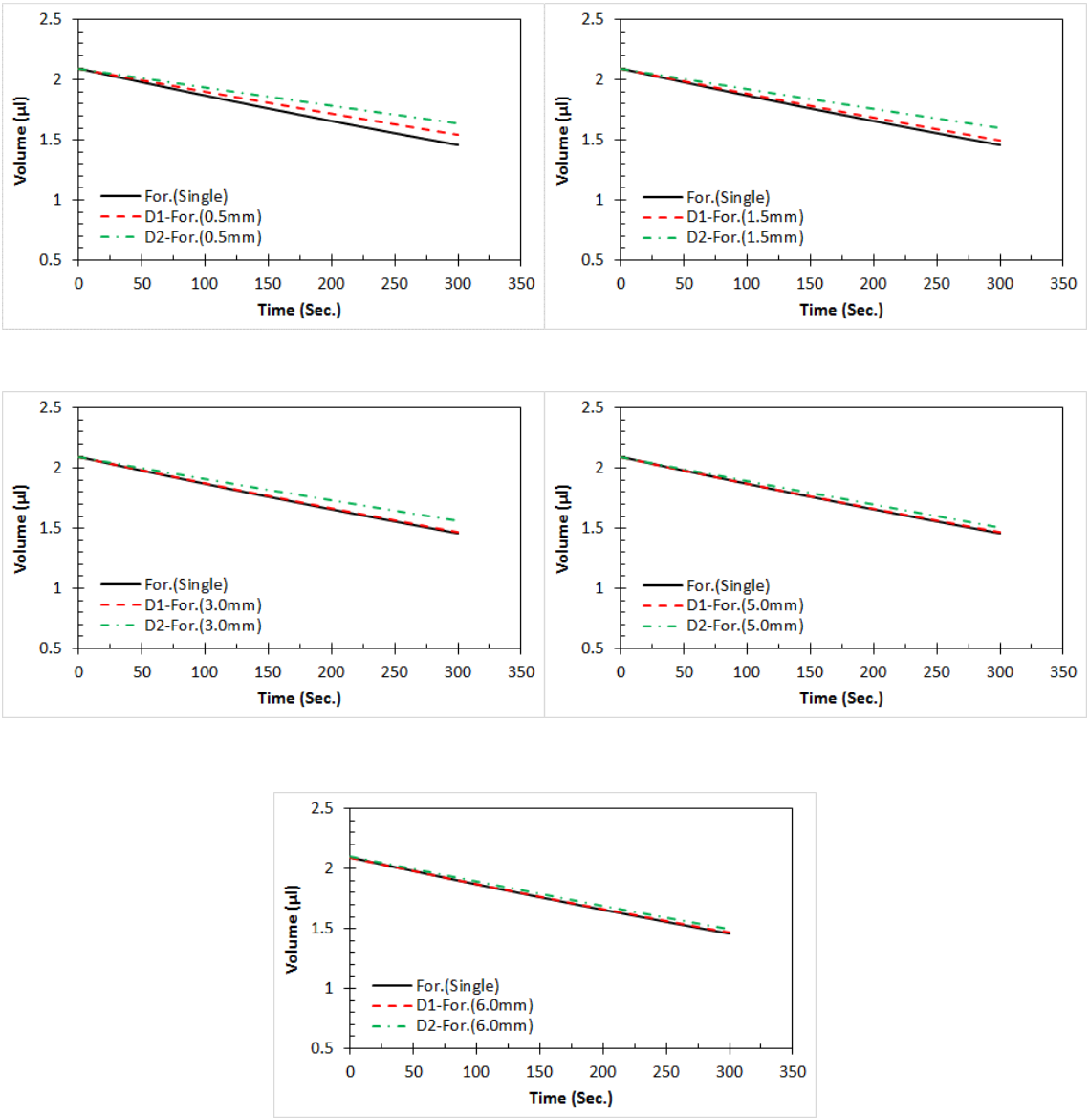

Figure C-4: The volume evolution profiles of parallel droplets at 300 s, and at U = 0.02 m/s and various separation distances compared to isolated single droplet (solid black line). Here, D1 and D2 represent the upstream and downstream droplets, respectively.

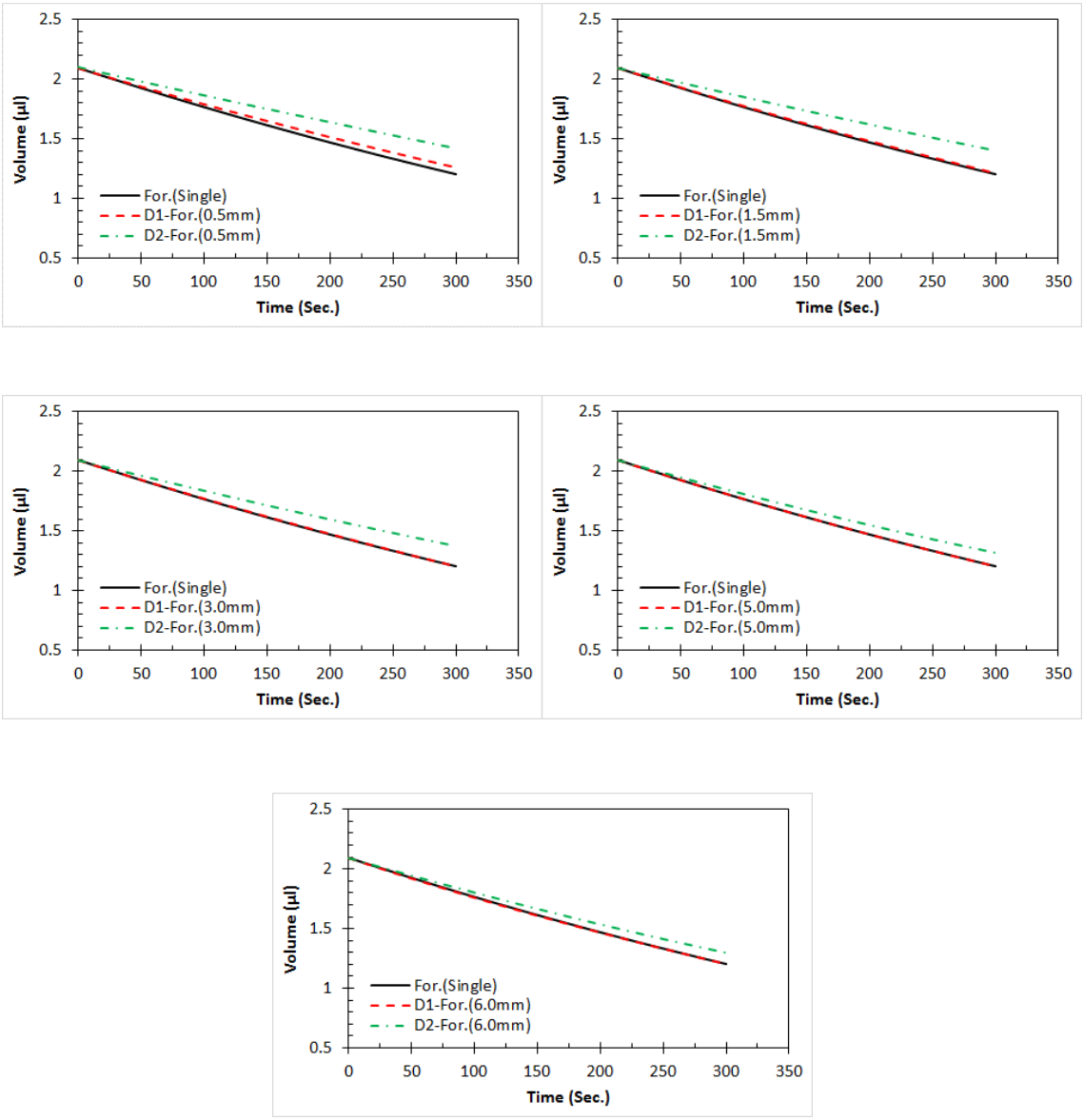

Figure C-5: The volume evolution profiles of parallel droplets at 300 s, and at U = 0.2 m/s and various separation distances compared to isolated single droplet (solid black line). Here, D1 and D2 represent the upstream and downstream droplets, respectively.

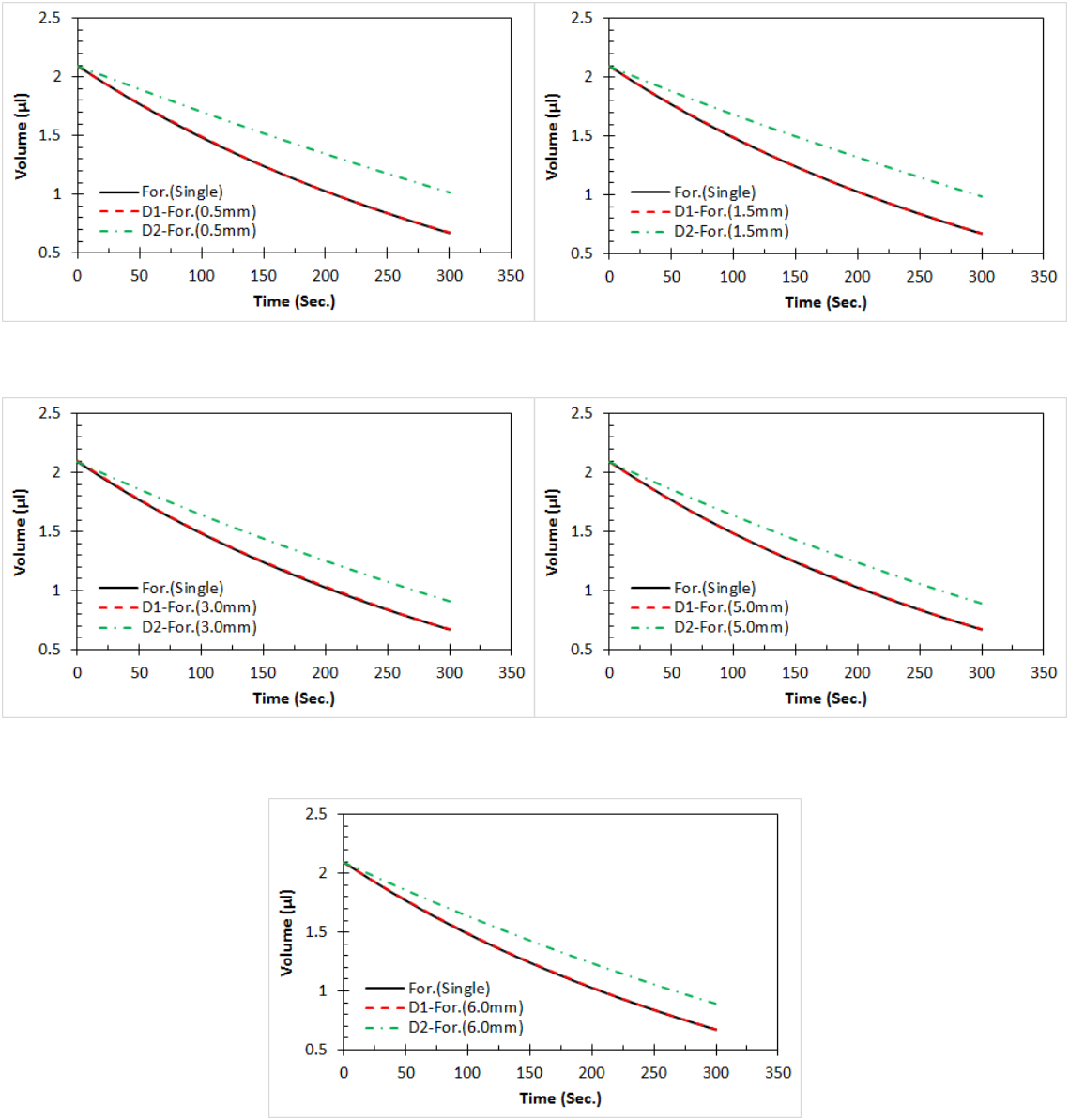

Figure C-6: The volume evolution profiles of parallel droplets at 300 s, and at U = 2.0 m/s and various separation distances compared to isolated single droplet (solid black line). Here, D1 and D2 represent the upstream and downstream droplets, respectively.

The evolutions of the volume of the upstream and downstream droplets with time and the curve fittings at various droplet distances and air speeds is illustrated in Figure C-7.

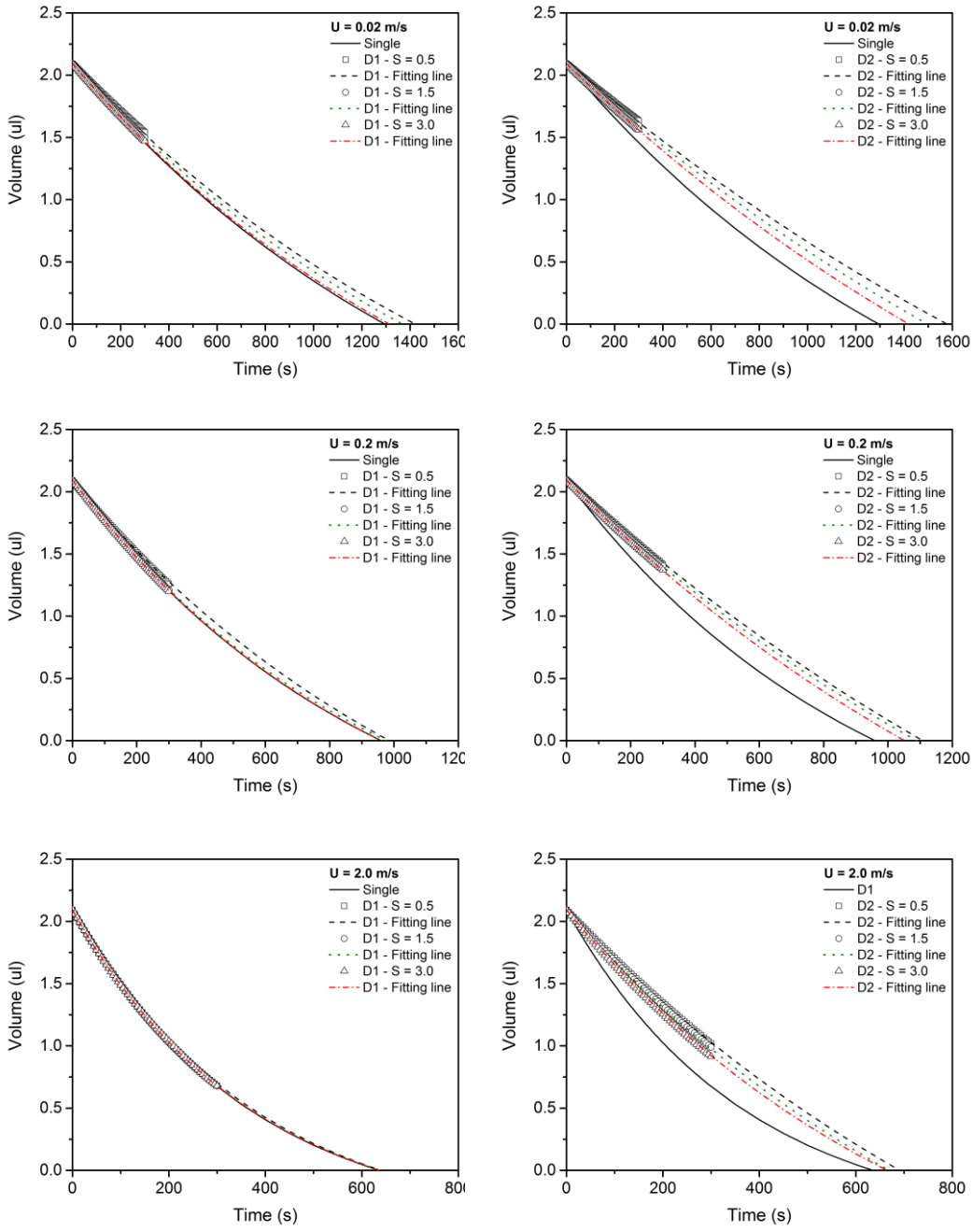

Figure C-7: Evolutions of the volume of neighbouring parallel droplets and the fitting lines for various separation distances and air speeds compared to the isolated single droplet. Here, D1 and D2 represent the upstream and downstream droplets, respectively.

The concentration levels above the upstream and downstream droplets and in the gap between them at various heights above the solid surface, at 300 s, and at the lowest and highest air speeds and for various droplet distances are shown in Figure C-8.

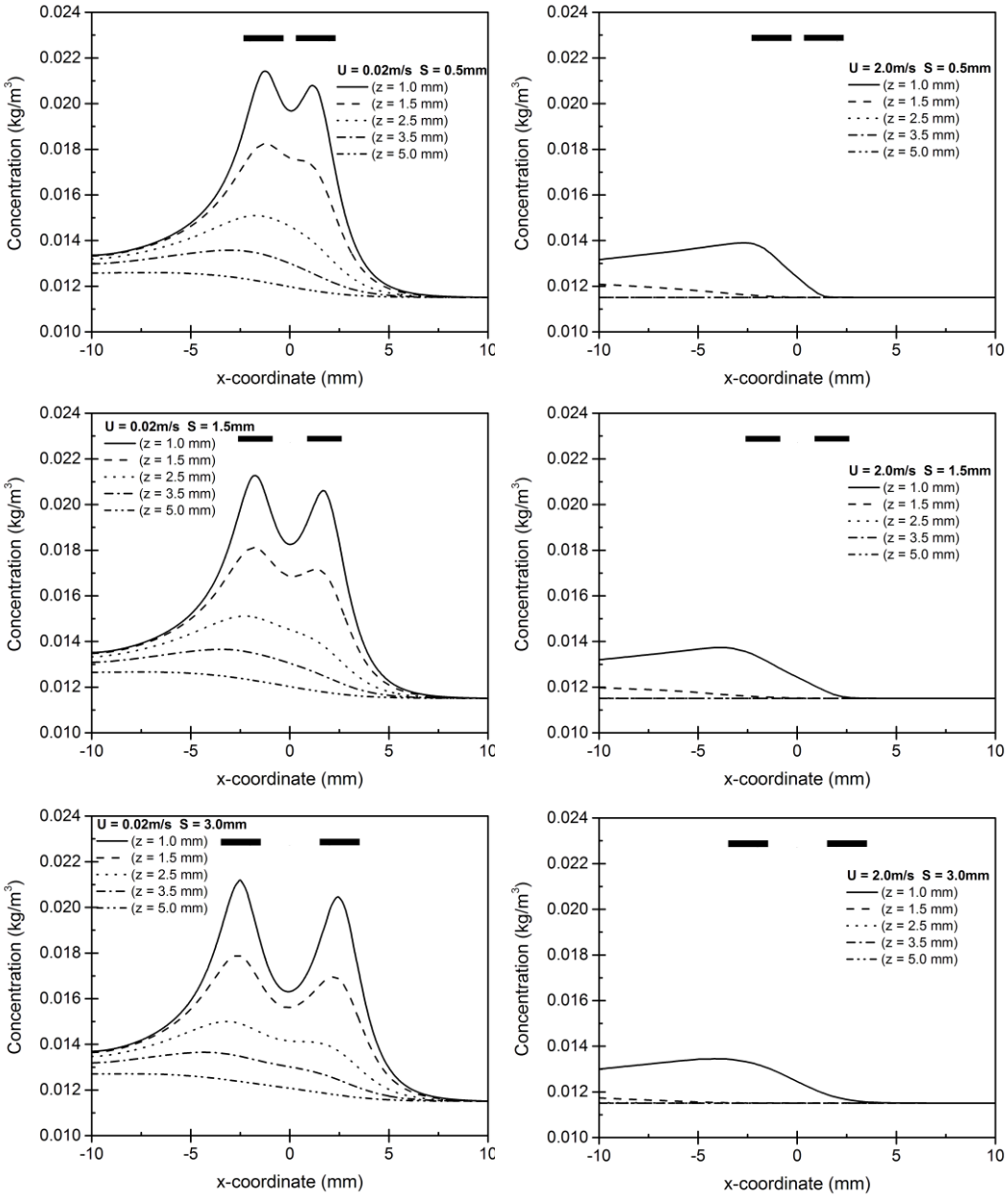

Figure C-8: Concentration levels along horizontal lines located in the y = 0 centre plane and at various heights above the substrate, at *t* = 300s, and at the lowest and highest air speeds. The positions of the droplets are indicated by the thick horizontal bars. The flow is from right to left.